GROWTH AND CHARACTERIZATIONS OF SEMICONDUCTOR QUANTUM WIRES

GROWTH AND CHARACTERIZATIONS OF SEMICONDUCTOR QUANTUM WIRES

By

KAI CUI, M. ENG., B. ENG.

A Thesis

Submitted to the School of Graduate Studies

in Partial Fulfillment of the Requirements

for the Degree

Doctor of Philosophy

McMaster University

DOCTOR OF PHILOSOPY (2009) McMaster University

(Department of Materials Science and Engineering) Hamilton, Ontario

TITLE: Growth and Characterization of Semiconductor Quantum Wires

AUTHOR: Kai Cui, M. Eng., B. Eng.

SUPERVISORS: Gianluigi A. Botton and David A. Thompson

NUMBER OF PAGES: xxv, 325.

Abstract

Semiconductor quantum wire (QWR) structure is a promising candidate for potential applications in long wavelength laser devices. In this thesis, the investigations were focused on the growth and characterization on the structural and optical properties of InAs quantum wires deposited on InGaAlAs lattice matched with InP substrate by gas source molecular beam epitaxy.

The practical growth parameters were first determined by studying the samples containing single InAs layer embedded within $In_{0.53}Ga_{0.37}Al_{0.10}As$ barrier layers. These parameters were then employed for fabricating multilayer quantum wires with different (1) spacer layer thicknesses; (2) quantum wire layer thicknesses; and (3) different **Al** concentrations in the spacer/barrier layer materials.

Structural properties of the quantum wires were characterized by (scanning) transmission electron microscopy based techniques. The composition variation, elastic field and the variation of QWR stacking patterns in multilayer samples were qualitatively studied through diffraction contrast imaging. Quantification of the **In** distribution in individual QWRs and the QWR-induced **In** composition modulation in barrier layers were obtained by electron energy loss spectrometry and energy dispersive X-ray spectrometry, respectively. These

experimentally observed structural features were explained through finite element simulations.

The optical properties of the QWR structures were studied by photoluminescence. Optical emission at room temperature was achieved from selected multilayer QWR samples after etching and rapid thermal annealing. The emission wavelength ranging from 1.53 to 1.72 μm makes the QWR structure suitable candidates for laser device applications.

This work contributes to the understanding of growth mechanism and the modeling on the physical properties of semiconductor QWR structures.

Acknowledgements

I first would like to show my most sincere gratitude to my supervisors, Dr. Gianluigi A. Botton and Dr. David A. Thompson, for their support, guidance and encouragement throughout the Ph.D program. Dr. Peter Mascher and Dr. Marek Niewczas are appreciated for their valuable advice as supervisory committee members.

I am also grateful to Dr. Michael D. Robertson at the Department of Physics, Acadia University, Wolfville, Nova Scotia, for his introduction and generous share of the basic FlexPDE software code for finite element simulations. Without his help, the calculation work in Chapter 7 would become more difficult. Dr. Jean-Luc Rouvière at GEA-Grenoble, France is acknowledged for designing the geometric phase analysis software, through which the map of local lattice spacing variation is derived in Figure 4-14.

I can not start my thesis and obtain the experimental findings without the precious help and collaborative work with the following people. Dr. Bradley J. Robinson at the Centre for Emerging Device Technologies conducted all the growth of quantum wire samples. Electronic structure calculations for the quantum wires in Chapter 5 were done by Dr. Mohamed A. Naser, at the

Department of Engineering Physics. Dr. Zhilin Peng fulfilled the deposition of SiO_2 layer on the as-grown samples. Mrs. Doris V. Stevanovic demonstrated the rapid thermal annealing process of the quantum wires.

I am thankful to several postdoctoral fellows who kindly offered trainings on the facilities. Dr. Carmen M. Andrei conducted the lab demonstration on obtaining the electron energy loss spectrum images. Dr. Oksana Hulko showed the technique of diffraction contrast imaging and the post-growth etching of the samples. Dr. Martin Couillard demonstrated the practical recipe and operation for TEM sample preparations through low-angle polishing on the Multiprep system. Dr. Alex. S.W. Lee helped collecting the atomic force microscope images and photoluminescence spectrum in Chapter 4. Dr. Christian Maunders obtained the high resolution high angle annular dark field image for this work, as shown in Figure 4-13 (d).

I would also like to thank the technical staffs at the Canadian Centre for Electron Microscopy. Mr. Fred Pearson is appreciated for his teaching in TEM sample preparations and operation of the microscopes. I am also grateful to the training on the atomic force microscope from Mr. Andy Duft. The work present in this thesis will not go smooth without their continuous help.

The financial support from Ontario Centre of Excellence for Photonics, the Canadian Research Chairs program and the Natural Sciences and Engineering Research Council of Canada is highly appreciated.

Table of contents

List of Figures

List of Tables

Chapter 1

Introduction

Overview

Self-assembled III-V semiconductor quantum wire (QWR) nanostructures have recently attracted significant attention due to their potential applications in long wavelength (1.5~2 μm) laser devices (Reithmaier et al. 2007; Lin et al. 2006). The first and most crucial step in making devices with QWRs is to establish the optimum growth conditions for these structures in terms of their structural and optical properties. This structural information, obtained on the nanometer scale for parameters such as composition and strain, provides insights necessary to model the physical properties and to help understand the growth of these nanostructures (Cui et al. 2009).

In this chapter, the basics of the as-grown QWR structures, such as definition, growth and characterization techniques, will be briefly reviewed. The research work in this thesis will be outlined.

1.1 Quantum wire structures

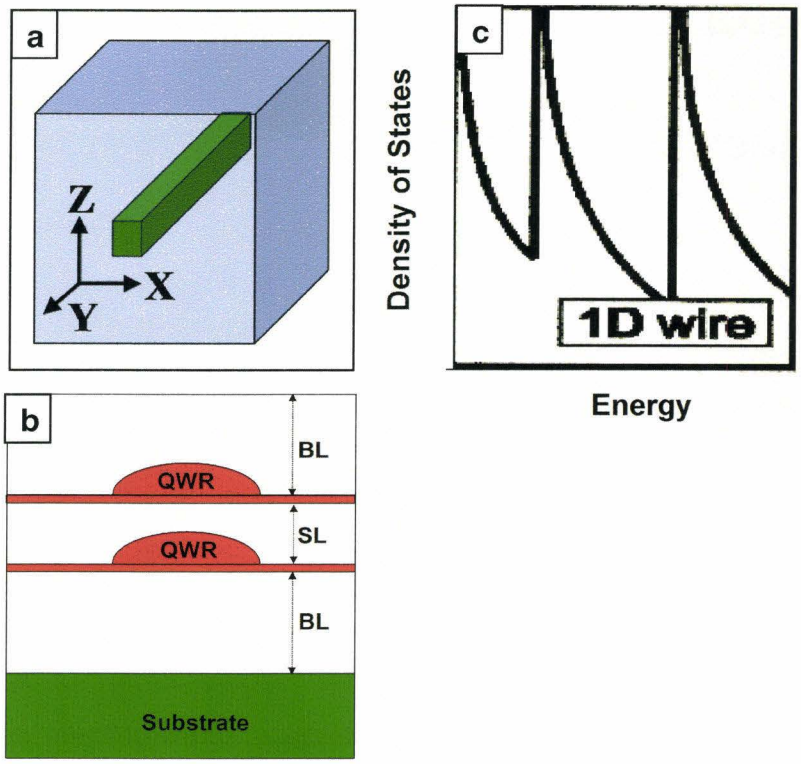

Figure 1-1: (a) A schematic drawing of a rectangular QWR (green) embedded within the barrier material (blue); and (b) a schematic diagram of the multilayer QWRs showing the substrate, barrier layers (BLs) and spacer layer (SL); and (c) density of states for electrons in a QWR, which is adapted from (Kapon 1993).

QWR refers to a one-dimensional structure buried within a barrier material, which possesses a higher electronic potential than that of the QWR material. As schematically shown in Figure 1-1 (a), one idealized rectangular QWR (green) is embedded in the barrier layer (blue) with the dimension along *Y* axis much longer than along *X* and *Z* axis. Also, two QWRs in adjacent epitaxial layers are schematically shown in Figure 1-1 (b). The layer between the adjacent QWR layers is defined as a spacer layer (SL). The bottom and top layers covering the QWR/SL ensembles are defined as barrier layers (BLs).

1.2 Optical properties and applications of QWRs

According to the solutions of Schrödinger's equation, the energy level of carriers (electrons and holes) inside a rectangular QWR (Figure 1-1 (a)) is given by (Kapon 1993):

$$E_{n_x,k_y,n_z} = \frac{\hbar^2\pi^2}{2m^*}\left(\frac{n_x^{\,2}}{l_x^{\,2}} + \frac{n_z^{\,2}}{l_z^{\,2}}\right) + \frac{\hbar^2 k_y^{\,2}}{2m^*} \quad \text{(1-1)}$$

where n_x and n_z represent quantum level numbers in the confined directions along X and Z axis, respectively. k_y is the wave-vector in the unconfined directions along Y axis of the QWR. l_x and l_z are the dimensions of the QWR along X and Z axis, respectively. m^* is the effective mass of the carriers and $\hbar$ is Planck's constant.

Based on the solution of equation (1-1), the density of states (DOS) for electrons in a QWR can be determined and a schematic plot is shown in Figure 1-1 (c). Compared with its counterparts with higher dimensionality, such as bulk materials (three dimensions) or quantum wells (two dimensions), the principle advantage of using the QWRs in lasers is the noticeable increase in the density of states (Alferov 2001), as shown by the sharp maxima in the DOS function (Figure 1-1 (c)). Because of the carrier confinement in the X and Z directions, by replacing the bulk or quantum wells in a laser structure with QWRs, superior

performances, such as a narrower spectrum line-width, reduced temperature sensitivity and lower threshold current, are expected (Alferov 2001; Yin et al. 2007). Therefore, QWRs are attractive for the active regions of semiconductor laser devices used in telecommunications operating at 1.55 μm (Kaminow et al. 2002) and broadband emitters with the wavelength over the optical windows between 1.6 and 2.0 μm (Ooi et. al, 2008).

1.3 Structural properties of QWRs

The optical properties, such as the emission wavelength, the width of the emission peak (characterized by the Full Width at Half Maximum (FWHM)) and temperature sensitivity of the emission, are determined by the structural properties of QWRs. Firstly, the size of the QWR is a major factor for determining the emission photon energy or wavelength. As shown in Figure 1-2, the photon emission ($h\nu$) at low temperatures (for example, 14 K) and low excitation laser power results mainly from the ground state recombination between confined electrons (in conduction band (CB), with a ground state energy level E_e) and confined heavy holes (in valence band (VB), with a ground state energy level E_h) in the individual QWR. According to equation (1-1), the energy level of carriers is associated with l_x and l_z of the QWRs along the confined directions X and Z, respectively. Also, the size uniformity of the as-grown QWRs influences the shape and width (FWHM) of the emission peak from the QWR assembles.

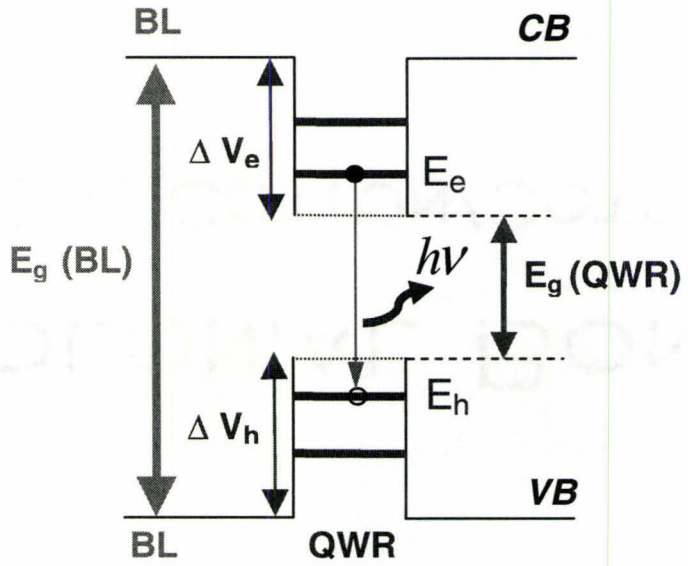

Figure 1-2: A schematic diagram showing the Type 1 band alignment for a QWR between the barrier layers.

Moreover, the shape of QWR modifies the solution of the Schrödinger's equation for the energy levels. For example, equation (1-1) is the solution for the rectangular QWR, as shown in Figure 1-1(a). However, different shapes of QWR in *X-Z* cross-sections, such as lens-shape (Cui et al. 2009), triangle (Sauerwald et al. 2005) or truncated triangle (Djie et al. 2006), have been experimentally observed. The Schrödinger equation shows different forms for each shape: as a result, the solutions for energy levels are different (Harrison 2005) from that shown in equation (1-1).

The solution for the energy levels also depends on the details of the band structure shown in Figure 1-2. The specific band structure will be determined by the strain and composition distributions within the QWRs. Firstly, the band discontinuities (ΔV_e and ΔV_h in Figure 1-2) are modulated by the strain field inside and around individual QWR (Grundmann 2002). Secondly, the multi-axial strain field around QWRs is proposed to be the cause of the experimentally observed temperature-insensitivity of the optical emission from QWRs (Wohlert et al. 1996; Lei et al. 2006a). Also, the inhomogeneous elemental distribution inside QWRs, which has been experimentally determined (Sauerwald et al. 2005; Molina et al. 2006; Cui et al. 2009), modifies both the positions and discontinuities between band edges in Figure1-2.

Due to the significant influence of the structural features on the optical properties, structural characterizations at high spatial resolution (on nanometer scale or better) are crucial for understanding and modeling of the optical properties of QWRs.

1.4 Fabrication of semiconductor QWRs

To obtain high quality semiconductor QWR arrays, epitaxial growth techniques, such as Molecular Beam Epitaxy (MBE) and Metalorganic Chemical Vapor Deposition (MOCVD), are typically used because of their advantages for: (1) the precise control of the epi-layer thickness on the monolayer scale (1 ML, about 0.3

nm for most III-V semiconductor compounds); (2) a high quality interface between QWRs and BLs; and (3) the high purity of the deposited materials (Ohring 2002). In this thesis, the QWR samples are grown by Gas Source MBE (GSMBE) using the facilities at McMaster University.

1.4.1 Fabrication strategies

The fabrication strategies for QWRs can be summarized into two categories: indirect and direct methods (Alferov 2001).

1.4.1.1 Indirect method

The indirect method was employed in early attempts at growing QWRs. Generally, the procedure includes the growth of a two dimensional quantum well structure on the substrate, followed by electron beam lithography and chemical etching to produce a one dimensional confinement pattern etched through the quantum well. Finally, over-growth was performed on the patterned quantum well surface to form QWRs (Kash et al. 1986; Wu, J. et al. 2008). However, there are limitations in applying the indirect method, such as the insufficient lateral resolution of the lithographic technique for producing surface features less than 100 nm (Wang, X.L., et al. 2006) and interface damage caused by the lithography and etching process. These drawbacks cause poor quality of the as-grown structures resulting in lasers with very high threshold current (Wu, J., et al. 2008). Therefore, the indirect method is not popular for the state-of-art growth of QWRs.

1.4.1.2 Direct method

There are two groups of techniques for the direct growth of QWRs: (1) growth on non-planar substrate; and (2) self-organized growth on a planar surface based on the Stranski–Krastanow (S-K) growth mode (Cullis et al. 2002).

1.4.1.2.1 Growth on non-planar substrate

In this technique, produced or intrinsic non-planar features (such as facets) in the substrate or BL are used to fabricate QWRs.

One typical example for the former case is the growth of V-shaped QWRs (Wang et al. 1995). The V-shaped grooves are firstly produced through chemical etching of the substrate, followed by the formation of the V-shaped QWRs at the bottom of the grooves through accumulation of the deposited materials driven by the surface chemical potential, the local minima of which locates at the bottom of the grooves (Wang, X.L. et al. 2006). Other QWRs fabricated through the former method include ridge-type QWRs (Wang, X.L. et al. 2000) and the QWRs on sidewalls (Nötzel et al. 1996).

The typical examples of the latter case include T-shaped QWRs on cleaved (110) wafer edges (Pfeiffer et al. 1990), QWRs grown on a vicinal substrate (Petroff et al. 1984) and QWRs on corrugated high-index substrate

(Higashiwaki et al. 1996). Comprehensive reviews on the growth of QWRs on a non-planar substrate can be found in recent literatures (Wang, X.L. et al. 2006; Wu, J. et al. 2008).

1.4.1.2.2 Growth through S-K mode on planar surface

A direct method of fabricating QWRs is through the self-organization process in the S-K growth mode with lattice mismatch between the epi-layer and substrate materials. The deposition initially starts with a layer-by-layer growth and the elastic strain energy increases linearly with the thickness of the epi-layer (Pearsall 2000). As the thickness of the deposited material reaches the critical value (Ohring 2002), three dimensional structures are formed on top of the two dimensional layer (called the wetting layer, WL) through elastic relaxation (Stangl et al. 2004) to reduce the accumulated elastic strain energy.

QWRs fabricated through the S-K growth mode have been realized on substrates using lattice mismatched epitaxial layers such as InAs/InP (Li et al. 1999; Alén et al. 2002), GaAs/GaP (Jonas Ohlsson et al. 1998) and InGaAs/GaAs (Ma et al. 2001). The driving force for QWR formation in a mismatched system is primarily the reduction of the elastic energy (Wu, J. et al. 2008). However, the anisotropic shape of the QWRs makes the growth mechanism more complex than that for the isotropic quantum dots, where the structure undergoes relaxation in all directions. It is believed that the formation of QWRs arises from the anisotropy in

the surface diffusion of the group III adatoms, which is related to the anisotropies in growth kinetics or surface stress during the deposition. The growth kinetics can be modified by either the alloying effect (Brault et al. 1998) or the growth front morphology (Sritirawisarn et al. 2007; Molina et al. 2007) of the BL materials. For example, anisotropic steps were found on a quaternary InGaAsP alloy (Sritirawisarn et al. 2007) and a binary InP (Molina et al. 2007) surface along $[0\bar{1}1]$ direction. The incident QWR materials deposited on the BL preferably nucleate on the upper terraces of such steps. Thus, anisotropic QWRs are observed with the long axis along $[0\bar{1}1]$ direction. Another proposed mechanism for the QWR formation is based on the anisotropic stress accumulation rate along different directions on the BL surface. The *in-situ* and in real time measurement of stress was carried out by García et al. (García et al. 2001), and it was shown that the magnitude of the accumulated stress was larger along $[011]$ direction than that along $[0\bar{1}1]$ direction during the deposition of InAs on InP. Therefore, relaxation of the InAs layer occurs preferentially along $[011]$ direction resulting in one-dimensional QWRs extending parallel to $[0\bar{1}1]$ direction.

The advantages of the QWRs grown through S-K mode can be summarized into two aspects. Firstly, compared with indirect methods, QWR structures obtained through the S-K mode can be defect-free by carefully

adjusting the growth parameters, such as the deposition rate, thickness of QWR layer and growth temperature. Such QWRs are optically active and are promising candidates for device applications. Secondly, no complex lithography or other growth techniques are required. Moreover, high quality, multi-layer QWR stacks, which can lead to more efficient laser performance, are easily grown by simply repeating the deposition of the QWR/SL unit, which are difficult to be achieved through other methods.

1.5 InP based QWR structures

It is well known that InP is a favored substrate material for making devices in near infrared wavelength region for optical fiber communications (Lee 1991). Also, InAs is a desirable candidate for the QWR material since it shows a Type 1 band alignment (Harrison 2005) with InP, as the type shown in Figure 1-2. The lattice mismatch between InAs and InP is 3.2%, which is favorable for growing QWRs through the S-K mode.

InAs QWRs can be either directly deposited on the InP substrate (Alén et al. 2002; García et al. 2001) or on a ternary or quaternary epi-layer grown lattice-matched on the InP substrate, such as InGaAs (Lin et al. 2008), InAlAs (Lei et al. 2006 a&b), InGaAlAs (Djie et al. 2006; Kümmell et al. 2006) and InGaAsP (Sritirawisarn et al. 2007). Compared with the binary or ternary alloys, the advantage of using the quaternary materials as BL is the freedom of adjusting the

band alignment between BL and QWRs (Figure 1-2) whilst maintaining the lattice-matching of BL with InP. Therefore, the optical emission wavelength from the QWR structure can be adjusted by changing the composition of the quaternary alloy.

Due to the design freedom, InAs QWRs on InP (100) substrate with $In_{0.53}Ga_xAl_{0.47-x}As$ quaternary alloy as BL is selected for most of the growths in this thesis.

Unlike the InAs/GaAs (100) system, in which the reproducible three-dimensional quantum dots are routinely obtained (Joyce et al. 2004), the formation of InAs nanostructure on an InP substrate is complex due to the lower mismatch (about 3.2%). According to the results from different research groups, quantum dots or QWRs were obtained under apparently very similar growth conditions (Stintz et al. 2003; Brault et al. 2002; Li et al. 2001). This means the morphologies of the InAs nanostructure are very sensitive to small variations in the growth conditions. A systematic study of the influence of each growth parameter is the motivation for this research.

1.6 Influence of the growth parameters

The most important parameters for MBE growth of semiconductor nanostructures include the strain, deposition rate, total thickness of QWR layer, growth

temperature and composition of the BL materials. In this work the average strain between the QWRs and substrate are kept constant by ensuring the BL has the same lattice constants as the InP substrate.

1.6.1 Deposition rate of QWR material

The deposition rate controls the population of adatoms on the growth front surface (Zhao et al. 2004a). Theoretically, at a low deposition rate, thermodynamic equilibrium under anisotropic diffusion is achieved and results in QWRs aligned along the crystallographic direction favorable for the faster diffusion of the adatoms (Zhang et al. 2003). Under a relatively high deposition rate, both the diffusion time and length of adatoms on the growth front surface will be shortened. Nanostructures with smaller sizes are expected (Meixner et al. 2003; Michon et al. 2005) compared to those grown with a lower deposition rate.

However the real process of MBE deposition of InAs/InP is not as simple as the theoretical predictions. QWRs could be obtained under both very low and very high growth rates. Zhao et al. (Zhao et al. 2004a) observed morphological transitions in InAs QWRs/InAlAs BLs/InP system under different deposition rates of InAs: QWRs were present at 0.005 monolayer (ML)/s, isotropic dots at 0.02 ML/s, and QWRs again at 0.2 ML/s and 0.35 ML/s. It was suggested that at the highest deposition rates (0.2 ML/s and 0.35 ML/s), when more InAs is deposited per unit area, per unit time, the diffusion is limited by the high deposition rate

which blocks the migration of adatoms to energetically favorable sites, and this leads to an instantaneous increase of elastic energy. As theoretically proposed by Liu et al. (Liu et al. 1998), one way to relax this extra energy is through the formation of QWRs along the fast diffusion direction of adatoms by the coalescence of initially formed small quantum dots. Thus, a suitable deposition rate must be determined by studying the structural and optical properties of QWR samples grown at various deposition rates.

1.6.2 Thickness of the QWR layer

As show in section 1.4.1.2.2, the critical thickness, where the transition from a 2-D to 3-D growth occurs, is an important parameter for designing the deposition thickness of QWRs. Unfortunately, it is hard to define the critical thickness for InAs in the InAs/InP system due to the complex surface conditions of the substrate or BL. During the deposition of the first several MLs of InAs, the anisotropic surface features (such as the alloying effect and surface morphology of the BL) predominate so that QWRs (Stintz et al. 2003; Zhang et al. 2003; Zhao et al. 2004b) form along the direction where the surface features extend. As more InAs is deposited, the accumulation of mismatch strain energy becomes important. Isotropic elastic relaxation is favorable according to the S-K growth mode and results in more isotropic nano-islands imposed on top of the anisotropic QWRs (Brault et al. 2002; Lei et al. 2006a). Also, the optical properties can be tuned by varying QWR layer thickness. Generally, a red-shift of the emission wavelength

(Kümmell et al. 2006; Sauerwald et al. 2005) is expected as the thickness of QWR layer increases. However, there should be an upper limit of the QWR thickness, at which defects, such as misfit dislocations, are generated and degrade the optical activity of the grown structure (Gutiérrez et al. 2005a). Therefore, by studying the samples with different QWR thicknesses, the best thickness needs to be determined for producing a defect-free QWR structure with good optical emission features.

1.6.3 Substrate temperature for QWR and BL

The substrate temperature for growing QWR and BLs should be determined by considering two factors. Firstly, the substrate temperature must be high enough so that sufficient surface diffusion can be achieved for the adatoms to find the binding sites and incorporate into the growing epitaxial layer (Herman et al. 2004). Also, it is advantageous to deposit the epitaxial layers at high temperatures in order to reduce the density of point defects (such as vacancies or anti-sites) (Liu et al. 1995). Secondly, the upper limit of the growth temperature should be determined by considering the desorption rate of the adatoms, i.e. if the temperature goes too high, it is more probable for adatoms to escape from the growth front surface rather than incorporate into the growing film (Meixner et al. 2003). Based on the work of Houdré et al. (Houdré et al. 1991), significant desoprtion of **In** has been found at 545 °C from the MBE-grown InAlAs and InGaAs layers lattice matched with InP substrate. Thus, the growth temperature

for the **In**-containing BLs and QWRs should not exceed 545°C in this work. The ideal proper growth temperature should be determined for producing QWRs with suitable structural and optical properties.

1.6.4 Barrier layer materials

Besides the controllable growth parameters, the optical emission from QWRs can also be tuned by changing the composition of the BL/SL since the both band discontinuities (ΔV_e and ΔV_h in Figure 1-2) and effective masses of the carriers vary with the BL/SL materials. Also, it will be shown in Chapter 5 that the structural properties, such as shape and dimensions of individual QWRs, as well as the alignment pattern of QWR stacks, are dependent on the composition of the BL/SL materials.

1.7 Requirements for QWR structure for devices

The one dimensional wire-like nanostructure can be used as the active region in laser devices. Various requirements need to be satisfied for carrier confinement and suitable optical performance.

1.7.1 Size

To achieve the 2-D confinement of carriers, the dimensions in *X-Z* cross-section (l_x and l_z in equation (1-1)) of individual QWRs should be comparable to the de Broglie wavelength of carriers, which is on the order of tens of nanometers

(Franchi et al. 2003). There is also a lower limit for QWR size i.e. there must be at least one energy level located in the potential well of QWR (Bryant et al. 2005), as shown in Figure 1-2. Also, for the QWR assemblies, a narrow size distribution is desired in order to get a sharp optical emission peak with high intensity (Pearsall 2000; Joyce et al. 2005).

1.7.2 Defect free

Here "defect" typically refers to extended defects such as misfit dislocations. These defects usually play the role of non-radiative recombination centers (Petroff et al. 1980) and degrade the optical performance of the QWR structure, as will be shown in Chapter 5. These defects can be suppressed by careful control of the growth parameter together with the proper structural design.

1.7.3 Band alignment

As defined in section 1.1 and shown in Figure 1-2, the CB/VB edge positions of the BL and QWR materials must satisfy the following relations:

$CB_{BL} > CB_{QWR}$ and $VB_{BL} < VB_{QWR}$.

This "Type1" band alignment required for quantum confinement of both electrons and holes can be achieved by proper selection of the BL and QWR materials.

1.7.4 Stacking of QWRs

Multilayer stacks of QWRs are required for laser devices due to two reasons. Firstly, the QWR density in the active region is increased to obtain strong interaction between the confined electrons and the electromagnetic field (Pearsall 2000). Secondly, an improvement of the uniformity in QWR sizes are expected when the strain field penetrates through QWR stacks at suitable SL thicknesses (Alén et al. 2002). Thus, superior optical properties, such as the narrower line width of emission peak, lower threshold current and higher optical gain (Pearsall 2000; Bryant et al. 2005; Ledentsov et al. 1996) than the single layer counterpart, are anticipated from the QWR stacks.

Three kinds of stacking patterns are often observed: (1) vertically correlated alignment; (2) vertically anti-correlated alignment; and (3) uncorrelated QWRs. However, the stacking pattern of QWRs is influenced by a variety of factors in MBE growth. Proposed mechanisms (Springholz 2005) for the variation of the stacking pattern include; (1) elastic interaction due to strain of the buried quantum structures, i.e. the strain field of the buried QWRs extending into upper SL determines the nucleation sites of the QWRs in each successive layer; (2) nucleation sites of QWRs modulated by a non-planarized SL growth front; and (3) nucleation sites of QWRs determined by the composition modulation in the ternary or quaternary SL alloys. Therefore, investigations on the role of thickness and composition of SL in determining the QWR stacking patterns are necessary.

1.7.5 Post-growth treatments

Two processing techniques are often applied to the as grown III-V semiconductor quantum structures: etching and rapid thermal annealing (RTA) (Lee et al. 2006; Hulko et al. 2008), in order to tune and possibly improve their optical properties before they are integrated into devices. The mechanism for modifying the optical properties of the as-grown samples through post-growth treatment can be summarized in two aspects. (1) Low temperature (700°C and lower for InP-based structure) annealing reduces the density of point defects accumulating around the interface between QWRs and BL/SLs due to the high magnitude of strain field (Djie et al. 2008). Superior optical properties, such as higher quantum efficiency, lower threshold current and narrower width of the emission peak, have been observed in an InAs-InGaAlAs-quantum-dash-in-well structure after undergoing RTA at 700°C compared to the as-grown one (Djie et al. 2006). (2) High temperature annealing (700-800°C) activates intermixing between QWR and BL/SL, which usually causes a blue-shift of the emission wavelength from the QWR structure through the modification of the band alignment (Djie et al. 2008). Therefore, post-growth annealing will be carried out in this work for selected samples in order to obtain the desired optical emission wavelength at room temperature (RT).

1.8 Characterization techniques

Structural and optical characterizations of QWRs play an important role in improving the design and growth of suitable structures for laser devices. In order to interpret and simulate the optical properties of QWRs, structural information on nanometer or even Angstrom scale should be obtained as input data for the calculating models (Sidor et al. 2007; Gioannini 2004). Also, investigation of the optical properties is important for evaluating the potential for device application of the grown QWR structure. The ultimate goal of characterizations is to optimize the growth parameters and produce multilayer QWR stacks with required optical properties for the proposed device application.

1.8.1 Techniques for structural characterization

In this thesis, techniques based on atomic force microscopy (AFM) and (scanning) transmission electron microscopy ((S)TEM) are employed for structural characterization of individual QWRs since the probe size used in each technique can be smaller than cross-sectional dimensions of QWRs.

1.8.1.1 AFM

AFM is a direct imaging technique from which preliminary information about the shape, size and surface density of free-standing QWRs is obtained. The AFM scanner is capable of resolutions as good as several nanometers in lateral direction and several angstroms in height (Stangl et al. 2004). There are two basic

operating modes in AFM: (1) the Contact Mode: the bending of a cantilever, on which the tip is mounted, is measured; and (2) the Tapping Mode: the change in resonance frequency due to the force is measured. (Stangl et al. 2004; Digital Instruments 2000). In the following chapters, AFM experiments were performed with a Nanoscope IIIa scanning probe microscope with Tapping Mode to investigate the morphology of uncapped QWRs. The schematic showing the operation of the AFM with Tapping Mode is illustrated in Figure 1-3. The fine tip, mounted on the cantilever, is moving over the surface of a sample in a raster scan. The cantilever is oscillated at or near the resonant frequency with an amplitude between 20 to 100 nm. During scanning, the tip slightly "taps" on the sample surface and the feedback loop keeps constant oscillation amplitude by maintaining a constant root mean square (RMS) of the oscillation signal acquired by the split photodiode A and B. The vertical position of the scanner in order to maintain a constant "setpoint" amplitude is recorded at each data point (x,y) to form the topographic image of the sample surface (Digital Instruments 2000).

AFM is one of the most popular surface characterization tools because of the simplicity of operation and the fact that there is almost no requirement for sample preparation as compared with other methods such as TEM. Also, AFM does not require the sample surface to be electrically conducting whereas this is a requirement in scanning electron microscopy (SEM). Even a surface covered with a thin layer of insulating oxide can still be characterized by AFM. However, there

are still several limitations for AFM. Firstly, only uncapped samples are characterized by AFM. As stated above, for fulfilling the quantum confinement, the wires must be embedded within BL/SL (Figures 1-1 (a) and (b)). The

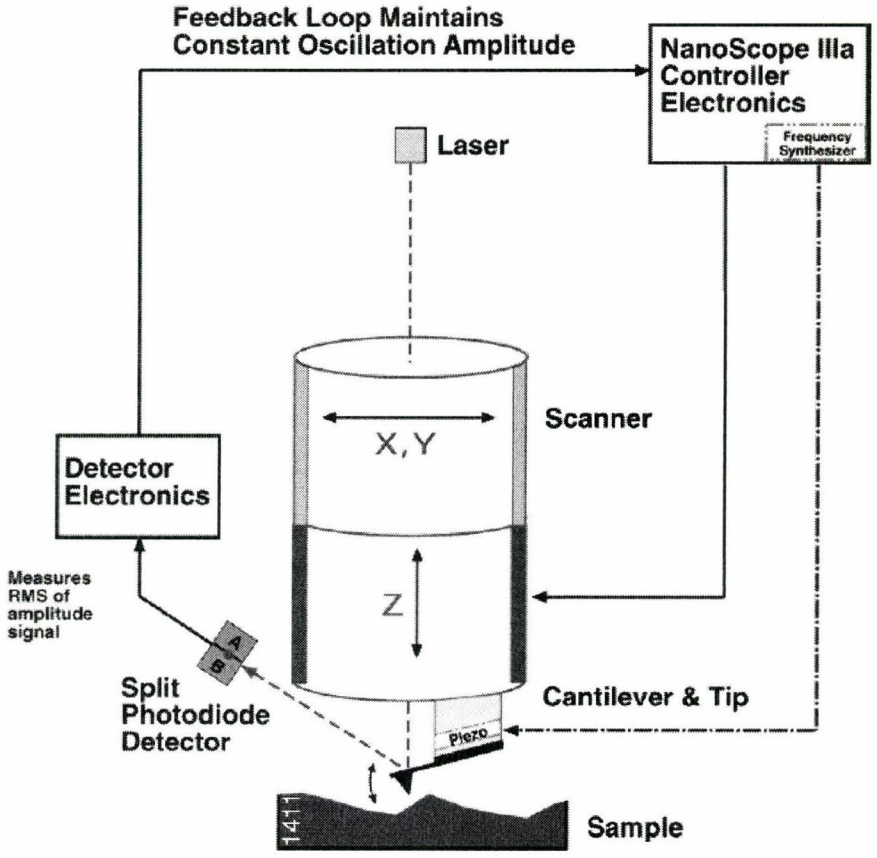

Figure 1-3: A schematic illustration of the Tapping Mode AFM. Adapted from (Digital Instruments. 2000).

structural features of the capped QWRs from overgrowth must be studied in cross-sectional specimens. Another problem is that AFM image is the convolution of the sample's surface morphology with the geometry of the tip (Digital

Instruments 2000). This effect must be taken into account if the lateral size of the QWR is smaller than the tip radius and the side-wall slope of the QWR exceeds half of the opening angle of the tip (Shchukin et al. 2004). Therefore, the lateral size of the QWR is usually overestimated due to this effect although the height can be accurately measured.

1.8.1.2 (S)TEM

The size, shape, composition and strain of individual capped QWRs are studied in cross-sectional samples by various imaging and spectroscopic techniques in a (S)TEM. A review of the characterization methods based on (S)TEM will be shown in Chapter 3 since most of the structural characterizations were carried out with (S)TEM based techniques in this thesis.

1.8.2 Techniques for optical characterization

The optical properties of the QWR structures are investigated by photoluminescence (PL), which is a non-destructive technique used to study the bandgap and impurity levels in semiconducting materials (Gfroerer 2000). As schematically illustrated in Figure 1-4, when a laser beam with photon energy $h\nu_0$, which is greater than the bandgap energy of the BL material, is focused on the sample, electrons will be excited from the valence band to conduction band leaving holes in valence band. These free carriers relax to the lowest available energy levels, usually the bottom of conduction band for electrons and the top of

valence band for holes. Photons with energy $h\nu$ will be emitted from the recombination between the electrons and holes in the lowest available energy

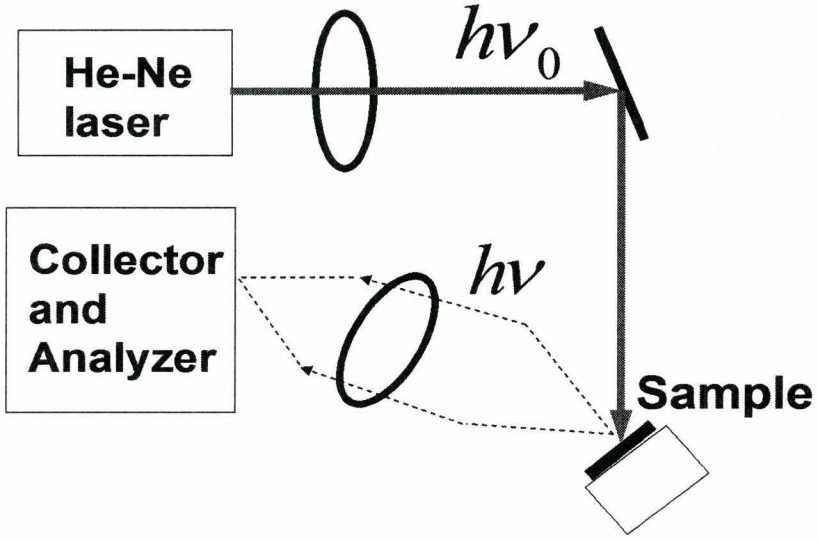

Figure 1-4: A schematic illustration of the experimental set-up for the photoluminescence measurements.

levels. The emitted photons are collected and analyzed for studying the electronic structure and optical properties of the grown samples. The quantum confinement of carriers in QWRs can be proved by the PL results if the generated photon energy of $h\nu$ is larger than the bandgap (E_g(QWR) in Figure 1-2) of the bulk QWR material.

By analyzing the features of the PL spectrum, such as wavelength, intensity, line shape and FWHM, average information on the QWR assemblies can be retrieved since the diameter of excitation laser spot is on the order of a

micrometer. The peak position (wavelength) contains information about the average size of QWRs and the FWHM is related to the size uniformity of the QWR assemblies. Also, if dislocations are present in the as-grown structures, light emission can only be obtained with the sample at low temperature and the PL intensity quenches faster as the temperature is increased than that in the defect-free samples.

In this thesis, optical properties of the QWR structures are investigated by means of temperature dependent PL and power dependent PL (Wang, Z.M., 2008). These experiments were carried using the following set-ups. The samples were mounted on the cold head of a closed-cycle He-refrigerated cryostat, the temperature of which could be controlled from 14 K to 300 K. For most experiments, the PL measurement system consisted of an Ar-ion pump laser operating at 488 nm and incident on the (100) surface of the sample. A collimating lens above the (100) surface was used to collect the PL signal and direct the emission into a Fourier transformation infrared (FTIR) spectrometer with an InAs detector (Pan 2002; Czaban et al. 2006). For the PL measurements under reduced laser power, a neutral density filter was placed in front of the laser source before it interacted with the sample.

1.8.3 Elastic field calculations

In addition to the investigation of the strain field by processing the TEM images (Chapter 3), numerical simulations are also carried out for this purpose. The

elastic field distribution around and within the QWRs is important for understanding the growth phenomenon, such as the alignment of QWRs (Molina et al. 2006) and the decomposition of the BL/SL alloys (Priester et al. 2000 & 2001). Two general methods are used to simulate the elastic field associated with the QWR structures, namely the continuum elasticity and atomistic simulations (Stangl et al. 2004). Due to its drawback of applicability to only limited number of atoms, and the longer computation time, the atomistic method is less frequently employed than the continuum elasticity approach for simulating the elastic field (Maranganti et al. 2007).

In the continuum elasticity method, the structure inside the simulating box is replaced by an elastic continuum and the elastic field distribution map is obtained by either solving the partial differential elastic equations (Pei et al. 2003; Robertson et al. 2005) or minimizing the elastic strain energy (Jogai 2000) in the structure. Analytical or numerical methods are employed to find the solutions for the elastic field distribution. However, the analytical method is only applicable to the nanostructures below a plain surface or in the approximation of small slopes at the surface (Stangl et al. 2004). A review with particular focus on the analytical results for the strain distribution in various buried nanostructures can be found in recent literature (Maranganti et al. 2007).

In this thesis, the numerical simulations using the finite element (FE) method was employed to solve the partial differential equations (shown in Chapter 7) and calculate the displacement, strain field distribution around QWRs and on the non-flat growth front surface of the BL/SL. The advantage of the FE method is that the elastic fields of the anisotropic QWRs, including the effects of the free surface, wetting layer and the experimentally determined compositional map, can be computed efficiently.

The software used for the FE calculations is FlexPDE 5.0 (PDE Solutions, Inc., 2005). In FlexPDE, the main principle of FE simulations can be summarized as follows. The domain of interest is divided into triangular cells or prisms of triangular cross-sections and the partial differential equations are solved simultaneously. More specifically, the program solves a partial differential equation by determining the values of the variables at discrete nodes, which are at the corners of the triangular cells and at midpoints between the corners. The resolved values at these nodes are recorded and interpolated to other points of the triangular cell (Backstrom 2005). The convergence of the solution is controlled by estimating the relative uncertainty in each variable and compares this to a pre-set accuracy tolerance in the program. If the value on any cell exceeds the tolerance, that cell is split and the solution is recomputed (PDE Solutions, Inc., 2005). This process is repeated until the estimated error in any variable is less than the accuracy tolerance of its total range over every cell in the calculating mesh.

1.9 Outline of the thesis

The main focus of this thesis is growth and characterization of QWR structures as well as contributing to the understanding of growth phenomena through numerical modeling. The contents of the chapters are organized as follows.

In Chapter 2, the growth technique and the basic structure of each layer in the as-grown sample are given. TEM or STEM based techniques are reviewed in Chapter 3 since TEM is the only technique employed to study the structural properties of capped QWRs in this work. The basics of TEM sample preparation methods are introduced since this is the most crucial step for good TEM and spectrum imaging results. Imaging techniques based on diffraction contrast, phase contrast and atomic number contrast are briefly introduced. Optimal experimental settings for investigating the structural features, such as size, shape and displacement, of QWRs are determined through the comparisons of different imaging methods. Analytical tools based on STEM are selected for obtaining quantitative elemental maps in both QWRs and BL/SLs.

The main focuses of Chapters 4 and 5 are the growth and characterization of various InAs QWRs/InGaAlAs/InP structures. In Chapter 4, the optimal growth conditions favoring the formation of QWRs with suitable optical properties are established by studying single layer QWR samples grown with different

conditions. Based on the determined growth conditions, multilayer QWR stacks were fabricated and studied in Chapter 5. The structural information, such as the dimensions, shape, strain and compositional map of individual buried QWRs, and the composition modulation in the BL, was obtained through TEM/STEM based techniques. The variation of stacking pattern and optical properties of QWRs as a function of the SL thickness, the QWR layer thickness and the composition of the SL/BL were determined.

Post-growth treatment of selected multilayer QWR structures is discussed in Chapter 6. The main purposes are: (1) obtain optical emission at RT by annealing of the point defects (Lochtefeld et al. 1996; Djie et al. 2006) between QWRs and BL/SLs; and (2) adjust the emission wavelength by intermixing (Djie et al. 2008) between QWR and BL/SL.

In Chapter 7, FE calculations on elastic fields are described for both single and multilayer QWR samples in order to interpret the growth phenomena and diffraction contrast patterns observed in the structural characterizations through TEM imaging.

The main findings and future work are summarized in Chapter 8.

Chapter 2

Sample Growth

Overview

The samples studied in this thesis are InAs QWRs deposited on an $In_{0.53}Ga_xAl_{0.47-x}As$ quaternary alloy (x ranges from 0 to 0.47, except for $In_{0.52}Al_{0.48}As$) which is latticed matched with the InP substrate. In this chapter, the QWR growth procedure is summarized for those samples which are characterized by their structural and optical properties in later chapters.

2.1 General growth conditions

All the samples were grown in a Gas Source Molecular Beam Epitaxy (GSMBE) system manufactured by SVT Associates. The facility and growth process are schematically shown in Figure 2-1. High purity group III metals are used as the sources in effusion cells. The precursors of group V species are gas sources of VH_3 compounds, specifically Arsine (AsH_3) and Phosphine (PH_3) for **As** and **P**, respectively. These precursors were thermally dissociated into group V dimers and impinged on the substrate surface together with the group III atoms to form the required III-V epi-layer through the surface diffusion and incorporation of the

adatoms into the proper atomic sites on the growth front surface (Panish et al. 1993).

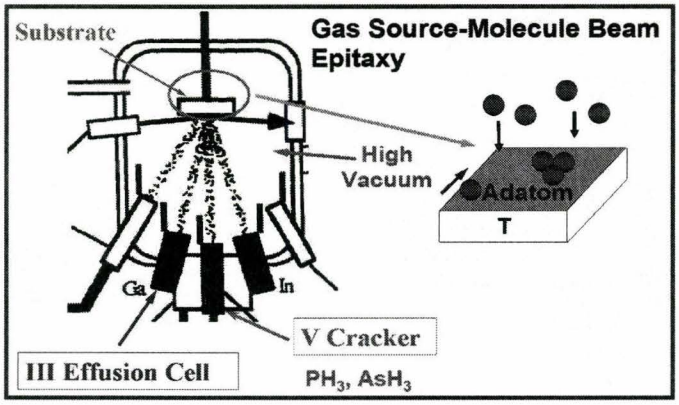

Figure 2-1: A schematic illustration of the Gas Source Molecular Beam Epitaxy (GSMBE) system and growth process.

The general structure of the as-grown samples is schematically shown in Figure 2-2. The multilayer/single layer structure was deposited on an n-type (100) InP substrate. In order to provide a smooth, clean growth front, an initial 200 nm InP buffer layer was grown at 470°C, at a rate of 1 μm/h directly on an epi-ready (100) InP substrate. In most samples, this was followed by a 50 nm $In_{0.53}Ga_xAl_{0.47-x}As$ BL (referred as lower BL), deposited at 0.8 μm/h. Because of the intrinsic 3.2% mismatch between the lattice parameters of InAs and InP, thin InAs layers form QWR structures through the Stranski-Krastanow growth mode (Cullis et al. 2002). Single or multilayer QWR structures were grown, capped or separated respectively, with the BL material. Most samples were capped with a 50 nm $In_{0.53}Ga_xAl_{0.47-x}As$ BL (referred as upper BL), followed by 100 nm InP

buffer, another 50 nm $In_{0.53}Ga_xAl_{0.47-x}As$ BL and a free standing InAs QWR layer for AFM characterization.

The quaternary alloy $In_{0.53}Ga_xAl_{0.47-x}As$ was chosen as the BL material due to two growth and design flexibilities: (1) the lattice parameter can be tuned to match that of InP by varying the ratio of **Ga** and **Al** as it can be considered as a combination of two ternary alloys $(In_{0.53}Ga_{0.47}As)_z(In_{0.52}Al_{0.48}As)_{1-z}$, both of which are lattice-matched with InP (Vurgaftman et al., 2001). The lattice match between the BL and substrate suppresses the generation of dislocations (Ohring 2002) in the as-grown structures; (2) the variable ratio of **Ga** and **Al** provides a degree of freedom for adjusting the band alignment and discontinuities between BLs and QWRs (Figure 1-2). Furthermore, the optical emission wavelength from the QWR structures can be tuned.

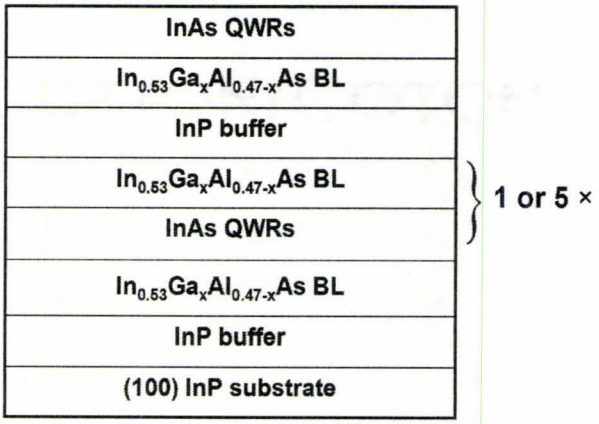

Figure 2-2: General structural for the InAs QWRs grown on $In_{0.53}Ga_xAl_{0.47-x}As$ BL lattice matched with (100) InP substrate.

2.2 Growth of single layer QWR samples

As mentioned in Chapter 1, the structural and optical properties of a QWR can be modified by changing the growth conditions. Based on our experience, four growth parameters imposed significant influence on the QWRs: (1) the growth rate (G.R.) of the InAs QWR layer; (2) the thickness of InAs QWR layer (t_{QWR}); (3) the growth temperature (G.T.); and (4) the composition of the BLs/SLs. The investigations on the growth for single layer QWRs focused on exploring the function of each parameter separately. Details of the growth conditions for each sample are summarized in Table 2-1.

2.3 Growth of multilayer QWR samples

After growing the single layer QWR samples, the growth parameters, under which well-developed QWRs with promising optical properties were obtained, were applied to the deposition of multilayer QWR structures. The variables included: (1) SL thickness between QWR layers; (2) thickness of QWR layers; (3) composition of the BLs and SLs. The growth rate and growth temperature were the same as those for sample G2 in Table 2-1. Each sample contained 5 repeats of InAs QWRs/$In_{0.53}Ga_xAl_{0.47-x}As$ SLs. The detailed growth conditions for multilayer samples are summarized in Table 2-2. The growth rate of the QWR layers was 0.4 ML/s and the growth temperature for BLs, SLs and QWR layers was fixed at 520 °C for all the samples.

In the following chapters, the structural and optical properties will be characterized for both single and multilayer QWR samples. The interpretation of the growth phenomenon and optical features will be investigated through FE simulations and PL experiments, respectively.

Table 2-1: Growth conditions for single layer QWR samples.

Sample number	G.R. for QWR (ML/s)	G.T. for QWR (°C)	t_{QWR} (ML)	Al content in BLs (a.t.%)
A1	0.4	520	4	10
A2	0.1	520	4	10
B1	0.4	520	4	10
B2	0.04	520	4	10
C1*	0.4	520	2.5	10
C2*	0.4	520	3.5	10
C3*	0.4	520	5	10
D	0.4	470	4	10
E	0.04	495	4	10
F	0.4	545	4	10
G1	0.4	520	4	10
G2	0.4	520	4	20
H	0.4	500	5.6	10
I	0.4	500	2.5	10
J	0.4	520	5	20

* A thin GaAs layer (0.6~1nm) was inserted above $In_{0.53}Ga_xAl_{0.47-x}As$ BL before depositing the InAs QWR layer.

Table 2-2: Growth conditions for multilayer layer QWR samples.

Sample number	SL thickness (nm)	t_{QWR} (ML)	Al content in BL (a.t.%)
K1	8	4	20
K2	15	4	20
K3	25	4	20
L1	8	3	20
L2	8	5	20
L3	8	7	20
M1	8	5	0*
M2	8	5	10
M3	8	5	30
M4	8	5	48**

* BLs and SLs were $In_{0.53}Ga_{0.47}As$
** BLs and SLs were $In_{0.52}Al_{0.48}As$

Chapter 3

Review of TEM techniques for characterizing semiconductor quantum structures

Overview

Characterizations of the structural properties, such as shape, size, and composition of the semiconductor nanostructures play a crucial role in understanding and tailoring the optical properties of such nanostructures (Stangl et al. 2004). The basic requirement for obtaining accurate and reliable structural information is that the probe size of the experimental tools must be smaller than the dimensions of individual nanostructure. According to this criteria, transmission electron microscopy (TEM) and scanning transmission electron microscopy (STEM) and spectroscopic methods are ideal for characterizing the capped QWR structures with the state of the art electron probe size reaching under 0.1 nanometer (for example the newly equipped aberration-corrected FEI Titan 80-300 cubed STEM at McMaster University provides a 0.07 nm electron probe). In this thesis, TEM/STEM based techniques were extensively used to study the structural properties such as composition, strain field and stacking pattern for single or multilayer QWRs in the InAs/$In_{0.53}Ga_xAl_{0.47-x}As$/InP epitaxial system.

The common problem in TEM investigation for nanostructures is that the images and spectra represent a convolution between the electron probe and the specimen (Browning et al. 2001). Local variation of thickness and specimen orientation make both the qualitative and quantitative interpretations of the imaging and spectroscopic results even more complex (Williams et al. 1996). Therefore, a good quality TEM sample is the most important pre-requisite for obtaining TEM images with optimal resolution and interpretable quantitative information. Here the term "good" refers to a sample with large electron-transparent areas, free from artifacts (such as amorphous region and contamination) and minimal variation of thickness across interfaces between different layers.

In this chapter, the sample preparation methods will be summarized and the practical procedures for each method will be shown first. The principles and applications of TEM/STEM based imaging and spectroscopic techniques used in this thesis will be reviewed.

3.1 Sample preparation techniques

TEM cross-sectional sample preparation methods for III-V semiconductors can be summarized into two categories: the standard procedure and low angle wedge polishing.

3.1.1 Standard procedures

Four steps are involved in preparing cross-sectional TEM specimens through standard procedures. They are cleaving and gluing; grinding and cutting; dimpling, and ion-milling (Goodhew 1985).

(1) Cleaving and gluing

After growth of the sample, two slices (8 mm in length and 1 mm in width) were cut along two major cleavage [011] and [$0\bar{1}1$] directions from the back surface of the (100) InP substrate (Figure 3-1 (a)). The two slices were glued together by epoxy with the epi-layers facing each other (Figure 3-1 (b)). Three silicon bars were glued to the outside of the InP slices to complete a sample structure as shown in Figure 3-1 (c). The whole structure was placed on a hot plate at about 150°C to cure for 7 minutes and harden the epoxy.

(2) Grinding and cutting

The sample structure was thinned with 600 grit sandpaper for both sides until the final thickness reached 300 μm. Two 3 mm diameter discs, shown by the dashed circle in Figure 3.1 (c), were cut from the sample structure using an ultrasonic disc cutter such that the two epi-layers run through the center of the disc. The discs were further polished with 2400 grit sandpaper on one side then mounted using epoxy with the polished side on the surface of a Molybdenum-ring, as shown in Figure 3.1(d).

(3) Dimpling

The central part of the sample disc was further thinned through dimpling down to 30~40 μm with a copper dimpling grinder. Final polishing is accomplished by using the soft polishing buffer wheel for 5 minutes. A disc with shiny and mirror-like surface is then ready for ion-milling.

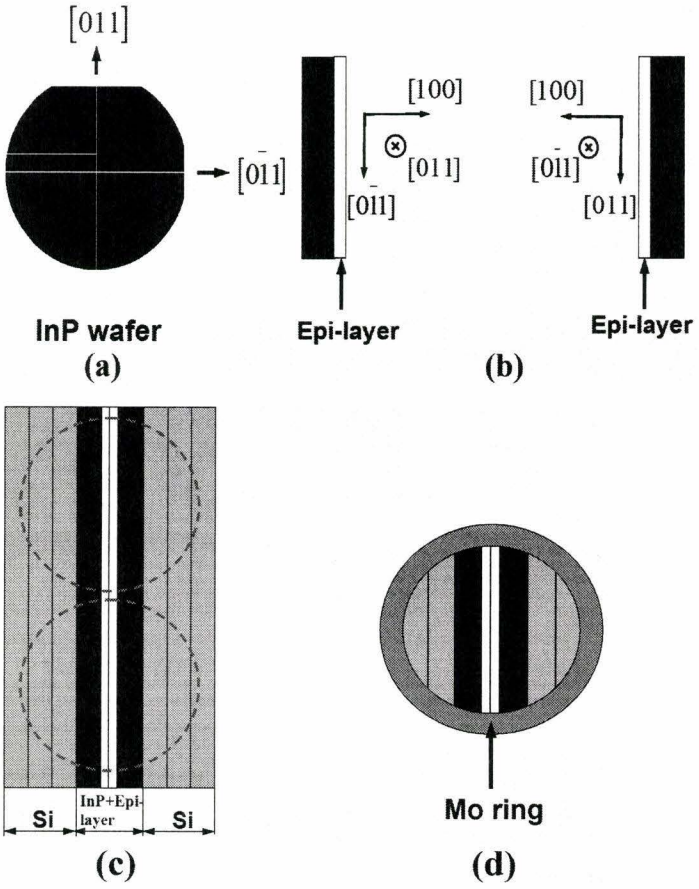

Figure 3-1: Schematic diagrams showing the standard procedures for TEM sample preparations. (a) Cleaving two slices along[011] and[0$\bar{1}$1], respectively. (b) Gluing the two slices. (c) Cutting of two discs. (d) Mounting the disc on the Molybdenum-ring.

(4) Ion milling

The central thinner part of the sample disc was ion-milled on a Gatan PIPS system with 4 keV Ar^+ ions at an incident angle of ±4°. When a small hole across the interfaces of the two slices appeared, electron transparency was achieved on the area adjacent to the hole. The sample was continuously rotated at 3.5 rotations per minute (rpm) all through the ion-milling process. A liquid $\mathbf{N_2}$ cold stage (about -170°C) equipped on the Gatan-PIPS system was employed to suppress the generation of **In**-rich clusters on the sample surface (Chew et al. 1987).

3.1.2 Low-angle wedge polishing

In addition to the **In**-rich clusters on InP-based samples, cross-sectional samples prepared through the standard procedures show other common problems. Amorphous layer formation on the sample surface may occur due to the ion bombardment and rapid thickness variation across the glued interfaces may occur because of the large starting sample thickness of tens of microns before ion-milling. These drawbacks increase the level of noise in high resolution TEM/STEM images and make quantitative interpretation of the results more problematic. In order to use the maximum potential of TEM/STEM and spectroscopic techniques, specimens with large uniform areas, 100 nm or less in thickness, and with damage-free surfaces are desirable. Low-angle wedge polishing perpendicular to the interfaces provides a practical solution for the problems present in the standard procedure by directly forming a low-angle wedge shaped sample and reducing the total ion-milling time (Voyles et al. 2003).

The main dilemma in low-angle polishing is that it is hard to find a versatile recipe for materials with different levels of fragility. The final quality of the specimen is very sensitive to the details of the polishing procedures. A good practical example dealing with typical semiconducting materials (Sapphire, Silicon and InP) with decreasing fragility can be found in Robertson et al. 2006 (a).

Low-angle polishing was carried out using an Allied High-Tech multi-prep system followed by ion-milling on the Gatan-PIPS for further thinning and cleaning of the samples. The steps involved are listed below:

(1) Cleaving, gluing and cutting

The cleaving procedure for two slices (8 mm in length and 1 mm in width) from the InP substrate was the same as the standard procedure (Figure 3-1 (a)). The shiny surfaces of the two slices were glued together with Epoxy Bond 110 from Allied High Tech Products, Inc. It is important to get the glue line between the two slices as thin as possible in order to prevent preferential removal of the materials from the area close to the glue line when the wedge is formed. Therefore, a minimal amount of epoxy should be used and the two glued slices should be compressed as hard as possible by clamping. After curing the epoxy on hot plate for about 10 minutes, the glued slices were mounted on a piece of glass slide and cut perpendicular to the glue line into small rectangular pieces. The length of the cut piece was about 3/4 of the diameter of a 3 mm Mo ring which has an elliptical hole in the center.

(2) Mount the sample on the polishing stub

The samples polished by multi-prep system were mounted on the TEM wedge polishing stub manufactured by Allied High Tech Products, Inc. First, planarization of the polishing stub was carried out by polishing it with a 15 μm grit-size diamond lapping film. To provide a smooth and defect-free supporting surface for the rectangular sample piece, a rectangular silicon wafer was glued on the stub surface by crystalbond™ wax. The sample was then mounted on top of the silicon wafer by crystalbond™ wax with the glue line between two cleaved sample slices perpendicular to the front edge of the silicon wafer.

(3) First-side polish

Before polishing, both sides of the sample piece should be planarized. After that, parallel polishing of the first side was carried out. A practical recipe showing the polishing sequences for the InP-based materials is summarized in Table 3-1.

After carrying out the above steps, a surface free of scratches and defects for the first side is expected. If not, the last two steps in Table 3-1 should be repeated until the quality of the surface is satisfactory under the observation with a good quality optical microscope.

(4) Mounting and gluing for the second side polish

The sample was mounted on the silicon wafer with the polished side facing down. Moreover, the front edge of the sample should be placed as close as

Table 3-1: A proposed recipe for the first-side polish.

Grit size (μm)	Finishing thickness (μm)	Rotation (RPM*)(CCW**)	Lubricant	Polishing Load (gram)
30	700	30	Water	2
15	500	30	Water	2
9	400	30	Water	2
6	350	30	Water	2
3	320	30	Water	1.5
1	4 minutes' polishing	20	Greenlube™	1
0.5	4 minutes' polishing	15	Greenlube™	0.5
0.1	4 minutes' polishing	15	Greenlube™	0
0.02 μm colloidal silica	4 minutes' polishing	20 (CW***)	Water	0

possible to the leading edge of the silicon wafer. Crazyglue™ was used for mounting the sample since it provides a superior bond over crystalbond™ wax based on our experience. After aligning the sample on the wafer, we wick the crazyglue™ from the sample edges in order to minimize the thickness of the glue layer underneath the sample. The glue was cured for three to four hours prior to polishing so that it can provide adequate support for the sample.

(5) Second-side polish

The sample was firstly parallel polished until the remaining thickness reached 200 μm followed by a low angle (2° between the surfaces of the sample

* Rotation per minute
** Counter clock-wise
*** Clock-wise

and polishing pad) polishing until the wedge shaped sample formed. A practical procedure for the second-side polishing is suggested in Table 3-2.

Table 3-2: A proposed recipe for the second-side polish.

Grit size (μm)	Finishing thickness (μm)	Rotation (RPM*) (CW**)	Lubricant	Polishing Load (gram)	Polishing angle (°)
9	200	20 (CCW***)	Water	2	0
9	100	20	Water	2	2
6	50	20	Water	2	2
3	20	20	Water	1.5	2
1	10	15	Greenlube™	1	2
0.5	0 (Wedge forms)	15	Greenlube™	0	2
0.1	0 (4minutes'polishing)	10	Greenlube™	0	2
0.02 μm colloidal silica	0 (4 minutes'polishing)	10 (CCW)	Water	0	2

After carrying out the above steps, a wedge shaped sample, without scratches and defects on both sides, should be produced. Otherwise, the last two steps in Table 3-2 should be repeated until the quality of the sample is satisfactory under the observation with a good quality optical microscope.

(6) Mount the sample on TEM grid

A thin layer of EPO-TEK®H22E epoxy was placed on one end of a Mo grid with the elliptical hole. The epoxy must be prepared at least 4 hours before in order to reduce the mobility of the sample sitting on the grid. The sample was mounted on the grid by catching the thick end of the wedge with the epoxy layer

* Rotation per minute
** Clock-wise
*** Conter clock-wise

on the TEM grid. The arrangement of the assembly is schematically illustrated in Figure 3-2. The sample thickness on the front edge of the polished wedge could be already electron transparent under the optimal conditions.

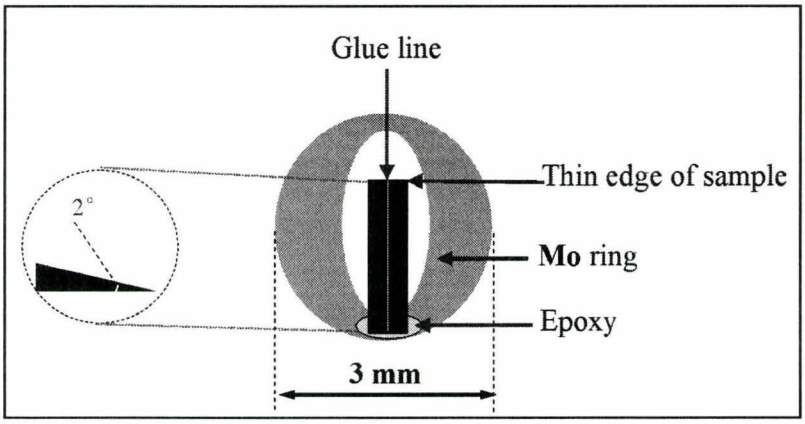

Figure 3-2: Schematic diagrams illustrating the configuration of the rectangular sample piece mounted on a Mo-ring with an elliptical hole in the center. The side-view on the left shows the ideal shape of a polished wedge.

(7) Ion-milling

The sample was treated by ion-milling to remove any residual contamination or colloidal silica particles, and the sample was further thinned until electron transparency was achieved. The ion-milling conditions used were gentler than those in the standard procedure since the thin end in the wedge shaped sample was already or very close to, electron-transparent. The ion milling was carried out on the thin end of the wedge with 3 keV Ar^+ ions at incident angles of ±3°, with the sample rotated at a rate of 3.5 rpm. A liquid N_2 cold stage was used throughout the ion-milling process. The total time required was about

15~30 minutes, which was shorter than for samples prepared through the standard procedures.

In this thesis, samples prepared from standard procedures were used for diffraction contrast imaging while samples prepared by low-angle polishing were employed for the quantitative analysis and high resolution imaging.

3.2 TEM/STEM imaging

3.2.1 Diffraction contrast imaging

The overall structure features and qualitative information about composition and strain variations in different layers, can be investigated by diffraction contrast imaging (Williams et al. 1996) performed with conventional TEM (CTEM). The specimen is illuminated by a parallel electron beam and tilted so that a set of atomic planes (for example {200}, {400} or {022} in this thesis) satisfy Bragg's law. The contrast in such images for crystalline materials is generated due to the different diffraction powers for the incoming electrons in different portions of the sample. Practically, in order to enhance the image contrast, the sample is usually tilted so that only the direct beam and one diffracted beam are strongly excited, which is called two-beam condition (Edington 1976). Bright field (BF) or dark field (DF) images can be formed by selecting either the direct or the diffracted beam in the diffraction pattern to generate the contrast. In order to suppress the contribution from aberrations and astigmatism, the practical DF image is taken

under the centered dark field (CDF) imaging mode, in which the incident beam is tilted so that the diffracted beam travels down along the optical axis. A typical diffraction pattern for III-V semiconductor on <011> zone axis and setting up for a BF image (with $\mathbf{g}_{0\bar{2}2}$) under two beam conditions are shown in Figures 3-3(a) and (b), respectively.

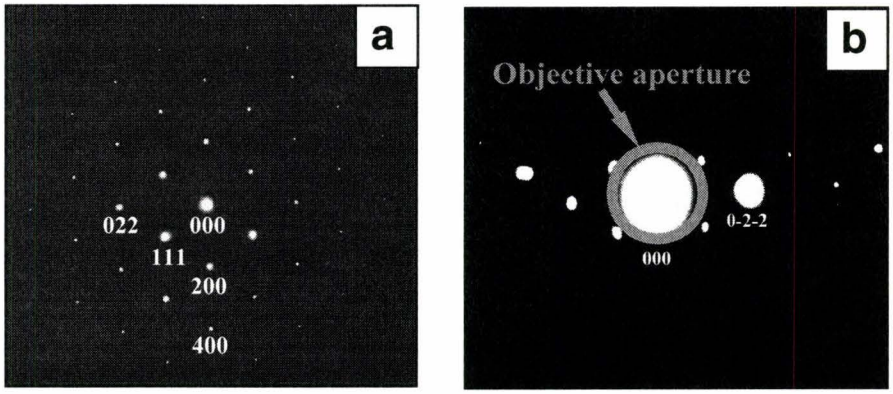

Figure 3-3: (a) A typical <011> diffraction pattern of III-V semiconductor material in zinc-blende structure. (b) Set-up for BF image with two beam condition.

The contrast in BF/DF CTEM images for thin specimens can be understood qualitatively by the kinematical theory (Hovsepian et al. 1999; Rosenauer 2003). The amplitude ϕ_g and intensity I_g of a diffracted beam $\mathbf{g}$ are given by:

$$\phi_g(s) = \int_0^t F_g(z) \exp\left[2\pi i(\mathbf{g} \bullet \mathbf{R(z)} + sz)\right] dz \qquad \text{(3-1)}$$

$$I_g(s) = \left|\phi_g(s)\right|^2 \propto \left|F_g(z)\right|^2 \qquad \text{(3-2)}$$

In the equations above, $F_g(z)$ is the structure factor for diffracted beam **g**; t, the thickness of the sample; z, the depth in the sample; $R(z)$, the displacement field along z direction; and s, the deviation parameter from the exact Bragg condition and $I_g(s)$ stands for the intensity of the diffracted beam.

From equations (3-1) and (3-2), the main dilemma in interpreting the diffraction contrast images is that the intensity recorded is actually the coupled information between the composition ($F_g(z)$), the displacement field ($R(z)$) and the Bragg deviation parameter (s). However, qualitative (LaPierre et al. 1996) or even quantitative (Leifer et al. 2002) structural information can still be derived from BF/DF images by choosing a suitable diffracted beam **g** for III-V semiconductor compounds in the zinc-blende structure (Harrison 2005). The methods for deriving information of composition and displacement field with different **g** vectors will be described as follows.

3.2.1.1 Composition sensitive imaging

By using the chemical sensitive diffraction, $\mathbf{g}_{200}$ (Rosenauer 2003; Bithell et al. 1991), the variation of composition across different layers can be directly viewed and intuitively interpreted in diffraction contrast images. Under the assumption of random distribution of group III (V) atoms on the group III (V) sublattice, the

structure factor for $\mathbf{g}_{200}$ diffraction from a zinc-blende semiconductor with average composition $\overline{III}$ - $\overline{V}$ is given by:

$$F_{200} = 4\left(f_{\overline{III}} - f_{\overline{V}}\right) \quad \text{——————} \quad (3\text{-}3)$$

In equation (3-3), $f_{\overline{III}}$ and $f_{\overline{V}}$ stand for the average atomic scattering amplitude of group III and V elements, respectively. Since the structure factor of $\mathbf{g}_{200}$ diffraction is more sensitive to the variation of chemical composition than displacement field (Rosenauer 2003), a rough estimation on the size, shape and distribution of a specific element in an individual quantum structure can be obtained through the chemical sensitive imaging as long as the contrast, which arises from the difference of average atomic scattering amplitudes between group III and V elements, is applicable enough between the quantum structure and BLs materials.

Various stacking patterns of InAs nanostructures grown between different BLs on an InP substrate (Lei et al. 2006 b; Lin et al. 2008) have been observed in cross-sectional DF images with $\mathbf{g}_{200}$. Also, qualitative or even quantitative compositional information can be derived from chemical sensitive imaging. By comparing the intensity ratio of the quantum dots (QD) and BLs in $\mathbf{g}_{200}$ DF images with those from calibrated samples, Lemaître et al. derived the quantitative **In** concentration in $In_xGa_{1-x}As$ QDs embedded in GaAs BLs (Lemaître et al. 2004). The QWRs/QDs induced **In** composition modulation (Joyce 2005; Shchukin et al. 2004) has been proposed based on the contrast

variations observed in the upper BL in TEM images taken with $\mathbf{g}_{200}$. Two typical examples include the observation of a band with brighter contrast than surrounding materials in an InGaAs BL directly above an InAs QD (Lin et al. 2008) and a "V"-shaped brighter contrast modulations in an InAlAs BL above the InAs QWRs (Lei et al. 2006 b; Brault et al. 2000), in $\mathbf{g}_{200}$ DF images.

Although the $\mathbf{g}_{200}$ is called a chemical sensitive diffraction, it is still difficult to derive quantitative information from such images for two reasons. Firstly, the displacement field still contributes to the image contrast taken with $\mathbf{g}_{200}$ which makes image interpretations complex. Numerical calculations are required for extracting quantitative information. Leifer et al. quantitatively analyzed $\mathbf{g}_{200}$ DF image contrast in $In_xGa_{1-x}As/GaAs$ system in order to understand the evolution of strain and chemical contrast as a function of **In** concentration (Leifer et al. 2002). Their results showed that finite element (FE) simulations of the 3D strain profile as well as dynamical (Williams et al. 1996) simulations for image contrast must be carried out in order to properly determine the **In** distribution in the $In_xGa_{1-x}As$ layer. By using a simple model investigating the contrast variations in DF $\mathbf{g}_{200}$ images as a function of QD size, shape, sample thickness, and the composition of the QD and BL materials, Beanland claimed that the QD size is not accurately determined by the brighter contrast region of the InAs QDs within the GaAs BL (Beanland 2005). Secondly, a sign reversal (Rosenauer 2003; Bithell et al. 1991) of the structure factor for the $\mathbf{g}_{200}$ reflection

occurs at a certain composition (for example, x= 0.60 for $In_xAl_{1-x}As$ and x= 0.37 for $In_xGa_{0.9-x}Al_{0.1}As$ on InP substrate) for ternary or quaternary semiconductor compounds. Therefore, without a rough knowledge of the nominal growth composition of the sample or the direct measurement of the composition, even an intuitively qualitative interpretation of the compositional variation in different regions by studying the contrast is not always reliable.

In summary, chemical sensitive imaging through diffraction contrast can only be used to acquire qualitative information with the pre-knowledge of the nominal composition. Quantitative analysis requires complex simulations or accumulation of experimental data from the standard samples.

3.2.1.2 Strain sensitive imaging

Another contrast mechanism arises from different deviation parameters s in different portions of the sample due to the displacement of atomic columns from their normal positions. For III-V compounds grown on (100) substrate, diffraction contrast in images taken with $\mathbf{g}_{400}$, or $\mathbf{g}_{022}$ reflects the variation of displacement field (Williams et al. 1996; Rosenauer 2003) parallel or perpendicular to the growth direction, respectively. The structure factors for these reflections in a zinc-blende semiconductor with average composition $\overline{III}$ - $\overline{V}$ can be written as $F_{400 or 022} = 4\left(f_{\overline{III}} + f_{\overline{V}}\right)$, which changes more slowly as a function of the composition than that of $\mathbf{g}_{200}$ reflection (Rosenauer 2003).

Strain-sensitive imaging is used in the following applications: (1) the observation of a capped QWR/QD structure is usually confirmed indirectly through the strain field contrast, resulting from the elastic relaxation during quantum structure formation through the S-K growth mode (Cullis et al. 2002), along the growth direction using the $\mathbf{g}_{400}$ reflection (Raz et al. 2004; Gutiérrez et al. 2005b) ; (2) defect generation (Gutiérrez et al. 2005a) (such as dislocations and stacking faults) from plastic relaxation* can be viewed through the bending and displacement of atomic planes close to the center of these defects with $\mathbf{g}_{400}$, or $\mathbf{g}_{022}$ reflections; (3) lateral composition modulation (LCM) (LaPierre et al. 1998) can be viewed with the $\mathbf{g}_{022}$ reflection through the strain field resulting from the different lattice parameters of adjacent regions rich or deficient of particular elements; and (4) lateral strain field (Robertson et al. 2006 b; Androussi et al. 1999) due to the elastic relaxation of a quantum structure can be observed in TEM images taken with $\mathbf{g}_{022}$.

Although the strain distribution can be viewed through CTEM images, it is hard to get any structural information of an individual quantum structure by directly interpreting the contrast. Usually the dimension of a strain field is larger than that of the corresponding quantum structures (Crozier et al. 2003). Also different shapes of QWR/QD may show the same strain contrast pattern (Liao et

* Plastic relaxation occurs when the layer thickness exceeds the critical value (Ohring 2002), which is determined by the mismatch between the epi-layer and substrate.

al. 2001). A comprehensive understanding of the strain contrast in CTEM images requires iterative simulations (for example FE simulation) of the elastic (such as strain and displacement) field distribution between the quantum structures and BLs. Only qualitative information can be derived from CTEM images after comparison of the image contrast with the simulated elastic field.

3.2.1.3 Experimental conditions for CTEM imaging

In this thesis, the CTEM imaging is carried out on a Philips CM 12 TEM operating at 120 kV and recorded on film or a charge coupled device (CCD) camera. Imaging conditions and information obtained from each **g** vector are summarized in Table 3-3.

Table 3-3: Information from different **g** vectors in CTEM images.

g	Type of diffraction	Type of image(s)	Information
200	Composition sensitive	BF, CDF	Shape and dimension of QWRs; stacking of multilayer QWRs; composition modulation in BLs
400	Strain sensitive	BF	Strain along the growth direction
022	Strain sensitive	BF	Strain along the lateral direction; LCM in BLs

Although qualitative structural information can be extracted from CTEM diffraction contrast imaging, the contrast is affected by coupling between

composition and strain field in both BF and DF images, which makes CTEM imaging inadequate for quantitative analysis.

In this thesis measurements of structural properties such as size, shape, strain distribution and composition variation in QWRs and surrounding BL materials will be obtained by high resolution TEM (HRTEM) imaging and spectroscopic techniques used for the direct measurement of composition.

3.2.2 HRTEM imaging

HRTEM techniques based on phase contrast imaging (performed in TEM mode) and high resolution high angle annular dark field (HR-HAADF) imaging (in STEM mode) will be used in this thesis. In HRTEM images, the positions of atomic columns can be resolved so that the size, shape and even strain in quantum structures can be studied in cross-sectional samples through analyzing the contrast and local variation of the atomic plane spacing. Moreover, the relaxation and displacement in atomic planes can be obtained by processing and analyzing the HRTEM images. Two methods, namely peak pair method (Galindo et al. 2007) and geometric phase analysis (Hÿtch et al. 1998) are widely used for this purpose.

3.2.2.1 Phase contrast imaging

The formation process of phase contrast image is schematically shown in Figure 3-4. The sample is illuminated by a parallel beam of electrons, which forms a

"coherent" source (Williams et al. 1996) to fulfill the pre-requisite for the phase contrast imaging. Instead of selecting only one beam in the diffraction pattern as in CTEM diffraction contrast images, all the spots with a frequency (here "frequency" refers to $\frac{1}{d_{hkl}}$ where d_{hkl} is the spacing of (hkl) plane) smaller than a

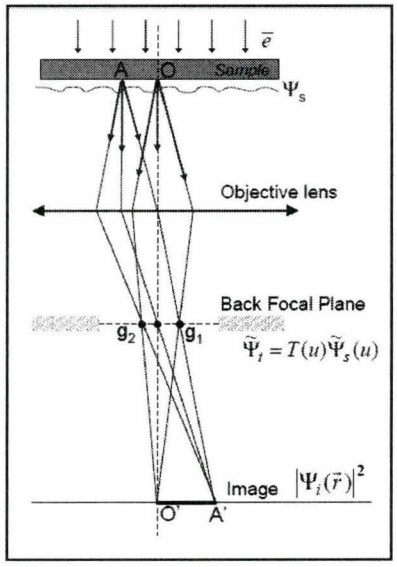

Figure 3-4: A schematic diagram illustrating the formation process of phase contrast imaging. Adapted from (Sarigiannidou, 2004).

cut-off frequency are included within the objective aperture for imaging. The interference (for example, A' in the image plane of Figure 3-4 results from the interference of g1, g2 and the direct beam) of the selected beams results in a lattice fringe image, which is, in some conditions of defocus, actually the 2D projection of the positions of atomic columns in the sample (Williams et al. 1996; Rosenauer 2003). The main disadvantage that limits the application of phase

contrast imaging is that the contrast is still strongly influenced by the electron diffraction in the sample. The image contrast is also sensitive to the variations of strain or displacement field, defocus or local thickness, and the lattice close to these areas can not be resolved (Spence 2003). Therefore, the complex sources responsible for the contrast variation make it difficult for direct interpretation of the phase contrast image. Correct interpretations of the phase contrast images must be necessarily accompanied by image simulations from many trial objects including imaging parameters and thickness of the sample. For strained quantum structures (such as QD/QWR) formed through S-K growth mode, the details of local lattices can not be resolved in phase contrast images due to the elastic relaxation at the interfaces between QD/QWR and BLs.

3.2.2.2 HR-HAADF imaging

HAADF images are formed in the STEM mode, where a fine electron probe (diameter on the order of Ångstrom scale) is scanned across each pixel in the selected area (Browning et al. 2001). In contrast with the simultaneous illumination in phase contrast imaging, each atomic column is illuminated sequentially so that the scattered electrons collected by the annular dark field (ADF) detector are regarded as from an "incoherent" source. As shown in Figure 3-5, HAADF images are formed by collecting the integrated intensity of high-angle (>50 mrad) elastically scattered electrons (Figure 3-6) on the ADF detector. Compared with the phase contrast imaging, these electrons are scattered to the

angles that are much larger than the Bragg angle (Williams et al. 1996), therefore, the diffraction contrast is practically suppressed in the HAADF image. According

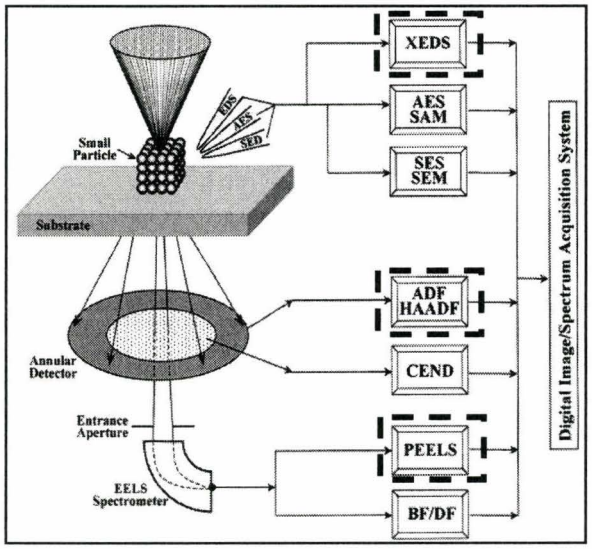

Figure 3-5: A schematic diagram illustrating the formation process of HAADF image and selected spectroscopic techniques used in this thesis (in dashed rectangles). Adapted from (Wang, 2000).

to the theory of Rutherford scattering (Browning et al. 1993), the cross-section for high-angle elastic scattering is proportional to the power n (n ranges from 1~2) of the atomic number of the elements present in the sample (Walther et al. 1997; Pennycook 1989). The contrast in HAADF images carries mainly the variation of the local atomic number Z at different regions of the sample. Therefore, a HAADF image is also called Z-contrast image in which the contribution from elastic field to the image contrast is suppressed. This advantage makes HAADF imaging suitable for determining the dimensions and shape of quantum structures

capped with BLs through analyzing the atomic number contrast between these two materials (Crozier et al. 2003; Kümmell et al. 2005).

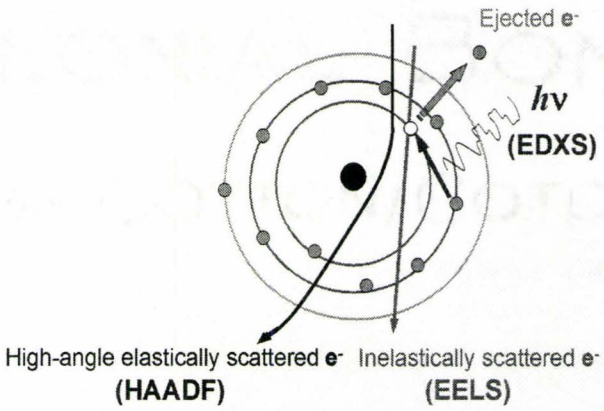

Figure 3-6: A schematic diagram illustrating the interaction of the incoming electrons with the atoms and the origin of HAADF, EELS and EDXS signals.

The atomic columns can be resolved in HAADF images when the STEM settings satisfy two pre-requisites. Firstly, the diameter of the electron probe must be smaller than the spacing of atomic planes in the specimen. Secondly, the convergence angle α of the electron probe must be adjusted so that overlapping regions of the adjacent convergent beam electron diffraction discs fall on the ADF detector to produce atomic resolution in the incoherent Z-contrast images (Rickerby et al. 1999).

As shown in Figure 3-5, another advantage of STEM-HAADF imaging is the chemical composition contrast can be directly viewed in image and the high-angle scattered electrons do not interfere with the signals for electron energy loss

spectrometry (EELS) or energy dispersive X-ray spectrometry (EDXS). Therefore, the analytical electron probes can be accurately focused on the small QWR area in HAADF images and quantitative information can be obtained simultaneously through EELS or EDXS analysis.

Although the contrast in HAADF images reflects the atomic number difference, recent studies by Wu et al. (Wu, X., et al. 2008) on highly strained InGaAsN quantum well structures show that the effect of strain still contributes to the image contrast unless the inner angle of the ADF detector reaches very high value of 90 mrad. Therefore, reliable quantitative compositional information in QWRs should be derived through the combined techniques of HAADF imaging and spectroscopic tools of EELS or EDXS.

In summary, the contrast in III-V semiconductor TEM/STEM images arises from complex physical processes. Correct interpretation of the image contrast is not always direct and intuitive. Simulations (such as image simulations or FE calculations) and other techniques (such as direct compositional analysis methods described below) must be employed to confirm the conclusions drawn from analyzing the contrast of images.

3.3 Quantitative compositional analysis

As mentioned above, quantitative compositional analysis should be carried out through the combination of HAADF imaging and spectroscopic techniques using STEM. The most used quantitative analysis tools include EDXS and EELS spectrum imaging (SI).

3.3.1 Spectrum imaging

SI performed on STEM-HAADF images is carried out in order to obtain the element distribution in a selected region of the specimen. The schematic description of the STEM-EELS-SI (STEM-EDXS-SI is a similar process) is shown in Figure 3-7. To fill the data cube (x, y, E), a digital scan is carried out by rastering the focused electron beam over each pixel (x, y) of the selected area in HAADF image (pixel by pixel for mapping a desired element distribution or over line scans across different layers showing the variation of the element along a specific path) with the third dimension (E) storing the EEL or EDX spectrum from each pixel. Through the analysis of the intensity variation of a certain energy loss edge at each pixel, the concentration variation in two dimensions for that element can be obtained. The details of EDXS, EELS and SI techniques can be found in a recent review by Botton in the book edited by Hawkes et al. (Hawkes et al. 2006).

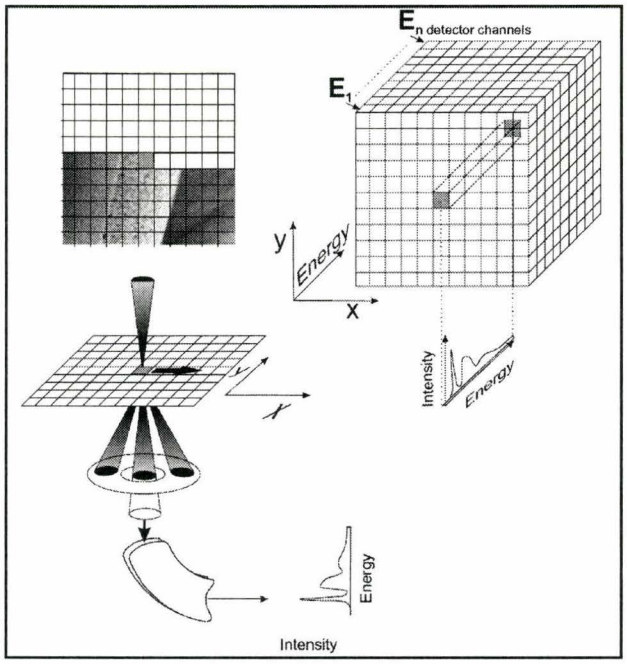

Figure 3-7: A schematic description of the STEM spectrum imaging (STEM-SI) technique. Adapted from (Hawkes et al. 2006)

3.3.2 EDXS

EDXS spectrum is formed by collecting the characteristic X-rays, which are generated from the ionization and relaxation (Figure 3-6) of inner shell electrons (Williams et al. 1996), on the EDXS detector. Compositional information at high resolution has been obtained for quantum structures by EDXS-SI combined with STEM-HAADF images since the size of the electron probe is comparable to the dimensions of these structures. For example, by elemental mapping and line scan profiles across the interfaces between QDs and BLs, the mismatch and composition were studied by EDXS-SI for vertical $In_xGa_{1-x}As$ QD arrays grown on a GaAs substrate (Zhang, Q., et al. 2001). EDXS-SI is also used to study the

growth mechanism of InAs QD structures on GaAs demonstrating the existence of a wetting layer (WL) between two adjacent InAs QDs. The detection of this WL serves as confirmation for proposed the S-K growth mode (Zhi et al. 2001; Schneider et al. 1999) for QD/QWR. Also, the measured distribution of group III elements in QDs and BLs obtained by EDXS-SI has been employed to studied the inter-diffusion between QDs and WL (DeGiorgi et al. 2001), or between QDs and BLs (Zhi et al. 2001; Liao et al. 2002)

With regards to QWR structures, EDXS line scans have been used to derive the local composition variation of **In** or **Al** within the InGaAs/InAlAs (411) **A** ridge QWRs (Jiang et al. 2000) and AlGaAs QWRs between AlAs BLs (Takeuchi et al. 1995), respectively.

Although the distribution of different elements in quantum structures and surrounding BLs with high spatial resolution and satisfactory accuracy (as high as 1 atomic %) (Williams et al. 1996) can be achieved through EDXS analysis, the problem of beam broadening and low acquisition efficiency limits its application. Because of the beam broadening on its way through the specimen (Williams et al. 1996), an EDXS profile with a gradual composition change appears even when the scan is performed across the interface with sharp composition variation on both sides. Moreover, three dimensional models for QDs or QWRs include the beam broadening and the position of the quantum structures in the cross-sectional

specimen must be applied to extract the "real" composition (Zhi et al. 2001; Harvey et al. 2001). Also, the characteristic X-ray is generated in a total solid angle of 4π sr and the typical collection angle is usually several tenths of a sr (Williams et al. 1996). Thus, it takes a long time (several minutes or even longer) to accumulate a statistically meaningful EDXS signal and the possible drift of the specimen during the data collection adds another uncertainty in interpreting the quantitative data. Procedures to correct this drift problem must be performed for EDXS data collected from small features, such as QWRs (Karim et al. 2006).

Due to the disadvantages described above, EDXS is only used in this work to study the features on a relative large scale, such as the composition modulation in BL. For the quantification, the Cliff-Lorimer ratio method is usually employed. The characteristic X-ray intensity for two elements (A and B) I_A, I_B and the atomic concentration C_A, C_B are related by the k factor through the equation: $\frac{C_A}{C_B} = k\frac{I_A}{I_B}$. The k factor between elements A and B can be extracted from the samples with well-known composition such as standard samples or a built-in reference. In order to derive composition of elements A and B from other regions of the same sample or from a different sample, the experimental settings, including the microscope settings, the sample orientation and thickness, must be kept identical to those applied to calculate the k factor.

3.3.3 EELS

Electrons suffer an energy loss due to the interaction with the inner shell electrons of a specific atom when they pass through the specimen (Lang 2003; Williams et al. 1996). An EELS spectrum records the counts of electrons as a function of the electron energy loss. When an inner shell electron of the atom is moved outside the potential field of the nucleus by the incoming electrons, such process is called ionization, which is shown as the core-loss edge (Egerton 1986) in an EELS spectrum. The amount of the energy loss of the incident electrons recorded at a core-loss edge carries the characteristic information of an element that is ionized. Also, the counts of electrons recorded at the core-loss edge are proportional to the concentration of the ionized element present in the specimen (Egerton 1986). Therefore, the position and integrated intensity of the core-loss edge in the EELS spectrum can be used for both identifying and quantifying an element, respectively. As shown in Figure 3-8 (the experimentally detected **In** $M_{4,5}$ edge, for example), before obtaining the signals of **In**, the background intensity ($\boldsymbol{I_B}$) in the EELS spectrum was estimated by extending the pre-edge portion of the spectrum with the inverse power law: $I_B = AE^{-r}$ (E is the energy loss; A stands for a scaling constant and r is the pre-edge slope exponent). After subtracting the background intensity ($\boldsymbol{I_B}$), the signals of **In** ($\boldsymbol{I_S}$) were then extracted by integrating the portion of spectrum above the background within an intergral window Δ.

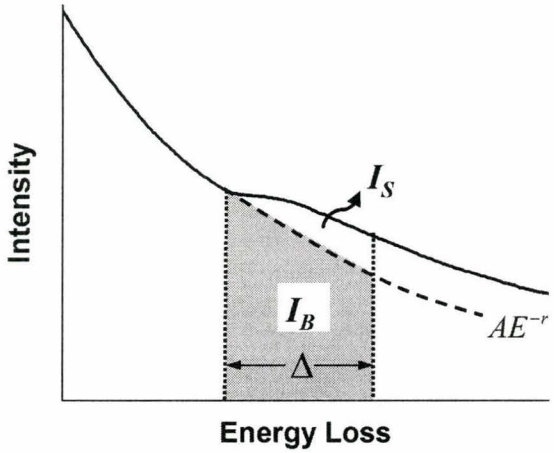

Figure 3-8: A schematic diagram illustrating the subtraction of background signals (I_B in the grey area) and the integral of the **In** $M_{4,5}$ edge signals (I_S above the background) within a window **Δ** in an EELS spectrum.

According to the theory developed by Egerton and co-workers (Egerton 1986), the principal equation for EELS quantification is:

$$N = \frac{I_S(\beta,\Delta)}{I_{Low}(\beta,\Delta)\sigma(\beta,\Delta)} \qquad \text{(3-4)}$$

where N is the number of atoms per unit area in the specimen, within thickness t, that contributes to the signal of the core-loss edge; β and Δ stand for the collection angle of the EELS spectrometer and the width of the energy window for signal integral (as shown in Figure 3-8), respectively. $I_{Low}(\beta,\Delta)$ is the integral intensity of the low-loss portion, starting from the zero-loss peak, extending over an energy loss window Δ recorded on the EELS spectrometer with collection

angle β. $\sigma(\beta,\Delta)$ is the partial ionization cross-section of the element in the sample contributing to the EELS core-loss edge.

Compared with EDXS, there are two main advantages of EELS analysis: (1) higher spatial resolution since the beam broadening is much smaller in EELS (Colliex 1985) than that in EDXS; and (2) higher collection efficiency because all the energy loss electrons will travel forward and be collected by the spectrometer (Williams et al. 1996). This reduces both the total collection time and the sample drift during data acquisition.

Because of the advantages over EDXS, EELS has been recently applied to study the composition of III-V semiconductor nanostructures. Molina et al. (Molina et al. 2006) mapped the distribution and studied the exchange of group V elements during the formation of InAs QWRs grown on, and capped with, InP, using EELS-SI with the **As** *M* and **P** *L* EELS edges. In addition, for InAs QWRs with InGaAlAs BLs grown on an InP substrate, Kümmell et al. (Kümmell et al. 2006) compared the intensity changes of the **In** *M* and **Ga** *L* ionization edges between EELS spectra and estimated the group III elemental concentrations in the QWRs by point analysis. Other works focused on the compositional analysis of InAs QDs in GaAs structures using the **In** $M_{4,5}$ edge (Crozier et al. 2003; Wang, P., et al. 2006; Kümmell et al. 2005; Chung et al. 2008).

Although compositional analysis for group III elements in semiconductor quantum structures has been achieved by EELS-SI for either point analysis (Kümmell et al. 2006) or line profiles (Crozier et al. 2003), there is still debate about the detailed elemental distributions in quantum structures embedded within BLs. Some researchers (Werner et al. 2000) have claimed that the maximum elemental signal is detected in regions close to the top of the quantum structures, while others (Crozier et al. 2003) believe that the maximum should appear in the central region of these structures. Since growth parameters are likely to affect the compositional distribution, it is therefore important to extract a clear concentration map of the group III element in QWR structures so that the optoelectronic properties and growth mechanism of these nanostructures can be properly understood.

Deriving the "true" cross-sectional composition of quantum nanostructures through EELS-SI is more straightforward in the case of QWRs than that for QDs. It is reasonable to assume that the QWRs, when viewed along their long axis, which in our work typically have a length larger than 100 nm (shown by AFM and TEM images in Chapters 4 and 5), occupy the whole sample thickness (less than 100 nm) along the electron propagation direction. While in the case of QDs, in order to extract reliable data about compositional information, this assumption does not work and models are needed, which compensate for the

interaction between the electron beam and the QDs and the BLs along the beam path in the cross-sectional samples (Crozier et al. 2003; Wang, P., et al. 2006).

The compositional information from quantum nanostructures is essential to understand and model other physical properties, such as optoelectronic and elastic properties, and growth phenomena that these structures exhibit. Chung et al (Chung et al. 2008) interpreted the band-tail structure observed in the photoluminescence spectra from his samples as resulting from the experimentally confirmed **In-Ga** intermixing regions at the interfaces between InAs QDs and GaAs BLs. Molina et al. (Molina et al. 2008) incorporated the experimental compositional map from InAs QWRs/InP to simulate the elastic strain distribution and successfully predict the nucleation sites of InAs QWRs in multilayer growth.

As mentioned above, since the EELS signals do not interfere with high-angle scattered electrons, which form the HAADF images, in this thesis, we will use the ideal combination of the HAADF imaging and EELS-SI to accomplish compositional analysis for individual QWRs (in single layer and multilayer samples) and to provide reliable quantitative composition profiles and maps of group III elements in both the QWRs and BLs.

3.3.4 Experimental conditions for HRTEM imaging and SI

The instruments involved in high resolution imaging and EDXS/EELS-SI compositional analysis include: a FEI Titan 80-300 Cubed STEM equipped with a spherical aberration corrector of the imaging lens used to record HR-HAADF image. The inner and outer angles of the ADF detector were 64 mrad and 141 mrad, respectively. HAADF imaging and EELS-SI were performed on a JEOL 2010 field-emission STEM equipped with Gatan Tridem imaging filter (GIF). The HAADF images recorded on the JEOL 2010 TEM were recorded using an ADF detector with inner and outer angles 70 mrad and 154 mrad, respectively. The software used for signal collection and data processing of the EELS spectra was Digital Micrograph (Gatan, Inc., GMS 1.6.0). The EDXS results were obtained with an Oxford Instruments plc x-ray detector and INCA software.

3.4 Summary

The sample preparation methods and (S)TEM based techniques for both imaging and quantitative analysis of semiconductor quantum structures were reviewed in this chapter. The CTEM diffraction contrast imaging taken with different **g** vectors under two beam conditions was employed to provide qualitative information about composition and elastic field in QWR structures. HR-HAADF is employed to determine the shape and dimensions of QWR in cross-sections. The quantitative compositional analysis is proposed to be performed with the combination of HAADF imaging and EELS/EDXS-SI.

Chapter 4

Single layer quantum wires

Overview

Initially, the influence of the growth conditions on the morphologies and optoelectronic properties of single layer QWR structures are explored. The objective is to determine the practical Gas Source Molecular Beam Epitaxy (GSMBE) growth parameters, which lead to the formation of the QWR structures with good quality of optoelectronic properties. The outcome of this work will then be applied to the growth of multilayer QWR structures to be presented in the next chapter. Characterization is focused on deriving meaningful structural and optical information through comparisons of samples grown by changing one growth parameter at a time. Characterization techniques for the samples include AFM, PL and TEM imaging. Quantitative compositional information was obtained by the STEM-based spectroscopic techniques described in detail in Chapter 3. This compositional information is important because: (1) it is the basis for understanding the growth mechanism of the QWRs in InAs/InP system; and (2) it can be used as the initial values for the numerical models used in simulating the elastic (Molina et al. 2006) and optoelectronic properties (Gioannini 2004). The purpose of accumulating the experimental data and theoretical results is to pave

the way for future fabrication of QWR structure-based devices for potential applications such as broadband emitters (Ooi et al. 2008) or lasers and optical amplifiers (Lelarge et al. 2007; Reithmaier et al. 2005). For applications involving optical fiber transmission, structures exhibiting an emission signal at a wavelength near 1.55 μm at room temperature (RT) are of significant technical importance.

4.1 Exploration on growth conditions

The standard growth structure was shown in Figure 2-2. Basic requirements for the as grown QWR samples include: (1) QWRs form on top of the lower BL and are completely covered by the upper BL; (2) no misfit dislocations are present at the interfaces between QWR and BLs, or between the InP buffer layer and initial BL; and (3) the samples exhibit PL emission from radiative recombination transitions of electrons and holes in the QWR region, at least in low temperature (14 K to 77 K) measurements.

As shown in Table 2-1, the role of each of four important parameters is examined separately on single layer QWR samples. The parameters include the growth rate of the QWR layer, the thickness of QWR layer, the growth temperature for both QWR and BLs, and the composition of the BLs.

All the samples grown for comparison in the same group were produced during a single cycle of MBE growth in order to minimize the uncertainties arising from small variations of the growth conditions within the MBE facilities, which may occur over time.

4.1.1 Growth rate

Samples produced for studying the effect of the growth rate on the QWR structure are A1 and A2 (group 1); B1 and B2 (group 2) shown in Table 2-1.

The AFM results providing the information on the morphologies of the free-standing QWRs for the four samples are shown in Figure 4-1. Generally, the shape of the InAs nanostructures on the surface can be described as 1-D wires since, for example in sample A1 (Figure 4-1 (a)), the average length along $[0\bar{1}1]$ direction is (256±92) nm while the average width along the [011] direction is (20±4) nm such that carrier confinement only occurs in the [011] and [001] directions. Comparisons of the QWR widths within the each group were obtained from averaging the widths obtained through a line scan across 25 wires along [011] direction in each AFM image. The average width of the QWRs estimated from the AFM images are (20±4) nm and (31±3) nm in samples A1 and A2, (17±3) nm and (24±3) nm in samples B1 and B2, respectively. Therefore, the average width of the QWRs becomes larger at lower growth rates. However, the

widths for samples A and B should not be quantitatively compared since they were grown in different MBE cycles.

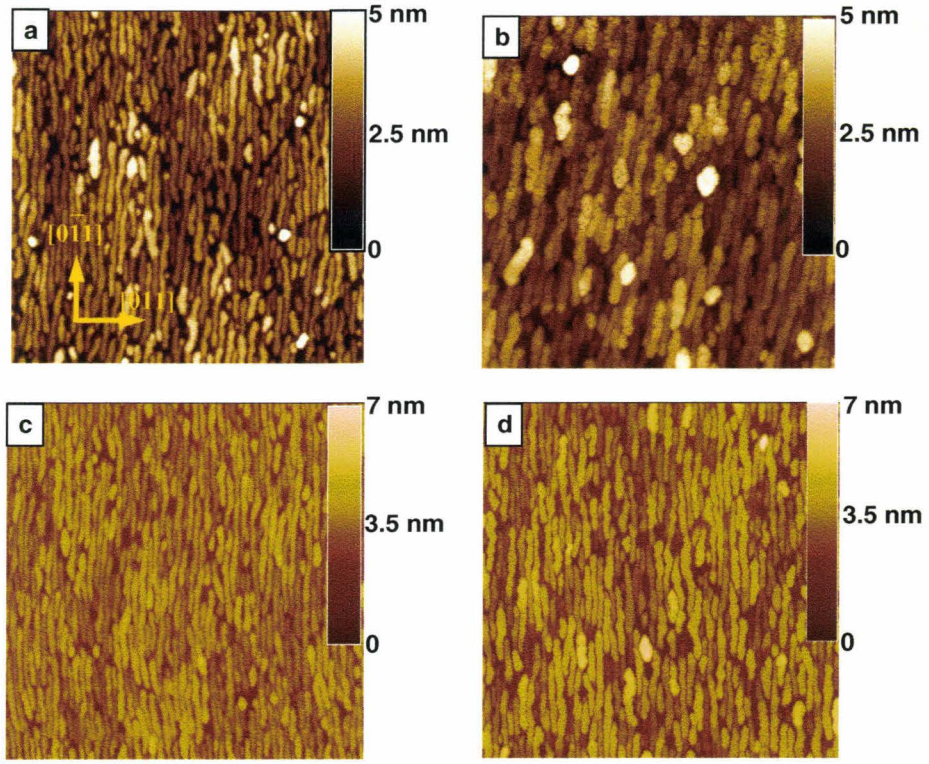

Figure 4-1: AFM images for samples with different deposition rates for InAs QWR layer. (a) A1: 0.4 ML/s and (b) A2: 0.1 ML/s; (c) B1: 0.4 ML/s and (d) B2: 0.04 ML/s. All the images are 1 μm by 1μm. and the insert in (a) shows the orientation for all images.

The PL spectra for samples B1 and B2, measured at 27 K, are shown in Figure 4-2 with the wavelength centered at 1.50 μm and 1.57 μm, respectively. Based on the experimental and theoretical results in literature (Kümmell et al. 2006; Maes et al. 2004; Fuster et al. 2005), the PL wavelength from self-assembled InAs QWRs on an InP substrate is more sensitive to the height

variation than that of the width. As estimated from the AFM images in Figure 4-1 (c) and (d), the heights are (2.6±0.36) nm and (3.0±0.40) nm for samples B1 and B2, respectively. From equation (1-1), the variation of height and width in samples B1 and B2 causes a change of 0.05 eV and 0.002 eV of the energy level positions, respectively.

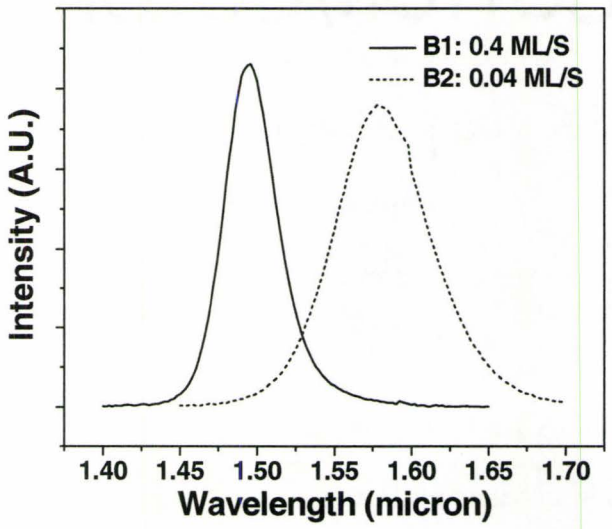

Figure 4-2: PL spectra at 27K for samples B1 and B2.

Therefore, the 70 nm red-shift of the PL wavelength corresponds primarily to the larger height, hence lower carrier confinement, is observed for sample B2 with the decreased growth rate. In addition, the full-width at half maximum (FWHM) of the PL spectra (Alén et al. 2002) yields information on the comparative height distribution of QWRs. The PL spectrum from QWRs with a small height distribution will show a narrower peak than from a sample with larger height

fluctuation. From Figure 4-2, it is determined that the FWHM is 39 nm and 60 nm for samples B1 and B2, respectively. Thus, the uniformity of the height distribution is improved by increasing the deposition rate of the InAs QWR layer.

4.1.2 Thickness of InAs

Three samples with different thickness of the InAs QWR layer (2.5 ML, 3.5 ML and 5ML for sample C1, C2, C3, respectively in Table 2-1) were grown to explore the effect of the InAs thickness on the structural and optical properties of QWRs. A thin GaAs layer (0.6~1nm) was deposited before the deposition of InAs QWR as a means to provide a more smooth growth front (Kim et al. 2003).

The AFM images for the three samples are shown in Figure 4-3. The morphologies of the free-standing InAs structures vary from a nearly flat surface with randomly distributed small particles in sample C1, with 2.5 ML InAs (Figure 4-3(a)), to wire-like structures when the thickness of InAs is increased to 5 ML (sample C3 in Figure 4-3(c)). Sample C2, with 3.5 ML InAs (Figure 4-3(b)), shows a morphology that is intermediate between C1 and C3 with less distinct wire-like formation than C3.

Cross-sectional TEM images (to be presented in section 4.2) confirm that the InAs has undergone a growth mode transition from layer-by-layer in sample

C1, where essentially only the wetting layer is formed, to well developed QWRs as the thickness of InAs layer increases.

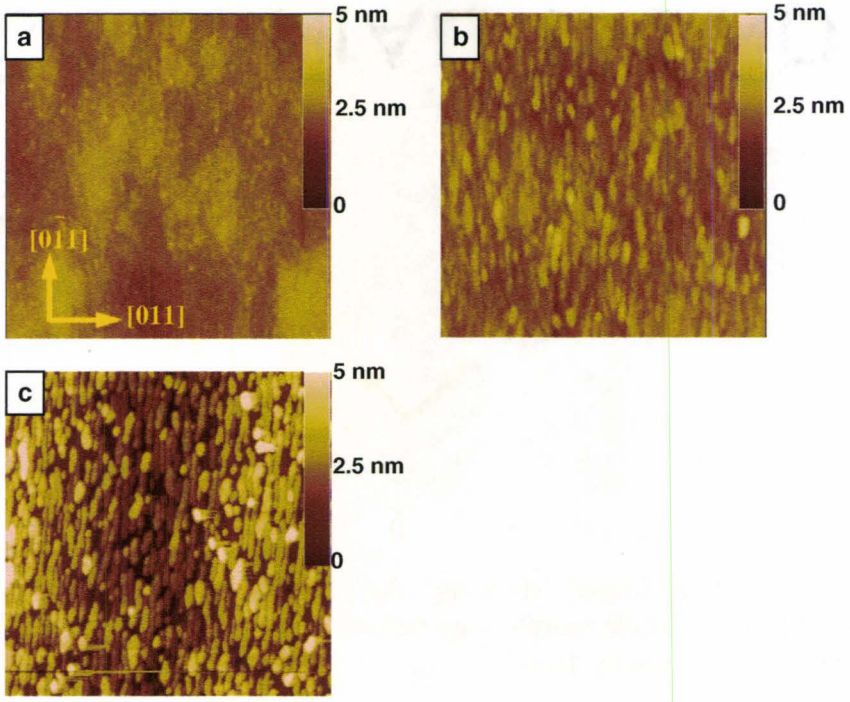

Figure 4-3: AFM images for samples with different InAs layer thicknesses. (a) C1: 2.5 ML; (B) C2: 3.5 ML; and (c) C3: 5 ML. All the image sizes are 1 μm by 1μm and the insert in (a) represents the orientations for all images.

This observed morphology variation confirmed that the formation of InAs QWRs in our system follows the well-established Stranski-Krastanow growth mode (Cullis et al. 2002) i.e. the QWRs are formed through the elastic relaxation of the mismatch strain energy between InAs and $In_{0.53}Ga_xAl_{0.47-x}As$ BLs above a critical thickness. The formation of InAs QWRs is believed to result from the nucleation of InAs modulated by the anisotropic surface features extending along [01$\bar{1}$] on $In_{0.53}Ga_{0.37}Al_{0.10}As$ growth front, as shown in Figure 4-4.

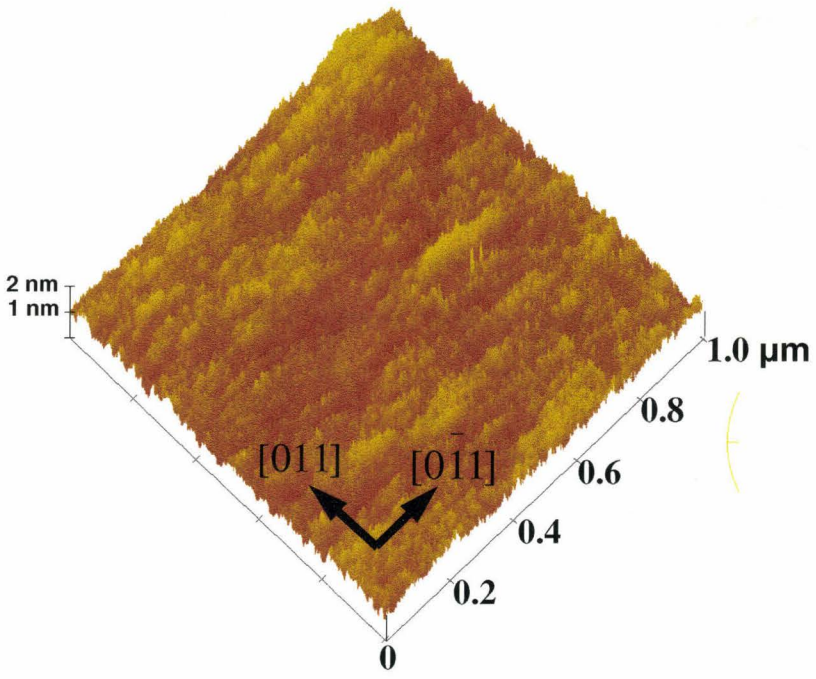

Figure 4-4: AFM image showing the three dimensional view of the $In_{0.53}Ga_{0.37}Al_{0.10}As$ surface morphology before the deposition of InAs QWRs. The size of the image is 1 µm by 1µm.

The variation of the optical properties with the thickness of InAs layer is shown in the PL spectra, measured at 60 K, for samples C2 and C3 (Figure 4-5). A red-shift of 100 nm of the PL wavelength is observed from 1.52 µm to 1.62 µm when the thickness of InAs is increased from 3.5 ML to 5 ML. This observation can also be attributed to the height variation of QWRs from the different thicknesses of InAs. As estimated from AFM images, the average height of QWRs in samples C2 and C3 are (1.6±0.3) nm and (3.6±0.6) nm, respectively and the widths of QWRs in samples C2 and C3 are (23.5±3.1) nm and (24.4±4.0) nm, respectively. As estimated from equation (1-1), the variations of height and

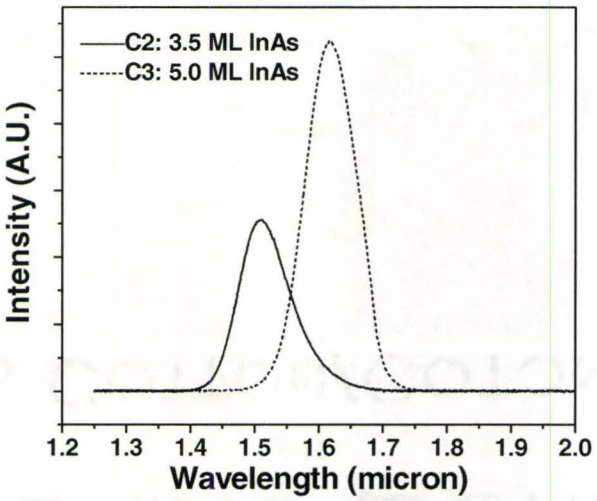

Figure 4-5: PL spectra at 60 K for samples C2 and C3.

width in samples C2 and C3 causes a change of 0.42 eV and 0.0018 eV in energy level positions, respectively. Therefore, the 100 nm red-shift of the PL wavelength is attributed to the larger height, hence lower carrier confinement energy, observed for sample C3 with the increase in the thickness of InAs layer.

4.1.3 Growth temperature

Three groups of samples (two in each group, A1 and D, B2 and E, F and B1, shown in Table 2-1) were grown to study the influence of the growth temperature on the structural and optical properties of the QWRs.

The AFM images for the three groups of samples are shown in Figure 4-6. Through comparison of the morphologies of the free-standing nanostructures in

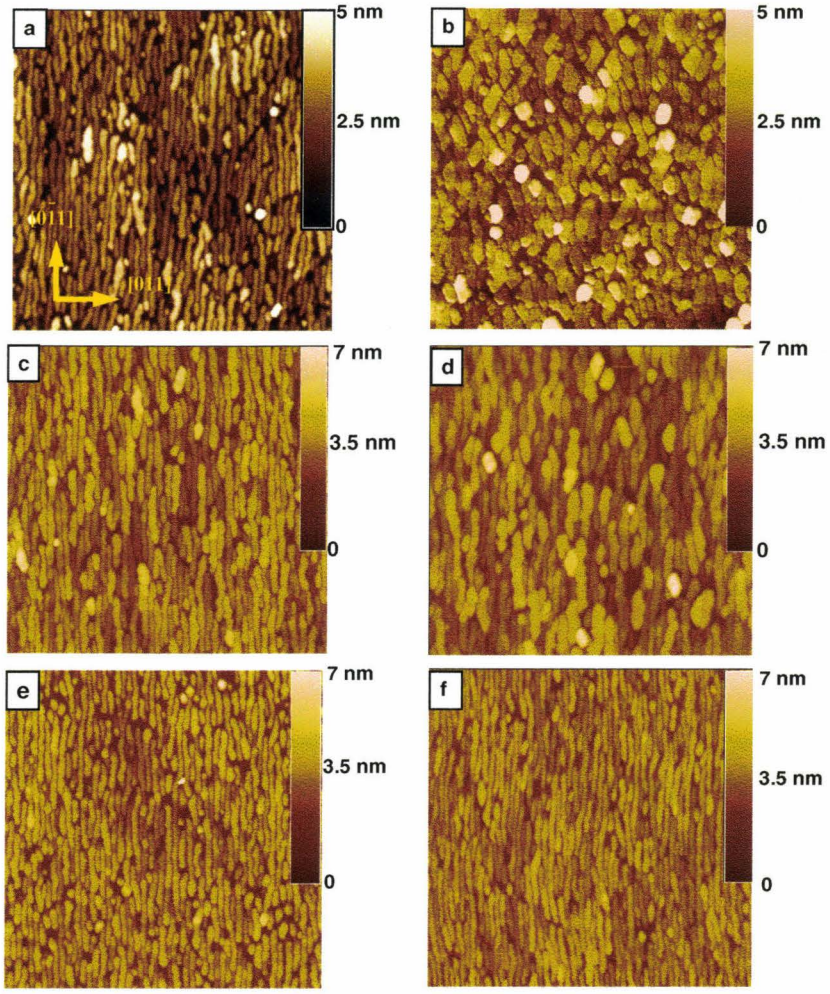

Figure 4-6: AFM images for samples grown at different temperatures (a) A1: 520 °C and (b) D: 470 °C; (c) B2: 520 °C and (d) E: 495 °C; (e) F: 545 °C and (f) B1: 520 °C. All the image sizes are 1 μm by 1μm and the insert in (a) represents the orientations for all images.

images, it is observed that for samples grown above 500 °C, well-developed QWRs were observed with their long axis lying along[$0\bar{1}1$]. At the lower growth temperatures, the length of the QWRs along [$0\bar{1}1$] decreases and the width along

[011] increases and the structures tend to more quantum dot- or quantum dash-like. This trend is most obvious from comparing samples A1 (Figure 4-6 (a)), and D (Figure 4-6 (b)), where the difference of growth temperature is the largest (ΔT=50 °C) among the three groups while all other parameters of growth remain the same. Well developed, long QWRs (with average length and width of (256±92) nm and (20±4) nm, respectively) appeared in sample A1 while short quantum dashes plus randomly distributed quantum dots (with average length and width of (90±29) nm and (37±6) nm, respectively) were obtained in sample D when the growth temperature was reduced to 470 °C. In the group of samples B2 and E, wire-like features were observed in sample E grown at 495 °C (Figure 4-6(d)), but still with a larger average width of (33±6) nm along [011] direction than that of (24±3) nm in sample B2 grown at 520 °C (Figure 4-6(c)). When the growth temperature exceeds 500 °C, similar morphologies of QWRs were observed in samples A1, F and B1 in Figures 4-6 (a), (e) and (f), in terms of average length ((256±92) nm, (272±66) nm and (261±109) nm for A1, F and B1, respectively) and width ((20±4) nm, (20±2) nm and (17±3) nm for A1, F and B1, respectively).

The AFM observations were further confirmed from the analysis of the optical properties through PL spectra, at 27 K, for samples B2 and E, F and B1 shown in Figures 4-7 (a) and (b), respectively. The positions of the peak wavelength are very close for the two samples in each group (1.56 μm and 1.57 μm for B2 and E, respectively; 1.49 μm and 1.50 μm for B1 and F, respectively).

The PL spectra clearly show that the peak intensity increases as the growth temperature is increased. This can be explained by the fact that the higher growth temperature results in a higher surface diffusion rate for the adatoms and this should lower the density of grown-in point defects, such as vacancies and anti-sites (Tuck 1988). Such defects would act as non-radiative recombination centers and reduce the intensity of the PL spectra.

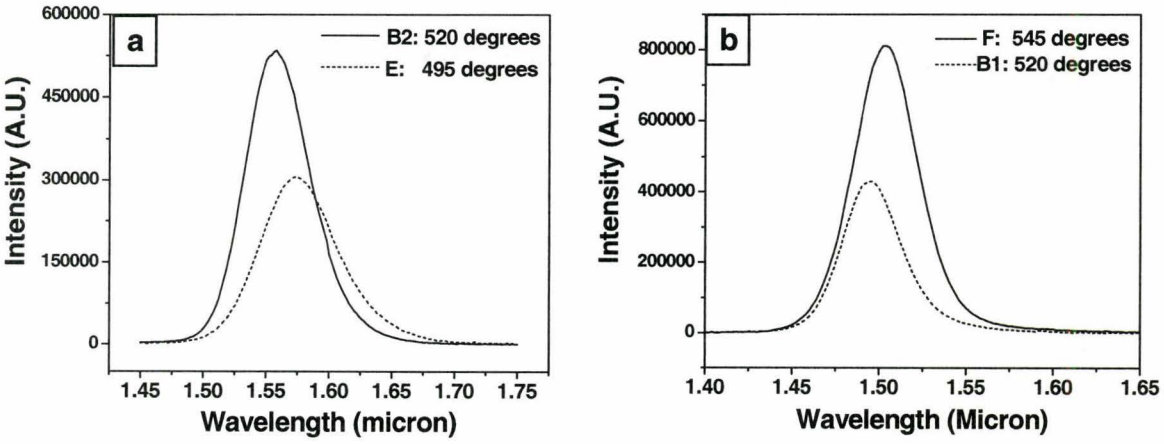

Figure 4-7: PL spectra at 27 K for samples grown at different temperatures. (a) samples B2 and E; and (b) samples F and B1.

4.1.4 Composition of the barrier layers

Two specimens with $In_{0.53}Ga_xAl_{0.47-x}As$ BLs containing 10 and 20 atomic percent (at.%) **Al** were grown for sample G1 and G2 in Table 2-1, respectively to evaluate the effect of the BL composition on the QWR structures. AFM images are shown in Figure 4-8. No significant morphological difference was noticed when comparing the length (with an average of (263±132) nm and (254±86) nm for G1 and G2, respectively) and width (with an average of (19±4) nm and (20±3) nm for

G1 and G2, respectively) of the QWRs in samples G1 and G2 along $[0\bar{1}1]$ and [011] directions, respectively.

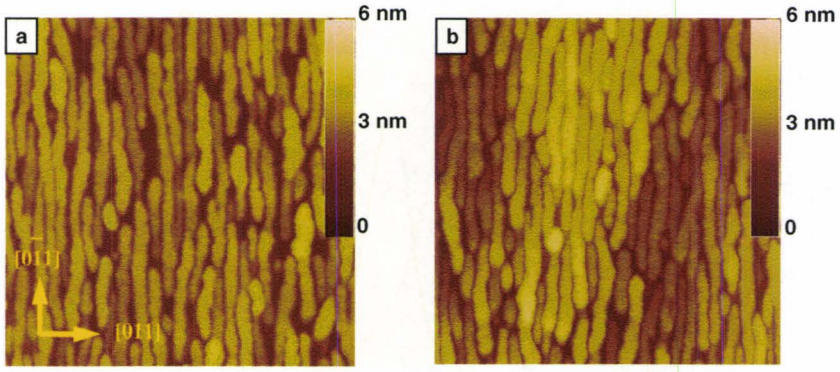

Figure 4-8: AFM images for samples with different **Al** content in BLs (a) G1: 10 % Al; and (b) G2: 20 % Al. Both of the image sizes are 0.5 μm by 0.5 μm. The insert in (a) represents the orientations for both images.

The PL spectra, at 14 K, for both samples are shown in Figure 4-9. The wavelength centered at 1.56 μm and 1.45 μm for sample G1 and G2, respectively. A blue-shift of 110 nm was observed as the **Al** content in the BLs was raised from 10% to 20%. The blue-shift was not from the difference of height since the average values are (2.6±0.3) nm and (2.6±0.4) nm for G1 and G2, respectively. This trend has also been both experimentally observed and theoretically explained for InAs layers embedded within $In_{0.53}Ga_xAl_{0.47-x}As$ BLs lattice matched with InP (Ustinov et al. 1998; Tournié et al. 1993). It is attributed to the higher transition energy between electrons and holes as band discontinuities (ΔV_e and ΔV_h in Figure 1-2) between BLs and InAs QWRs are increased with **Al** content in the BLs. Therefore, the observed blue-shift of the PL wavelength as the **Al** content

varied from 10% to 20% should be associated with the different band alignment patterns between BLs and InAs QWRs in samples G1 and G2.

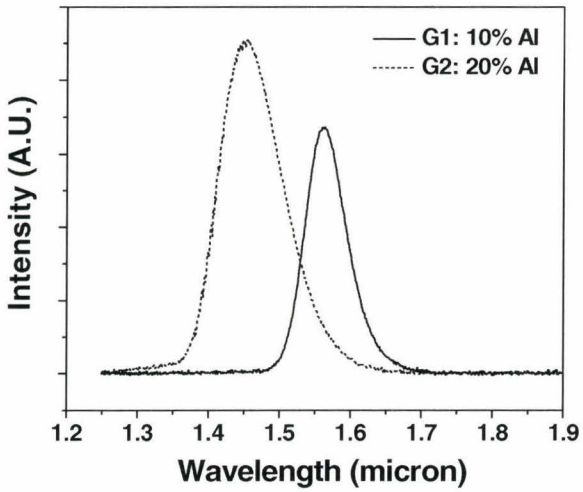

Figure 4-9: PL spectra at 14K for QWR samples covered by BLs with different composition.

4.1.5 Summary

Each growth parameter that influences the structural and optical properties for the single layer QWRs has been investigated. It is worth summarizing the practical growth conditions favoring the formation of QWRs exhibiting promising optical properties for device applications (especially for 1.55 μm emission) before discussing multilayer QWRs in the next chapter.

Growing the InAs at 0.4 ML/s generates long, aligned QWRs. As shown in Figure 4-2, the PL spectrum at 27 K for sample B1 grown at 0.4 ML/s shows a shorter (1.50 μm) emission wavelength than that (1.57 μm) from samples B2 grown at 0.04 ML/s. Also, the FWHM of the PL spectrum is narrower for the

sample grown at higher deposition rate suggesting a more uniform height of the QWRs grown at the higher growth rate. Therefore, based on these results, the QWR layers in all multilayer samples will be deposited at a growth rate of 0.4 ML/s.

Although sample F grown at 545 °C shows higher PL intensity than sample B1 grown at 520 °C, the higher growth temperature is undesirable for MBE growth on an InP substrate due to the significant desorption of **In** at 545 °C, which has been confirmed by Houdré et al. (Houdré et al. 1991). As a compromise, the growth temperature for $In_{0.53}Ga_xAl_{0.47-x}As$ and InAs layers is set to 520 °C for growing the multilayer QWR samples.

Since the PL wavelength can be tuned by changing the thickness of the InAs QWR layer (Figure 4-5) or by varying the concentration of **Al** in the BLs (Figure 4-9), the role of the QWR thickness and the composition of the BLs will be further investigated in the multilayer QWR samples.

4.2 Structural characterizations: Part I-Imaging

The structural properties of the QWR samples were studied by the TEM-based techniques because of the combined advantages of superior spatial resolution and the feasibility of imaging the layered-structure in cross-sectional specimens.

The basic structure for the TEM samples is similar to the one shown in Figure 2-2. The thickness of the InAs QWR layer deposited between the $In_{0.53}Ga_{0.37}Al_{0.10}As$ BLs is 5.6 ML (sample H in Table 2-1). An AFM image of free-standing InAs nanowires on the top surface of sample H is presented in Figure 4-10 (a). The long axis of the wire was along the $[0\bar{1}1]$ direction with typical lengths ranging from 100 nm to 250 nm.

4.2.1 Diffraction contrast imaging

The sample is first characterized by diffraction contrast imaging under two beam conditions. As stated in Chapter 3, qualitative information, such as the compositional variations and strain field due to the displacement of the atomic columns, can be directly investigated through the contrast recorded in the images.

4.2.1.1 The composition variations

The bright field (BF), Figure 4-10 (b), and dark field (DF), Figures 4-10 (c) and (d), TEM images taken with $\mathbf{g}_{200}$ are shown. The cross-sectional view of all the deposited layers can be seen in Figure 4-10 (b). The QWRs are visually observed by the darker contrast present between the $In_{0.53}Ga_{0.37}Al_{0.10}As$ BLs. The position of buried QWRs is indicated by the blue arrows in this figure. All the interfaces between different layers are smooth; i.e. (1) no misfit dislocations are observed in spite of the 3.2% mismatch between the InAs QWRs and $In_{0.53}Ga_{0.37}Al_{0.10}As$ BLs, which means the thickness of the InAs (5.6 ML) is still between the critical values

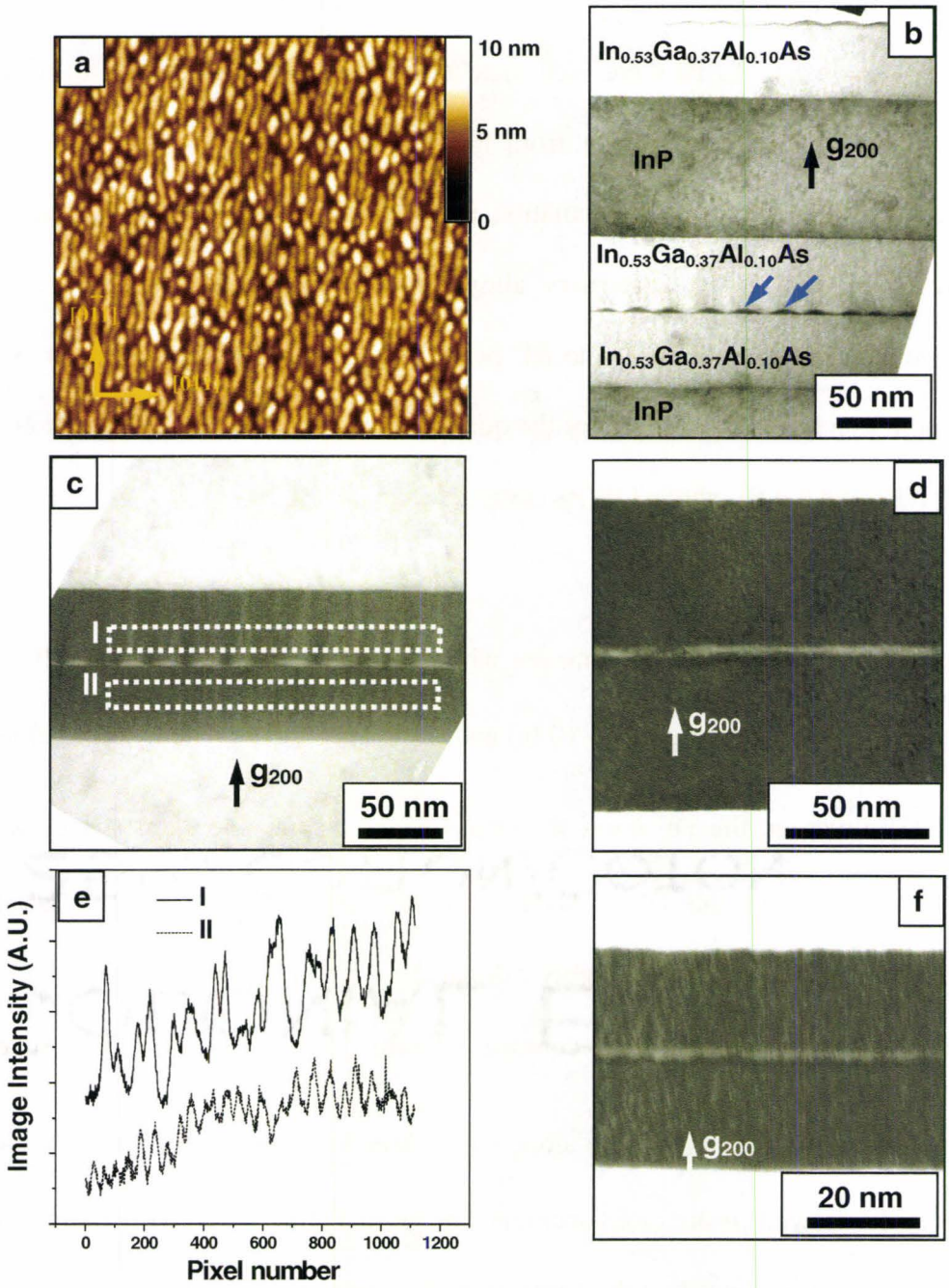

Figure 4-10: (a) AFM image (1μm by 1μm) for sample H (5.6 ML InAs); (b) BF TEM image showing the layered structure and interfaces; (c) and (d) DF images showing the contrast modulation in upper BL; (e) intensity profiles in rectangular regions **I** and **II** in (c); (f) DF image of sample I with 2.5 ML InAs. (b), (c) and (f) are projected close to $[0\bar{1}1]$ zone axis while (d) is projected close to [011] zone axis.

of elastic and plastic relaxations (Pearsall 2000); and (2) the lattice constants of the $In_{0.53}Ga_{0.37}Al_{0.10}As$ BLs are well-matched with those of InP since no misfit dislocations appear to propagate from the InP/BL interface. As mentioned in section 2.1, the range of **In** fluctuation is only 1 at.% when the lattice match between $In_{1-x-y}Ga_xAl_yAs$ quaternary alloy and InP is fulfilled. Therefore, the average concentration of **In** in the BL below the QWRs (referred as lower BL) can serve as a built-in reference for the quantitative analysis of the composition in the QWRs and the BL above QWRs (referred as upper BL).

The cross-sectional DF images with $\mathbf{g}_{200}$ taken close to $[0\bar{1}1]$ and [011] zone axes are shown in Figures 4-10 (c) and (d), respectively. When viewed along the $[0\bar{1}1]$ direction, the DF cross-sectional images display the "lens-shape-like" brighter contrast in the QWR layer than the surrounding BLs. The lateral dimension (i.e. the width) is roughly estimated as 20 nm. In the image obtained close to [011] zone axis, brighter contrast with one dimensional "wire-like" shape extending the whole lateral width along $[0\bar{1}1]$ direction is observed. The length of the wire as viewed in the cross-sectional image in Figure 4-10 (d) is more than 100 nm. Therefore, based on the contrast in these images, the shape anisotropy of the QWRs is preserved after covering them with the upper BL.

A close observation of the Figure 4-10 (c) reveals that there exist bright "stripe-like" contrast modulations in the upper and lower BLs. The profiles in Figure 4-10 (e) are obtained by measuring the intensity variations in the rectangular box in the upper (profile **I**) and lower (profile **II**) BL. Larger periodicity and higher amplitude above the base value were observed in profile **I** than those in profile **II**. More specifically, the brighter contrast in the upper BL appears as multi-stripes which are distributed directly above the QWRs.

Qualitatively, the contrast modulations in BF/DF images with $\mathbf{g}_{200}$ for zinc-blende III-V semiconductors can be intuitively interpreted as a result of the compositional modulations, usually for **In** (Lei et al 2006 b; Brault et al. 2000) as shown in equations (3-2) and (3-3). However, several considerations must be taken into account when attempting to explain these experimental observations. Firstly, strictly speaking, correlating the brighter regions in the BLs with higher **In** concentrations by visual observation is not always correct because the sign reversal of the $\mathbf{g}_{200}$ structure factor occurs at certain compositions (Rosenauer 2003; Bithell et al. 1991). In fact, based on our calculations (see details in **Appendix A**), the sign reversal of the $\mathbf{g}_{200}$ structure factor occurs at $x = 0.37$ for an $In_xGa_{0.9-x}Al_{0.1}As$ alloy on an InP substrate. In DF images, regions with local **In** concentration of either $1 \geq x \geq 0.54$ or $0 \leq x \leq 0.2$ will show brighter contrast than the rest of the BL with nominal composition of $In_{0.53}Ga_{0.37}Al_{0.10}As$. Secondly, it is observed that the brighter "stripe-like" contrast modulation occurs only in the

images taken close to $[0\bar{1}1]$ zone axis through a comparison of the contrast in the upper BL of Figures 4-10 (c) and (d). The intensity in the upper BL appears more uniform in the image taken close to [011] zone axis (Figure 4-10 (d)), than that in Figure 4-10 (c). Therefore, the brighter "stripe-like" contrast modulation observed in the upper BL can unequivocally be described as a one-dimensional phenomenon that occurred in the direction ([011]) perpendicular to the long axis of the QWRs. Thirdly, the contrast modulation in the upper BL arises from the presence of QWR in the sample. This statement is supported by the analysis of the DF TEM image ($\mathbf{g}_{200}$, taken close to $[0\bar{1}1]$ zone axis) of sample I in Table 2-1 with 2.5 ML InAs, as shown in Figure 4-10 (f). This sample orientation is the same as the one used for taking Figure 4-10 (b) and (c). Thus, if QWRs were present they would be viewed end-on. It is therefore observed from this figure that a sample consisting of 2.5 ML of InAs (as opposed to 5.6 ML) appears to be below the critical thickness for a morphological transition from 2-D growth to 3-D growth since the InAs layer still appears in the layer-by-layer growth stage of the Stranski-Krastanow growth mode (Cullis et al. 2002). No well-developed QWRs were observed in this stage. Moreover, the contrast in the BL above the InAs layer is more uniform than the one observed in Figure 4-10 (c). From these observations, it is therefore apparent that this sample contains a 2-D InAs quantum well rather than 1-D InAs QWRs. In addition, the contrast modulations present in Figure 4-10 (c) are not observed. Thus, it can be concluded that the

observed contrast modulations in the upper BL are one dimensional phenomena along the [011] direction and are activated by the presence of the QWRs. Finally, although the images taken with $\mathbf{g}_{200}$ are less sensitive to the strain field than those with other **g** vectors, large strain and distortion would also contribute to the contrast in the chemical sensitive image of the zinc-blende structured semiconductor materials (Beanland 2005). Therefore, spectroscopic techniques that are both insensitive to strain and can be simultaneously employed for direct compositional measurements should be used in order to correctly interpret the contrast modulations in upper BL. The results will be shown and discussed in section 4.3.

4.2.1.2 Strain field

The distribution of strain field due to the displacement of atomic planes along the growth direction is shown in BF images taken with $\mathbf{g}_{400}$. The images close to the $[0\bar{1}1]$ and [011] zone axes are shown in Figures 4-11 (a) and (b), respectively. The presence of the strain field is reflected by the lobe-like darker contrast pairs (indicated by the white arrows in Figures 4-11 (a) and (b)) distributed on both sides of the QWR layer along the growth direction. The periodicity of these dark lobe pairs is smaller when the QWRs are viewed close to the $[0\bar{1}1]$ zone axis as compared to the images taken close to [011] zone axis. However, caution must be taken in order not to interpret the size and distribution of the dark lobe pairs as the

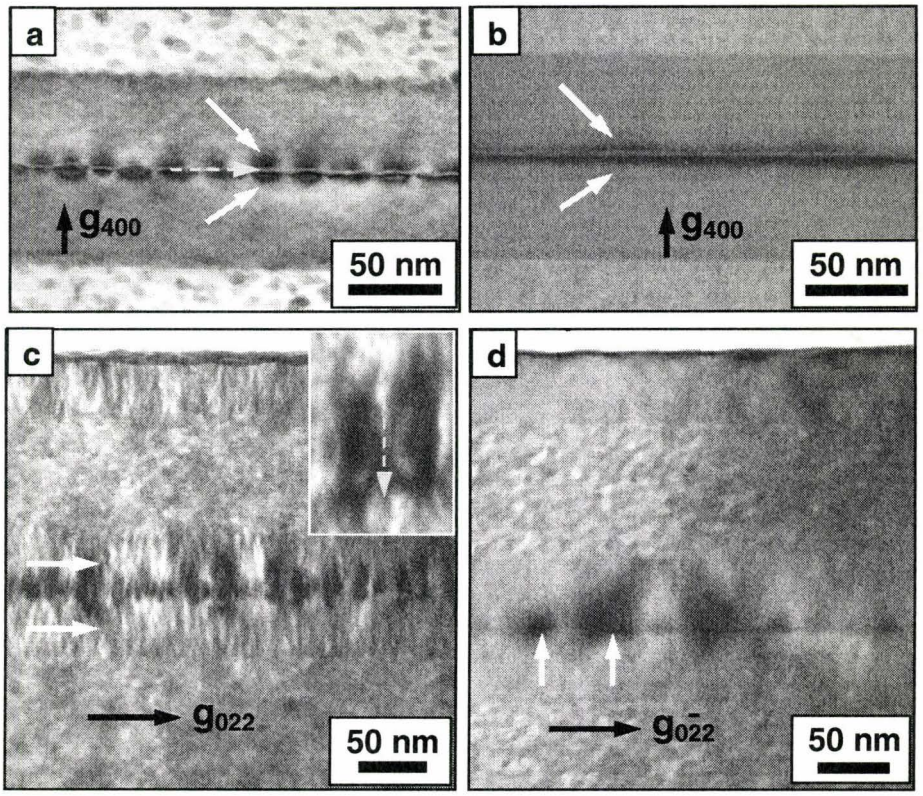

Figure 4-11: BF TEM images showing the strain field distribution along growth direction in (a) and (b); and perpendicular to the growth direction in (c) and (d). (a) and (c) are projected close to $[0\bar{1}1]$ zone axis, while (b) and (d) are close to [011] zone axis. The postions of upper and lower BL, where LCM occurs, are indicated by white arrows in (c).

dimensions of the QWRs. The origin of this special contrast pattern will be investigated by FE simulations in Chapter 7.

The strain field distribution perpendicular to the growth direction is studied through the contrast in the images taken with $\mathbf{g}_{022}$ or $\mathbf{g}_{0\bar{2}2}$ as shown in Figures 4-11 (c) and (d), respectively. The strained areas around the QWR in the

cross-sectional images are reflected by the dark-lobe pairs on both sides along the lateral [011] or [$0\bar{1}1$] direction. A "butterfly-like" contrast pattern is observed when the QWRs are viewed close to the [$0\bar{1}1$] zone axis, as shown by the insert in Figure 4-11 (c). Larger dark lobe pairs appear when the images are taken close to [011] zone axis as in Figure 4-11 (d). As discussed above, such contrast patterns can not be directly correlated with either the dimensions or the positions of the QWRs. FE simulation results discussed in Chapter 7 will demonstrate that observed lobe-pair like contrast is actually from the lateral elastic displacement of the atomic planes due to the QWRs as strained inclusions within the BL matrix.

As mentioned in Chapter 3, another application of the images taken with **g**={022} is to study the lateral composition modulations (LCM) of the ternary or quaternary alloys through the strain field between the adjacent regions with different compositions. The LCM in the $In_{0.53}Ga_{0.37}Al_{0.10}As$ is observed as very fine "stripe-like" contrast modulations present in both upper and lower BLs (indicated by white arrows), when the QWRs were viewed close to the [$0\bar{1}1$] zone axis in Figure 4-11 (c). However, the contrast from LCM is not as obvious as that in Figure 4-11 (c) when the image is projected close to the [011] orientation, as shown in Figure 4-11 (d). Only darker lobes are observed in Figure 4-11 (d) with rather uniform contrast in both the upper and lower BLs, thus suggesting that the LCM of $In_{0.53}Ga_{0.37}Al_{0.10}As$ displays a smaller periodicity along [011] than that

along [0$\bar{1}$1] direction, i.e. it extends along the same direction of [0$\bar{1}$1] as that of QWR activated contrast modulations observed in Figure 4-10 (c).

4.2.2 High resolution phase contrast and HAADF imaging

4.2.2.1 Phase contrast imaging

The cross-sectional, phase contrast, high resolution TEM (HRTEM) images projected on [0$\bar{1}$1] zone axis for a free-standing and a buried QWR are shown in Figures 4-12 (a) and (b), respectively. As mentioned in Chapter 3, the bright intensity maximum comes from the interference of the diffracted beams selected in the objective aperture, and therefore the diffraction effects still contribute to the contrast of the images. The positions of atomic columns are well-resolved for the free-standing QWRs in Figure 4-12 (a), however the existence of the buried QWRs can only be detected through the darker contrast (indicated by the white arrows) between BLs as shown in Figure 4-12 (b) and (c), even though the former was taken with a spherical-aberrations corrected TEM. This indicates that the contrast variations in the phase contrast images are sensitive to the distribution of the strain field inside and adjacent to the stressed QWRs. In order to resolve the shape, size and even the lattice planes inside the QWRs, (high resolution) high angle annular dark field ((HR)-HAADF) imaging is needed since the contribution from electron diffraction as modulated by the strain field can be effectively

suppressed and atomic number contrast between QWRs and BLs can be visualized.

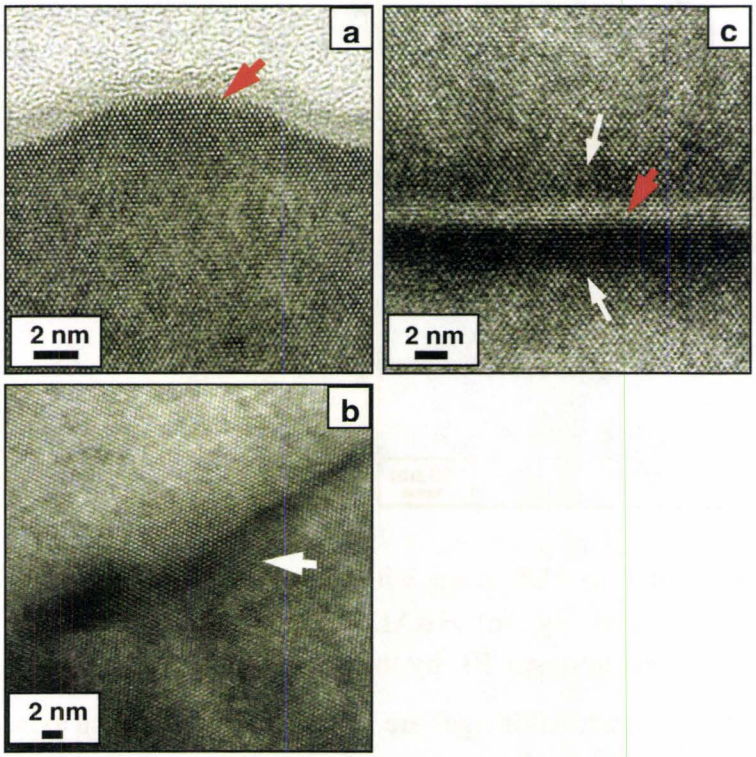

Figure 4-12: HRTEM images for (a) a free-standing QWR; (b) and (c) buried QWRs. (a) and (b) are projected on $[0\bar{1}1]$ zone axis while (c) on [011] zone aixs.

4.2.2.2(HR)-HAADF imaging

In order to get atomic number contrast in HAADF imaging, the inner angle (β) of the ADF detector must be properly set and calibrated. The influence of this parameter on the contrast of the ADF images can be visulized from the different appearance of the QWR regions (within the rectangular box) in Figures 4-13 (a) and (b), both of which were taken on the $[0\bar{1}1]$ zone axis for the same area with

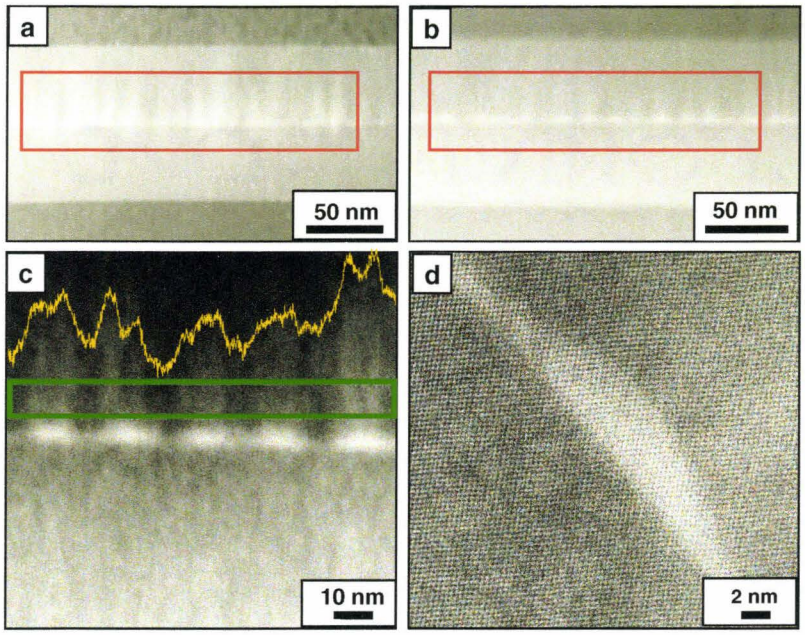

Figure 4-13: (a) and (b) ADF image with inner collector semi-angle β=37.5 mrad and 70 mrad, respectively. (c) HAADF image with β=70 mrad showing the contrast modulations in upper BL by the insert intensity profile. (d) HR-HAADF image with β=64 mrad. All images are recorded on [0$\bar{1}$1] zone axis.

calibrated β=37.5 mrad and 70 mrad, respectively. The positions and shape of the QWRs can be easily discerned through the atomic number contrast between QWR and BLs in the latter case. The contrast in the former image comes mainly from the strain between QWR and BLs since the ADF detector still collects the diffracted electrons when the collection angle is 37.5 mrad. According to our experience, the practical value of β must be greater than 50 mrad on JEOL 2010 microscope in order to produce HAADF images, where the atomic number contrast for the InAs/InGaAlAs/InP structure is dominant.

The contrast modulations in the upper BL similar to those in Figure 4-10 (c) are also detected in HAADF image (β=70 mrad), as shown by the intensity profile in Figure 4-13 (c). However, the intensity modulations in Figure 4-13 (c) can not be interpreted unambiguously as an indicator for pure compositional variations since the presence of the large localized strain may also lead to the bright contrast in ADF and HAADF images (Wu, X., et al. 2008) contrary to what might be expected from the simple atomic number contrast mechanism alone. Therefore, a more direct measurement of the composition for the brighter stripes in the upper BL is required to study the origin of such contrast modulations as discussed further in section 4.3.2.

A HR-HAADF image for a single QWR is shown in Figure 4-13 (d) with the inner and outer angles of FEI ADF detector set as 64 mrad and 140 mrad, respectively. A more reliable estimate of the shape and dimensions of a single QWR can be achieved by studying the atomic number contrast. The nominal InAs QWR appears brighter than the surrounding $In_{0.53}Ga_{0.37}Al_{0.10}As$ BLs since the average atomic number of the nominal QWR material (InAs) is higher than that of the BLs. From the HR-HAADF image, the upper boundary of the QWR can be described as "lens-shape" with height about 6 nm and base width of 20 nm.

4.2.2.3 Image analysis with geometric phase method

Image analysis was carried out for HR-HAADF image by the geometric phase analysis (GPA) (Rouvière et al. 2005) in order to study the change of local lattice spacing along a specific direction. One-dimensional analysis is performed by choosing one reflection **g** in the power spectrum generated by the Fourier transformation of the original image. Then the phase image from this reflection was calculated and used for determining the displacement field according to the procedures developed by Sarigiannidou et al. (Sarigiannidou et al. 2005).

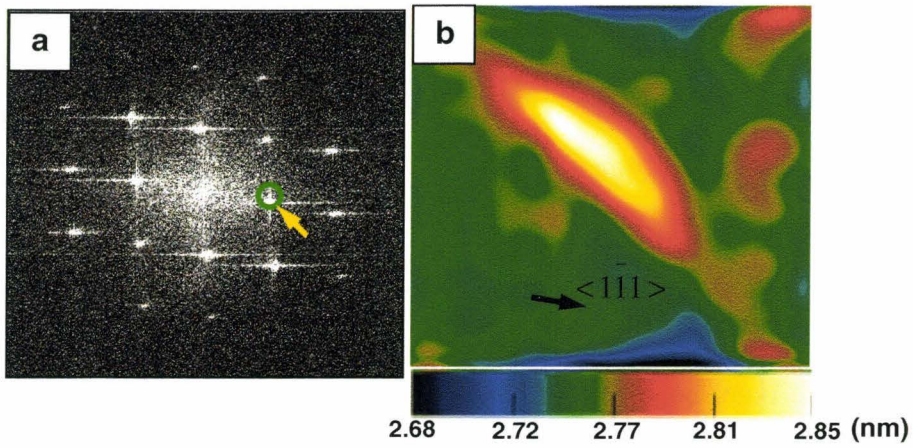

Figure 4-14: Image analysis through GPA. (a) The power spectrum generated from the Fourier transformation of the HR-HAADF image in Figure 4-13 (d) and the $(1\bar{1}1)$ spot is select for one dimensional analysis. (b) The $(1\bar{1}1)$ atomic plane spacing map obtained by GPA analysis.

The GPA was performed on HR-HAADF in Figure 4-13 (d). One of the strongest reflections $\mathbf{g}=1\bar{1}1$ in the power spectrum image (Figure 4-14 (a)) was selected and the map of the local spacing variation along $[1\bar{1}1]$ direction is shown

in Figure 4-14 (b). The largest value (shown as white area in the "temperature" scale map of Figure 4-14 (b)) is detected in the center of the QWR with decreasing magnitude towards the interface between QWR and BLs. Such spacing variation is believed to arise from the variation of local **In** concentrations (to be discussed in section 4.3.1) since the lattice parameter of InAs is the largest among binary components (InAs, GaAs and AlAs) of the current structure investigated.

4.2.3 Summary

Part of the structural features of the QWRs within the BLs has been made clear by interpreting the contrast in images from various TEM-based techniques. The shape and dimensions of the QWRs were obtained with HR-HAADF image. The displacement field is viewed by diffraction contrast imaging and analyzed with GPA on HR-HAADF image. Through the diffraction contrast imaging with the chemical sensitive $\mathbf{g}_{200}$ reflection, the compositional variations across each layer can be visually observed and the "bright-stripe" like contrast modulations in upper BLs were observed and are attributed to the presence of QWRs.

In order to further investigate these qualitative results, it is important to carry out quantitative compositional analysis for three reasons. Firstly, the validity of the lattice spacing map obtained from the HR-HAADF image analysis must be confirmed by comparing it with the "true" compositional map of individual QWR. Secondly, the investigation on the influence of QWRs on the deposition of upper

BL, such as the bright stripe-like contrast modulations in Figure 4-10 (c) and Figure 4-13 (c), requires the direct compositional measurements of the BL. Finally, the quantitative compositional information is a crucial component for the proper modeling and understanding of the physical properties (such as the optical properties) these QWR structures exhibit.

4.3 Structural characterizations: Part II-Composition

Quantitative compositional analysis was carried out for both the QWRs and the BLs using the combined techniques of EELS/EDXS SI and HAADF imaging (with the inner angle β=70 mrad of the ADF detector). The growth parameters for the sample investigated are those of sample H in Table 2-1. The experimental work was performed on a JEOL 2010 field emission microscope. A nominal probe size of 0.5 nm was used. Detailed calibration with an MgO cube crystal according to the standard procedures for beam size measurement (Williams et al. 1996) showed that the actural probe size was 0.9 nm.

4.3.1 EELS-SI analysis for QWRs

4.3.1.1 EELS quantification method

The quantification of the **In** signal is performed in two steps using an approach equivalent to *k*-factor method (Williams et al. 1996): (1) subtraction of the background intensity (I_B) in the EELS spectrum for the **In** $M_{4,5}$ edge, as shown in Figure 3-8; (2) the **In** concentration (N) was obtained by ratioing the integrated

EELS signal (**In** $M_{4,5}$ edge) intensity detected at each analysis point ($I_S(\beta,\Delta)$) to the average EELS signal intensity from the reference $In_{0.53}Ga_{0.37}Al_{0.10}As$ BL ($I_{S-ref}(\beta,\Delta)$) below the QWRs. The quantification equation can be expressed as:

$$N = \frac{I_S(\beta,\Delta)}{I_{S-ref}(\beta,\Delta)} \times N_{ref} \quad \text{——————————} \quad (4\text{-}1)$$

where $N_{ref} = 0.53$, the EELS signal collection angle β=32.6 mrad and integral window Δ=60 eV. The reference **In** composition (N_{ref}) of the BL below QWRs was calibrated by double crystal X-ray diffraction and is known to an accuracy of ± 0.01.

4.3.1.2 Validity of the quantification issues

The quantitative determination of the **In** distribution using equation (4-1) was based on the assumption that the QWRs occupied the full thickness of the specimen along the $[0\bar{1}1]$ direction in cross-sectional HAADF images. This assumption was believed to be reasonable since the sample thickness of the area investigated varies in the range from 30~55 nm as estimated from the inelastic mean free path of electrons traveling in the $In_{0.53}Ga_{0.37}Al_{0.1}As$ BLs (**Appendix B**). The wires were generally much longer than the specimen thickness as revealed by the AFM images shown in Figure 4-10 (a).

The validity of equation (4-1) for quantification is based on two factors and assumptions. Firstly, uniform thickness is assumed for the whole area where EELS-SI is applied. This assumption is reasonable since the sample for quantitative analysis is prepared by the low-angle polishing from which a low angle (2°) wedge-shaped sample with uniform thickness across the interfaces is generated as mentioned in Chapter 3. Thus, homogeneous thickness is guaranteed for scan areas of EELS-SI by the geometry of the TEM sample. Secondly, for the EELS data quantification (equation (3-4) in Chapter 3), the ratio of the concentration of the **In** detected at a pixel in the QWR (N) and that at a pixel from the reference area (N_{ref}) can be written as:

$$\frac{N}{N_{ref}} = \frac{I_S(\beta,\Delta)}{I_{S-ref}(\beta,\Delta)} \times \frac{I_{Low-ref}(\beta,\Delta)}{I_{Low}(\beta,\Delta)} \times \frac{\sigma_{ref}(\beta,\Delta)}{\sigma(\beta,\Delta)} \quad \text{(4-2)}$$

Since the partial ionization cross-section ($\sigma(\beta,\Delta)$) of the **In** $M_{4,5}$ edge does not vary with the local chemical composition (Williams et al. 1996), the third term in equation (4-2) equals 1 and it can be written as:

$$\frac{N}{N_{ref}} = \frac{I_S(\beta,\Delta)}{I_{S-ref}(\beta,\Delta)} \times \frac{I_{Low-ref}(\beta,\Delta)}{I_{Low}(\beta,\Delta)} \quad \text{(4-3)}$$

Three spectra containing the zero loss peaks were recorded in the lower BL, the QWRs and upper BL under the same conditions as those for collecting the EELS signals for quantification in section 4.3.1.3. The measured ratio of integrated intensity for $I_{Low}(\beta,\Delta)$ (Δ=60 eV) in the three spectra is 0.95: 1: 1.01. Based on these measurements, it is thus reasonable to approximate the second term in

equation (4-3) to 1 when the EELS-SI is taken across the $In_{0.53}Ga_{0.37}Al_{0.1}As$ BLs and InAs QWRs. Therefore, equation (4-3) can be simplified as equation (4-1).

Electron beam broadening due to electron scattering within the sample was another factor necessary for the interpretation of quantitative EELS SI. For the conditions used in EELS-SI, the estimated beam broadening ranged from 0.07 nm to 0.14 nm when the local thickness of the sample, the geometrical broadening, and the cut-off angle (Egerton 1986) for the **In** $M_{4,5}$ edge were considered (**Appendix C**). Also, the delocalization (Egerton 1986) of the inelastic scattering is estimated as 0.26 nm (**Appendix D**) for In $M_{4,5}$ edge. The influence of beam size, beam broadening and delocalization on the mapping results, when added in quadrature, are on the order of 1 nm in diameter (about 2 pixels by 2 pixels in the EELS-SI map of Figure 4-17 (a), which will be shown in section 4.3.1.3) and therefore significantly less than the length scale of the compositional gradients observed in the maps.

A last point to be made for the quantification is that the analysis from EELS SI mapping is not influenced by the strain between QWRs and BLs. One example is shown in Figure 4-15, where an EELS mapping is performed for a single QWR in a low-angle ADF (LAADF, β=37.5 mrad) image recorded on the $[0\bar{1}1]$ zone axis, as shown in Figure 4-15 (a). LAADF imaging is still sensitive to

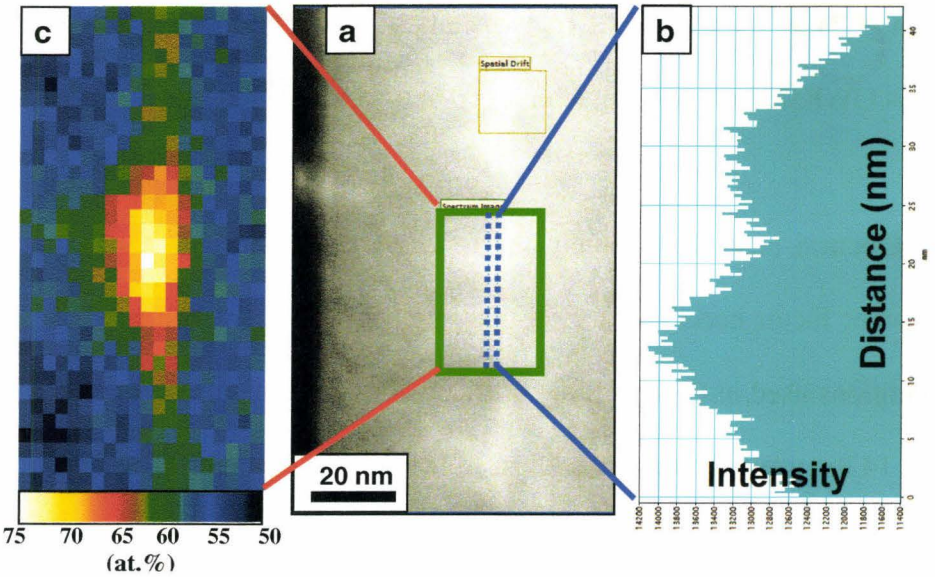

Figure 4-15: (a) LAADF image recorded on [0$\bar{1}$1] zone axis; (b) the intensity profile for the area within the dotted-blue rectangular box; (c) **In** map in "pseudo-temperature" scale obtained by EELS SI for the green rectangular box.

diffraction contrast and provides information about the strain distribution around the QWR. From the image contrast, shown by the intensity profile in Figure 4-15 (b), two peaks clearly appear on both sides of the selected area in the small dotted-blue rectangular box. Without knowing the information about the collection condition (i.e. we used a LAADF imaging condition), visually, the contrast could be misinterpreted as the existence of two QWRs on both sides of the selected area. However, only one QWR is found from the quantitative **In** concentration map shown in Figure 4-15 (c), where the maximum **In** signal is detected in the middle of the selected area, corresponding to the minimal intensity shown in Figure 4-15 (b). As mentioned in section 4.2.2.2, the strain field still imposes its contrast on LAADF images but does not affect the quantitative signals

in the EELS-SI maps. Therefore, under our experimental settings, the "true" compositional information can be detected from the EELS signal in which the contribution and potential artifacts from strain field have been effectively suppressed.

4.3.1.3 Quantification results

(I) EELS line profiles

The EELS line profiles extended across the BLs and the QWR were obtained by scanning the electron beam across the QWR centers along both the growth and lateral directions, as shown in Figures 4-16 (a) and (b), respectively. The common feature of the two profiles is that the **In** signal maximum appears in the center of the QWR. Gradually decreased **In** signal was detected as the beam is moved towards the interface between the QWR and BLs.

To obtain a reliable average integrated intensity ($I_{S-ref}(\beta,\Delta)$) from the reference lower BL, a fitting of the experimental intensity curve is carried out, as shown in Figure 4-16 (c) for fitting the raw data from Figure 4-16 (a). It is observed from the inserted concentration scale in Figure 4-16 (a) that the measured maximum **In** content is about 75% of the total atomic concentration for all the group III elements.

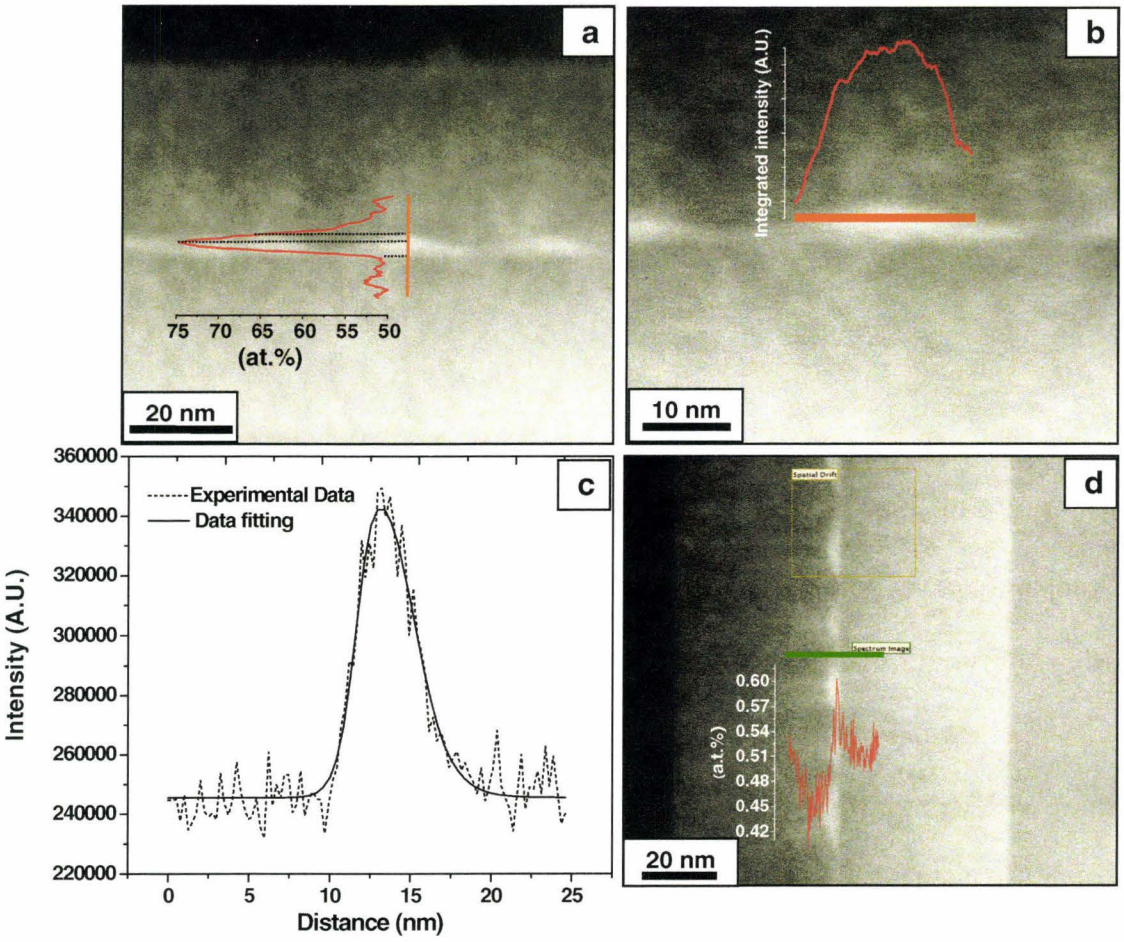

Figure 4-16: EELS line profiles for **In** distribution (a) along growth direction; (b) along lateral direction; (c) data fitting for profile in (a); (d) across the base between two adjacent QWRs.

An EELS line profile taken between the bases of the adjacent QWRs along the growth direction showed a signal peak with a detected value of 60% **In** appearing between the BLs, as shown in Figure 4-16 (d). It can be interpreted as the existence of wetting layer (WL) necessary for QWR formation expected from the Stranski-Krastanow growth mode (Cullis et al. 2002). The FWHM of the **In** profile in this figure is estimated as about 0.6 nm (~ 2 ML), which is smaller than

the electron beam size. Therefore, the "real" In concentration in the WL is underestimated. If the interaction between the electron beam and the upper, lower BLs and WL is considered, the maximal concentration of **In** in the WL should be about 64%.

(2) EELS mappings

In order to study the elemental distribution in greater detail, **In** concentration maps were obtained by selecting one or more QWRs for EELS-SI, as shown in Figures 4-17 (a) and (b), respectively. Three distinct regions were identified in the **In** map of a single QWR (Figure 4-17 (a)) based on the **In** concentration. Starting from the centre of the QWR and proceeding outwards toward the interfaces with the BLs, the following regions were observed: (1) an **In**-rich center (shown as yellow and white in the pseudocolour "temperature" scale) with 70-75% **In**; (2) a thin intermediate layer (red) containing 65-70% **In**, and (3) an outer layer (green) with an **In** concentration of about 60%. The maximum **In** concentration of 75% at the center of the QWR is consistent with the EELS line scan results shown in Figure 4-16 (a). An **In** EELS spectrum image including four QWRs is shown in Figure 4-17 (b). The concentrations and **In** distributions shown in this image were consistent with the results from a single QWR presented in Figure 4-17 (a). The residue of the WL is confirmed by the presence of the thin layer, highlighted by arrows in Figure 4-17 (b), connecting the bases of adjacent QWRs. This WL has an **In** concentration of about (60~65)% (consistent with the line profile in

Figure 4-16 (d)), which is significantly greater than the surrounding $In_{0.53}Ga_{0.37}Al_{0.1}As$ BLs.

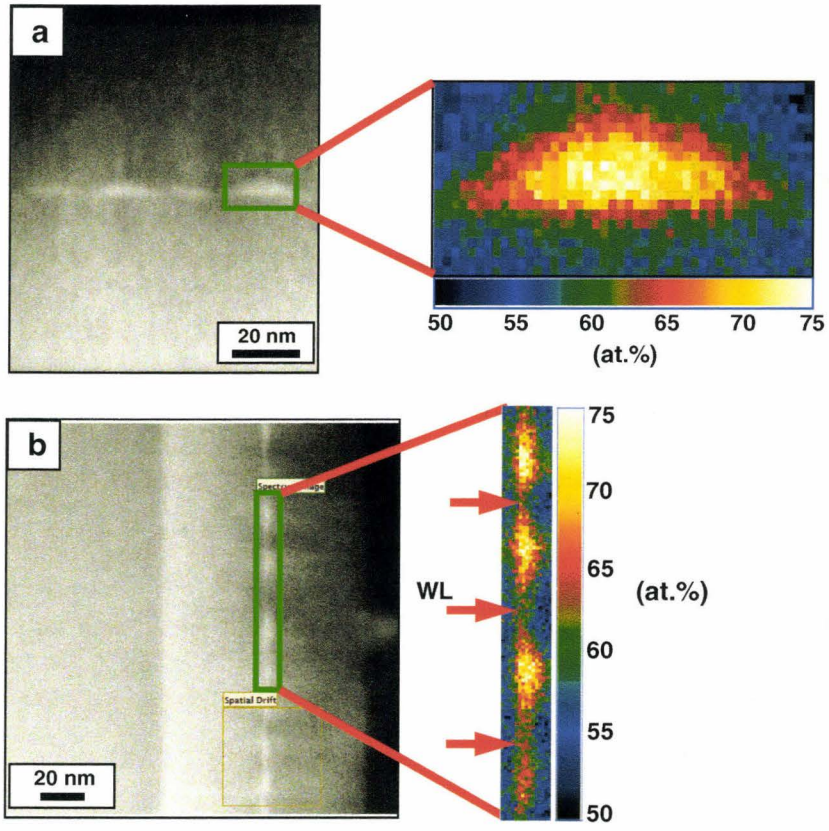

Figure 4-17: EELS maps for **In** distribution in (a) a single QWR; (b) four QWRs. The HAADF images were taken on [0$\bar{1}$1] zone axis with inner detector angle β=70 mrad.

4.3.1.4 Interpretations of the indium distribution

The **In** concentration profiles and maps shown in Figures 4-16 and 17 can be explained by the intermixing of group III elements between the InAs QWRs and the surrounding $In_{0.53}Ga_{0.37}Al_{0.1}As$ BLs during the growth process. The main

driving forces for elemental exchange were the compositional gradients for **In** and **Ga** in the adjacent layers (Wang, Y., et al. 2006). Diffusion of **Al** was neglected since **Al** exhibits very little migration at the temperatures used in the current MBE growths (Kasu et al. 1993). Also, most of the intermixing is believed to occur during the capping process of the QWRs with upper BL, as confirmed by recent experimental results in literature (Eisele et al. 2008; Chung et al. 2008). According to the nominal composition of each layer during the capping process of the InAs QWRs, a net flux of **In** from the QWR would diffuse into the $In_{0.53}Ga_{0.37}Al_{0.1}As$ BL, and a net flux of **Ga** from the BL would diffuse toward the inner part of QWR. Therefore, through diffusion, the outermost layers of the QWRs would be expected to yield more **In** to the BLs than the inner regions. At the same time, the concentration of **In** in the BL regions close to the QWR would be increased. As a result, the typical **In** distribution map in Figure 4-17 were observed.

4.3.2 Composition modulation in the upper BL

In order to clarify and quantify the contrast modulations detected in TEM/HAADF images (Figure 4-10 (c) and Figure 4-13 (c)), EELS/EDXS SI were performed. Firstly, the EELS scan, shown in Figure 4-18 (a), performed along the lateral [011] direction across two bright "stripes" above a QWR confirmed that the contrast modulations in the upper BL originated from the **In** composition modulation since the peaks of the **In** signal clearly coincided with the positions of

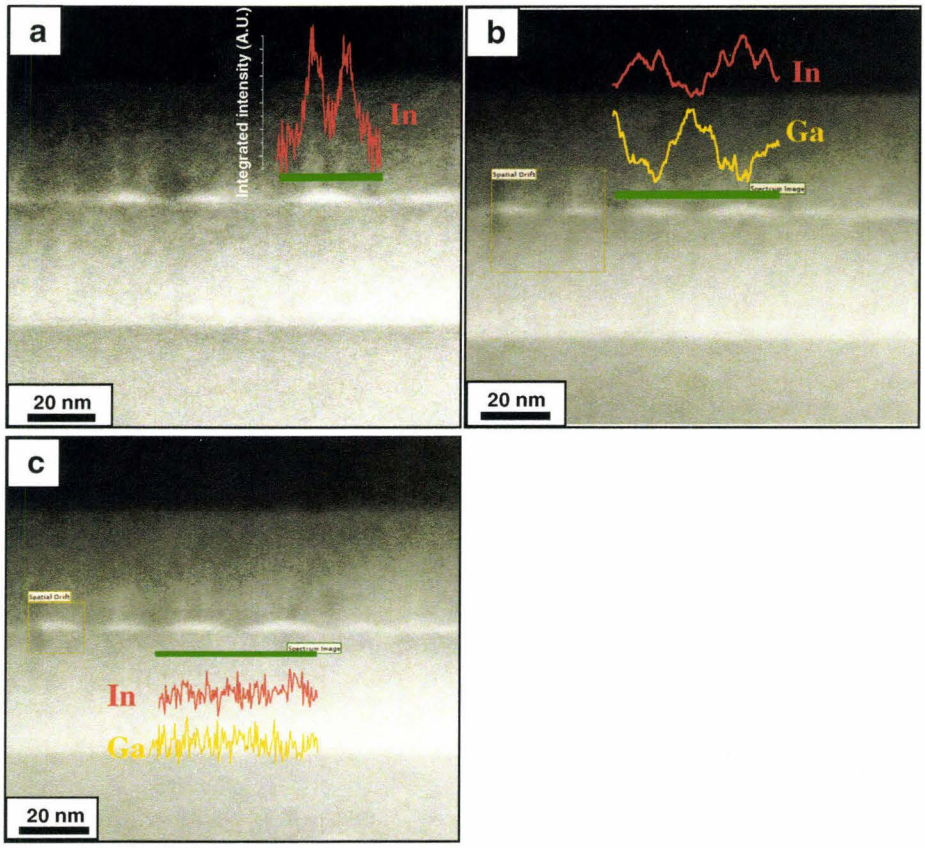

Figure 4-18: EELS profiles for the **In** composition modulations in BLs. (a) Profile across two bright "stripes" in the upper BL; (b) profile above two QWRs and (c) profile in the lower BL. All the HAADF images were taken with ADF detector inner angle β=70 mrad on [0$\bar{1}$1] zone axis.

the two bright "stripes" in the HAADF image. Another EELS line-scan above two adjacent QWRs, shown in Figure 4-18 (b) reveals the qualitative distribution of the **In** and **Ga** in upper BL. A local maximum **In** signal was detected in the area directly above QWRs while the local maximum **Ga** signal lies above the gap between two adjacent QWRs. Similar EELS scans were applied to the BL just

underneath the QWR as shown in Figure 4-18 (c). Only small (within 2%) fluctuations of the **In** and **Ga** signals, which may just arise either from the lateral composition modulation (LCM) of $In_{0.53}Ga_{0.37}Al_{0.1}As$ (Roura et al. 1996; Wang et al. 2005) or random noise in the signals, were observed in comparison with the noticeable compositional modulations displayed in Figure 4-18 (b).

Quantification for the **In** fluctuations in the upper BL by EDXS is given in Figure 4-19 using the **In** L_α and **Ga** K_α lines. First, an EDXS line scan was obtained from the lower BL and the *k*-factor between **In** and **Ga** was extracted using the Cliff-Lorimer equation: $\frac{C_{In}}{C_{Ga}} = k\frac{I_{In}}{I_{Ga}}$, where C_{In}, I_{In} and C_{Ga}, I_{Ga} represent the concentration/EDXS integrated peak intensity of **In** and **Ga**, respectively. Next, an EDXS line scan was performed in the upper BL and the **In** concentration was extracted based on $C_{In} + C_{Ga} = 1 - C_{Al} = 0.9$ where an uniform **Al** concentration of 0.1 was assumed, as reflected by the relatively constant **Al** signal in Figure 4-19 (a). These two expressions can be manipulated to yield the concentration of the **In** as a function of the measured **In** and **Ga** EXDS signals, $C_{In} = \frac{0.9kI_{In}}{kI_{In} + I_{Ga}}$. The quantitative results are shown in Figure 4-19 (b) and the amplitude of the **In** modulation in upper BL is estimated between 7~12% (the maximum **In** concentration varies between 60% and 65%).

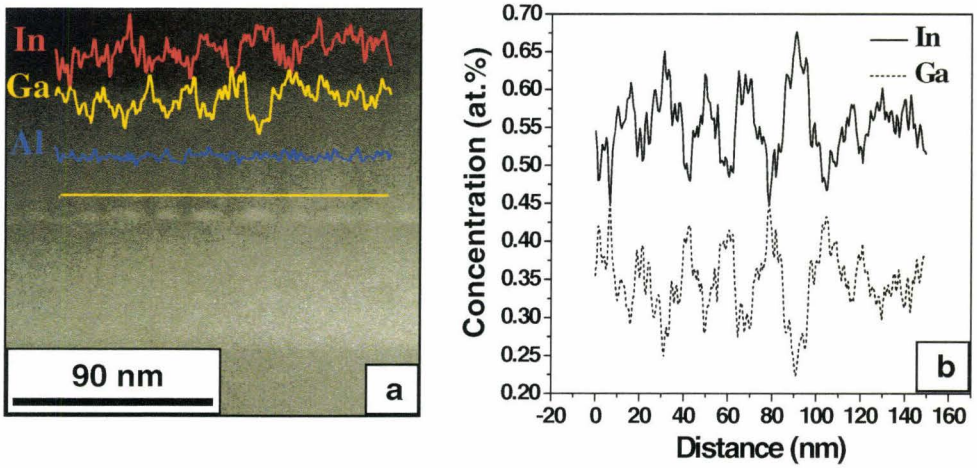

Figure 4-19: EDXS quantification for **In** compostion modulation in upper BL. (a) EDXS signal for **In, Ga** and **Al**; (b) quantification result using *k*-factor method.

4.3.3 Summary

In concentration maps inside and around the QWRs were obtained through EELS-SI. The **In** composition modulation in the upper BL was confirmed and quantified by EELS and EDXS SI, respectively. This information will be used as input for modeling the elastic and electronic properties to interpret the experimentally observed structural and optical features of the QWRs in later chapters.

Chapter 5

Multilayer quantum wires

Overview

Multilayer QWRs were grown in order to further investigate both the structural features and optical response these structures exhibit under different growth conditions and configurations. The alignment patterns of the QWRs, which depend on the thickness and composition of the SLs/BLs, as well as the QWR layer thickness, are of significant practical importance for device applications in both tuning the optical properties and controlling the defect generation in the active regions. Also, optoelectronic devices based on multilayer of QWRs show superior performance, such as lower threshold current at room temperature (Suárez et al. 2006), than those with the active regions made up of single layer QWRs.

In this chapter, the effect of (1) SLs thickness; (2) the QWR layer thickness; and (3) the composition of the SL/BL materials on the structural and optical properties of the multilayer QWRs were investigated. Particular focus is put on: (1) studying the variation of the alignment patterns of QWR stacks with each parameter; and (2) investigation of the origin and interpretation of the PL spectra.

The basic configuration of the multilayer QWR structure was shown in Figure 2-2. Every sample includes five repeats of the basic structural unit of QWR/SL. As determined in Chapter 4, the QWR layers and SLs/BLs were grown at 520 °C with growth rates for the BLs/SLs and QWR layers at 0.8 μm/h and 0.4 ML/s, respectively.

5.1 Effect of the spacer layer thickness

Four samples were grown to study the effect of the SL thickness on the properties of the multilayer QWRs. The samples are numbered as G2 and K1, K2, K3 in Tables 2-1 and 2-2. Sample G2 was a single layer of InAs QWRs grown as a reference specimen. The other three samples contained five QWR layers with SL thicknesses of 8 nm, 15 nm and 25 nm between adjacent QWR layers for samples K1, K2 and K3, respectively. The QWR/SL assembly was deposited on a 50 nm thick BL (lower BL) and overgrown with another 50 nm BL (upper BL). InAs layers, 4ML thick, were deposited on the BL/SL to form QWRs and the composition of the SLs and BLs was fixed as $In_{0.53}Ga_{0.27}Al_{0.20}As$. A free-standing wire layer with 4 ML InAs was also deposited on the top surface of these samples for AFM studies.

5.1.1 Structural characterization

5.1.1.1 AFM

Similar features of the free-standing wires were observed in the four samples. A typical AFM image, shown for sample K3 (25 nm SL, 4 ML InAs), is displayed in

Figure 5-1. The wire-like shape is anisotropic with the long axis extending along $[0\bar{1}1]$ direction and the average length of the wires is over (233±71) nm.

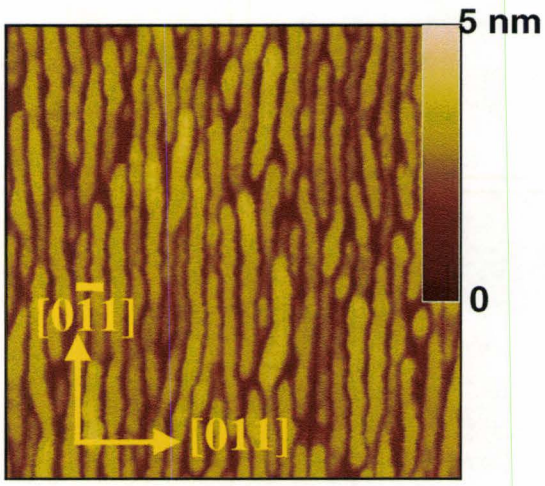

Figure 5-1: AFM images for sample K3 (25 nm SL, 4 ML InAs), the image size is 0.5 μm by 0.5 μm.

5.1.1.2 TEM

The alignment patterns of the QWR stacks were analyzed by cross-sectional TEM imaging, as shown in Figure 5-2. The QWRs showed vertical alignment with the smallest SL thickness (8 nm) for sample K1 in Figure 5-2 (b). With the thickness of the SL was increased, the vertical alignment of QWRs became less prominent than that in sample K1, as shown in Figures 5-2 (c) and (d) for samples K2 (15 nm SL) and K3 (25 nm SL), respectively.

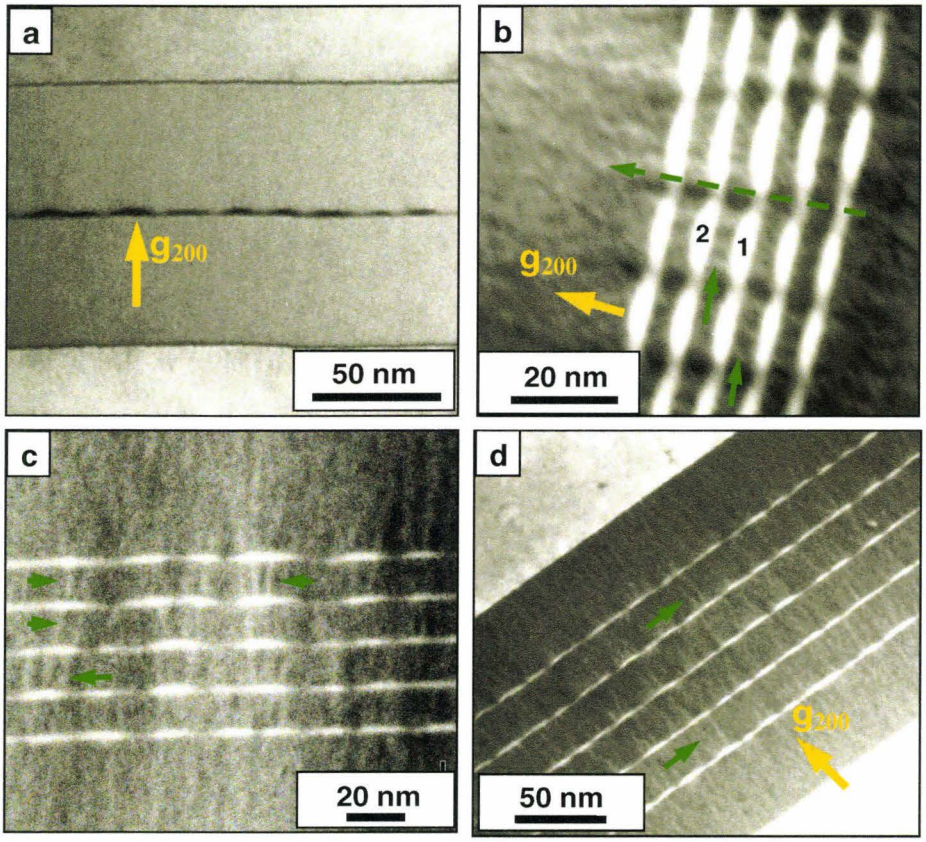

Figure 5-2: Cross-sectional TEM images of (a) BF image of sample G2 (single layer, 4 ML InAs); (b) DF image of sample K1 (8 nm SL, 4 ML InAs); (c) HAADF image of sample K2 (15 nm SL, 4 ML InAs); and (d) DF image of sample K3 (25 nm SL, 4 ML InAs). The BF and DF images were taken with $\mathbf{g}_{200}$. The HAADF image was taken with inner angle $\beta = 70$ mrad of the ADF detector. All the images were projected close to (a, b and d) or on (c) $[0\bar{1}1]$ zone axis. The green arrows and dashed green arrow pointed out the **In**-rich stripes and **In**-deficient regions in the SLs, respectively.

A "stripe-like" brighter contrast modulation was detected in the SLs and upper BL, as indicated by the green arrows in the DF or HAADF images in Figures 5-2 (b)-(d). As observed in the single layer QWR samples (Figures 4-18 (a) and (b)), this contrast variation has been attributed to the local **In** composition modulations in the upper $In_{0.53}Ga_{0.37}Al_{0.10}As$ BL induced by the presence of the

QWRs. It is shown in **Appendix A**, however, that positive contrast (i.e. higher intensity in the DF images) is expected when $1 \geq \mathbf{x} \geq 0.54$ or $0 \leq \mathbf{x} \leq 0.43$, where **x** stands for the local **In** concentration of the $In_xGa_{0.8-x}Al_{0.2}As$ alloy. Therefore, EELS-SI mapping is necessary for interpreting the contrast modulation in the SL in an unambiguous manner. A compositional map from sample K2 (15 nm SL) showing the **In** distribution in two neighboring QWR layers and the intervening SL is displayed in Figure 5-3 (a). Firstly, similar to the single layer QWRs (Figure 4-17), three regions with different **In** concentrations appear for individual QWRs with the composition of $In_{0.75}Ga_{0.25}As$ at the **In**-rich center, assuming the diffusivity of **Al** is negligible (Kasu et al .1993). Secondly, a wetting layer (WL) with ~60% **In** was detected at the gaps between adjacent QWRs, as shown in Figure 5-3(b). Finally, it is unambiguously clear that the brighter "stripes" observed in Figures 5-2 (b)-(d) are regions with higher local **In** concentration (60% of the total group III elements, shown as green "stripes" in the "temperature" scale map in Figure 5-3 (a)) than the rest of the SL. The positions and base width of the QWRs in the upper layer were associated with the **In**-rich "stripes" originating from the QWRs in the lower layer, as shown in the QWRs pairs (**1** and **2** in lower and upper layer, respectively) in Figure 5-2 (b) for sample K1 (8 nm SL) and Figure 5-3 (a) for sample K2 (15 nm SL). Particularly, it is observed in sample K2 that the base width of QWRs grow larger relative to the first layer and some QWRs appeared to split in the upper layers, as shown in

Figure 5-2 (c). However, the base width of QWRs in sample K1 (Figure 5-2 (b)) is more uniform than that in sample K2.

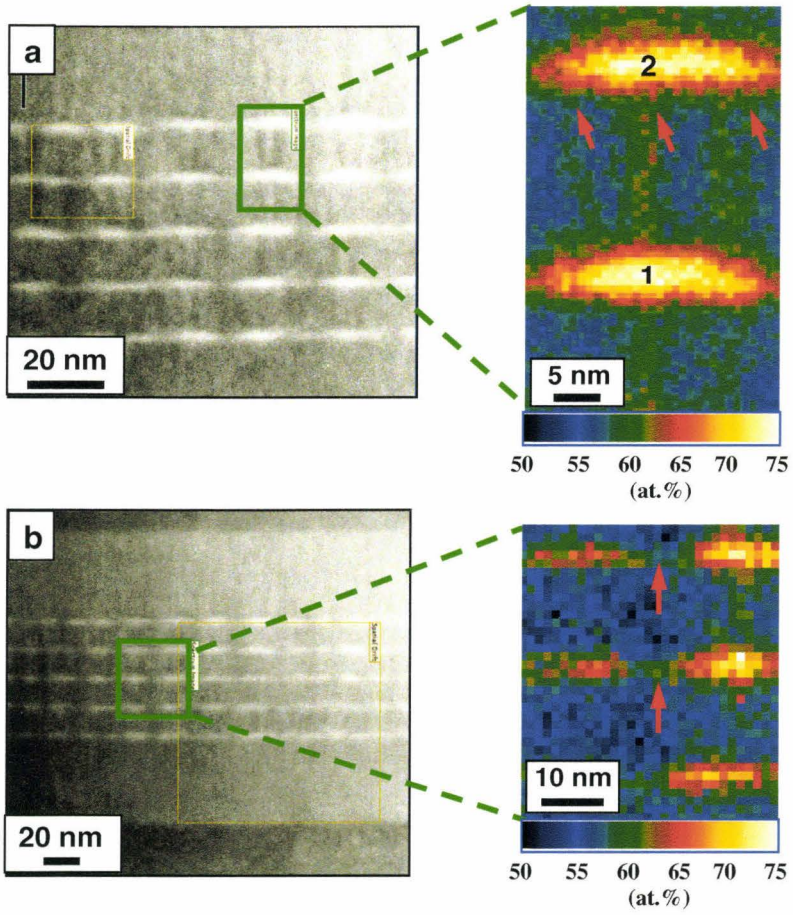

Figure 5-3: HAADF images (left) and EELS-SI maps (right) from sample K2 (15 nm SL, 4 ML InAs) showing the "pseudo-temperature" scaled **In** distribution map in (a) QWRs and SLs; (b) between QWRs. The red arrows in (a) illustrate the role of the **In**-rich "stripes", originate from QWR **1,** in determining the position and base width of QWR **2**. The red arrows in (b) point out the existence of wetting layer. The HAADF images were taken on $[0\bar{1}1]$ zone axis with inner ADF detector angle $\beta = 70$ mrad.

These observations appear to be correlated with the divergence of the **In**-rich "stripes" between QWR layers, as the SL thickness was increased from 8 nm to 15 nm. Also bands of darker contrast, representing the **In**-deficient regions, are clearly observed in the area between the aligned QWR columns in sample K1 (8 nm SL), as indicated by the dashed green arrow in Figure 5-2 (b). Therefore, **In** composition modulations with alternating **In**-rich (above QWRs) and **In**-deficient (above gaps between adjacent QWRs) regions were formed in the BL/SLs. The origin of such composition modulations will be investigated in Chapter 7 by finite element (FE) simulations.

An estimation of the average QWR height was performed by analyzing the contrast in cross-sectional TEM images in Figure 5-2 and the result is summarized in Table 5-1. It is found that the average height of the buried QWRs increases as the SL thickness was decreased.

Table 5-1: The average height and PL wavelength (77K) for multilayer QWRs with different SL thicknesses.

Sample #	G2	K1	K2	K3
SL thickness (nm)	N/A	8	15	25
Average height (nm)	3.0±0.25	4.0±0.60	3.5±0.55	3.1±0.45
PL wavelength (μm)	1.50	1.60	1.54	1.51

A qualitative explanation of this trend is based on the influence of the chemical potential on the nucleation process of QWR layers grown above the base layer. The incoming InAs will preferably nucleate at the SL growth front surface where a local minimum of the chemical potential of **In** (μ_{In}) is present (Molina et al. 2006). Also it is known that the flux of the mass transfer is proportional to the gradient of μ_{In} (Porter et al. 2001). On a flat SL growth front surface (assumed by the fact that the bases of QWRs in each layer appear flat in Figure 5-2) in samples K1 through K3, the gradient of μ_{In} comes mainly from the variation of the local lattice parameter, which include the contributions from (1) the tensile strain field due to the relaxation of the underlying QWRs; and (2) the propagation of **In**-rich stripes in the SLs, for example shown in Figure 5-3 (a). For InAs QWRs grown on InGaAlAs lattice-matched with InP, a larger lattice parameter results in a reduction of μ_{In}. With a small SL thickness of 8 nm in sample K1, both the tensile strain field and the QWR-induced **In**-rich "stripes" are expected to distribute in the SL within a width defined by the base width of QWR in the underlying layer according to the St. Venant's principle (Hirth et al. 1982). Thus, a larger lattice parameter, i.e. the local minimum of μ_{In} is expected to be present on the SL growth front directly above underlying QWRs. Therefore, a correlated QWR stacking pattern is observed in sample K1. As the SL thickness was increased to 15 nm in sample K2, the magnitude of the tensile strain field from QWR decreases (Pearsall 2000). Also, it is reasonable to assume the contribution

to the gradient of μ_{In} from the **In**-rich "stripes" is the same as that in sample K1 since no significant **In** content change is observed in individual **In**-rich "stripes" through the whole 15 nm SL, as shown in Figure 5-3 (a). Therefore, the total effect of increasing the SL thickness is a reduction of the gradient of μ_{In} on the SL growth front surface. Thus, the height of QWRs decreases from sample K1 (8 nm SL) to sample K2 (15 nm SL) as a result of the reduced mass transfer flux of **In** adatoms, which is proportional to the gradient of μ_{In}. As the thickness of SL was further increased to 25 nm in sample K3, the diminished tensile strain field from QWRs in the lower layer together with a constant (or possibly reduced) **In** content in the **In**-rich "stripes" leads to a further reduction of the gradient of μ_{In}. Therefore, an even smaller average QWR height than those in sample K1 and K2 was observed in sample K3.

Moreover, in sample K2 with 15 nm SL, some of the **In**-rich "stripes" are observed to diverge from the growth direction as shown in Figure 5-2 (c). Thus, the contribution to μ_{In} from the tensile strain field and that from **In**-rich "stripes" do not overlap as well with each other as in the case for sample K1 (8 nm SL in Figure 5-2 (b)). It results in a wide area with lower chemical potential than the surroundings on the growth front surface. Therefore, the increase in base width and even splitting of QWRs were observed in upper layers of sample K2, as observed in Figure 5-2 (c).

5.1.2 Optical characterization

The optical properties of the four samples were studied through temperature-dependent PL. The PL spectra at 14 K and 77 K are shown in Figure 5-4 (a) and (b), respectively. A red-shift of the PL wavelength is found between spectra in Figure 5-4 (b), which correlates with the QWR height increasing (Kümmell et al. 2006; Maes et al. 2004; Fuster et al. 2005) as the SL thickness decreases, as summarized in Table 5-1.

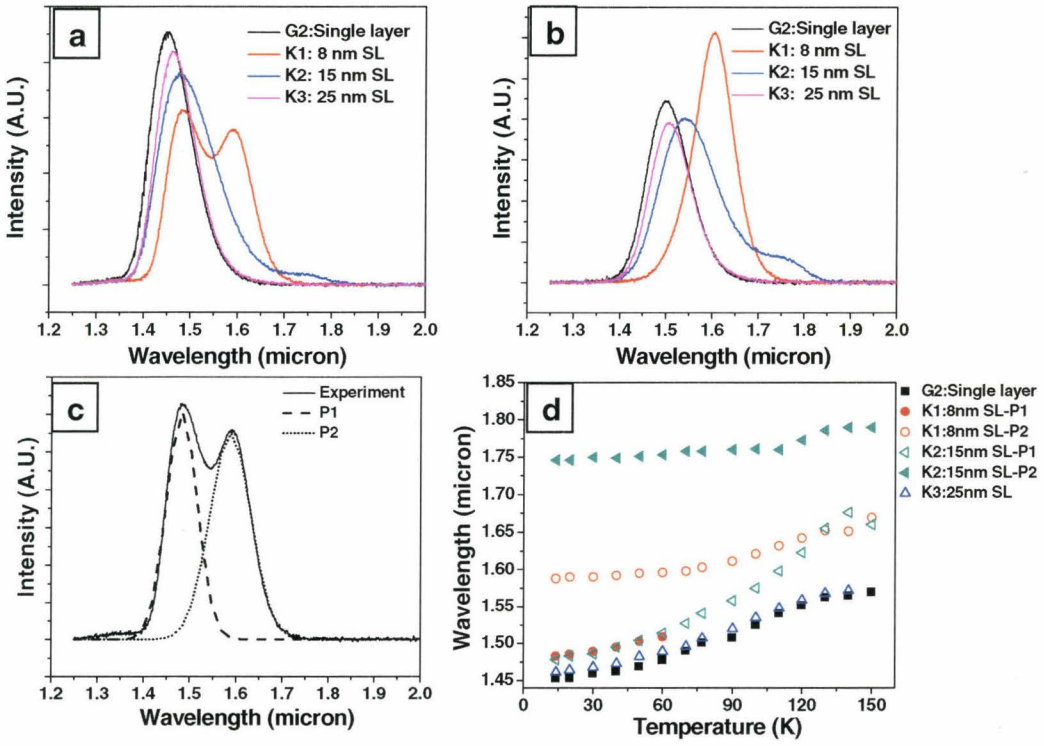

Figure 5-4: (a) and (b) PL spectra for samples G2 (single layer), K1 (8 nm SL, 4 ML InAs), K2 (15 nm SL, 4 ML InAs) and K3 (25 nm SL, 4 ML InAs) at 14 K and 77 K, respectively; (c) Deconvolution for the 14 K PL spectrum from sample K1 into components **P1** and **P2**; (d) Variation of wavelength as a function of temperature for PL peaks or components from each sample.

Multi-components are detected in the PL spectra of samples K1 (8 nm SL) and K2 (15 nm SL) at 14 K, as shown in Figure 5-4 (a). Deconvolution of the PL spectra into two Gaussian components was undertaken for these samples. Figure 5-4 (c) shows the spectrum from sample K1 at 14 K yielding a shorter wavelength component **P1** at ~1.49 μm and a longer wavelength component **P2** at ~1.6 μm. The origin and behavior of each component will be further discussed in section 5.3.

The red-shift of each peak within temperature range from 14 to 150 K (Figure 5-4 (d)), is compared with the bandgap shrinkage predicted by the Varshni equation (Adachi 2005) in Figure 5-5. The bandgap change due to the different thermal expansion coefficients between QWR and BL/SL materials is very small and estimated as about 0.08 meV from 14 to 77 K. Therefore, the wavelength variation from the thermal stress between QWR and BLs/SLs will be neglected in later discussions. As temperature increases for samples K1 and K2, the red-shift of the shorter (longer) wavelength component **P1** (**P2**) is faster (slower) than that expected from simply bandgap variations. The red-shift rates of samples G2 and K3 which exhibit only single PL emission peaks are essentially identical and both show a greater red-shift than the Varshni predictions. The different red-shift rates of each peak or component will be discussed in section 5.3.

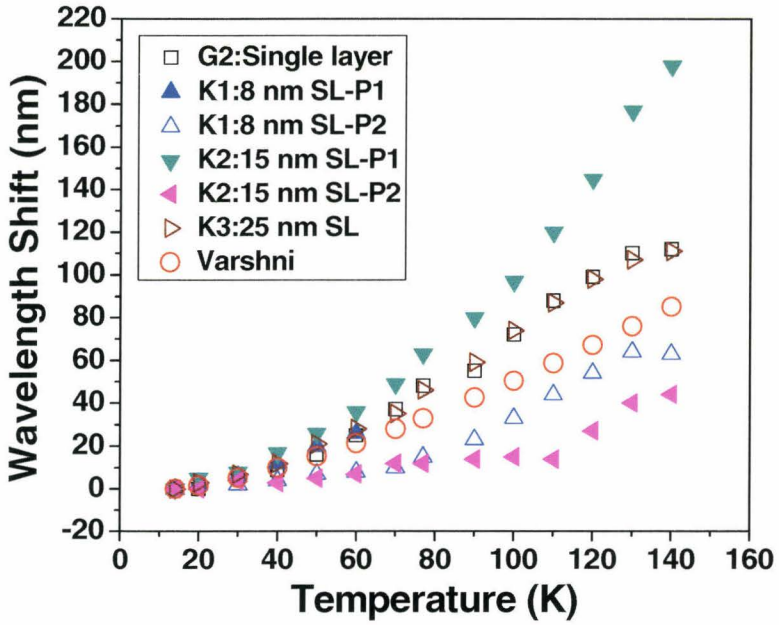

Figure 5-5: Comparison of wavelength shift of each peak with the bandgap shrinkage predicted by the Varshni equation for multilayer QWR samples with different SL thicknesses.

Comparing the PL spectra in Figures 5-4 (a) and (b) for sample K1, it is reasonable to ascribe the single peak at ~1.6 μm present at 77 K to component **P2** in the 14 K spectrum since the actual shift of the peaks due to the temperature change is small, as can be seen from the small shifts of the single PL peaks from 14 to 77 K for samples G2 (single layer) and K3 (25 nm SL). Hence it can be concluded that the longer wavelength component (**P2**) increases in intensity relative to the shorter one (**P1**) as the temperature increases in both samples K1 and K2. Also, the temperature-independent emission wavelength from component **P2** in samples K1 and K2 were observed between 14 and 77 K. This behavior will be discussed in section 5.3. Moreover, component **P1** in sample K1 has been

quenched at 70 K, while **P2** survived up to 150 K. In sample K2 (15 nm SL), component **P1** continues to dominate at 77 K. Both **P1** and **P2** coexist till 150 K and a single **P2** peak at ~1.79 μm was not observed until 160 K. For K3 (25 nm SL), only a single peak is observed at all temperatures and it is almost identical with the PL peak from the single layer sample G2 in terms of wavelength and line-shape, as shown in Figure 5-4 (a), (b) and (d). The similarity of the PL spectra from G2 (single layer) and K3 (25 nm SL) indicates that a SL of ≥ 25 nm can be essentially considered infinite and the QWR layers will perform independently as single layer QWRs. Also, similar QWR heights were found in samples G2 and K3 as shown in Table 5-1 and these gave rise to similar PL wavelengths, line-shapes, and wavelength red-shift change with temperature (Figure 5-5) of the PL emission spectra for both samples.

5.2 Effect of the InAs quantum wire layer thickness

Four samples were grown to study the effect of the InAs QWR layer thickness on the properties of the multilayer structures. They are numbered in Table 2-2 as samples L1, K1, L2 and L3; all contain five layers of QWRs with the nominal InAs thickness of 3 ML, 4 ML, 5 ML and 7 ML, respectively. The thickness and composition of the SL are fixed as 8 nm and $In_{0.53}Ga_{0.27}Al_{0.20}As$, respectively.

5.2.1 Structural characterization

5.2.1.1 AFM

The AFM images of the four samples are displayed in Figure 5-6. Anisotropic

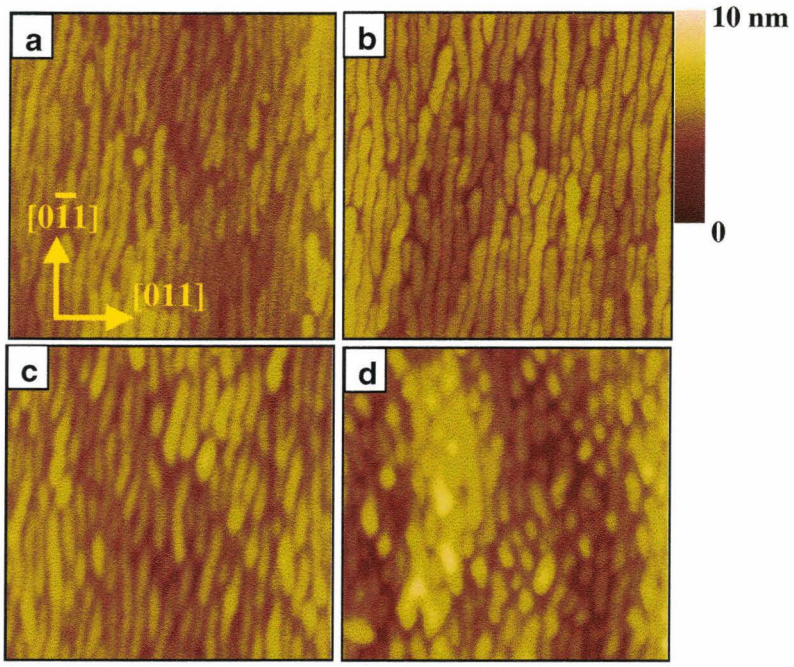

Figure 5-6: AFM images for samples (a) L1 (3 ML InAs); (b) K1 (4 ML InAs); (c) L2 (5 ML InAs); and (d) L3 (7 ML InAs).The insert in (a) represents the orientations for images (a)-(d). The scale right to image (b) is a common height scale for (a)-(d). The sizes of all images are 0.5 μm by 0.5 μm.

wires are observed with the dimension along [0$\bar{1}$1] direction larger than that along [011] direction. As the thickness of InAs layer increases, the morphologies of the free-standing nanostructures vary from anisotropic shallow wires (Figure 5-6 (a) for sample L1 with 3 ML InAs) to higher wires (Figures 5-6 (b) and (c) for sample K1 and L2 with 4 ML and 5 ML InAs, respectively) and finally to more laterally isotropic dot-like features in sample K3 (Figure 5-6 (d)) when the

thickness of InAs reaches 7 ML. As shown by the average length and height estimated from AFM images listed in Table 5-2, the trend of morphology evolutions is for the height to increase and the length along $[0\bar{1}1]$ to decrease as the QWR layer thickness increases.

Table 5-2: The average height and length for multilayer QWRs with different QWR layer thicknesses.

Sample #	L1	K1	L2	L3
InAs thickness (ML)	3	4	5	7
Average height (nm)	1.7±0.3	2.6±0.3	2.9±0.3	4.3±0.9
Average length (nm)	214±50	237±48	132±43	62±25

5.2.1.2 TEM

The structural properties of the QWR stacks were investigated by cross-sectional $\mathbf{g}_{200}$ DF TEM images taken close to $[0\bar{1}1]$ zone axis, as shown in Figure 5-7. Firstly, the alignment patterns of the QWRs follows a transition from a mixture of oblique and correlated stacks in sample L1 (3 ML InAs, Figure 5-7 (a), with the oblique direction highlighted by the dotted white arrows) to vertically correlated QWRs in samples K1 (4 ML InAs), L2 (5 ML InAs) and L3 (7 ML InAs) as shown in Figures 5-7 (b)-(d). Secondly, the QWR base is only flat for the first layer, and becomes increasingly wavy in the **n**th ($2 \le n \le 5$) layers as the InAs layer becomes thicker. This phenomenon is prominent in sample L2 (5 ML InAs)

and L3 (7 ML InAs), shown in Figures 5-7 (c) and (d). These two observations can be qualitatively understood by the fact that a higher residual strain field

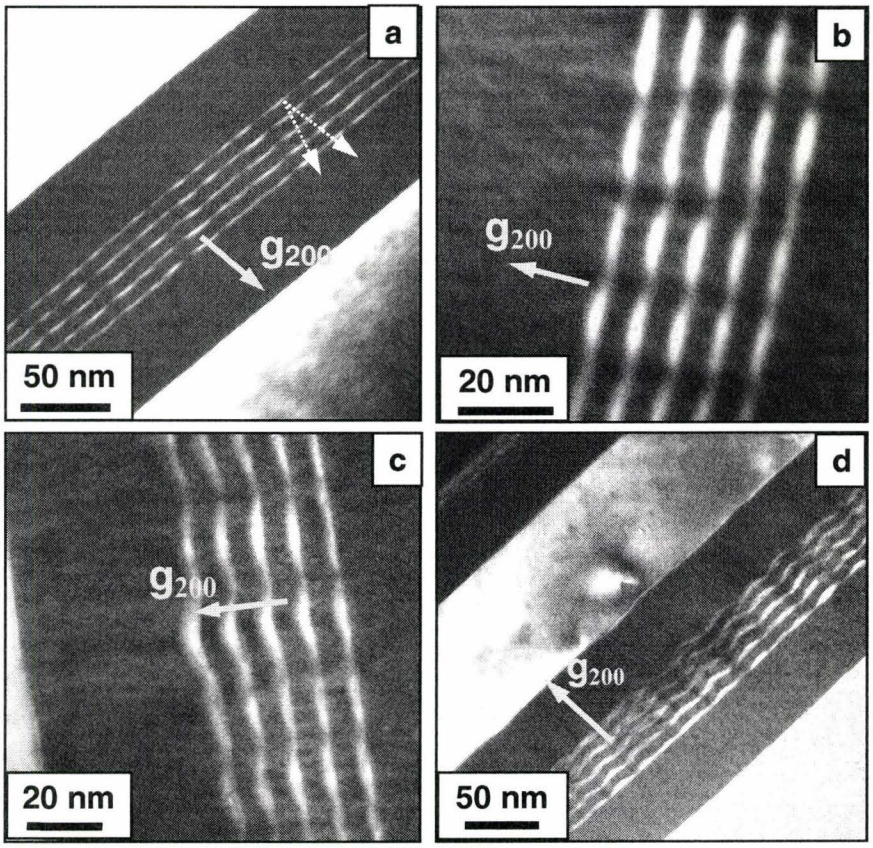

Figure 5-7: Cross-sectional DF TEM images of sample (a) L1 (3 ML InAs); (b) K1 (4 ML InAs); (c) L2 (5 ML InAs); and (d) L3 (7 ML InAs). All the images were taken with $\mathbf{g}_{200}$ close to $[0\bar{1}1]$ zone axis.

generated from the QWRs is expected on the growth front of the 8 nm-SLs as the QWR layer thickness increases. Therefore, the vertical correlation of QWRs is prominent in the samples with thicker InAs. Also, the growth front of the SLs will result in a wavy morphology in order to release the strain energy as the QWRs

become higher in the layer below. Therefore, the subsequent layers of QWRs, which nucleated on the SL areas directly above the QWR in the lower layer, will show a wavy base.

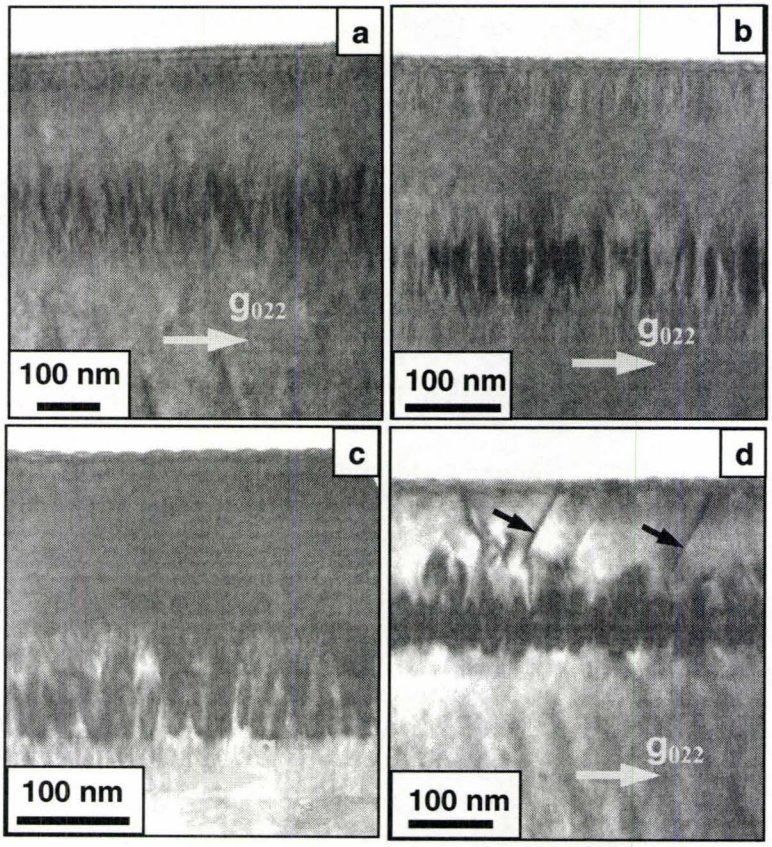

Figure 5-8: BF cross-sectional TEM images with $\mathbf{g}_{022}$ of (a) sample L1 (3 ML InAs); (b) sample K1 (4 ML InAs); (c) sample L2 (5 ML InAs); and (d) sample L3 (7 ML InAs). All the images were taken close to $[0\bar{1}1]$ zone axis.

BF TEM images with $\mathbf{g}_{022}$ for each sample are shown in Figure 5-8, and misfit dislocations, extending from the QWR stacks into the upper free standing QWR layer, were observed in sample L3 when the thickness of the QWR layer

was increased to 7 ML. Based on the criteria for growing the QWR structures mentioned in section 4.1, the thickness of the InAs layer should not exceed 7 ML in order to avoid the presence of dislocations. Another feature observed in Figure 5-8 is that when the QWRs are vertically correlated as the case in samples K1 (4 ML InAs), L2 (5 ML InAs) and L3 (7 ML InAs), the "butterfly-like" contrast pairs appeared in the images similar to the contrast observed in single layer QWR sample shown in Figure 4-11. However, this contrast pattern is not obvious for sample L1, in which the QWRs are lower in height and vertical alignment is not completely achieved when only 3 ML of InAs was deposited. It will be shown in Chapter 7 through FE simulations that this special contrast pattern arises from the overlap of the lateral displacement field generated by the relaxation of the QWR stacks.

5.2.2 Optical characterization

The PL spectra at 14 K and 77 K for all the samples are shown in Figure 5-9 (a) and (b), respectively. The PL spectra from sample L1 (3 ML InAs) and K1 (4 ML InAs) displayed two peaks (with **P1** and **P2** standing for the shorter and longer wavelength deconvoluted components, respectively). Only single peaks were detected from sample L2 and L3 as the thickness of the QWR layers was increased to 5 and 7 ML, respectively. The variation in the number of peaks can be attributed to the reduced height dispersion of QWRs with the thickness. The heights for capped QWRs in samples L1, K1 and L2 are (2.7±0.8), (4.0±0.6) and (4.6±0.4) nm, respectively, as estimated from TEM images. This trend has also

been experimentally confirmed by Gendry et al. for the InAs QWRs grown on and capped with InP (Gendry et al. 2004).

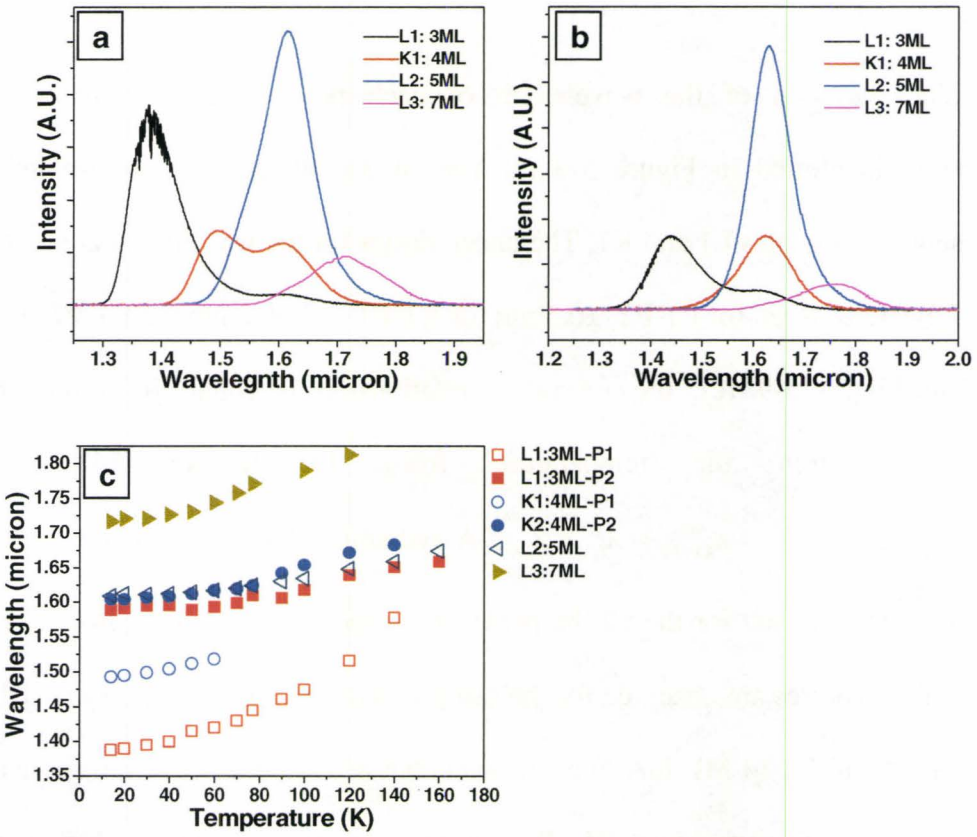

Figure 5-9: (a) and (b) PL spectra for samples L1 (3 ML InAs), K1 (4 ML InAs), L2 (5 ML InAs) and L3 (7 ML InAs) at 14 K and 77 K, respectively; (c) variation of wavelength as a function of temperature for PL peaks or components from each sample.

The spectrum of sample L3 shows the lowest integrated intensity among the four samples within the temperature 14~120 K. Moreover its intensity quenches at lower temperature (quenched out at T=120 K) than the other spectra (for example, 140 K for K1 and 160 K for L1 and L2) probably because of the

presence of misfit dislocations, which worked as non-radiative recombination centers (Petroff et al. 1980) in the active region of the QWR layers and upper BL, as shown in Figure 5-8 (d).

The variation of the wavelength of each peak or component with temperature is plotted in Figure 5-9 (c) after deconvoluting the spectra into components for samples L1 and K1. The uncertainties for the wavelength are ±0.6 nm for L1-**P1**, ±0.8 nm for L1-**P2**, ±0.5 nm for K1-**P1** and ±0.2 nm for K1-**P2**. As shown in Figure 5-9 (c), the following relationship is found in terms of wavelength within the temperature from 14 K to 140 K: $\lambda_{L1-P1} < \lambda_{K1-P1} < \lambda_{L1-P2} \approx \lambda_{K1-P2} \approx \lambda_{L2} < \lambda_{L3}$. A red-shift of the wavelength with temperature is observed for the all the peaks or components, as shown in Figure 5-10. Similar features are observed for the samples with multiple-components (L1 (3 ML InAs) and K1 (4 ML InAs)) as those shown in Figure 5-5, i.e. the shorter (longer) wavelength component **P1** (**P2**) shows a faster (slower) red-shift rate than that from bandgap variation. For samples with single peak in the PL spectra, a slower red-shift rate than the bandgap change predicted from Varshni equation is found in sample L2 while a faster one is found in sample L3. A further discussion on these observations will be shown in section 5.3.

5.3 Investigation on the origin of the multiple-components

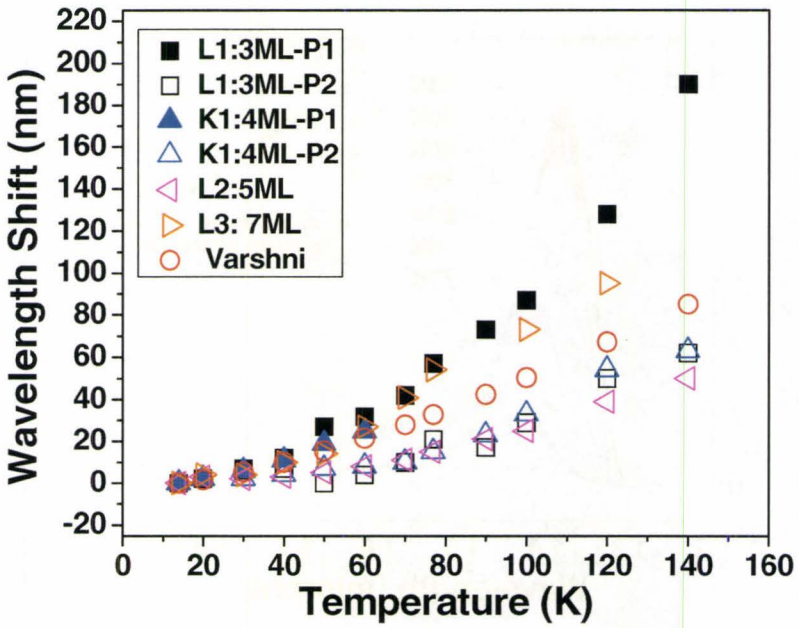

Figure 5-10: Comparison of wavelength shift of each peak or component with the value predicated from the Varshni euqation for multilayer QWR samples with different InAs thicknesses.

5.3.1 Variations of the components with temperature

In an attempt to understand the meaning of the multiple-components observed in PL spectra of samples K1 (8 nm SL, 4 ML InAs), K2 (15 nm SL, 4 ML InAs) and L1 (8 nm SL, 3 ML InAs), the variation of the PL spectra as a function of temperature were investigated. Samples K1 and L1 were chosen as typical examples since the relative peak intensity at 14 K of components **P1** and **P2** in sample K1 are comparable while **P1** is more prominent than **P2** in sample L1, as shown in Figure 5-9 (a). In order to get a reliable estimation on the shape and intensity variation of each component with temperature, the PL spectra were taken with the laser spot fixed at a particular area of the sample surface in order to

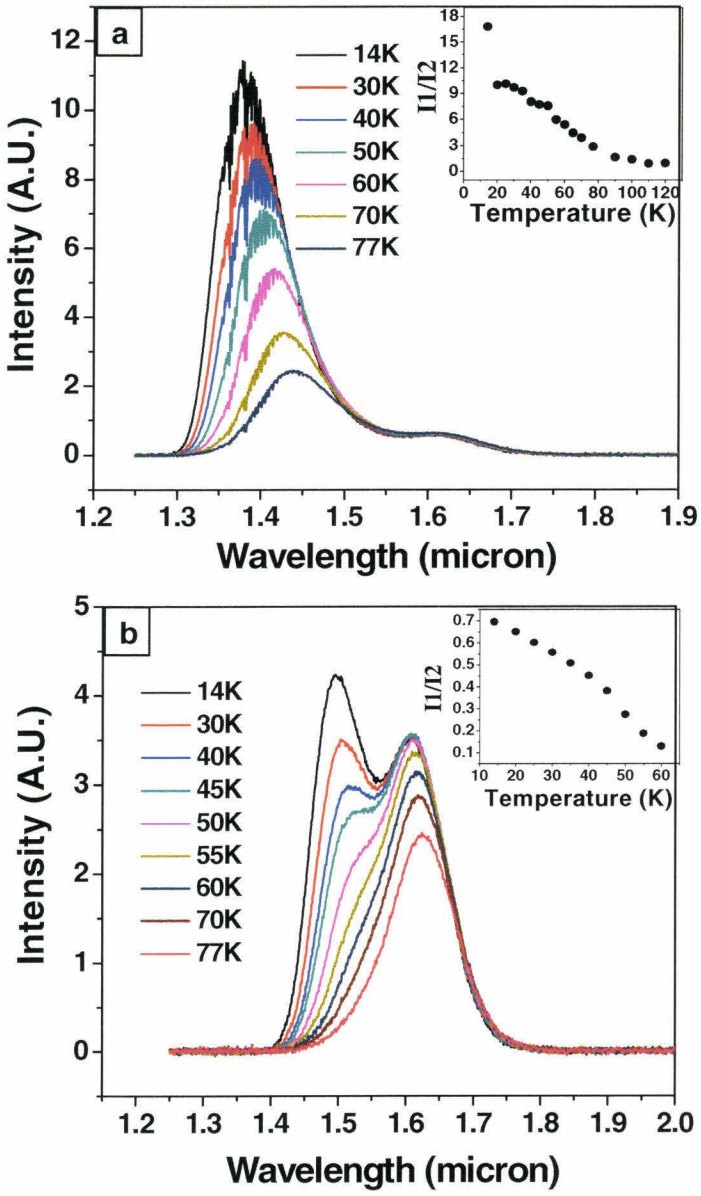

Figure 5-11: Temperature-dependent PL spectra taken at fixed spots for sample (a) L1 (3 ML InAs); and (b) K1 (4 ML InAs). The inserts in each figure show the variation of the integrated intensity ratios (**I1/I2**) between shorter (**P1**) and longer (**P2**) wavelength components.

exclude any possible spectrum variation due to the inhomogeneity of QWRs in different portions of the wafer. The detailed variation of the PL spectra as a function of temperature is shown in Figures 5-11 (a) and (b) for samples L1 and K1, respectively. To make clear comparisons, the integrated intensity ratio (**I1/I2**) between the deconvolved components **P1** and **P2** (for example, in Figure 5-4 (a)) with temperature is shown as inserts in Figure 5-11. The component **P1** quenches faster than **P2** as reflected by the shape variation of PL spectra with temperature in Figure 5-11. As a result, the relative intensity ratio (**I1/I2**) drops continuously within the temperature range, where both of them exist, as presented in the inserts of Figure 5-11. The maximum errors from deconvolving the PL spectra are less than 7% and 3% in amplitude and width, respectively for both samples K1 and L1. Therefore, the decreasing ratio of (**I1/I2**) with temperature is reliable under such small uncertainties.

5.3.2 Variations of the multiple-components with excitation power

The variation of the PL spectra showing multiple-components were also studied at various power levels of the excitation laser by putting a neutral density filter in front of the laser source before the beam interacted with the sample. The laser spot on the sample was fixed to exclude any spectrum variations due to spatial inhomogeneity of the QWRs across the wafer. The normalized PL spectra of samples L1 (8 nm SL, 3 ML InAs) and K1 (8 nm SL, 4 ML InAs) taken with power levels of 0.0099 to 9.9 mW at 14 K are shown in Figures 5-12 (a) and (c),

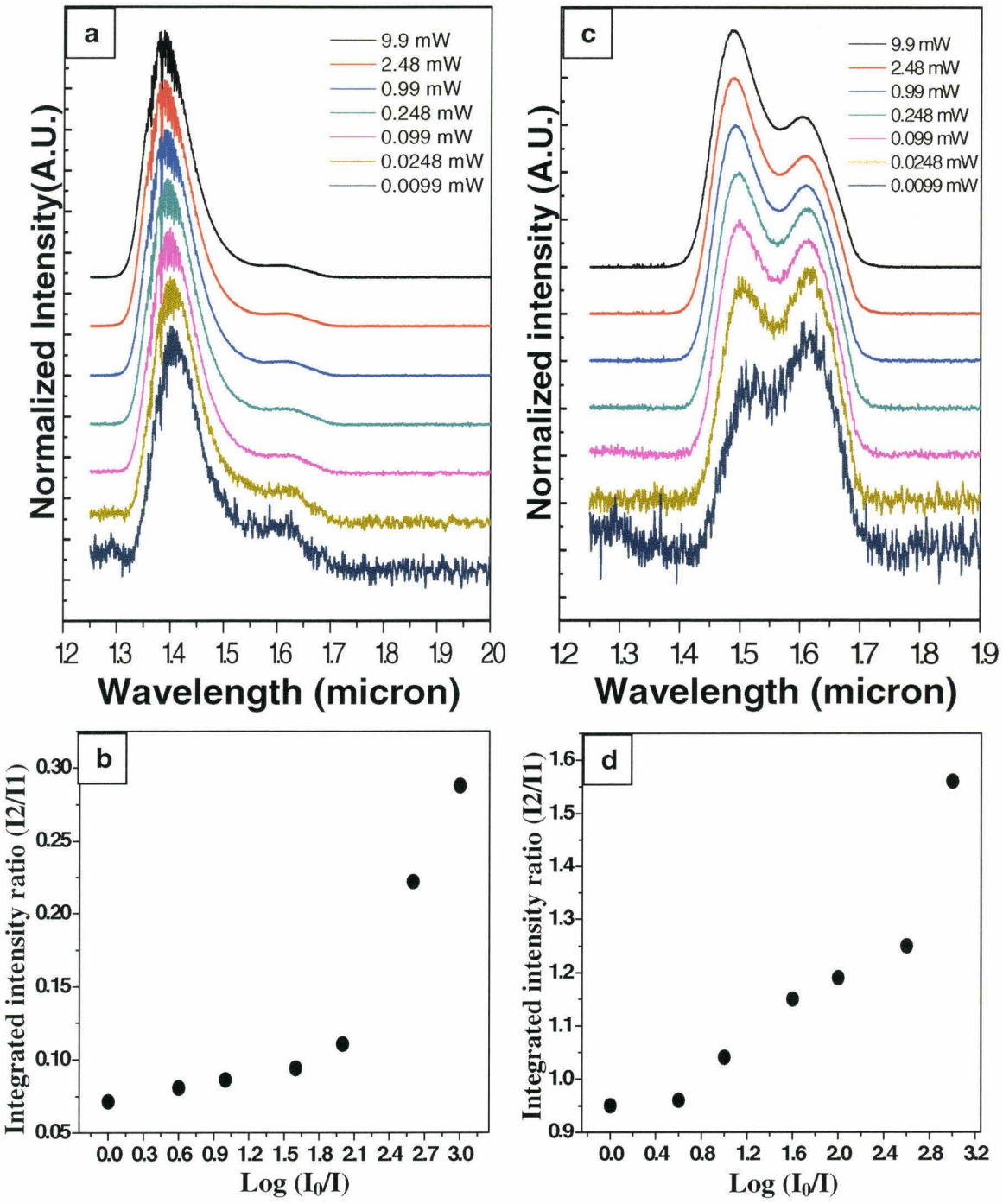

Figure 5-12: Normalized PL spectra taken at reduced laser power in (a) sample L1 (8 nm SL, 3 ML InAs) and (c) sample K1 (8 nm SL, 4 nm InAs). The variation of the integrated intensity ratio (**I2/I1**) with the laser power of the deconvoluted components **P1** and **P2** are shown for (b) sample L1 and (d) sample K1. All the spectra were taken at 14 K with original laser power $\mathbf{I_0}$=9.9 mW.

respectively. Two common features are appreciated. Firstly, both **P1** and **P2** were detected over the whole range of excitation powers. This observation indicates that both **P1** and **P2** arise from two different radiative recombination transitions. Secondly, **P2** becomes relatively more prominent as the excitation is reduced, which can be seen by the increasing integrated intensity ratio (**I2/I1**) with the laser power reduced, shown in Figures 5-12 (b) and (d). The maximal uncertainties for the deconvolved components **P1** and **P2** in sample L1 and K1 are less than 3% in both amplitude and width. Therefore, the observed increasing ratio of **I2/I1** with reduced excitation power should be reliable under such small errors.

5.3.3 Origin of the multiple-components

Generally, there are three possibilities accounting for the presence of multiple-components in PL spectra from multilayer semiconductor quantum structures. They are (1) the recombination of the carriers (electrons and holes) from both the ground and excited states (Wang 2008); (2) the splitting of electronic states due to the overlap of electron wave-function from the vertically coupled quantum structures in adjacent layers (Komori et al. 1997; Schliwa et al. 2001); and (3) recombination of carriers in quantum structures belonging to different size families (Wang 2008; Zhang, Y.C., et al. 2001; Brusaferri et al. 1996; Mazur et al. 2006). In order to investigate the origin of the multiple-components in the PL

spectra of sample K1 (8 nm SL, 4 ML InAs) and L1 (8 nm SL, 3 ML InAs), electronic structure calculations for sample K1 was carried out as a typical example.

The first possibility can be excluded in our case since the two components coexisted even when the initial laser power was reduced from 9.9 mW to 0.0099 mW, as shown in Figure 5-12. Also, the separation, as illustrated by the electronic structure calculations in Figure 5-13, between the ground and the first excited states of electrons is on the order of 100 meV, which is larger than the ~57 meV (estimated as $\frac{1240}{\lambda_{P1}} - \frac{1240}{\lambda_{P2}}$ with λ_{P1} ~1.49 μm and λ_{P2} ~1.60 μm) separation between components **P1** and **P2,** observed from the 14 K PL spectra of sample K1 in Figure 5-12 (c).

In order to assess whether the second mechanism is responsible, electronic structure calculations were carried out for two vertically coupled QWRs. The results in Figure 5-14 (a) show that the splitting of the ground state of electrons from vertical coupling is about 14 meV when the inter-QWR separation (defined as the distance between the top of the lower QWR and the base of the upper QWR in adjacent layer) is d=4 nm. This is consistent with sample K1 where the SL is 8 nm and the average height of QWR is 4 nm, as shown in Table 5-1. Thus, a separation of 14 meV would be expected for **P1** and **P2** in PL spectra based on

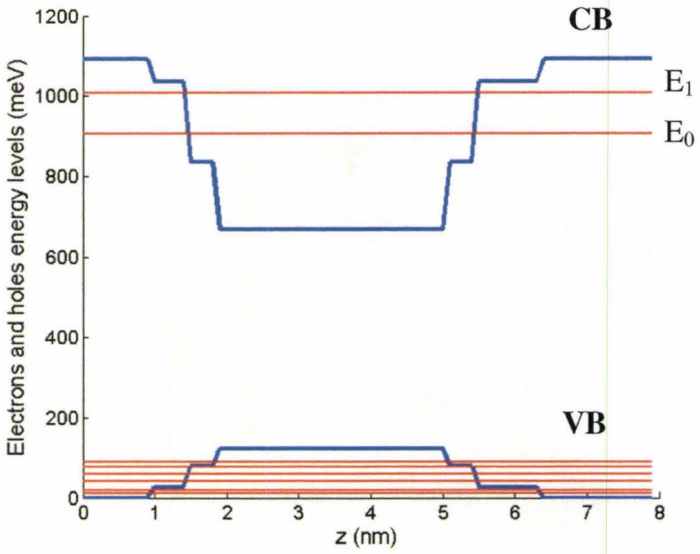

Figure 5-13: The calculated conduction and valence band energy eigenvalues for one QWR in sample K1 (8 nm SL, 4 ML InAs). The height and base width of the QWR are 4 nm and 18.4 nm, respectively, which are the average values estimated from TEM images. The ground state of electrons locates at E_0=906 meV, first excited state at E_1=1009 meV. *Z* axis stands for the distance along the QWR height. The steps in the band edges are from the compositional gradient in single QWR.

this calculation if the two components arise from the splitting of the ground states due to vertical coupling. However, this value does not agree with the experimentally observed value of ~57 meV separation between **P1** and **P2**. Also, if electron wave-function was responsible for the two peaks, it should be more prominent overlap in sample L2 (8 nm SL, 5 ML InAs) and L3 (8 nm SL, 7ML InAs) since higher QWRs, hence smaller inter-QWR separations are present in these two samples compared to those in sample K1 (8 nm SL, 4 ML InAs). Based on the results in Figures 5-14 (b), larger splitting of the electronic ground state will result from smaller inter-QWR separations: for example, d=2 nm and 3 nm produce splittings of 55 meV and 28 meV, respectively. Thus, multiple-

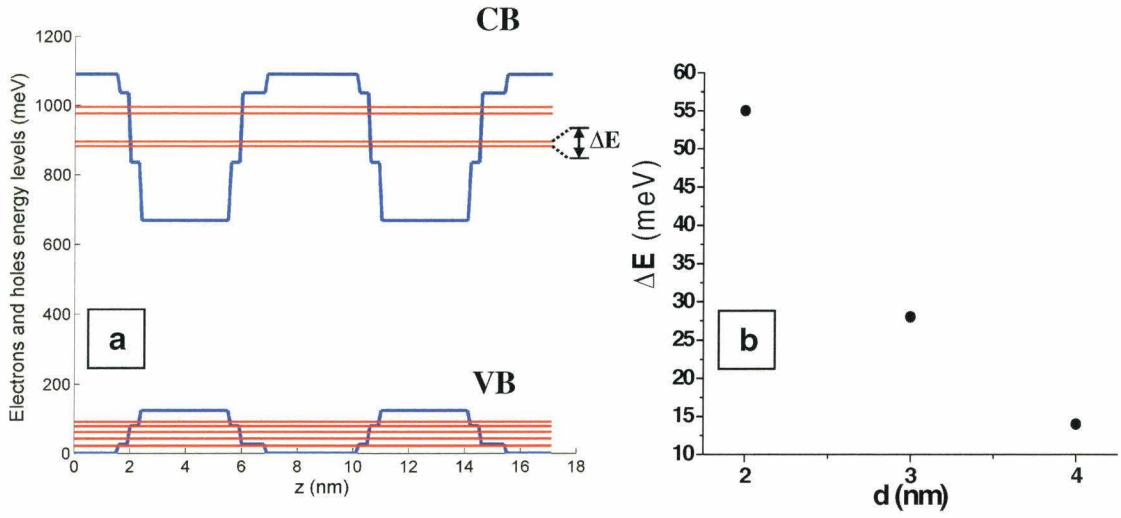

Figure 5-14: (a) The calculated conduction and valence band energy eigenvalues in two vertical aligned QWRs with experimentally observed inter-QWR separations d= 4 nm. *Z* axis stands for the distance along the QWR height. (b) The calculated energy splitting ΔE due to electronic coupling as a function of inter-QWR separation d. The values of ΔE are 14, 28 and 55 meV for the 4, 3 and 2 nm inter-QWR separations in adjacent layers, respectively.

components with larger separations would be expected (Komori et al. 1997) in PL spectra from samples L2 and L3 than those in sample K1. However, as shown in Figure 5-9 (a) and (b), the spectra from these two samples are mainly composed of a single peak as compared with the two components present in sample K1. Therefore, we exclude the possibility that the multiple-components come from vertical electronic coupling between QWRs in adjacent layers.

As stated in Chapter 4, the PL wavelength is mainly determined by the QWR heights if the growth conditions and the surrounding BL materials are identical for different samples (Kümmell et al. 2006; Maes et al. 2004; Fuster et al.

2005). Thus, it is suggested that the multiple-components in PL spectra are due to the recombination of the ground state carriers within QWRs belonging to different height families. The height distribution of the QWRs was obtained by analyzing the contrast in the cross-sectional DF ($\mathbf{g}_{200}$) images for over three hundred QWRs.

The interval of height measurement should be determined by considering the following factors: (1) Firstly, one should consider the height fluctuation on an individual QWR along the long axis ([$0\bar{1}1$] direction), which can be estimated by analyzing the AFM images. A typical height profile of individual QWR is shown in Figure 5-15. The distance between the two red reverse triangles is 100 nm, which is the typical thickness of the cross-sectional TEM specimen. The amplitude of the height fluctuation is estimated as 0.14±0.03 nm (about 1/2 monolayer) by analyzing the profile of 30 different QWRs. (2) Secondly, one should account for the sensitivity of the PL wavelength variation with the height of the QWRs. For example, it has been shown in literature that a 2 ML fluctuation in height for InAs QWRs within InP BLs can cause a red-shift of 80 meV in wavelength (Alén et al. 2002). This effect shows that the emission wavelength is very sensitive to the variation of QWR height. Therefore, we select the width of the interval for the height histogram classification as 0.25 nm (close to 1ML) to establish the QWR height distribution.

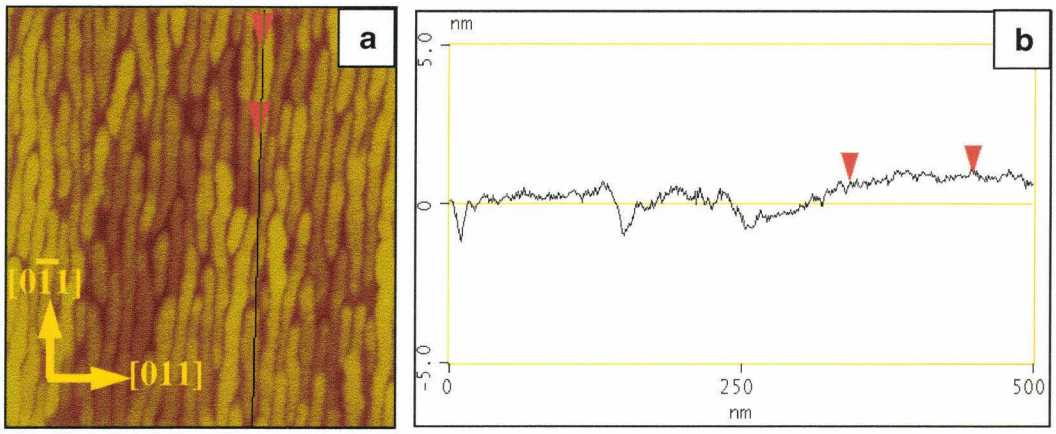

Figure 5-15: Height fluctuation on an individual QWR in sample K1 (8 nm SL, 4 ML InAs). (a) AFM image; and (b) a typical height profile along the dark line in (a). The height fluctuation was estimated as 0.14±0.03 nm between the two reverse triangles separated 100 nm in (b) for 30 individual QWRs. The size of AFM image is 0.5 μm by 0.5 μm.

The QWR height distribution histogram is shown in Figure 5-16. The 0.14 nm of height fluctuation on a single QWR is taken as the error bar for the measurement. Two prominent height ranges, which are from 3.75 nm to 4 nm and from 4.25 to 4.5 nm, respectively, are observed although the error bars on the height measurement, due to the height fluctuation on individual QWRs, introduces some overlap on adjacent classes. Using these average measurements, the theoretical calculations (in later Figures 5-19 (a) and (b)) on the electronic structure predict a wavelength of 1.50 and 1.58 μm for the ground state emissions from the shorter and taller QWRs, respectively, which agrees well with the experimental observations shown in Figure 5-12. Therefore, it is reasonable to attribute the presence of multiple-components in the PL spectrum of sample K1 (8 nm SL, 4 ML InAs) as arising from the ground state emission in QWRs belonging

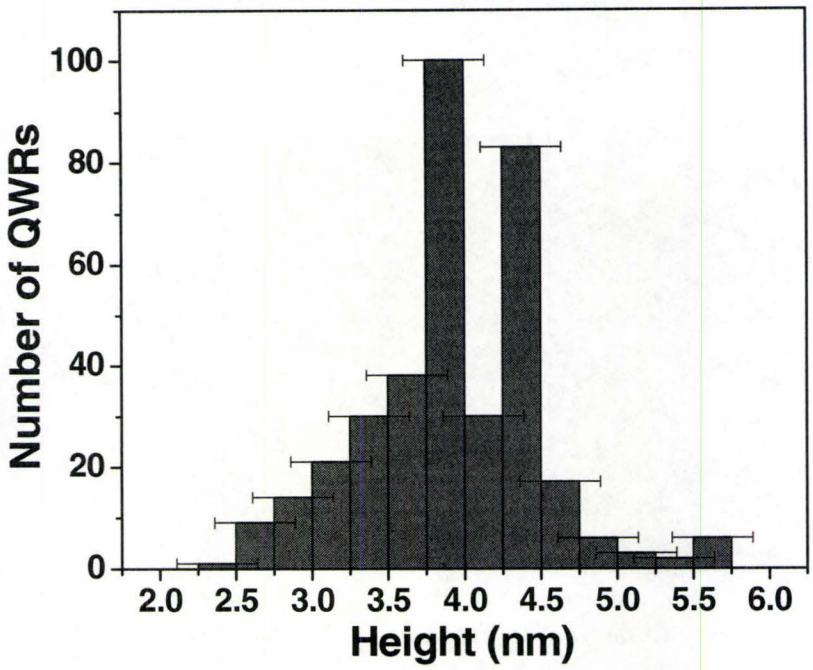

Figure 5-16: Histogram showing the two dominant heights of QWRs in sample K1 (8 nm SL, 4 ML InAs).

to the two dominant height families. This interpretation can also be applied to explain the multiple-peaks observed in PL spectra from sample K2 (15 nm SL, 4 ML InAs) and L1 (8 nm SL, 3 ML InAs). In these samples, the PL intensity from **P2** << **P1** so the smaller height QWRs should be dominant. The coexistence of the higher (highlighted by arrows) and shorter QWRs are observed in samples L1 and K2, as revealed by the TEM images in Figures 5-17 (a) and (b), respectively. The shorter QWRs are seen to constitute the majority of the total number of QWRs in both samples, and this observation is in good agreement with the

prominent shorter wavelength component **P1** in the PL spectra from sample K2 and L1, as shown in Figure 5-4 and Figure 5-9, respectively.

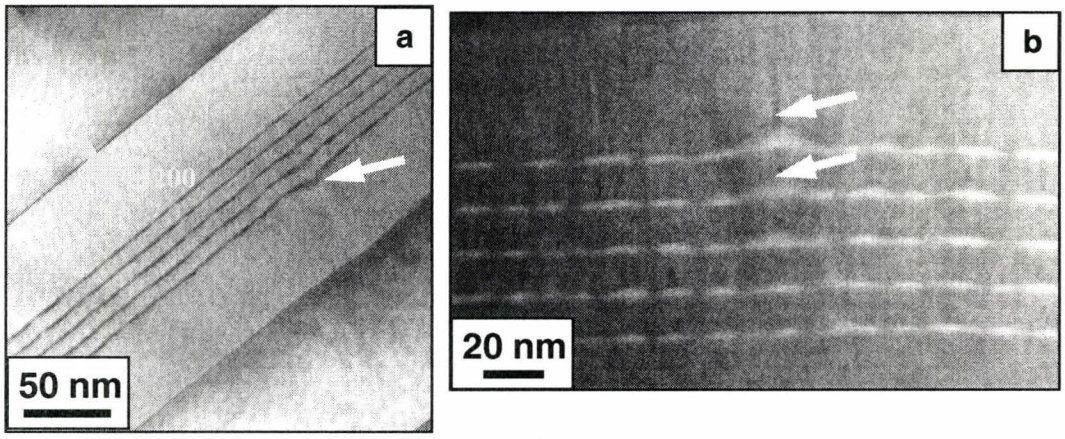

Figure 5-17: Cross-sectional TEM images of (a) BF $\mathbf{g}_{200}$ image of sample L1 (8 nm SL, 3 ML InAs); and (b) HAADF image of sample K2 (15 nm SL, 4 ML InAs), showing the coexistence of the higher and shorter of QWRs. The images are taken close to (a) or on (b) $[0\bar{1}1]$ zone axis.

5.3.4 Interpretation on the components variations

The suggested model for the interpreting the variation of the multiple-components is schematically illustrated in Figure 5-18. For simplicity, two assumptions are made. Firstly, as shown in Figure 5-18 (a), two QWRs with larger and smaller heights are placed adjacent to each other. Secondly, the same aspect ratio (h/D) is assigned for QWRs with different heights. A wetting layer with thickness about 0.5 nm is also included underneath the QWRs as experimentally observed

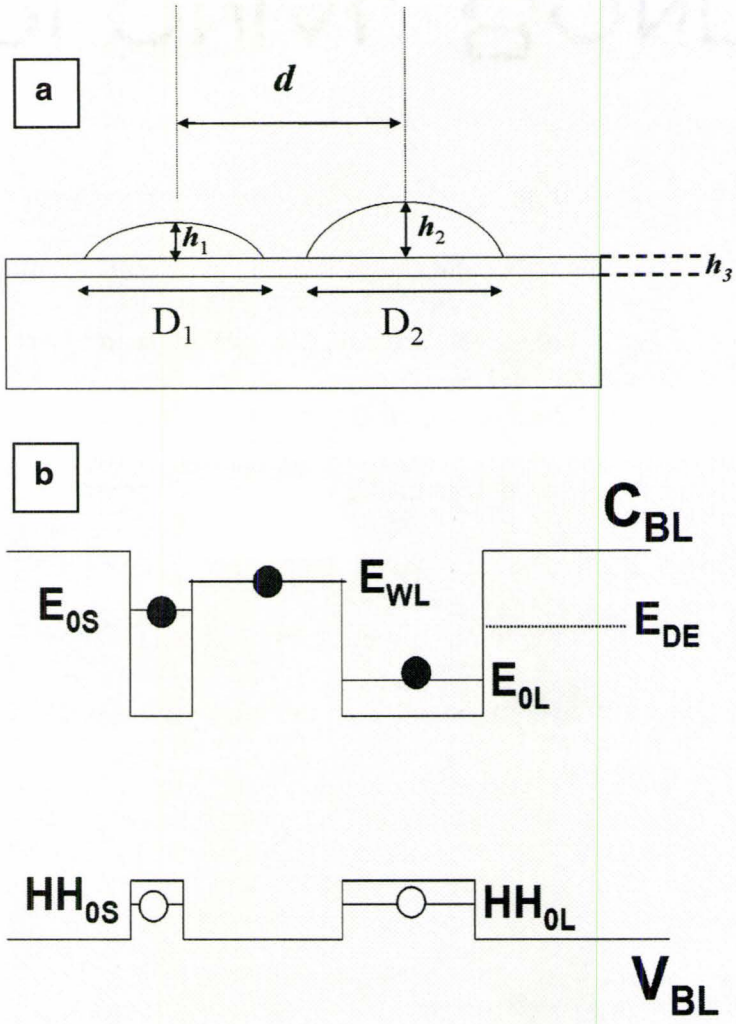

Figure 5-18: Schematic drawing of (a) dimensions of the QWRs with different heights, h1=3.8 nm, h2=4.4 nm for the QWR heights and h3=0.5 nm for the thickness of the wetting layer. D1=18.4 nm, D2=21.3 and d=21.6 nm as estimated from DF TEM images. (b) Relative energy levels of the electrons (solid circles) and holes (open circles) in the QWRs with different heights. $\mathbf{C_{BL}}$ and $\mathbf{V_{BL}}$ stand for the conduction and valence band edge of the BL/SL materials, respectively. $\mathbf{E_{0S}}$ and $\mathbf{E_{0L}}$ represent the ground states of electrons in shorter and higher QWRs, respectively. $\mathbf{HH_{0S}}$ and $\mathbf{HH_{0L}}$ are the ground states of heavy holes in shorter and higher QWRs, respectively. $\mathbf{E_{WL}}$ stands for the intermediate level of electrons residing in the wetting layer. $\mathbf{E_{DE}}$ represnts the deep level introduced by dislocations.

by the brighter contrast present between the bases of the adjacent QWRs in the same layer, as displayed in Figure 5-2 (b). The schematic diagram showing the ground state energy levels of electrons and heavy holes in QWRs with different heights is displayed in Figure 5-18 (b). A deeper energy level for electrons is found in QWR with larger height than that in QWRs with smaller height, while the positions of heavy hole levels are close to each other in QWRs with different heights. Thus, in the samples where the two predominant height families (for example, Figure 5-16) are detected, the longer (shorter) wavelength component **P2** (**P1**) arises from the photons (Figure 1-2) generated through carrier recombination in QWRs with larger (smaller) height. This model will be applied to explain the multiple-components variation in PL spectra as a function of temperature (Figure 5-11) and excitation power (Figure 5-12), respectively in the discussions below.

5.3.4.1 Multiple-components variations with temperature

The variation of PL spectra with multiple-components as a function of temperature (Figure 5-11) is explained by thermally activated carrier transfer, which has been extensively studied by both experiments (Wang 2008; Polimeni et al. 1999; Brusaferri et al. 1996) and theoretical calculations (Sanguinetti et al. 1999; Bansal 2006) for quantum dot structures. Two facts are important to understand the unusual features observed in PL spectra with multiple-components, such as the varied relative intensity between **P1** and **P2** with temperature (Figures

5-11), and the faster red-shift of wavelength observed in **P1** compared to **P2** (Figures 5-5 and 5-10). Firstly, a deeper electronic ground state energy level is present in the QWR with larger height ($\mathbf{E_{0L}}$) than that in the QWR a smaller height ($\mathbf{E_{0S}}$), based on the results shown in literature (Maes et al. 2004) and our own calculations (Figures 5-19 (a) and (b)). Secondly, an intermediate electron energy level of the wetting layer ($\mathbf{E_{WL}}$) lower than the conduction band edge of the BL ($\mathbf{C_{BL}}$) material is present between QWRs because of the higher **In** concentration (~60%) in the wetting layer (Figure 5-3 (b)) than that (53%) in the surrounding BL materials (Vurgaftman et al. 2001). Therefore, a smaller separation of the electron energy levels is found between $\mathbf{E_{WL}}$ and $\mathbf{E_{0S}}$ than that between $\mathbf{E_{WL}}$ and $\mathbf{E_{0L}}$. As the temperature is increased, it is easier for electrons populated at shallow energy level ($\mathbf{E_{0S}}$) to escape into the intermediate level ($\mathbf{E_{WL}}$) than for those at deep energy level ($\mathbf{E_{0L}}$). Further transfer will result in the trapping of carriers in the deeper local energy level $\mathbf{E_{0L}}$ followed by the radiative recombination there. This process is schematically shown in Figure 5-18 (b) and the total effect is the transfer of thermally activated carriers from QWRs with smaller height to those with larger height (Brusaferri et al. 1996; Zhang, Y.C., et al. 2001; Polimeni et al. 1999).

One experimental proof of this proposed mechanism is the higher rate of red-shift of component **P1** (from shorter QWRs) than the bandgap shrinkage, as

observed in Figures 5-5 and 5-10. More specifically, at low temperatures (for example, 14~40 K), the red-shift with temperature of every peak or component

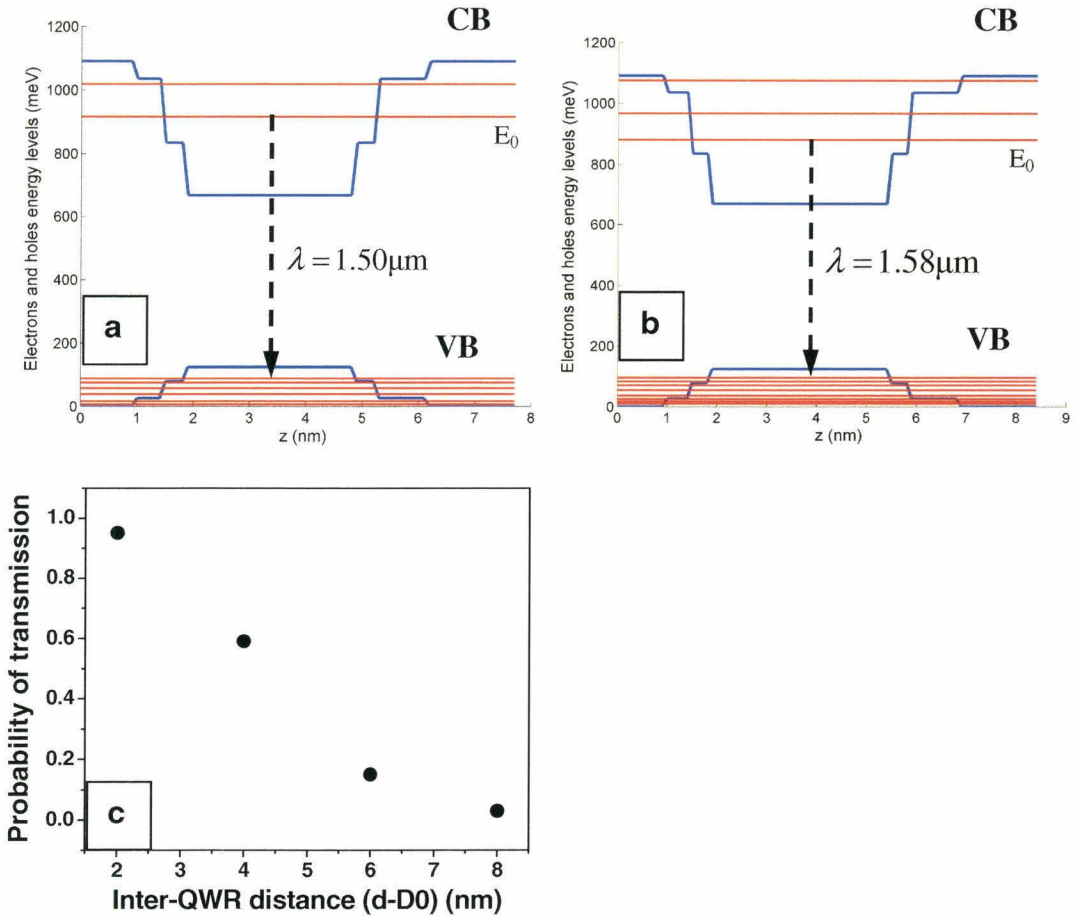

Figure 5-19: (a) and (b) the calculated conduction and valence band energy eigenvalues in QWRs with a height of h1=3.8 nm (E0=917 meV) and h2=4.4 nm (E0=880 meV), respectively. *Z* axis stands for the distance along the QWR height. (c) the plot showing the trend of transmission probability of electrons between adjacent QWRs as a function of inter-QWR distance (d-D0) estimated from the electronic structure calculations.

agrees well with the bandgap change of $In_{0.75}Ga_{0.25}As$, the material constituting the **In**-rich core of individual QWRs (Figure 5-3 (a)). At higher temperatures, the deviation of **P1** (for example, **P1** of sample K2 in Figure 5-5; **P1** of sample L1 in

Figure 5-10) from the bandgap shrinkage becomes significant since the effect of thermally activated carrier transfer increases (Polimeni et al. 1999). Whereas, for the component **P2** (in samples K1, K2 and L1) or single peak (sample L2) from higher QWRs, the lower red-shift rate compared to the bandgap change is proposed to arise from the deeper localized energy levels of carriers and this effect has been observed in quantum dot structures (Polimeni et al. 1999; Dai et al. 1997).

Based on the considerations above, a slow quenching rate of the PL intensity from the longer wavelength component **P2** (generated from the carrier recombination between $\mathbf{E_{0L}}$ and $\mathbf{HH_{0L}}$ in QWRs with larger height) is expected compared to the shorter wavelength component **P1** (generated from the carriers recombination between $\mathbf{E_{0S}}$ and $\mathbf{HH_{0S}}$ in QWRs with smaller height) due to the thermally activated carrier transfer from the smaller height QWRs to higher ones as temperature increases. Therefore, a continuously decreased intensity ratio between **P1** and **P2 (I1/I2)** is detected within temperature range where both **P1** and **P2** exist, as shown in Figure 5-11.

In addition, this model can be applied to explain the red-shift of wavelength in the PL spectra with single peaks. For QWRs with smaller height, such as K3 (25 nm SL, 4 ML InAs) and G2 (single layer, 4 ML InAs), a red-shift greater than that from the bandgap shrinkage, as shown in Figure 5-5, can be

attributed to the carrier transfer from the shallow energy level ($\mathbf{E_{0S}}$) to deep level ($\mathbf{E_{0L}}$), arising from the height dispersion of QWRs in the sample. This effect is similar as that observed for component **P1**. However, because of the relatively uniform height distribution in K3 and G2, the deviation of the red-shift from that of the bandgap change are smaller than that observed for component **P1** in sample K2 (15 nm SL, 4 ML InAs) in Figure 5-5. Also, for QWRs with larger height, such as sample L2 (8 nm SL, 5 ML InAs), the slower red-shift change compared to that of the bandgap change (Figure 5-10) can be understood by the deep energy level, as occurs for component **P2** in sample K1, since there is close similarity of line shape (wavelength and width) between samples K1 and L2 in the PL spectra at 77 K (Figure 5-9 (b)). Finally, in sample L3 (8 nm SL, 7 ML InAs), the dislocations (Figure 5-8 (d)) close to QWRs may introduce deep energy levels ($\mathbf{E_{DE}}$ in Figure 5-18 (b), below $\mathbf{E_{WL}}$), which may work as additional carrier transfer channels (Gelczuk et al. 2007). Thus, the shallower barrier between $\mathbf{E_{0L}}$ and $\mathbf{E_{DE}}$ compared to that between $\mathbf{E_{0L}}$ and $\mathbf{E_{WL}}$ will cause a larger red-shift with temperature in sample L3 than that from the bandgap shrinkage.

5.3.4.2 Multiple-components variations with excitation laser power

Although the model based on thermally activated carrier transfer is successfully applied to interpret the variations of shorter (longer) wavelength component **P1** (**P2**) with temperature, it is not applicable to explain the change of the spectra and intensity ratio (**I2/I1**) under different excitation powers (Figure 5-12) since the

thermally activated transfer is suppressed due to the small thermal energy of carriers (1.2 meV) at 14 K.

Carrier transfer mechanism based on tunneling of carriers between QWRs belonging to different height families through phonon-assisted process (Wang 2008; Mazur et al. 2006; Rodt et al. 2003), which is prominent at low temperature, is suggested to be responsible for the varied integrated intensity (**I2/I1**) in Figure 5-12. It has been experimentally proved that the tunneling facilitates the carrier relaxation from shallow to deep local energy levels in adjacent quantum structures, such as the quantum dot-quantum dot (Rodt et al. 2003) or quantum dot-quantum well (Mazur et al. 2006) systems. Thus, it is proposed the tunneling of carrier from QWRs with smaller height to those with larger height (referred as inter-QWR tunneling) exists in samples L1, K1 and K2 at 14 K. Also, the effectiveness of the inter-QWR tunneling is determined by the overlap of the electronic wave-function (Wang 2008), which drops quickly on the inter-QWR separations (Sidor et al. 2007). As a rough estimation, the calculated transmission probability for sample K1, which reflects the overlap of the electronic wave-function, is plotted as a function of inter-QWR distance (d-D0) (D0=(D1+D2)/2) in Figure 5-19 (c). The probability drops quickly with the inter-QWR distance, which means the carrier tunneling only occurs within the adjacent QWR pairs separated by a finite distance. Taking into account the possibility of inter-QWR carrier transfer, we can interpret the spectra variations with excitation power as follows. At the

lowest excitation power (I=0.0099mW), carriers excited into the BL/SL will relaxed into the shorter and higher QWRs. With the assistance of the acoustic phonons (Mazur et al. 2006), part of these carriers were transferred from shorter to higher QWRs through tunneling. Further increase of the excitation power lead to significant carrier population by the higher QWRs and increased pumping of the shorter QWRs. Thus, the maximal intensity ratio (**I2/I1**) was detected at the lowest excitation power and the ratio dcreased continuously as the excitation laser power was increased (Figures 5-12 (b) and (d)).

5.3.5 Summary on the investigations of the multiple-components

In summary, the multiple-components in the PL spectra of sample L1 (8 nm SL, 3 ML InAs), K1 (8 nm SL, 4 ML InAs) and K2 (15 nm SL, 4 ML InAs) arise from radiative recombination between ground states of the carriers in QWRs belonging to different height families. The decreasing contribution of component **P1** to the PL spectra with elevated temperature (Figure 5-11) and reduced excitation powers (Figure 5-12) is suggested to be associated with the carrier redistribution, from QWRs with smaller height to those with larger height, through thermally activated carrier transfer and phonon-assisted carrier tunneling, respectively.

5.4 Effect of Al content in barrier and spacer layers

As shown in Chapter 4, the optical properties of QWR structure can be tuned by changing the **Al** content in the BL/SL, which modifies the band edge offsets

between QWRs and the BLs/SLs (Figure 1-2). Thus, the role of the **Al** content in BLs/SLs on the structural and optical properties of the multilayer QWRs was investigated. The samples for this purpose are numbered as M1, M2, M3 and M4 in Table 2-2 with the **Al** content of 0, 10%, 30% and 48%, respectively in BLs/SLs. Although the **Al** content was changed, the lattice match between the BLs/SLs and InP substrate was kept the same for all the four samples, as confirmed by the double-crystal X-ray diffraction for the calibrated samples in which 800 nm BL material was directly deposited on the InP buffers. Therefore, the BL or SL composition in sample M1 and M4 should be $In_{0.53}Ga_{0.47}As$ and $In_{0.52}Al_{0.48}As$, respectively. The thickness of the BLs below and above the QWR stacks was increased to 200 nm in order to observe the propagation direction and depth of the **In**-rich stripes (for example, Figure 4-18 and Figure 5-3(a)) in the upper BL. The thicknesses of InAs layers and SLs were fixed as 5 ML and 8 nm, respectively.

5.4.1 Structural characterizations

5.4.1.1 AFM

The three-dimensional AFM images for the free-standing nanostructures are shown in Figure 5-20, from which the wire-like anisotropic structures along $[0\bar{1}1]$ direction have been observed in all the four samples. The only difference is that the lateral width of wires along [011] in sample M1 ($In_{0.53}Ga_{0.47}As$ BL/SL) is

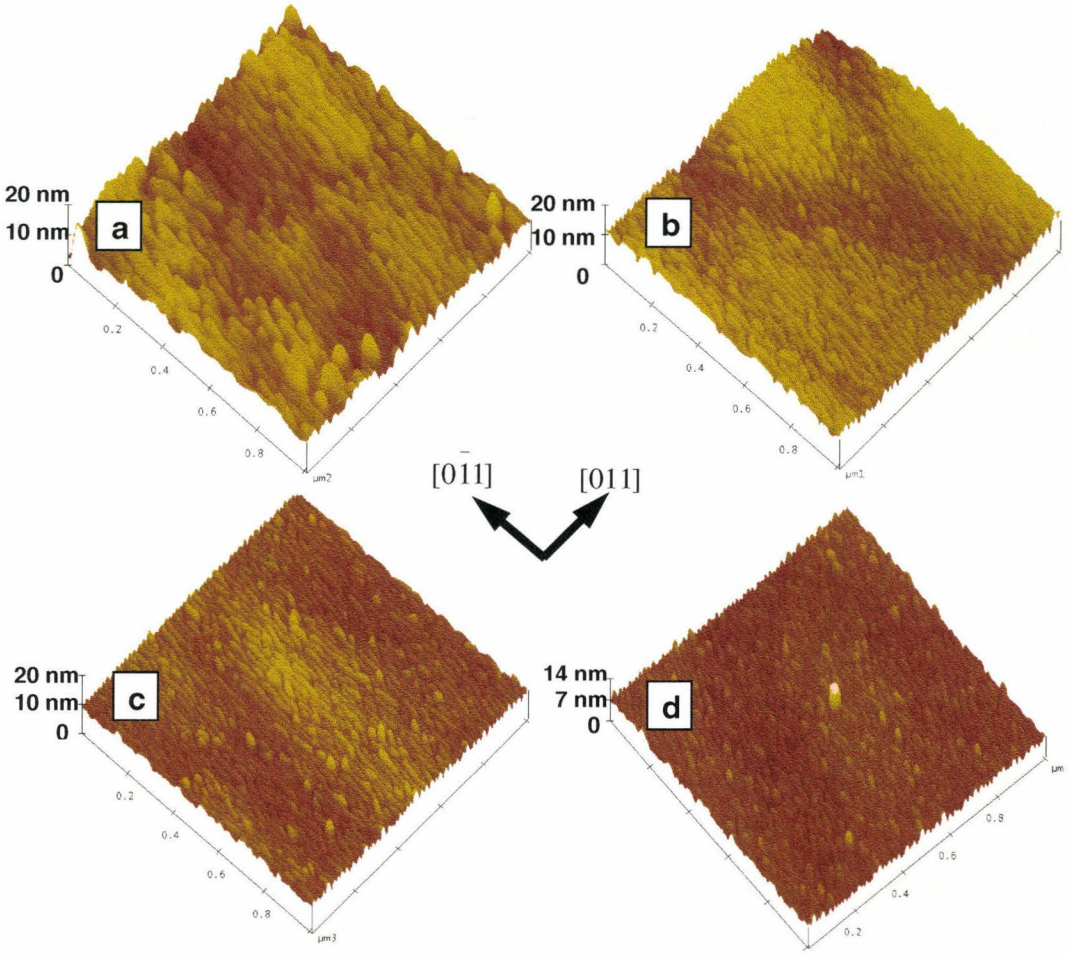

Figure 5-20: 3-D AFM images of sample (a) M1 ($In_{0.53}Ga_{0.47}As$ SL/BL); (b) M2 ($In_{0.53}Ga_{0.37}Al_{0.10}As$ SL/BL); (c) M3 ($In_{0.53}Ga_{0.17}Al_{0.30}As$ SL/BL); and (d) M4 ($In_{0.52}Al_{0.48}As$ SL/BL). The insert in the middle of this figure shows the surface orientation of all the four images. The sizes of all images are 1μm by 1μm.

Table 5-3: Average width and length for QWRs with different **Al** content in BL/SL.

Sample #	M1	M2	M3	M4
Al content (at.%) in BL/SL	0	10	30	48
Average Width (nm)	30.1±5.9	20.3±3.4	20.3±4.0	17.8±3.4
Average length (nm)	286±103	280±113	222±75	192±84

larger than the rest. The length of the QWRs along [0$\bar{1}$1] is greater than 150 nm in all samples, as shown in Table 5-3.

5.4.1.2 TEM

The samples are further characterized by TEM imaging in order to study the variation of alignment pattern of the QWR stacks, the compositional modulations and defects as the **Al** content in BLs/SLs was changed.

5.4.1.2.1 Alignments of QWR stacks

The DF cross-sectional TEM images ($\mathbf{g}_{200}$) are displayed in Figure 5-21. Vertically aligned QWR stacks (AAAA…sequence) were observed in sample M1 and M2 with 0 and 10 % **Al** in BLs/SLs, respectively. In contrast, anti-correlated alignment (ABAB…sequence) of the QWR layers is observed in sample M4 as the **Al** content in BLs/SLs is increased to 48 %. A combination of the vertically aligned and anti-correlated QWRs was observed in sample M3 with 30% **Al** in BLs/SLs. A close observation shows that in terms of size, there exist two families of QWRs in sample M3: a minority of higher and wider ones and a majority of shorter and narrower ones. The former forms an aligned pattern, while the latter ones prefer to arrange themselves in an anti-correlated way, as shown in Figure 5-21 (c).

5.4.1.2.2 Lateral compositional modulation in lower BL

Lateral contrast modulations were observed along [011] direction in the BL below the QWR stacks (referred as lower BL) in sample M1 ($In_{0.53}Ga_{0.47}As$ BL/SL) and M2 ($In_{0.53}Ga_{0.37}Al_{0.10}As$ BL/SL), as indicated by the dashed arrows in

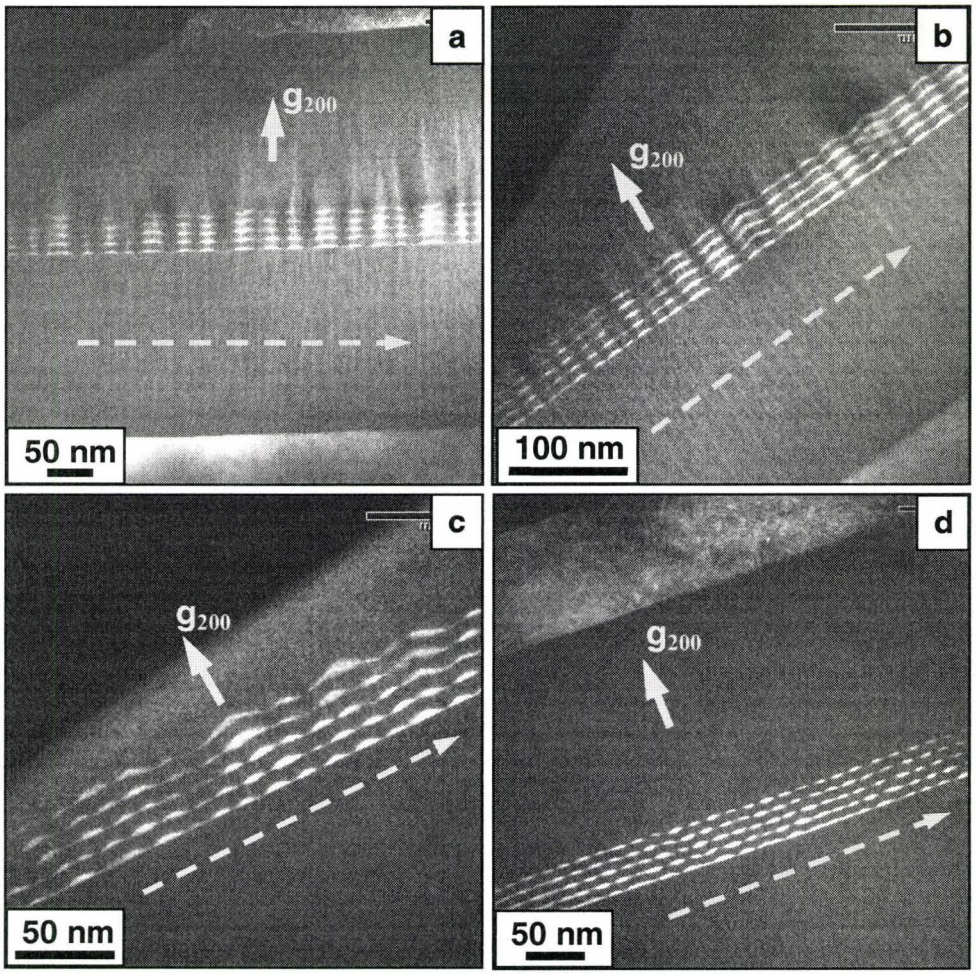

Figure 5-21: DF $\mathbf{g}_{200}$ TEM images of sample (a) M1 ($In_{0.53}Ga_{0.47}As$ BL/SL), (b) M2 ($In_{0.53}Ga_{0.37}Al_{0.10}As$ BL/SL), (c) M3 ($In_{0.53}Ga_{0.17}Al_{0.30}As$ BL/SL) and (d) M4 ($In_{0.52}Al_{0.48}As$ BL/SL). All the images are taken close to $[0\bar{1}1]$ zone axis.

Figures 5-21 (a) and (b) (with the modulations perpendicular to the dashed arrows), respectively. However, such contrast modulations was reduced as the **Al** content in BL/SL was increased to 30% and 48% in sample M3 and M4, respectively, as shown in Figures 5-21 (c) and (d). These lateral contrast variations can be interpreted as the result of the lateral composition modulations

(LCM) of the BL materials. The observed variation of LCM with **Al** content in lower BL can be qualitatively explained by two points. Firstly, from the point of view of kinetics, the **Al** atoms display lower surface mobility than those of **In** and **Ga** at the current growth temperature (Kasu et al. 1993). Therefore, the **Al** atoms tend to distribute uniformly in the MBE-grown ternary or quaternary alloys, as revealed by the EDXS results in Figure 4-19 (a). Secondly, from the thermodynamic arguments, as the **Al** content was increased from 0 to 48 % at the growth temperature for BL/SL of 520°C, the composition of the InGaAlAs alloy lattice matched to InP moves out of the spontaneous decomposition region (Panish et al. 1993). Based on these two considerations, the BL materials with higher **Al** contents tend to form a uniform alloy rather than those displaying LCM at lower **Al** contents.

5.4.1.2.3 QWR shape variation

High magnification DF TEM images for sample M1 ($In_{0.53}Ga_{0.47}As$ BL/SL), M2 ($In_{0.53}Ga_{0.37}Al_{0.10}As$ BL/SL) and M4 ($In_{0.52}Al_{0.48}As$ BL/SL) are shown Figures 5-22 (a)-(c). The shapes of QWRs in the first layer are similar in all the three samples since they all display a convex lens-shaped upper boundary and a flat base (pointed out by dotted arrows) when viewed edge on close to $[0\bar{1}1]$ zone axis. However, the QWRs in the second to fifth layer display different shapes from that in the first layer as the growth continues. The QWRs in sample M1 show a relative flat upper boundary with the base locating on a concave valley of

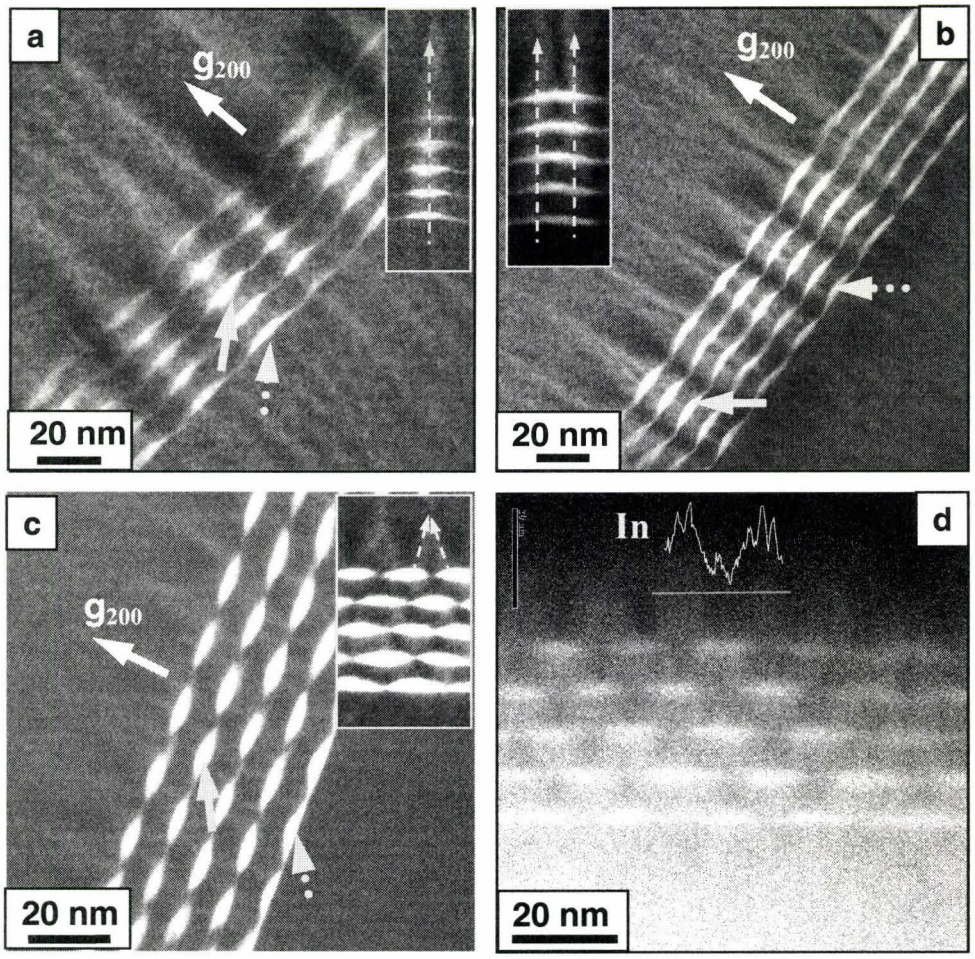

Figure 5-22: (a)-(c) High magnification DF $\mathbf{g}_{200}$ TEM images of sample (a) M1 ($In_{0.53}Ga_{0.47}As$ BL/SL); (b) M2 ($In_{0.53}Ga_{0.37}Al_{0.10}As$ BL/SL); and (c) M4 ($In_{0.52}Al_{0.48}As$ BL/SL). (d) HAADF image of sample M4 and EELS line profile showing the **In** signal variation above one QWR. The inserts in (a)-(c) showing the propagation directions of the **In**-rich stripes through the SLs and upper BL. All the images are taken close to or on $[0\bar{1}1]$ zone axis. The inner angle of the ADF detector for (d) is β =70 mrad.

the SL growth front, as shown in Figure 5-22 (a). For QWRs in sample M2 with $In_{0.53}Ga_{0.37}Al_{0.10}As$ as BLs/SLs, the upper boundary is lens-shaped and the bases of the QWRs in the second to fifth layers become flat or slightly convex

(indicated by the arrow in Figure 5-22 (b)) compared with those in sample M1. As the **Al** content is further increased to 48% for sample M4 in Figure 5-22 (c), QWRs with an elliptical shape are observed in upper layers; i.e. the QWRs are convex on top and concave on bottom. The centers of these QWRs locate in the concave valleys on the growth front of the SLs, which are above the gap between two adjacent QWRs in the underlying layer.

5.4.1.2.4 Indium composition modulation in BL and SL

The brighter stripe-like contrast was observed in SLs and upper BLs for all the samples in Figure 5-22. Besides the variation of the stacking pattern and shape of the QWRs, the change of the propagation orientation of such brighter stripes is also observed, as highlighted by the dotted arrows in the insert images in Figure 5-22. Single brighter stripes extending across the concave centers of the QWRs were observed for sample M1 ($In_{0.53}Ga_{0.47}As$ BL/SL), as shown in the insert image in Figure 5-22 (a) and Figure 5-21 (a). A splitting of the brighter stripes into multiple-branches (mostly with two stripes) extending above the side walls in the QWR stacks was observed in sample M2 ($In_{0.53}Ga_{0.37}Al_{0.10}As$ BL/SL) as shown in Figure 5-22 (b) and the insert image. In sample M4 ($In_{0.52}Al_{0.48}As$ BL/SL), a weaker "brighter-stripe like" contrast modulation is observed than those in sample M1 and M2, as can be seen by comparing the contrasts and propagation depths of these brighter stripes in the upper BLs in Figures 5-21 (a), (b) and (d). Converging brighter stripe pairs (insert image acquired with longer

exposure time in Figure 5-22 (c)) were observed in the upper BL directly above the gap between two adjacent QWRs.

As has been shown in Chapter 4, the brighter stripes present in $In_{0.53}Ga_{0.37}Al_{0.10}As$ BL are interpreted as **In**-rich regions based on EELS SI results in Figure 4-18. For $In_{0.52}Al_{0.48}As$, an EELS line profile (Figure 5-22 (d)), taken in the upper BL across both the area directly above one QWR and that above the gap between two adjacent QWRs, shows the coincidence between the peaks of **In** signal and the position of the brighter stripes. Also, based on the calculations in **Appendix A** for $In_{0.53}Ga_{0.47}As$ ternary alloy, it is reasonable to correlate the brighter contrast observed in Figure 5-22 (a) with the higher local **In** composition in the $In_{0.53}Ga_{0.47}As$ BLs/SLs since an **In** modulation with an amplitude about 32.6% (refer to **Appendix A**) is not expected comparing with the maximal reported value of 20% in literature (Pearson et al. 2004) for highly strained GaAs/InAs short period superlattice. Therefore, the stripes present in BLs /SLs in all the samples in Figure 5-22 are interpreted as the **In**-rich regions from the local composition modulations.

As discussed in Chapter 4, the **In** composition modulation in BL/SL above QWR layers is a one dimensional phenomenon along [011] direction. The **In** composition modulations observed in Figure 5-22 also possess this feature as reflected by the relatively uniform contrast observed in the upper BL in DF

images taken close to [011] zone axis, as shown in Figure 5-23. Along the dashed arrows, no short-period composition modulation as those shown in Figure 5-22 is detected for either sample M1 ($In_{0.53}Ga_{0.47}As$ BL/SL) or M4 ($In_{0.52}Al_{0.48}As$ BL/SL) along[$0\bar{1}1$] direction.

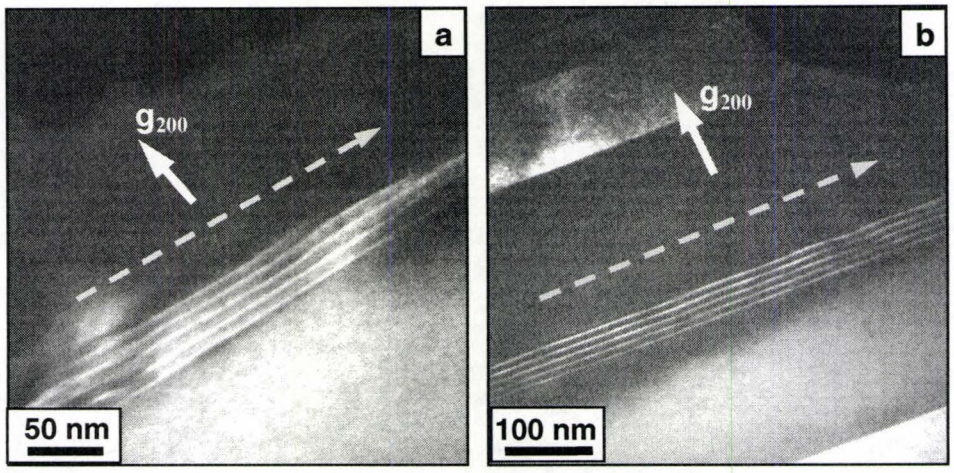

Figure 5-23: DF $\mathbf{g}_{200}$ TEM images of sample (a) M1 ($In_{0.53}Ga_{0.47}As$ BL/SL); and (b) M4 ($In_{0.52}Al_{0.48}As$ BL/SL), taken close to [011] zone axis.

It is believed that the **In** composition modulation in SLs or upper BL is activated by the the QWRs, which is the case for the single layer sample shown in Chapter 4. This statement is supported by two experimental observations through a comparison of the contrast in the upper and lower BLs in the multilayer samples. Firstly, the **In**-rich stripes show a smaller period along [011] direction in the lower BL than that in the upper BL, as shown in Figures 5-21 (a) and (b) for sample M1 ($In_{0.53}Ga_{0.47}As$ BL/SL) and M2 ($In_{0.53}Ga_{0.37}Al_{0.10}As$ BL/SL), respectively. Secondly, the converging **In**-rich stripes in sample M4

($In_{0.52}Al_{0.48}As$ BL/SL) were observed only in the upper BL close to the fifth QWR layer but not in the lower BL just below the first QWR layer, as shown in Figures 5-21(d) and 5-22 (c).

5.4.1.2.5 Defects and elastic field

The defects are viewed through BF TEM images with $\mathbf{g}_{02\bar{2}}$ taken close to $[0\bar{1}1]$ zone axis, as shown in Figure 5-24. Misfit dislocations (pointed out by the dotted arrows) extending from the QWR layers to upper BL are observed in samples M1 ($In_{0.53}Ga_{0.47}As$ BL/SL) and M2 ($In_{0.53}Ga_{0.37}Al_{0.10}As$ BL/SL). However, no such defects are found in samples M3 ($In_{0.53}Ga_{0.17}Al_{0.30}As$ BL/SL) and M4 ($In_{0.52}Al_{0.48}As$ BL/SL). The most obvious difference is that the vertically aligned QWR stacks were formed in samples M1 and M2, while the dominant anti-correlated stacks were observed in samples M3 and M4. Since the misfit dislocations arises from the in-plane strain in the heteroepitaxy (Ohring 2002), it is worth studying the strain field in QWR layers with different alignment patterns through FE simulations, which will be shown in Chapter 7.

In addition, different lateral contrast patterns along [011] direction were observed. In samples M1 and M2 (Figures 5-24 (a) and (b)), butterfly-like contrast pattern appeared in the QWR regions, while dotted (cross-hatched) patterns were observed in QWR layers of samples M3 and M4 (Figures 5-24 (c) and (d)). The contrast patterns in samples M1 and M2 are similar to those

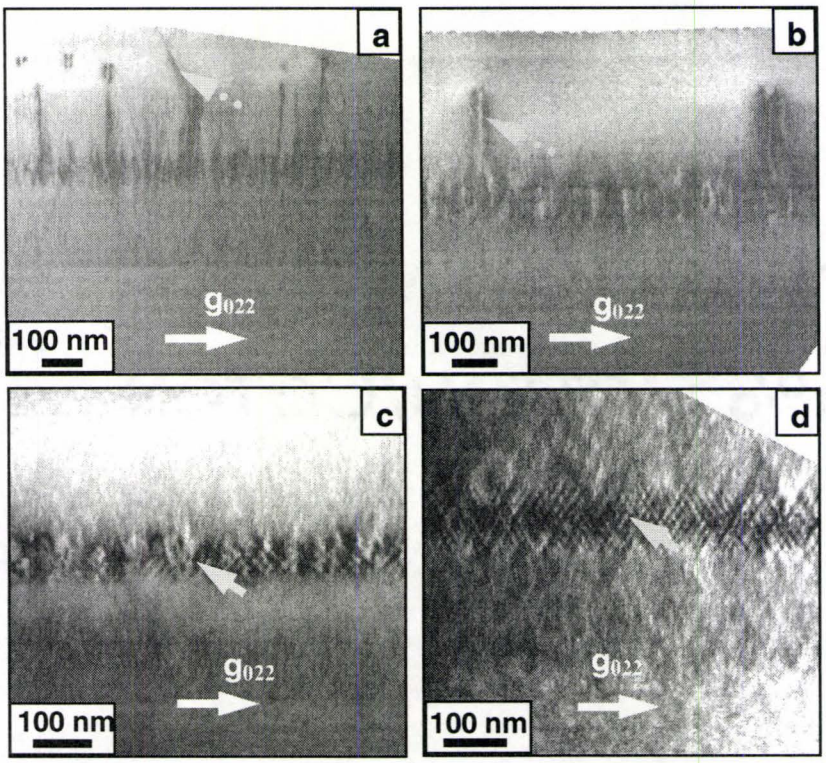

Figure 5-24: BF $\mathbf{g}_{022}$ TEM images of sample (a) M1 ($In_{0.53}Ga_{0.47}As$ BL/SL); (b) M2 ($In_{0.53}Ga_{0.37}Al_{0.10}As$ BL/SL); (c) M3 ($In_{0.53}Ga_{0.17}Al_{0.30}As$ BL/SL); and (d) M4 ($In_{0.52}Al_{0.48}As$ BL/SL). All the images are taken close to $[0\bar{1}1]$ zone axis.

observed in single layer QWR (Figure 4-11 (c)) and vertically stacked QWRs (Figures 5-8 (b)-(d)). In Chapter 7, we will show that the contrast pattern observed in M1 and M2 arises from the overlap of the displacement field of different QWR layers from the correlated alignment, while the dotted (cross-hatched) pattern observed in samples M3 and M4 is from the cancellation of displacement field between the anti-correlated QWRs.

5.4.1.2.6 Summary of TEM observations

In summary, the shape and stacking pattern variations of the multilayer QWRs have been observed in samples with different **Al** contents in BLs/SLs. Firstly, correlated QWR stacks were observed in samples M1 ($In_{0.53}Ga_{0.47}As$ BL/SL) and M2 ($In_{0.53}Ga_{0.37}Al_{0.10}As$ BL/SL), while dominant anti-correlated alignment patterns were found in samples M3 ($In_{0.53}Ga_{0.17}Al_{0.30}As$ BL/SL) and M4 ($In_{0.52}Al_{0.48}As$ BL/SL). Secondly, one dimensional **In** composition modulations with different propagating orientations were observed in samples M1 through M4, as the **Al** content in BLs/SLs was increased from 0 to 48%. The origin of these experimental observations will be investigated by calculating the chemical potential density and displacement/strain field with FE modeling in Chapter 7.

5.4.2 Optical characterizations

The PL spectra from sample M2 ($In_{0.53}Ga_{0.37}Al_{0.10}As$ BL/SL), M3 ($In_{0.53}Ga_{0.17}Al_{0.30}As$ BL/SL) and M4 ($In_{0.52}Al_{0.48}As$ BL/SL) at 14 and 77 K are shown in Figures 5-25 (a) and (b), respectively. No PL signal was detected from sample M1 ($In_{0.53}Ga_{0.47}As$ BL/SL) due to the high density of dislocations (Figure 5-24 (a)), which acted as the nonradiative centers (Petroff et al. 1980) to trap the excited carriers. The PL signal from sample M3 can be deconvolved into two components **P1** (shorter wavelength) and **P2** (longer wavelength) from two different QWR families in Figure 5-21 (c). As discussed in section 5.3, **P1** (**P2**) comes from the radiative recombination between electrons and holes within the QWRs with smaller (larger) height. A blue-shift of the PL wavelength is

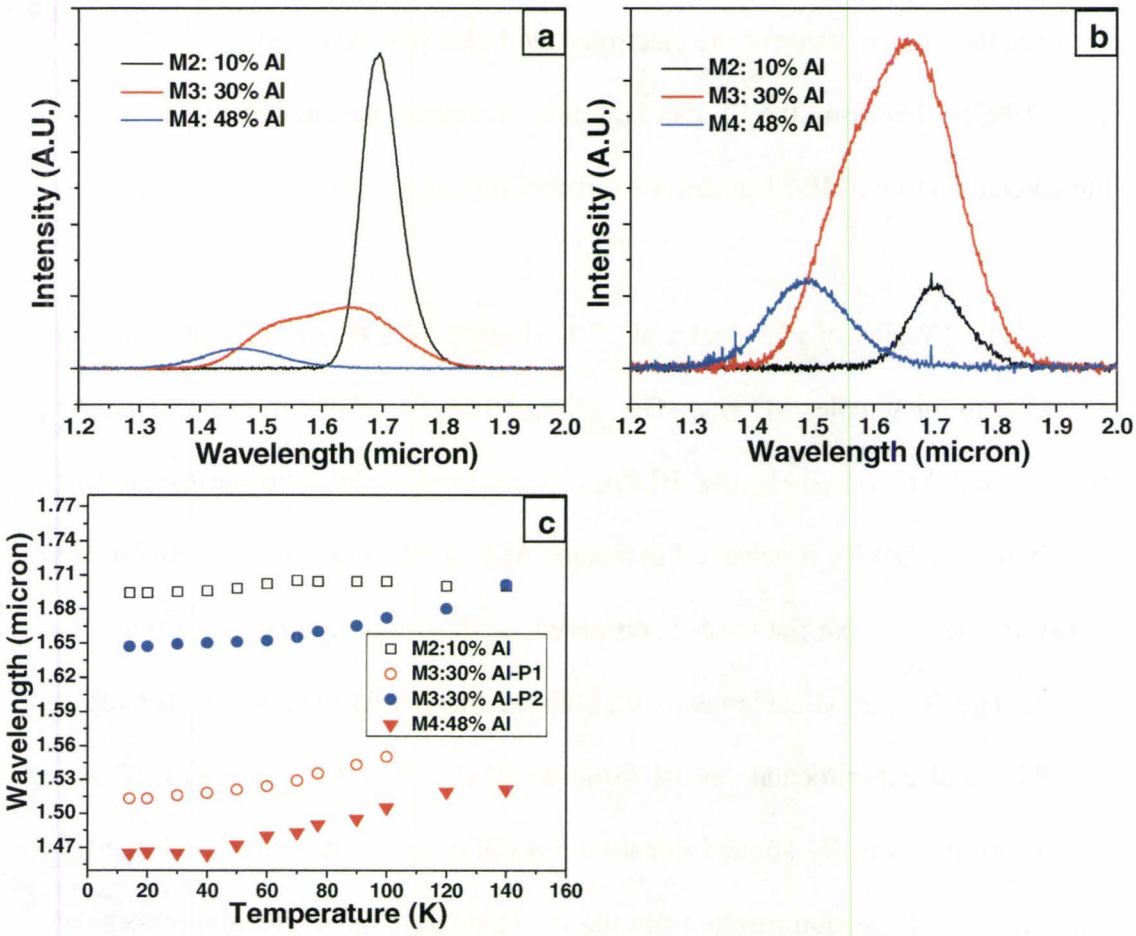

Figure 5-25: (a) and (b) PL spectra of sample M2 ($In_{0.53}Ga_{0.37}Al_{0.10}As$ BL/SL), M3 ($In_{0.53}Ga_{0.17}Al_{0.30}As$ BL/SL) and M4 ($In_{0.53}Al_{0.48}As$ BL/SL) at 14 K and 77 K, respectively. (c) Plot of the wavelength as a function of temperature.

observed as the **Al** content increased in the BLs/SLs, as shown by the plot of wavelength versus temperature in Figure 5-25 (c). This trend is in good agreement with the observations in single layer QWRs embedded between BLs with 10 % and 20 % **Al,** as shown in Figure 4-9. As stated in Chapter 4, the detailed band discontinuities of valence and conduction bands between the QWR layers and

SLs/BLs increases with the **Al** content, resulting in a larger energy separation between the ground states of the electrons and holes (Ustinov et al. 1998; Tournié et al. 1993). Therefore, the PL can be tuned to shorter wavelength by increasing the **Al** content in the BL/SL materials surrounding the QWRs.

The FWHM of PL spectra at 77 K (Figure 5-25 (b)) is 113 nm, 181 nm and 153 nm for samples M2 ($In_{0.53}Ga_{0.37}Al_{0.10}As$ BL/SL), M3 ($In_{0.53}Ga_{0.17}Al_{0.30}As$ BL/SL) and M4 ($In_{0.52}Al_{0.48}As$ BL/SL), respectively. Thus the narrowest size distribution of QWRs is achieved in sample M2, in which a correlated alignment of QWRs with relative flat bases is observed, as shown in Figures 5-21 (b) and 5-22 (b). This is in good agreement with both the theoretical predictions (Tersoff et al. 1996) and experimental results (Solomn et al. 1997) for the improved size uniformity in vertically aligned quantum dot (QD) stacks. It is proposed that the narrower size dispersion results from the modulation of the nucleation process of the QDs in upper layers by the strain field from the underlying QDs, which is imposed on the flat SL growth front directly above. Similar to the case for QD stacks, the improved size homogeneity in QWR stacks in sample M2 was also proposed as a result from the strain field modulated nucleation of QWRs in upper layers when the growth front of the SL is flat.

5.5 Summary

The dependence of the structural and optical properties of the multilayer QWRs on the spacer layer thickness, the QWR layer thickness and the **Al** content in the BLs/SLs has been investigated. The main findings include:

1. The alignment pattern variation of QWR stacks.

The vertical alignment of QWRs were observed with the $In_{0.53}Ga_{0.27}Al_{0.20}As$ SL thickness at 8 nm and QWR layer thickness fixed at 4 ML. However, this correlation became less prominent as the SL thickness was increased to 15 and 25 nm. With the $In_{0.53}Ga_{0.27}Al_{0.20}As$ SL thickness fixed at 8 nm, vertical stacks of QWRs were achieved when the QWR layer thickness was 4, 5 and 7 ML. When the thicknesses of SL and QWR layer were fixed at 8 nm and 5 ML, respectively, vertically aligned QWR stacks were observed in the samples with the **Al** content of 0 and 10% in BLs/SLs. A transition from correlated to anti-correlated QWRs occurred as the **Al** content in BLs/SLs was increased to 30% and 48%.

2. Optical properties

Generally, the PL emission from multilayer QWRs can be tuned towards longer wavelength through (1) the reduction of SL thickness; (2) the increase of QWR thickness and (3) the reduction of **Al** content in BLs/SLs. The multiple-components detected in the PL spectra of specific samples were attributed to carrier recombination in the ground states from QWRs belonging to different

height families. Transfer of carriers from QWRs with smaller height to those with larger height is suggested to be responsible for the variation of each component with temperature and excitation laser powers.

Chapter 6

Post-growth treatments of the multilayer quantum wire samples

Overview

As mentioned in previous chapters, the purpose of growing multilayer QWR structures is to provide potential candidates for optoelectronic devices that can operate at room temperature (RT), such as the 1.55 μm long wavelength laser for telecommunications (Kaminow et al. 2002) or broadband emitters with the emission wavelength over the optical windows between 1.6 and 2.0 μm (Ooi et. al. 2008). However, the PL measurements shown in Chapters 4 and 5 revealed that the PL signals were completely quenched above 200 K in both single and multilayer QWR samples.

In this chapter, post growth treatments, which include the removal of the top **As**-containing layers through chemical etching and rapid thermal annealing (RTA), were performed on the selected multilayer QWR samples in order to obtain detectable PL signals at RT. The standards for sample selection are: (1) a narrow PL line-width, which means a relatively narrow size distribution in that specimen, is observed in PL spectra; and (2) no dislocations should be observed in

the cross-sectional TEM images. Based on these criteria, sample L2 (8 nm $In_{0.53}Ga_{0.27}Al_{0.20}As$ SL, 5 ML InAs) and K3 (25 nm $In_{0.53}Ga_{0.27}Al_{0.20}As$ SL, 4 ML InAs) in Table 2-2 were selected for post growth treatments based on the PL measurements (Figures 5-4 (a) and 9 (a)) and TEM observations (Figure 5-8 (c)).

6.1 Removal of the top As-containing layers

The top layer of free-standing InAs wires and the $In_{0.53}Ga_{0.27}Al_{0.20}As$ layer lying between the top InAs layer and InP layer, as shown by the dashed rectangular box in Figure 6-1, were removed through chemical etching. The purpose of this step is

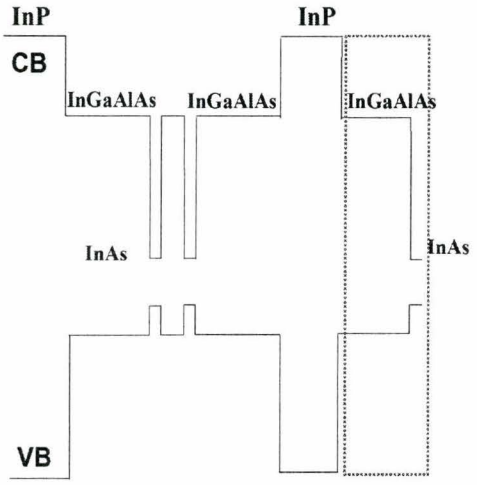

Figure 6-1: The schematic diagram showing the band alignment in the QWR structure along the growth direction and the etched top **As**-containing layers.

to increase the PL intensity from the buried QWR stacks since a flatter surface than that in the as-grown sample can be produced after removal of the free-standing InAs wires. Thus, the effect of the photon scattering by the rough surface will be suppressed.

6.1.1. Etching procedures

The samples were soaked in an etching solution of H_3PO_4, H_2O_2 and H_2O (volume ratio 3:1:40) for 1 minute. The etched samples were then cleaned with distilled water to remove the residual etching solution.

6.1.2. Structural properties after etching

The after-etching cross-sectional TEM image of sample L2 (8 nm $In_{0.53}Ga_{0.27}Al_{0.20}As$ SL, 5 ML InAs) is displayed in Figure 6-2. The top InP layer is smooth and has not suffered any etching since it was still 100 nm in thickness (Figure 6-2), which is the same as the as-grown sample.

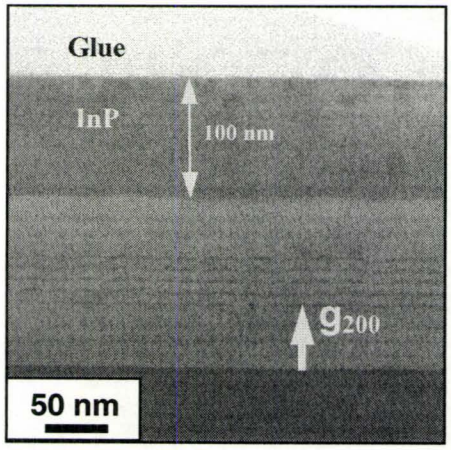

Figure 6-2: Cross-sectional BF TEM image ($\mathbf{g}_{200}$) of sample L2 (8 nm $In_{0.53}Ga_{0.27}Al_{0.20}As$ SL, 5 ML InAs) after removal of the top InAs and $In_{0.53}Ga_{0.27}Al_{0.20}As$ layers through chemical etching. The images are taken close to $[0\bar{1}1]$ zone axis.

6.1.3 Optical properties after etching

The PL spectra taken at 77 K for the as-grown and etched samples of sample L2 (8 nm $In_{0.53}Ga_{0.27}Al_{0.20}As$ SL, 5 ML InAs) are shown in Figure 6-3 (a). The PL

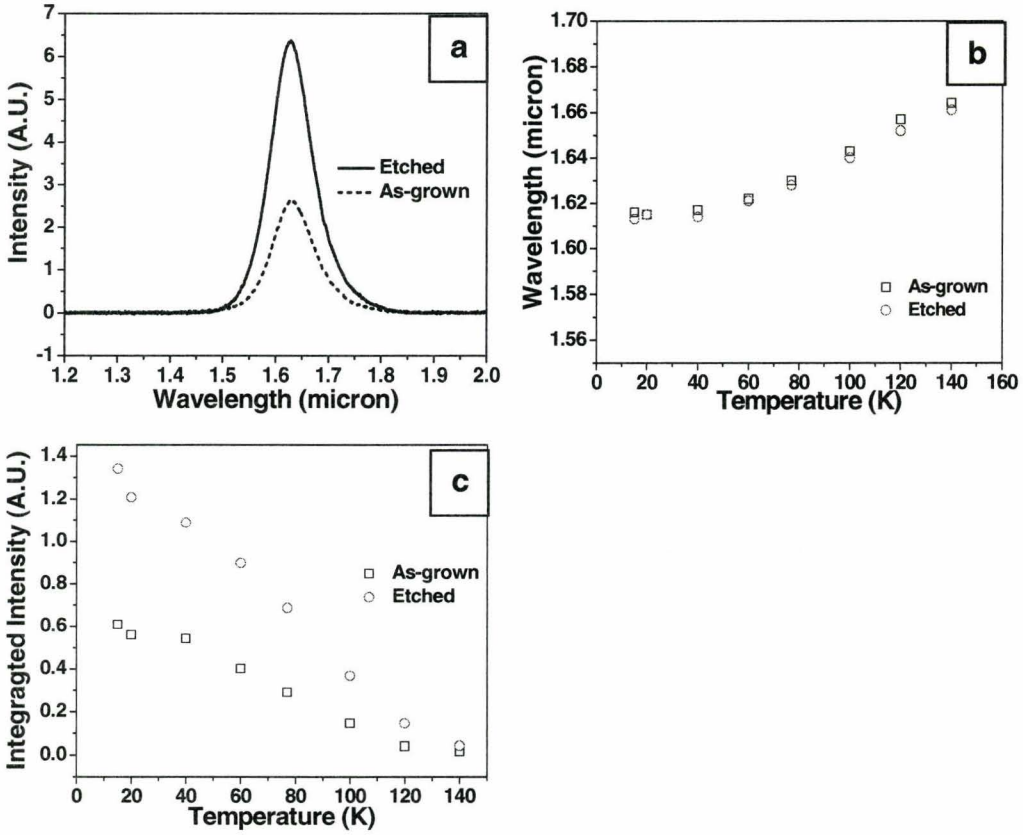

Figure 6-3: Comparisons between the optical properties of the as-grown and etched samples of L2 (8 nm $In_{0.53}Ga_{0.27}Al_{0.20}As$ SL, 5 ML InAs) (a) PL spectra at 77 K; (b) wavelength versus temperature; and (c) integrated intensity versus temperature.

wavelengths versus temperature plots were identical for both samples within the temperature range from 14 to 140 K, as shown in Figure 6-3 (b). However, the integrated PL intensity detected from the etched sample was twice of that from the as-grown one. For both samples, the intensity decreases with increasing

temperature and is quenched at 140 K, as is seen in Figure 6-3 (c). RT PL emission was not obtained at this stage.

6.2 Rapid thermal annealing

Rapid thermal annealing (RTA) was performed for two reasons. Firstly, the density of point defects around QWRs could be reduced upon RTA at relatively low temperature (Lochtefeld et al. 1996; Djie et al. 2006), resulting in higher PL intensity than the as-grown sample. Secondly, annealing of the samples at higher temperatures could activate the intermixing between group III elements in our nominal InAs QWRs/ $In_{0.53}Ga_{0.27}Al_{0.20}As$ system, resulting in a blue-shift (Djie et al. 2008) of the PL wavelength from the as-grown sample.

Chemical etching was subsequently carried out on the annealed samples according to the procedures listed in section 6.1.1 to get enhanced PL signals at RT with the desired wavelength for potential device applications.

6.2.1 Sample preparation

The samples were capped with 100 nm SiO_2 by plasma enhanced chemical vapor deposition at 300 °C in order to enhance the intermixing of group III elements through generating additional group III defects at the interfaces between top As-containing layers and SiO_2 layer (Hulko et al. 2008) upon RTA.

6.2.2 Annealing and etching

The samples were annealed in an enclosed graphite boat for 30s within a nitrogen atmosphere. They were placed between Si proximity caps since the best PL results were expected through this treatment compared with capping of GaAs or InP wafers (Hulko et al. 2008; Hulko et al. 2006).

Four samples from sample L2 (8 nm $In_{0.53}Ga_{0.27}Al_{0.20}As$ SL, 5 ML InAs) with SiO_2 cap were annealed at 650°C, 700°C, 750°C and 800°C, respectively. Two samples from sample K3 (25 nm $In_{0.53}Ga_{0.27}Al_{0.20}As$ SL, 4 ML InAs) with SiO_2 cap were annealed at 700°C and 750°C, respectively.

Chemical etching was performed for the annealed samples before the PL measurements. All the annealed samples with SiO_2 cap were firstly soaked in buffered HF solution (volume ratio $HF:H_2O=1:10$) for 2 minutes to remove the SiO_2 cap followed by the removal of the top InAs and $In_{0.53}Ga_{0.27}Al_{0.20}As$ layers according to the procedures shown in section 6.1.1.

6.2.3 Structural properties after annealing

The cross-sectional TEM images showing the structural features of sample L2 (8 nm $In_{0.53}Ga_{0.27}Al_{0.20}As$ SL, 5 ML InAs) after annealing are shown in Figure 6-4. The images from samples annealed at 700°C and 800°C are displayed as typical examples since the morphology variation in samples annealed at 650°C and 750°C should be less significant than for those annealed at 700°C and 800°C,

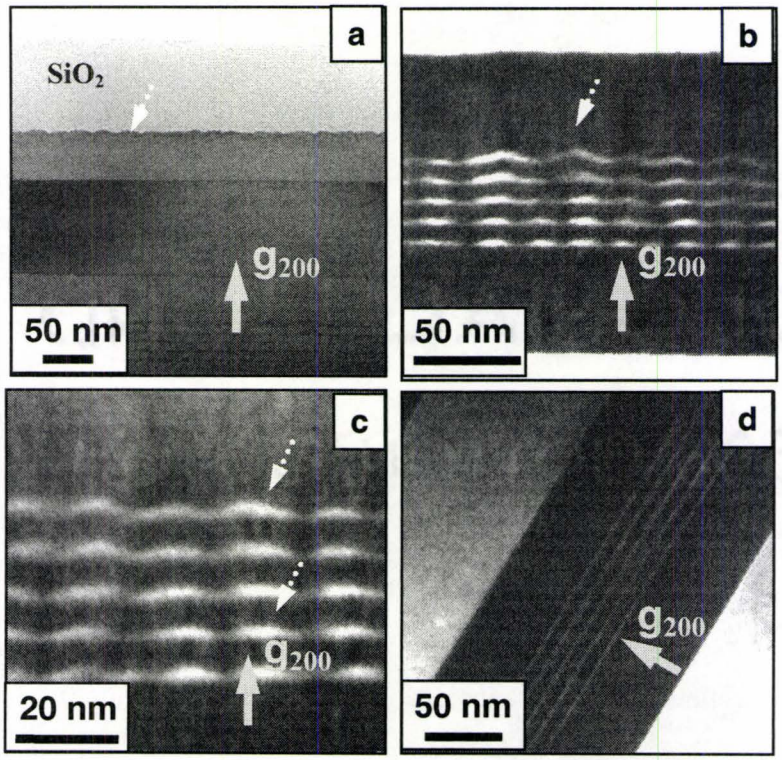

Figure 6-4: Cross-sectional TEM images with $\mathbf{g_{200}}$ for sample L2 (8 nm $In_{0.53}Ga_{0.27}Al_{0.20}As$ SL, 5 ML InAs) annealed at (a) and (b) 700°C; (c) and (d) 800°C. (a) BF image showing the sample capped with SiO_2 layer. (b),(c) and (d) are DF images showing the shape of QWRs after annealing. (a), (b) and (c) were taken close to $[0\bar{1}1]$ zone axis while (d) close to [011] zone axis.

respectively. After annealing at 700°C, the lens shape was preserved in the InAs free-standing nanostructures viewed close to $[0\bar{1}1]$ zone axis, as revealed by the ripple and rough surface feature (indicated by the dotted arrow) underneath the SiO_2 cap layer in Figure 6-4 (a). The lens shape was also preserved for the capped InAs layers, as shown in Figure 6-4 (b). With the annealing temperature increased to 800°C, the anisotropic wire-like morphologies were still observed as confirmed

by studying Figure 6-4 (c) and (d) when the QWRs were viewed edge-on and along the length, respectively. Moreover, the vertical alignment of QWRs and the **In** composition modulation (indicated by the dotted arrows) in the BL/SLs, which also appeared in the as-grown sample (Figure 5-7 (c)), were detected in the annealed samples, as shown in Figure 6-4 (b) and (c). We can therefore conclude that no significant morphology variation is introduced to the multilayer QWRs by the current RTA treatments.

6.2.4 Optical properties after annealing and etching

6.2.4.1 PL from sample L2

The optical properties for the annealed plus etched and etched-only samples of sample L2 (8 nm $In_{0.53}Ga_{0.27}Al_{0.20}As$ SL, 5 ML InAs) are shown in Figure 6-5. The wavelength of the PL spectra at 77 K does not change significantly from the etched-only sample for the samples annealed at temperatures less than 800°C, as observed in Figure 6-5 (a). In terms of the PL intensity, RT PL signals were detected in samples annealed at 700°C and above, as shown in Figure 6-5 (c) and (d). While the PL signal of the etched-only and 650°C annealed samples quenched out at 200 K and 260 K, respectively. The RT PL wavelengths of 1.72 μm, 1.70 μm and 1.63 μm were observed for the 700°C, 750°C and 800°C RTA samples, respectively. The variation of wavelength with temperature, between 20 K and 300 K, for different samples are plotted in Figure 6-5 (b), from which similar wavelengths are detected in the etched-only sample and those annealed at

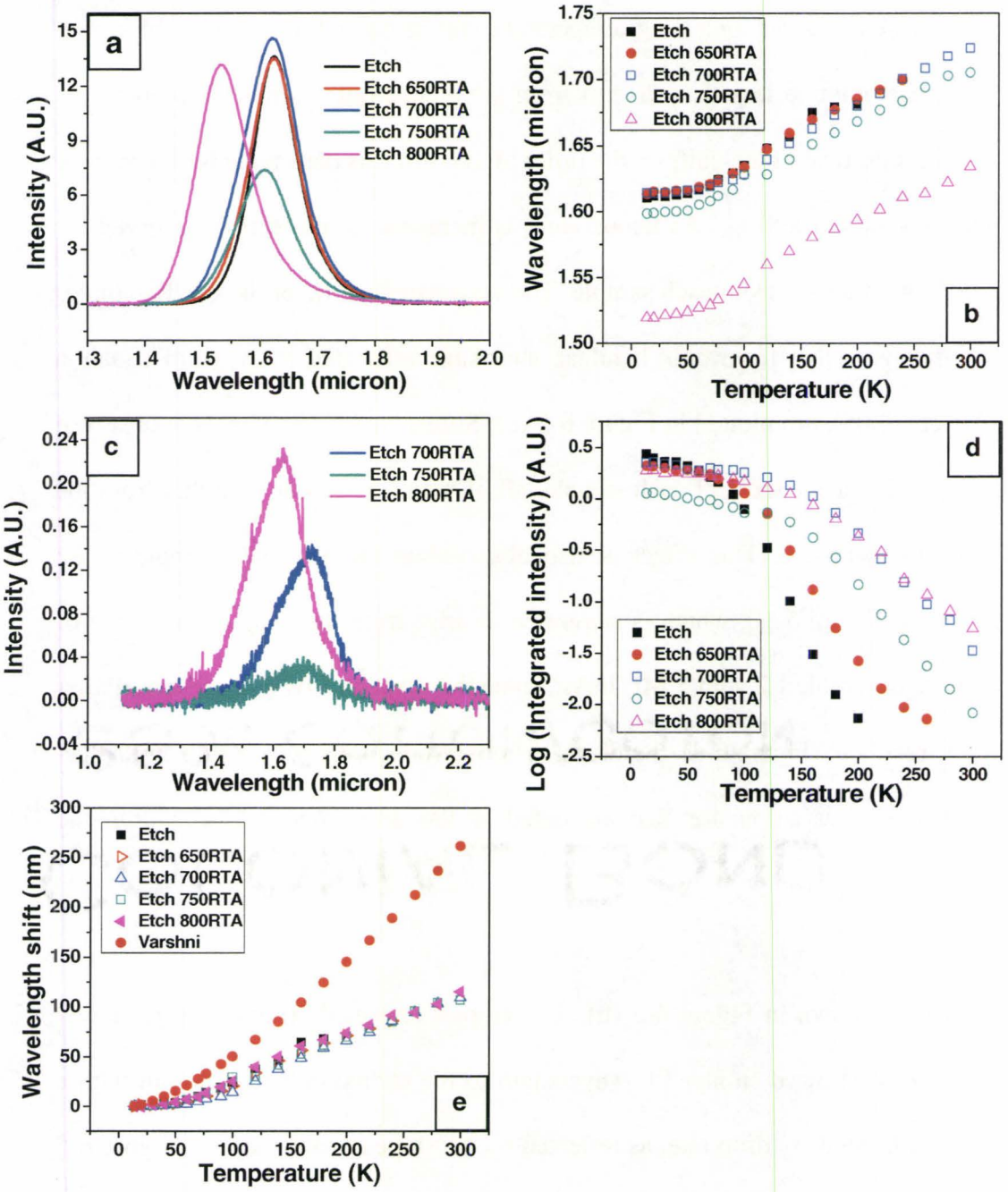

Figure 6-5: Optical properties of the annealed plus etched and etched-only samples of L2 (8 nm $In_{0.53}Ga_{0.27}Al_{0.20}As$ SL, 5 ML InAs). (a) PL spectra at 77 K; (b) wavelength versus temperature; (c) PL spectra at 300 K; (d) integrated intensity variations versus temperature showing the different rates of decline for the PL intensity from each sample; and (e) the wavelength shift versus temperature.

650 and 700°C over the whole temperature range where detectable PL signals were present. As the annealing temperature was increased to 750°C, a blue-shift with an amplitude less than 20 nm from the etched-only sample was observed, while a significant blue-shift on the order of 100 nm was detected after the sample was annealed at 800°C. As temperature is increased, a red-shift is observed for the PL wavelength from each sample. The wavelength shifts of the QWR samples, together with that from bulk bandgap shrinkage estimated by Varshni equation (Adachi 2005), are plotted in Figure 6-5 (e). Similar red-shift rates were observed for the PL wavelengths of each sample, all of which is slower than that from the bandgap shrinkage. This effect is also observed in the as-grown sample of L2 shown in Figure 5-10, which is suggested to arise from the deep energy level of carriers in sample L2 with 5 ML InAs. Since the shape of QWR is preserved after RTA treatment (Figure 6-4), therefore, the observed slower wavelength shifts than the bandgap variation are also attributed to the deep energy level within the QWRs.

As shown in Figure 6-5 (b), the samples annealed at temperatures lower than 800°C showed similar PL wavelength to the etched only sample but with a slower PL intensity drop rate, as reflected by the slope of each curve in Figure 6-5 (d). These results indicated the intermixing of group III elements between QWRs and SLs/BL did not occur since no significant blue-shift of PL wavelength between the annealed and etched only samples was observed. Thus, RTA at

temperatures lower than 800°C played the role of reducing the density of point defects (not detected within the TEM resolution limit), which subsequently worked as the non-radiative recombination centers (Petroff et al. 1980) responsible for the quench of PL intensity with temperature. However, these point defects did not contribute to the intermixing because they are suggested to be trapped preferentially around the interfaces between QWRs and SLs/BLs due to the higher stress (Djie et al. 2006) than other areas. Thus, the reduction of the point defects density (Lochtefeld et al. 1996; Djie et al. 2006) around QWRs upon RTA resulted in less reduction of the PL intensity in the annealed samples than the etched-only one, as observed in Figure 6-5 (d).

For the sample annealed at 800°C, an intermixing between group III elements in QWRs and SLs is believed to occur because of the 100 nm blue-shift of the PL wavelength from that of the etched-only sample. Also, the reduction of the defect density is suggested to occur since RT PL signal was observed in Figures 6-5 (c) and (d).

6.2.4.2 PL from sample K3

The PL spectra measured at 77 K from sample K3 (25 nm $In_{0.53}Ga_{0.27}Al_{0.20}As$ SL, 4 ML InAs), both as-grown and annealed (700°C and 750°C) are shown in Figure 6-6. The wavelengths at 77 K are 1.51 μm, 1.49 μm and 1.46 μm for the as-grown, 700°C and 750°C annealed samples, respectively. Thus, the blue-shift

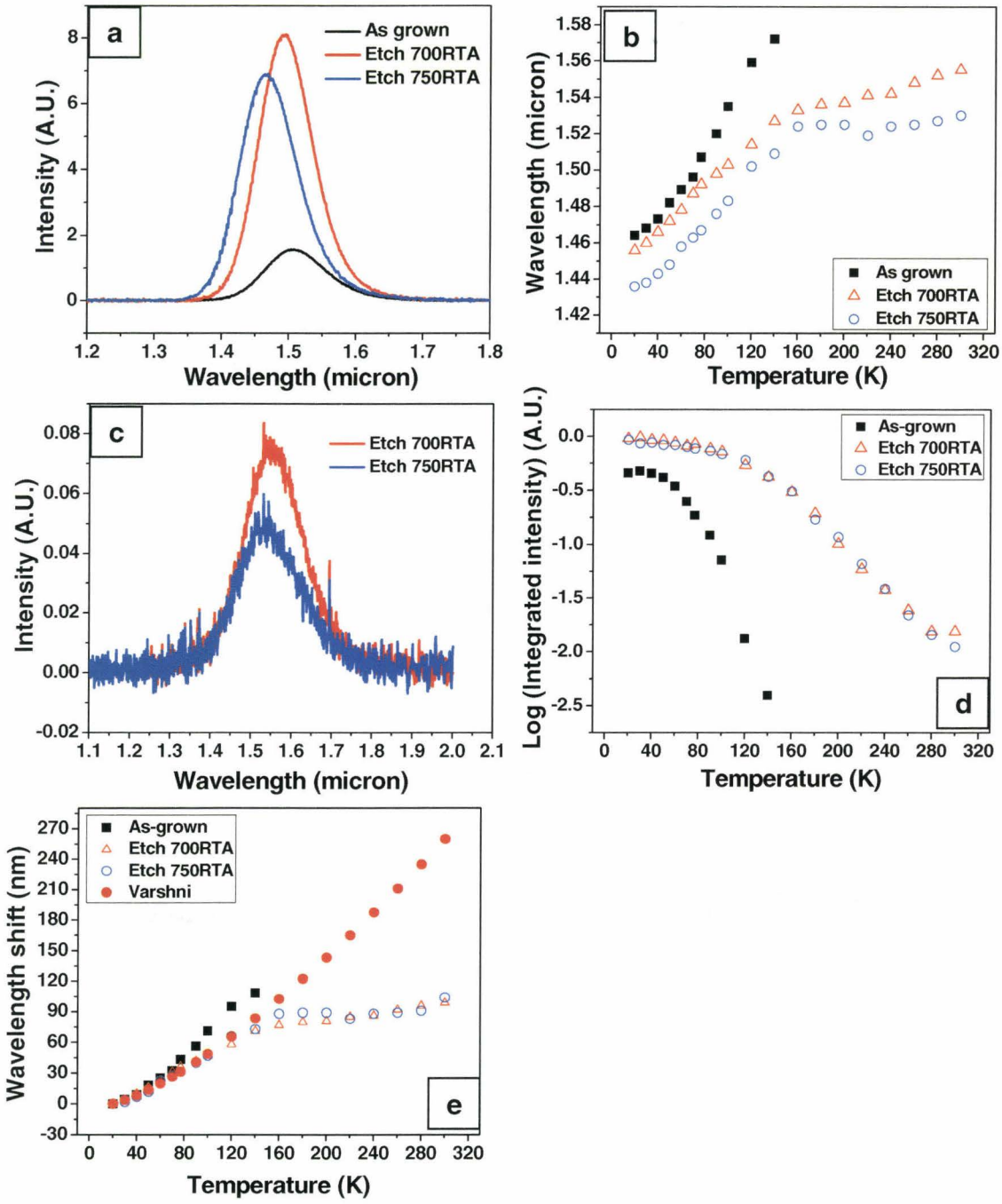

Figure 6-6: Optical properties of the as-grown and annealed samples of K3 (25 nm $In_{0.53}Ga_{0.27}Al_{0.20}As$ BL, 4 ML InAs) (a) PL spectra at 77 K; (b) wavelength versus temperature; (c) PL spectra at 300 K; (d) integrated intensity versus temperature showing the different rates of decline for the PL intensity from each sample; and (e) the wavelength shift versus temperature.

increases with the annealing temperature, as shown in Figures 6-6 (a) and (b). Also, for the annealed samples, the PL was measurable up to RT (Figure 6-6 (c)). The plots of wavelength and PL intensity versus temperature are shown in Figures 6-6 (b) and (d), respectively. The results suggest that the RTA at 700°C and 750°C for sample K3 produced a reduction of point defects present at the interface of QWR/SL, leading to the increased intensity, and the presence of some intermixing between the QWRs and surrounding $In_{0.53}Ga_{0.27}Al_{0.20}As$ layers results in the observed blue-shifts.

Another feature worth noting is the improved temperature-insensitivity of the PL wavelength in the annealed samples. The wavelength shift of each sample is compared with that from bandgap shrinkage estimated on Varshni equation (Adachi 2005), as shown in Figure 6-6 (e). At the temperatures lower than 140 K, a faster red-shift rate of the PL wavelength is observed for the as-grown sample (has been observed and discussed in Chapter 5), while those from the annealed samples agree well with the bandgap variation. Changes of curve slope were observed in the wavelength-temperature plots (Figure 6-6 (b)) at 160 K, above which the wavelength becomes much less dependent on temperature for the annealed samples. The observed total red-shifts of the PL wavelength are 22 nm and 6 nm for the samples annealed at 700°C and 750°C, respectively from 160 K to 300 K; whereas the Varshni equation would predict a red-shift of 157 nm over this temperature range. The mechanism responsible for the temperature

insensitive PL emission in QWRs structure is not clear. It is usually attributed to the existence of the specific multi-axial strain in the QWRs, which balances the thermal expansion of the lattice with temperature (Wohlert et al. 1996; Chou 2000). We proposed that the strain states around the QWRs in the annealed samples are different from those in the as-grown sample due to point defect reduction and group III elements intermixing after RTA, both of which will modify the strain distribution around the QWRs. Therefore, the improved temperature insensitivity of PL wavelength above 160 K in the annealed samples from K3 is suggested to arise from the introduction of the specific multi-axial strain field around QWRs through annealing. Also, it should be noted that this temperature-independent PL emission was not observed in the samples annealed at 700 and 750°C for L2, as shown in Figures 6-5 (b) and (e). The sizes of the capped QWRs are larger in sample L2 than those in sample K3, as discussed in Chapter 5. The RTA treatment procedures (temperature and time) were the same for both samples, thus it may requires even longer annealing time to change the strain state around large QWRs in sample L2. Therefore, it is proposed that the different optical behavior of samples L2 and K3 is due to the different strain state around QWRs after RTA.

At RT, the PL wavelengths are 1.55 μm and 1.53 μm for the 700°C and 750°C annealed samples, respectively. As mentioned above, the 1.55 μm emission at RT is of great technical importance for telecommunications. Therefore, the

sample K3 containing five layers of 4 ML InAs QWRs with 25 nm $In_{0.53}Ga_{0.27}Al_{0.20}As$ SLs could potentially be used to fabricate a 1.55 μm temperature-insensitive laser-based devices, operating at normal operating ambient, after treating the as-grown sample with a RTA at 700°C for 30 s.

The morphology of the InAs layers after RTA at 700°C is shown in the cross-sectional TEM images in Figure 6-7. When viewed close to $[0\bar{1}1]$ zone axis,

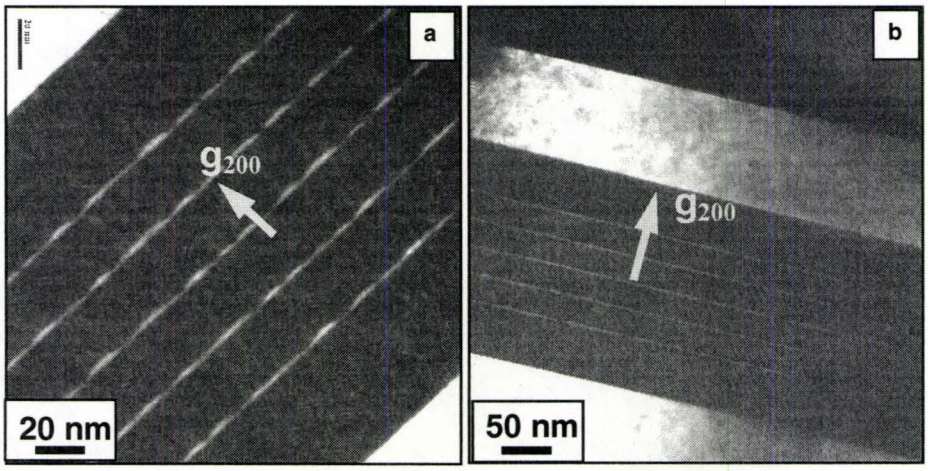

Figure 6-7: Cross-sectional DF TEM images with $\mathbf{g_{200}}$ for sample K3 (25 nm $In_{0.53}Ga_{0.27}Al_{0.20}As$ BL, 4 ML InAs) annealed at 700°C, (a) a micrograph taken close to $[0\bar{1}1]$ zone axis; and (b) close to [011] zone axis.

the randomly distributed QWRs display similar dimensions as those observed in the as-grown sample (Figure 5-2 (d)). Also, when viewed close to [011] zone axis, the "wire-like" contrast was observed in the InAs layers. Therefore, the QWR morphology is preserved after sample K3 was annealed at 700°C for 30 s.

6.3 Summary

Post growth treatments including RTA and chemical etching were performed on two multilayer QWR samples. PL signals were successfully improved and room temperature PL signal peaked at 1.53 to 1.72 μm were obtained through the reduction of the point defects and intermixing of group III elements between the InAs QWRs and surrounding $In_{0.53}Ga_{0.27}Al_{0.20}As$ layers. The application of the post growth treatment techniques makes the PL emission wavelength from the multilayer QWR samples quite insensitive to temperature changes. Thus the treated QWR structures are attractive candidates for device applications, such as telecommunications and broadband emitters, operating at room temperature.

Chapter 7

Finite Element Simulations

Overview

As shown in Tables 2-1 and 2-2, the InAs QWRs were embedded within InGaAlAs BL/SLs lattice matched with the InP substrate. Because of the mismatch between the QWRs and BL/SLs, according to the St. Venant's principle (Hirth et al. 1992), elastic strain and displacement fields from relaxation of the QWRs are expected in the BL/SL regions close to QWRs. These fields play an important role in the successive deposition of the BL/SL and other layers of QWRs. Simulations of these elastic fields are important for two practical considerations in the QWR structure growth and design: (1) interpretation of the experimentally observed growth phenomena, such as a complex displacement field around the QWRs (Yoo et al. 2004) and surface alloy decomposition (Priester et al. 2001) of BL/SL; and (2) prediction for the nucleation sites of the multilayer QWRs (Molina et al. 2006 & 2008) to interpret the origin of different QWR stacking patterns.

In this chapter, finite element (FE) simulations were carried out to calculate the displacement field, in-plane strain and chemical potential density in the single and multilayer QWR structures to interpret: (1) the diffraction contrast

observed in TEM images, as shown in Figures 4-11 and 5-24; (2) the origin of the **In**-rich stripes in the BL/SL above QWRs, as shown in Figures 4-18 and 5-22; and (3) the transition between correlated and anti-correlated QWR stacking patterns in multilayer samples with different BL/SL materials, as revealed in Figure 5-21. Continuum elastic theory (Hirth et al. 1992) was applied to all the calculations since its validity has been confirmed in the mismatched III-V semiconductor heterostructures, even on monolayer (~0.3 nm) scale (Bernard et al. 1994).

7.1 General models for FE simulations

FE simulations in three dimensions (3D) were performed to study the anisotropic elastic field distribution with FlexPDE 5.0 software (PDE Solutions, Inc., 2005). Calculations were carried out for both capped and uncapped structures with the dimensions of a typical QWR measured from [100]-[011] cross-sectional TEM images and EELS-SI maps. For the capped QWR structure within $In_{0.53}Ga_{0.37}Al_{0.10}As$ BLs, the experimental compositional information extracted from the EELS elemental maps (for example, Figure 4-17 (a)) is fed back into the FE model in order to provide a more realistic representation of the actual structure. The three elastic constants, C_{11}, C_{12} and C_{44}, for binary materials of InAs, GaAs and AlAs (Vurgaftman et al. 2001) were interpolated for ternary or quaternary alloys according to Vegard's Law (Vegard 1921). These elastic

constants were transformed to fit the [011] (*X*)- [$0\bar{1}1$] (*Y*)- [100] (*Z*) coordinate system used in the 3D simulation models according to the results listed in literature (Okada et al. 1997).

A typical 3D mesh containing two columns of correlated QWRs covered with $In_{0.53}Ga_{0.37}Al_{0.10}As$ SLs and BLs is shown in Figure 7-1. Generally, from the bottom to the top along the epitaxial growth direction ([100], set as "*Z*" axis), the mesh for all simulations include an In(GaAl)As BL underneath the QWRs, repeated WL/In(Ga)As QWRs/SL units and upper BL covering the structure. The boundary conditions used were (1) traction-free (i.e. stresses $\sigma_{zz} = \sigma_{zx} = \sigma_{zy} = 0$) for the top surface perpendicular to *Z* axis; and (2) normal zero displacements for the side walls (boundary surfaces perpendicular to *X* ([011]) or *Y* ([$0\bar{1}1$]) axis). The partial differential equations were based on standard linear, anisotropic elasticity theory (Hirth et al. 1992). It is assumed that the total forces imposed along *X, Y, Z* directions are all equal to zero in the simulating box. Thus the equations of the elastic stress σ_{ij} are given as:

$$X: \frac{\partial \sigma_{xx}}{\partial x} + \frac{\partial \sigma_{xy}}{\partial y} + \frac{\partial \sigma_{xz}}{\partial z} = 0$$

$$Y: \frac{\partial \sigma_{yx}}{\partial x} + \frac{\partial \sigma_{yy}}{\partial y} + \frac{\partial \sigma_{yz}}{\partial z} = 0$$

$$Z: \frac{\partial \sigma_{zx}}{\partial x} + \frac{\partial \sigma_{zy}}{\partial y} + \frac{\partial \sigma_{zz}}{\partial z} = 0$$

$$\sigma_{ij} = \sigma_{ji} (i, j = x, y, z)$$

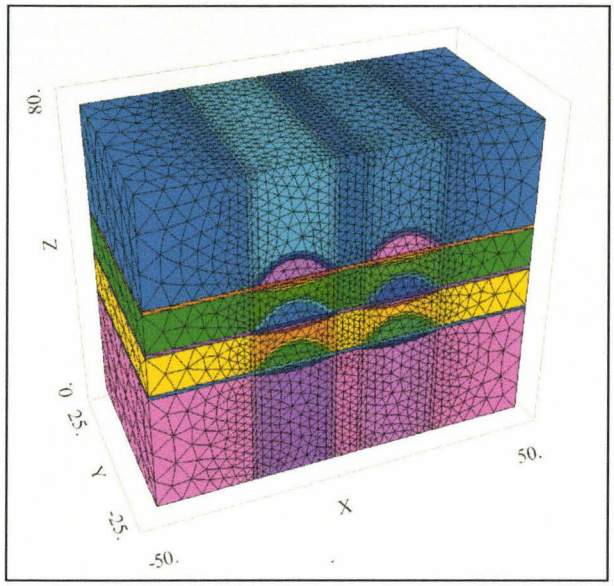

Figure 7-1: Typical 3D meshes showing the basic structure of the FE simulation models. *X*, *Y* and *Z* correspond to the [011] , [0$\bar{1}$1] and [100] directions, respectively. The numbers on *X*, *Y* and *Z* axis are in units of nanometers.

The convergence of the final solutions was set on the order of 10^{-3} or lower which implied that the estimated error in any variable was less than 0.1 % of its total range over every cell in the mesh (PDE Solutions, Inc., 2005).

7.2 Displacement field calculations

The displacement fields parallel and perpendicular to the growth direction of the QWRs were investigated in order to interpret the diffraction contrast, which is modulated by the distortion of the atomic planes according to Bragg's law (Williams et al. 1996) and equation (3-1) in Chapter 3. The calculations were carried out for the both the single layer and multilayer QWRs with different

stacking patterns. The geometric parameters of the QWRs and the definitions of the elastic variables are listed in **Appendix E**, where a typical FE code for Figure 7-1 is shown. The dimensions of all simulating boxes in this section are 100 nm, 50 nm along *X, Y* and (70~100) nm along *Z* axes, respectively.

7.2.1 Displacement field in single layer QWR sample

The model for the single layer QWR samples include three adjacent QWRs with the experimentally determined compositional map incorporated for an individual QWR. The displacement field around the central QWR is studied since the influence from the neighboring QWRs is included in the calculations.

7.2.1.1 Displacement field perpendicular to growth direction

In this section, the simulations will be used to interpret the "butterfly-like" contrast patterns observed in TEM images (for example, Figure 4-11 (c)).

The *X-Z* contour of the simulated displacement field along the *X* direction (*X*-displacement) is displayed in Figure 7-2 (a). The displacement field distributes symmetrically and shows the identical order of magnitude and opposite signs on both side-walls of the middle QWR, as pointed out by the arrows. The sign of the *X*-displacement vectors are negative (towards the minus *X* direction) and positive (towards the plus *X* direction) on the left and right side of the QWR, respectively. Along the dashed arrow passing through the center of the QWR, there exists a natural plane where no deformation is detected due to the symmetrical shape of

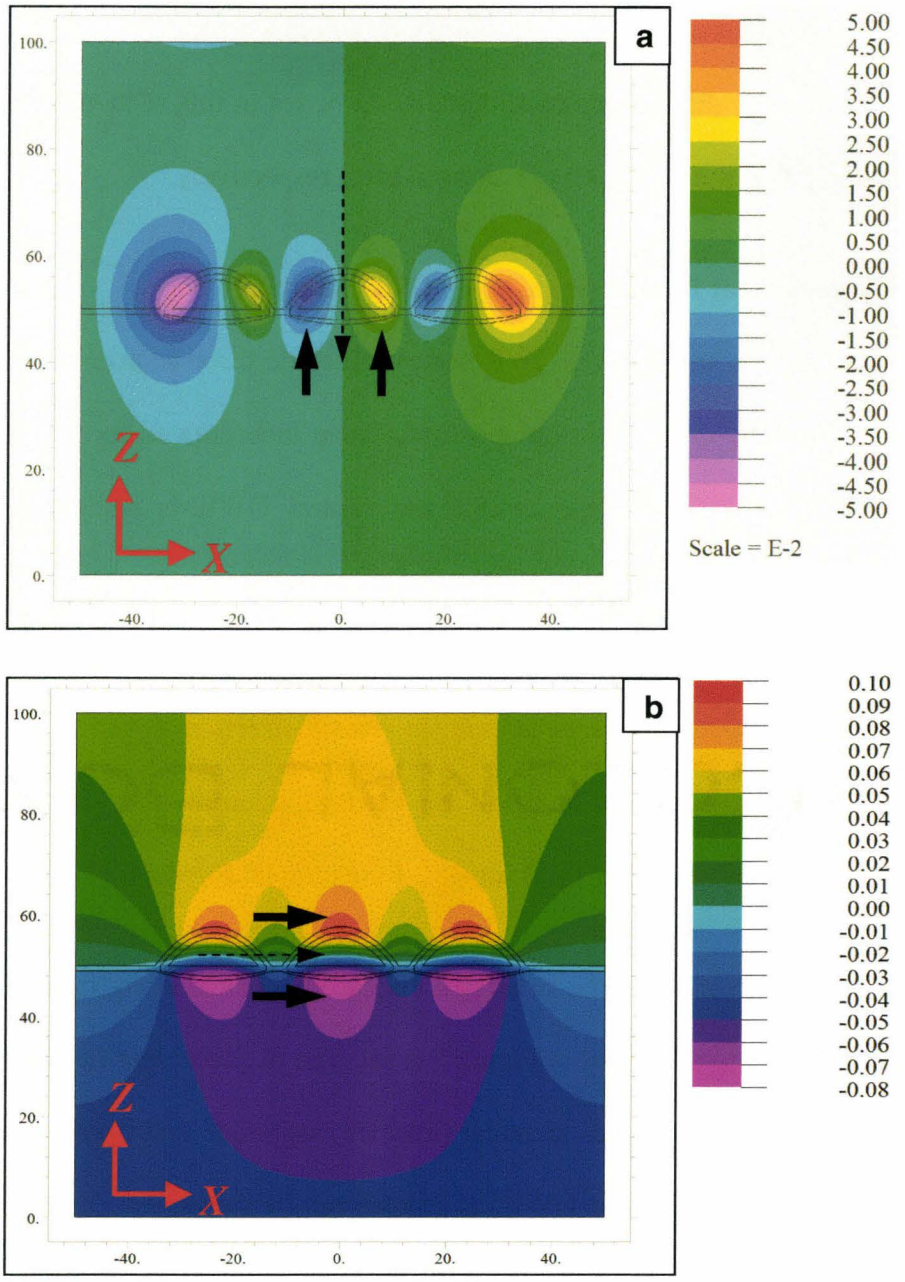

Figure 7-2: *X-Z* contours of the simulated displacement field in a single layer QWR:(a) *X*-displacement and (b) *Z*-displacement. The numbers on *X* and *Z* axis are in units of nanometers. The scales in (a) and (b) are in units of nanometers.

the QWR and a balance of stresses in the simulating box based on the continuum elastic theory (Hirth et al. 1992). The shape of the deformed area around an individual QWR can be described as "butterfly-like", which is similar to the diffraction contrast pattern observed in TEM images with $\mathbf{g}_{022}$ shown, for example in Figure 4-11 (c). A close observation of the TEM contrast reveals the existence of a narrow area between the two "wings" of the "butterfly" pattern (indicated by the dashed arrow in the insert of Figure 4-11(c)), the contrast of which is similar to the un-deformed BL region. Therefore, the simulated and experimental results show good agreement in the *X*-displacement field around QWRs in terms of both the shape of the deformed area and existence of the un-deformed plane. By correlation of the simulation and experimental results, the "butterfly-like" contrast pattern observed in TEM images with $\mathbf{g}_{022}$ should be interpreted as a result of the modulation of electron diffraction by the displacement field around an individual QWR rather than the existence of two QWRs (corresponding to the two "wings" of the contrast pattern).

7.2.1.2 Displacement field along growth direction

In this section, the simulation results will be used to interpret the "lobe pairs-like" contrast patterns observed in TEM images (for example, Figure 4-11(a)).

The *X*-*Z* contour of the simulated displacement field along *Z* direction (*Z*-displacement) is shown in Figure 7-2 (b). The deformation field distributes in

both the upper and lower BLs around the middle QWR, as indicated by the arrows. The sign of the *Z*-displacement vectors are positive (toward the "top surface" in the simulating box along *Z*) and negative (towards the "bottom surface" in the simulating box along *Z*) in the upper and lower BL, respectively. Along the dashed arrow passing through the QWR in the *X* direction, there exists an area with the *Z*-displacement close to zero. The shape of the *Z*-displacement field in the upper and lower BLs around the middle QWR can be described as "lobe pairs-like", which is similar to the diffraction contrast pattern observed in TEM images with $\mathbf{g}_{400}$ as shown in Figure 4-11 (a). A close observation of the TEM image reveals the existence of an area between the "lobe pairs" (indicated by the dashed arrow in Figure 4-11 (a)), the contrast of which is similar to the un-deformed BL region. The simulated and experimental results show good agreement in *Z*-displacement around the QWR in terms of the shape of deformed area and existence of the un-deformed area between the "lobe pairs". Through correlation of the simulation and experimental results, the "lobe pairs-like" contrast in TEM images with $\mathbf{g}_{400}$ should also not be interpreted as the positions of QWRs but as the *Z*-displacement field generated from the relaxation of the mismatch between QWR and BLs.

7.2.2 Displacement field in multilayer QWR stacks

In this section, the simulation results will be used to interpret either the "butterfly-like" or dotted (cross-hatched) contrast patterns observed in TEM images for

correlated or anti-correlated QWR stacks (for example in Figures 5-24 (b) and 5-24 (d)), respectively.

7.2.2.1 Correlated QWR stacks

FE simulations of the *X*-displacement were carried out in a model structure similar to that of sample M2 (aligned QWR stacks with 8 nm $In_{0.53}Ga_{0.37}Al_{0.10}As$ SL, 5 ML InAs) in Table 2-2. The simulated results are shown as *X*-*Z* contour in Figure 7-3 (a). Due to the correlated alignment, the *X*-displacement field with the same sign from the QWRs in the same column overlaps and forms a large deformed band (indicated by the dashed circles) in the SL regions between adjacent QWR columns. This deformed band extends along the *Z* axis through the whole thickness of the repeated units of QWR/SL. The simulation results can be applied to interpret the diffraction contrast pattern observed in TEM image (Figure 7-3 (b)) with $\mathbf{g}_{022}$ for sample M2 (8 nm $In_{0.53}Ga_{0.37}Al_{0.10}As$ SL, 5 ML InAs). The experimentally observed "butterfly-like" diffraction contrast (pointed by arrows in Figure 7-3(b)) penetrating the QWR stacks can be attributed to the overlap of the *X*-displacement field at the SL regions between adjacent QWR columns.

7.2.2.2 Anti-correlated QWRs

For the purpose of comparison, the *X*-displacement field calculation was also performed on the anti-correlated QWR stacks with the same dimensions and

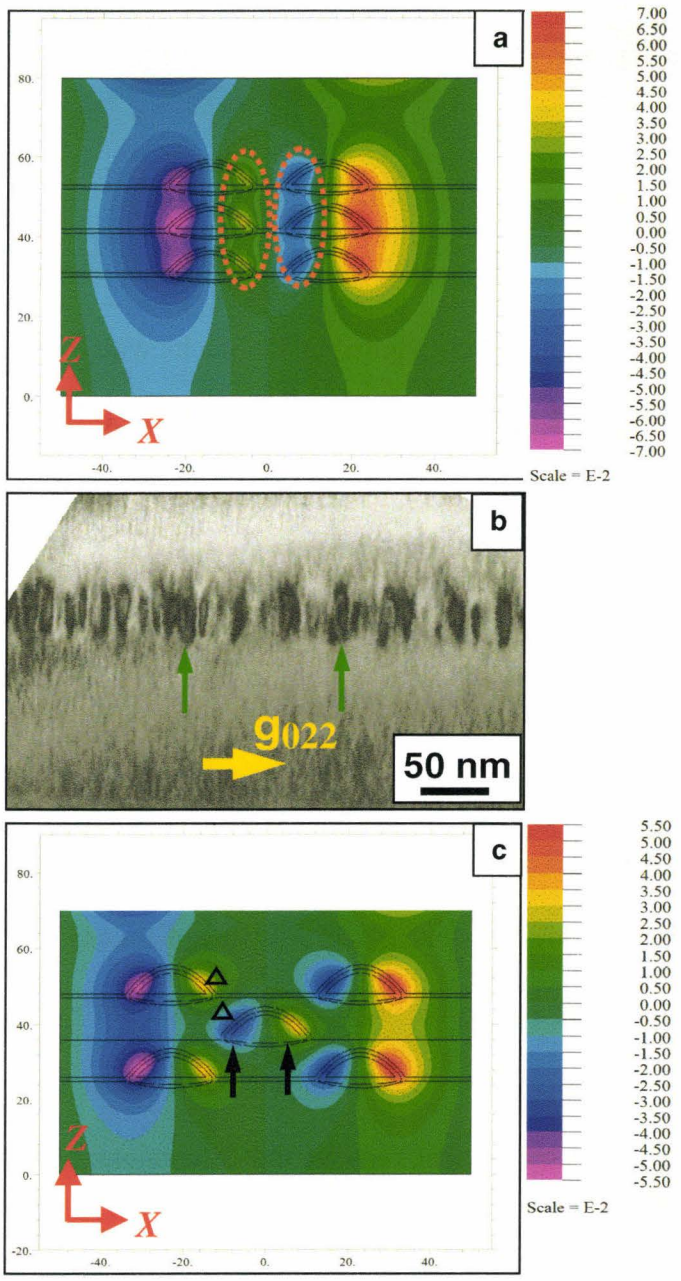

Figure 7-3: (a) *X-Z* contour of the simulated *X*-displacement for correlated QWRs. (b) TEM BF image with $\mathbf{g}_{022}$ for sample M2 (8 nm $In_{0.53}Ga_{0.37}Al_{0.10}As$ SL, 5 ML InAs) taken close to the $[0\bar{1}1]$ zone axis. (c) *X-Z* contour of the simulated *X*-displacement for anti-correlated QWRs. The numbers on *X* and *Z* axis in (a) and (c) are in units of nanometers. The scales in (a) and (c) are in units of nanometers.

composition as those in Figure 7-3 (a). The *X-Z* contour in Figure 7-3 (c) reveals that the *X*-displacement field around the central QWR shrinks to a limited area on both sides of that QWR (shown by the arrows) as compared with the large overlap band in Figure 7-3 (a) for the correlated QWRs. The smaller deformed area in the anti-correlated QWR stacks than those in Figure 7-3 (a) arises from the cancellation of the *X*-displacement fields with different signs between QWR neighbors in different layers (for example, the two deformed areas marked with triangles in Figure 7-3 (c)).

To simulate the *X*-displacement field for experimentally observed anti-correlated QWR stacks embedded in $In_{0.52}Al_{0.48}As$ SLs/BLs (sample M4 (8 nm $In_{0.52}Al_{0.48}As$ BL, 5 ML InAs)), the shape and dimensions (different from those shown in Figure 7-3 (c)) of the QWRs measured from Figure 5-22 (c) were incorporated into the FE model. The composition of the QWRs is assumed to be pure InAs since the migration ability of **Al** is very low under current growth conditions (Kasu et al. 1993), and the intermixing between **In** in the QWRs and **Al** in the SL is assumed to be negligible. The *X-Z* contour in Figure 7-4 (a) display similar features as that in Figure 7-3 (c), such as the limited area of deformation (shown by arrows) distributed on both sides of the central QWR. This feature is believed to arise from the anti-correlated stacking pattern of QWRs but not from the change of structural properties, such as shape, dimensions and composition between the QWRs in $In_{0.52}Al_{0.48}As$ BLs/SLs and those in

$In_{0.53}Ga_{0.37}Al_{0.10}As$ BLs/SLs by comparing the *X*-displacement field in Figures 7-3 (a) and (c).

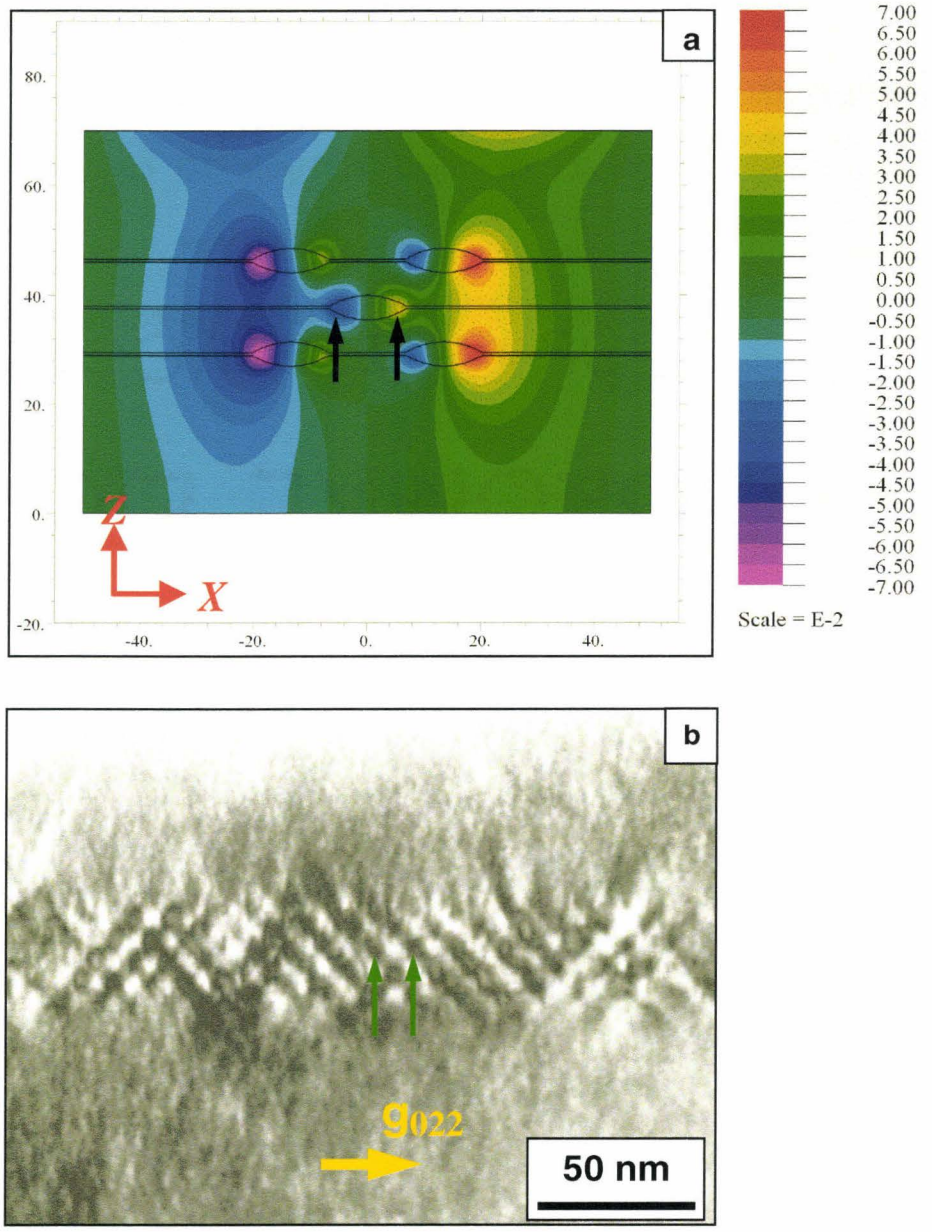

Figure 7-4: (a) *X*-*Z* contour of the simulated *X*-displacement field for anti-correlated QWRs in $In_{0.52}Al_{0.48}As$. The numbers on *X* and *Z* axis are in units of nanometers. (b) BF TEM images with $\mathbf{g}_{022}$ for sample M4 taken close to $[0\bar{1}1]$ zone axis. The scale in (a) is in the unit of nanometers.

The simulation results shown in Figure 7-4 (a) can be applied to interpret the diffraction contrast pattern observed in BF TEM images with $\mathbf{g}_{022}$ for sample M4, as shown in Figure 7-4 (b). The experimentally observed bright-dark dotted (cross-hatched) pattern (indicated by arrows) can be attributed to the limited *X*-displacement field on both sides of individual QWRs, arising from the cancellation of the displacement field with different signs between QWR neighbors in different layers.

Based on the results in Figures 7-3 (a) and 7-4 (a), the different diffraction contrast patterns observed in TEM images shown in Figure 5-24 can be interpreted as a result of the overlap and cancellation of the *X*-displacement among QWRs in correlated and anti-correlated stacks, respectively.

7.3 In-plane strain calculations

In this section, FE simulations on the in-plane strain were carried out in order to interpret defect generation in QWRs with different stacking patterns.

As shown in Figure 5-24, misfit dislocations were observed in the correlated QWR stacks (samples M1 (8 nm $In_{0.53}Ga_{0.47}As$ SL, 5 ML InAs) and M2 (8 nm $In_{0.53}Ga_{0.37}Al_{0.10}As$ SL, 5 ML InAs)) but not in the anti-correlated QWRs (sample M4 (8 nm $In_{0.52}Al_{0.48}As$ BL, 5 ML InAs)) although the nominal

thickness of the BLs/SLs and QWR layers are identical in all samples. It is well known that the elastic strain energy present in the epi-layer can be released through the generation of misfit dislocations. The elastic energy is proportional to the square of the in-plane strain between the QWR and SL/BL materials (Ohring 2002). More specifically, the elastic energy per unit area (E_e) in epi-layer is:

$$E_e = Y_{oung} d\varepsilon^2 /(1-\nu) \quad \text{(7-1)}$$

where Y_{oung} is the Young's modulus, d and ν stand for the thickness and Poisson's ratio of the epi-layer, respectively. The in-plane strain along X axis (ε_{xx}) is simulated for the correlated (sample M2) and anti-correlated (sample M4) QWRs to study the influence of the QWR stacking patterns on E_e stored in the SLs. The calculation models are the same as those in Figures 7-3 (a) and (c), 7-4 (a).

The X-Z contour of ε_{xx} in the correlated and anti-correlated stacks with the same QWRs (in terms of composition, shape and dimensions) and SLs ($In_{0.53}Ga_{0.37}Al_{0.10}As$) are displayed in Figure 7-5 (a) and (b), respectively. The difference of ε_{xx} is demonstrated in two aspects: (1) the magnitude of the tensile strain in the SL above QWRs is larger in the correlated stacks (between 0.7~0.8%, indicated by arrows in Figure 7-5 (a)) than that in the anti-correlated case (between 0.2~0.3%, indicated by arrows in Figure 7-5 (b)); and (2) the magnitude (between 0.4%~0.7%) of the compressive strain in the SL region between QWRs is similar for both cases. However, the strained area is larger in the correlated

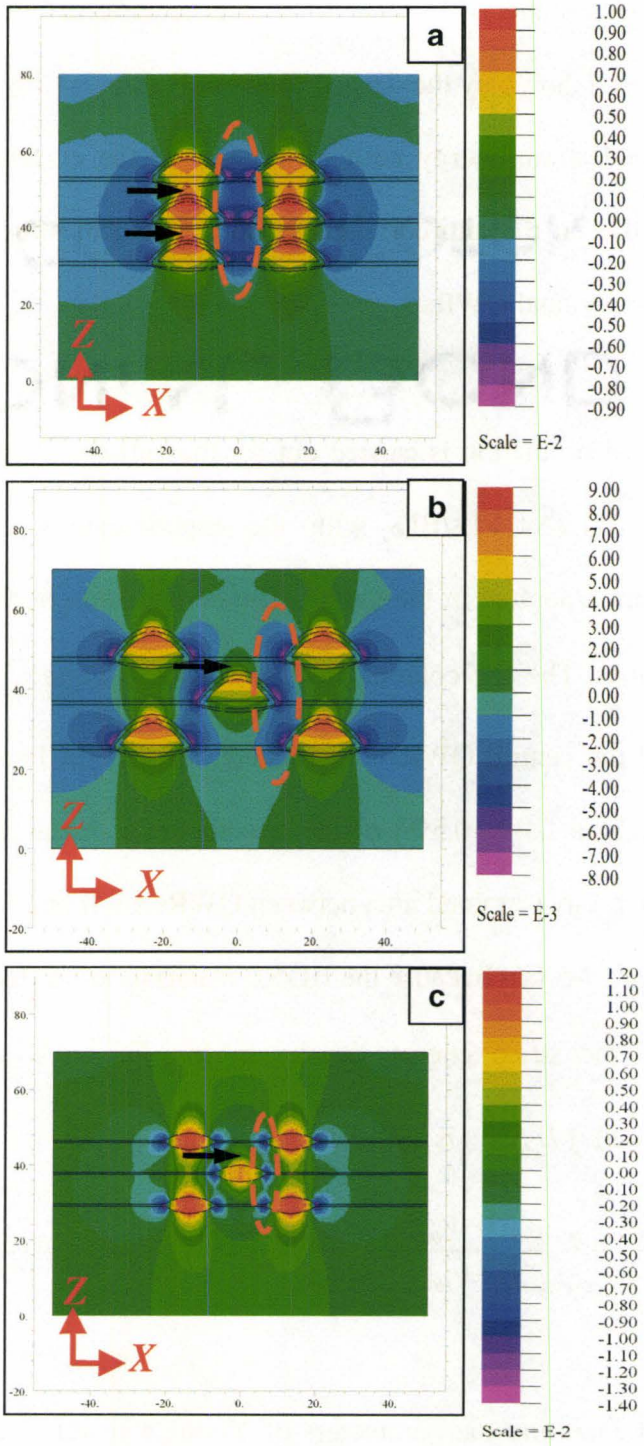

Figure 7-5: *X-Z* contours of the simulated in-plane strain ε_{xx} in (a) correlated and (b) anti-correlated QWR stacks within $In_{0.53}Ga_{0.37}Al_{0.10}As$ BLs/SLs. (c) anti-correlated QWRs within $In_{0.52}Al_{0.48}As$ BLs/SLs.

stacks (shown by the dashed circle in Figure 7-5 (a)) than that in the anti-correlated case (shown by the dashed circle in Figure 7-5 (b)). Based on equation (7-1), the total strain energy built in the SLs of the correlated QWR stacks is larger than that in the anti-correlated case if identical structural information is assigned to individual QWRs.

Further simulation is carried out for the anti-correlated QWRs embedded in the $In_{0.52}Al_{0.48}As$ SLs/BLs with the experimentally obtained shape and dimensions incorporated in the model. The composition of the QWR is assumed to be pure InAs. The *X*-*Z* contour of ε_{xx} is shown in Figure 7-5 (c) and the strain field around the central QWR is compared with that in Figure 7-5 (a). Smaller magnitude (about 0.4%~0.5%) of the tensile strain in the SL above QWR and smaller compressive strained area between QWRs are found in Figure 7-5 (c) than those in Figure 7-5 (a). Because the BL/SL materials are different in the two cases, the ratio of the strain energy density in $In_{0.53}Ga_{0.37}Al_{0.10}As$ ($E_{eInGaAlAs}$) and $In_{0.52}Al_{0.48}As$ SL ($E_{eInAlAs}$) is calculated as:

$$\frac{E_{eInGaAlAs}}{E_{eInAlAs}} = \frac{Y_{oung-InGaAlAs}(1-\nu_{InAlAs})d\varepsilon_{InGaAlAs}^{\ 2}}{Y_{oung-InAlAs}(1-\nu_{InGaAlAs})d\varepsilon_{InAlAs}^{\ 2}}.$$

After inputting the parameters of Young's modulus and Poisson's ratios for each material (Adachi 2004), the ratio can be simplified

as: $\frac{E_{eInGaAlAs}}{E_{eInAlAs}} \approx \frac{\varepsilon_{InGaAlAs}^{\ 2}}{\varepsilon_{InAlAs}^{\ 2}}$ where $\varepsilon_{InGaAlAs}$ and ε_{InAlAs} stand for the in-plane strain ε_{xx} generated by the QWR stacks in $In_{0.53}Ga_{0.37}Al_{0.10}As$ and $In_{0.52}Al_{0.48}As$ SLs, respectively. Based on the simulation results in Figures 7-5 (a) and (c), it is concluded that the strain energy present in the $In_{0.53}Ga_{0.37}Al_{0.10}As$ SLs from the correlated QWR stacks is higher than that in the $In_{0.52}Al_{0.48}As$ SLs from anti-correlated QWRs. The SL thickness of 8 nm is probably larger than the critical thickness (Ohring 2002) for defect generation in the former case than in the latter. Therefore, dislocations were observed in TEM images in the former case but not in the latter as a requirement of releasing the higher strain energy built in the SL from the correlated QWR stacks.

7.4 Chemical potential distribution on the growth front

In terms of thermodynamics, the driving force controlling the migration of incoming adatoms on the growth front surface is the gradient of chemical potential (Stangl et al. 2004). A net flux of certain kind of adatoms is transferred from the region with higher chemical potential to the one with lower chemical potential (Porter et al. 2001). In practice, the chemical potential density (CPD, in units of J/m^3) for each kind of adatom is calculated separately in order to qualitatively explain the segregation of that adatom on different portion of the growth front surface (Ledentsov et al. 1996). In this section, the CPD calculations are carried out to investigate the origins of two experimentally observed

phenomena in previous chapters: (1) the **In**-rich stripes in the BL/SL above QWRs, for example in Figure 4-18; and (2) different stacking patterns of QWRs embeded in BL/SL materials with different **Al** content, as shown in Figure 5-21.

Generally speaking, both of the growth phenomena can be regarded as a result of **surface segregation** of **In** adatoms on the growth front. It is different from its bulk counterpart, spinodal decomposition (Porter et al. 2001), in two aspects: (1) "the surface segregation occurs only on the growth front surface and is frozen as growth continues" (Priester et al. 2000); and (2) "at the usual MBE growth temperature (between 500 and 520 °C in our cases), bulk diffusion is negligible, the only cations (**In**, **Ga** and **Al**) allowed to exchange belong to the upper 2 ML's (the surface layer and the layer just underlying it)" (Priester et al. 2000 &1998). Because of these features of surface segregation, only the CPD on the growth front surface will be calculated for each kind of group III adatom and applied to explain the origins of the observed growth phenomena.

The surface chemical potential ($\mu_{surface}$) of a certain kind of adatom under a given surface morphology is expressed as the summation of energy contributions from different sources (Molina et al. 2006):

$$\mu_{surface} = \mu_0 + E_{elastic} + E_{surface} + E_{mixing} \qquad \text{——————(7-2)}$$

where μ_0 stands for the chemical potential on a non-deformed bulk material. $E_{elastic}$ and $E_{surface}$ represent the contributions from elastic strain energy and surface energy to the total chemical potential. E_{mixing} is related to the entropy of mixing of the formed alloy. For each term in equation (7-2), the following facts should be considered: Firstly, the QWRs are one-dimensional nanostructures, occupying the whole thickness along the Y axis in the FE model, as shown in Figure 7-1. Secondly, the **In** segregation in the BL/SL above QWRs is also a one-dimensional phenomenon, as has been confirmed in Figure 4-10. Therefore, equation (2) can be re-written as (Ledentsov et al. 1996; Biasiol et al. 1998):

$$\mu_{surface} = \mu_0 + \frac{Y_{oung}[\varepsilon_{xx}(r) - \varepsilon_0^{III}]^2 \Omega}{2} + \kappa(r)\gamma_{In(GaAl)As}\Omega + k_B T \ln c(r) \qquad (7\text{-}3)$$

where Y_{oung} is the Young's modulus and ε_0^{III} is the intrinsic mismatch between III-As (III=**In**, **Ga** or **Al**) and InP (or lattice-matched BL/SL materials) substrarte in our FE models. Ω is the atomic volume of the adatom, $\kappa(r)$ and $\gamma_{In(GaAl)As}$ stand for the local curvature and surface energy of the In(GaAl)As alloy covering the growth front, respectively. k_B is the Boltzmann constant and T is the growth temperature (K) of the BL/SL. $c(r)$ stands for the local concentration of the adatom. In the following sections, a two-step calculation will be performed. In step (1), the origin of the **In**-rich stripes is investigated; and in step (2), the concentration fluctuation of such **In** composition modulation is estimated based on the results obtained in step (1).

In step (1), a uniform impingement of **In** adatoms on the growth front area with X dimensions of 100 nm (will be shown in the model in section 7.4.2.1 and Figure 7-8 later), is assumed. Thus, the last term in equation (7-3) can be neglected since $c(r)$ is the same on the whole growth front surface at this stage. Equation (7-3) can now be expressed as:

$$\mu_{surface} = \mu_0 + \frac{Y_{oung}[\varepsilon_{xx}(r) - \varepsilon_0^{III}]^2 \Omega}{2} + \kappa(r)\gamma_{In(GaAl)As}\Omega \quad \text{——————} \quad (7\text{-}4)$$

After dividing Ω for both sides, equation (7-4) is re-arranged as:

$$\frac{\mu_{surface}}{\Omega} = \frac{\mu_0}{\Omega} + \left\{ \frac{Y_{oung}[\varepsilon_{xx}(r) - \varepsilon_0^{III}]^2}{2} + \kappa(r)\gamma_{In(GaAl)As} \right\} \quad \text{——————} \quad (7\text{-}5)$$

The first term on the right side can be ignored since it is identical for individual adatoms of the same kind. In the following calculations for step (1), only the sum of the two terms of elastic strain and surface energy density in the bracket on the right side of equation (7-5) is considered. It will be referred to as the "partial chemical potential density" (PCPD) in the FE results. The definitions and parameters for each variable are listed in **Appendix F**. As defined, the convex surface possesses a positive curvature resulting in an increase of the local PCPD through the surface energy density term. While a concave morphology means a negative curvature and reduces the contribution of surface energy density to PCPD. Therefore, the total PCPD at a point on the BL/SL growth front surface is determined by the combinative effect of the elastic strain and surface energy density as shown in equation (7-5). In all models in this section, the total length

along *X*, *Y* and *Z* axis in the simulation box are 100 nm, 50 nm and 70 nm, respectively. One program for studying the origin of the **In**-rich stripes is included in **Appendix G**, as a typical example showing the calculation procedures on the PCPD. The occurrence of **In** composition modulation is determined by the gradient of PCPD obtained in step (1).

In step (2), thermodynamic equilibrium is assumed (Moison et al. 1991) between locations with higher (region **1**) and lower (region **2**) PCPD on the growth front, i.e.

$$\mu_{surface-In1} = \mu_{surface-In2} \quad \text{——————} \quad (7\text{-}6)$$

Then the **In** composition modulation is estimated with equations (7-3) and (7-6), i.e.

$$\mu_0 + \left\{ \frac{Y_{oung}[\varepsilon_{xx}(r) - \varepsilon_0^{III}]^2}{2} + \kappa(r)\gamma_{In(GaAl)As} \right\}_1 \Omega_{In} + k_B T \ln c_1(r)$$
$$= \mu_0 + \left\{ \frac{Y_{oung}[\varepsilon_{xx}(r) - \varepsilon_0^{III}]^2}{2} + \kappa(r)\gamma_{In(GaAl)As} \right\}_2 \Omega_{In} + k_B T \ln c_2(r)$$

——————— (7-7)

7.4.1Validity of the calculation method for PCPD

As shown in equation (7-5), both the strain and surface curvature contribute to the PCPD. Firstly, the modification of **In** distribution by the strain field can be acknowledged by the variation of the QWR stacking patterns in samples with different SL thicknesses (samples K1 (8 nm $In_{0.53}Ga_{0.27}Al_{0.20}As$ SL, 4 ML InAs)

through K3 (25 nm $In_{0.53}Ga_{0.27}Al_{0.20}As$ SL, 4 ML InAs) in Figures 5-2 (b), (c) and (d)) or samples with different InAs QWR layer thicknesses (such as samples L1 (8 nm $In_{0.53}Ga_{0.27}Al_{0.20}As$ SL, 3 ML InAs) and L2 (8 nm $In_{0.53}Ga_{0.27}Al_{0.20}As$ SL, 5 ML InAs) in Figures 5-7 (a) and (c)). Secondly, the **In** distribution influenced by the surface curvature can be discussed in two parts as shown by the DF TEM images and EELS-SI map in Figures 7-6 (a) and (b), respectively. (1) The first effect is the modulation of the **In** distribution within QWRs. As observed in the DF image (where higher intensity detected at central regions of the QWRs indicates higher **In** concentration, as has been confirmed by EELS-SI maps in Figures 4-17 (a) and 5-3 (a)), the **In** distribution in the QWRs grown on relatively flat SL surfaces (for example, the aligned QWRs in column **I**) is similar to that in single layer QWRs (for example EELS-SI of Figure 4-17), i.e. the maximal **In** signal was detected at the central region of individual QWRs. Thus, the dashed arrow connecting the local intensity maxima within QWRs in column **I** is parallel to the alignment direction ([100]) of the stack. However, as the SL surfaces become wavy, as observed for the aligned QWRs in column **II** through layers **2** to **5**, the local maxima of intensity deviate from the QWR centers and are displaced to the side-walls of the QWRs, as shown by the dashed arrow connecting the local maximum intensity in column **II**. This trend can be visually confirmed by the EELS-SI map, where the maximum of **In** signal is shifted away from the "peak" positions (pointed out by arrows in Figure 7-6 (b)) and resides at

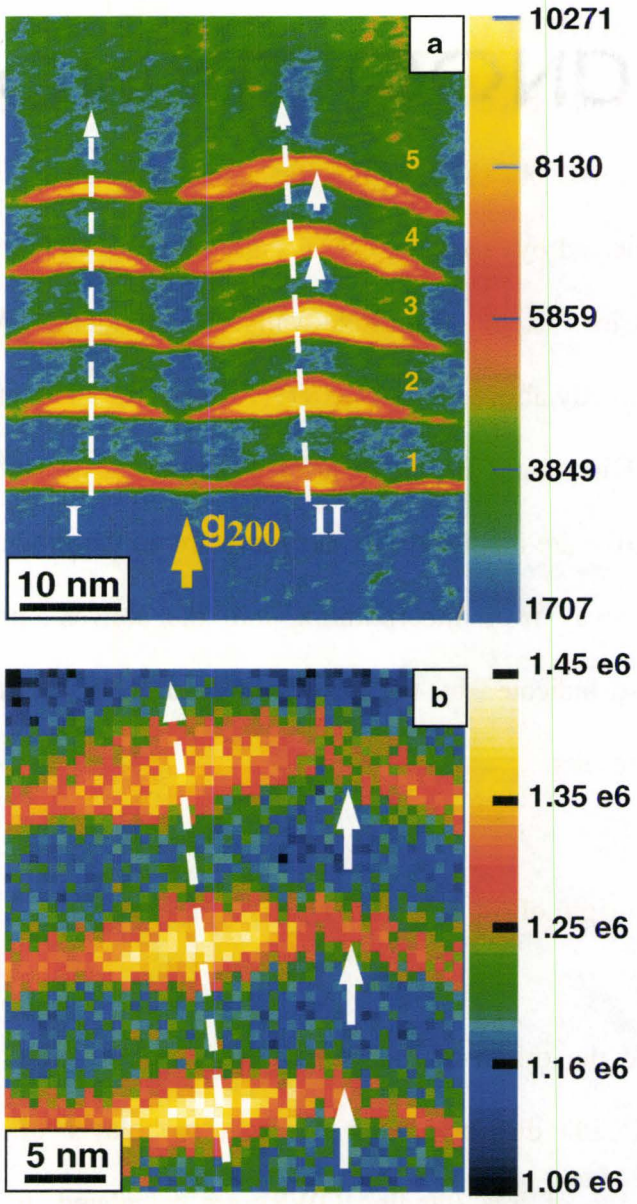

Figure 7-6: Influence of the surface curvature on the **In** distribution. (a) DF TEM image. (b) EELS-SI map. The QWRs are in $In_{0.53}Ga_{0.27}Al_{0.20}As$ SLs/BLs. "Pseudo-temperature" scale is applied to both images in order to enhance the visibility of signal variations in QWRs. The scale bars in (a) and (b) stand for image intensity and counts of **In** signal, respectively. They are all in units of counts.

the side-walls of QWRs. (2) The second effect is the modulation of **In** segregation in SL/BL. As has been confirmed in EELS-SI in Figure 5-3 (a), the higher intensity in SL/BL observed in DF images is associated with **In**-rich stripes, which are indicated by color "green" in Figure 7-6 (a). In both columns **I** and **II**, the **In**-rich stripes extend from side-walls of individual QWRs and leave the SL/BL area directly above the convex QWR center deficient of **In**. Therefore, the distribution of incoming **In** adatoms from deposition of both InAs QWRs and InGaAlAs SL/BL are modulated by the curvature on the growth front surface, i.e. they migrate away from incorporating into the convex "peak" positions (for example, those indicated by the arrows in Figure 7-6 (b)) as revealed by the experimental results.

7.4.2 Step 1: origin of the In-rich stripes

7.4.2.1 Model

To investigate the origin of the **In**-rich stripes observed in the BL/SL above QWRs, the PCPD distribution on the first monolayer of the InGaAlAs BL deposited on top of free standing QWRs are calculated. It is noticed that the modulation of **In** becomes less prominent in the BL/SL as more **Al** content is introduced due to the low mobility of **Al** at current growth temperature of 520°C, as shown in Figures 5-21 and 5-22. Three assumptions were made for the modeling: firstly, the QWRs are assumed to be made up of pure InAs, since Eisele et al. (2008) and Chung et al. (2008) have claimed that significant intermixing

between **In** and **Ga** occurred during the capping but not at the formation stage of the quantum structures; secondly, the composition modulation of **In** and **Ga** (revealed by the EDXS profiles in Figure 4-19) above the surface segregation of the InGaAlAs alloy (Dorin et al. 2002; Priester et al. 2001); thirdly, the morphology of the first monolayer of capping BL on top of the QWRs copies the shape of the QWR, which means the first monolayer of BL covering the QWR is assumed to possess the same curvature as that of the QWR. This assumption is supported by the BF TEM image for sample J in table 2-1 (with $\mathbf{g}_{200}$ in Figure 7-7) showing the surface morphology of 2 nm (about 6 ML) InGaAlAs BL covering the nominal 5 ML InAs QWRs. The convex peaks of the BL growth front were observed directly above the QWRs and relatively flat portion was found in the area above the gap between QWRs.

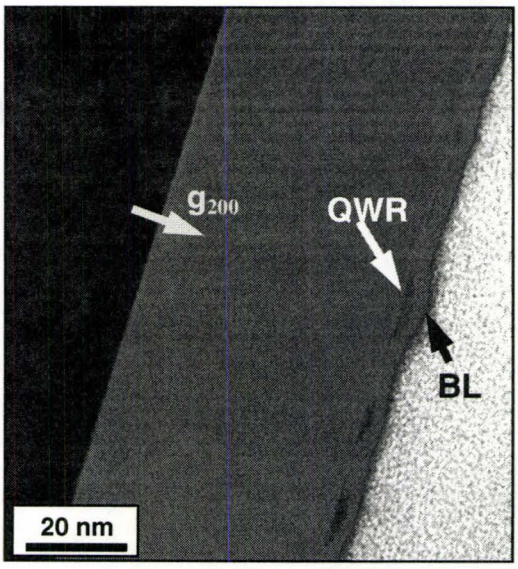

Figure 7-7: TEM BF image with $\mathbf{g}_{200}$ showing the growth front morphology with 2 nm $In_{0.53}Ga_{0.27}Al_{0.20}As$ BL deposited on the QWR.

Based on the above assumptions, the model for studying the PCPD distribution on the growth front surface includes two InAs QWRs and 0.35 nm (~ 1 ML) of InGaAlAs BL directly covering the QWRs. The geometrical arrangements are shown by the *X-Z* and *X-Y* contours in Figure 7-8. The growth front surface is assumed to be made up of 0.35 nm BL covering the repeated unit of InAs QWR/gap between QWRs/InAs QWR. Therefore, only the PCPD distributions on the growth front surface directly above QWRs and that above the gap between QWRs were studied to show how the **In**-rich stripes were formed.

7.4.2.2 Calculation results

The PCPD distributions for **In** (μ_{In}) and **Ga** (μ_{Ga}) on the growth front surface (pointed out by the arrows in Figure 7-8 (a)) are shown as the *X-Y* contours in Figures 7-8 (b) and (c), respectively. Generally, a lower magnitude of μ_{In} appears on the growth front directly above QWRs than that above the gap between QWRs. Moreover, the local minima of μ_{In} on the BL growth front above individual QWR splits into two bands (indicated by the green arrows in Figure 7-8 (b)) distributing on both side walls. The local maximum of μ_{In} appears on the BL growth front above the gap between two adjacent QWRs, as pointed by the yellow arrow in Figure 7-8 (b). In contrast, the local minimum and maximum of μ_{Ga} appear on the BL growth front above the gap between QWRs (green arrow) and that above individual QWRs (yellow arrow), respectively.

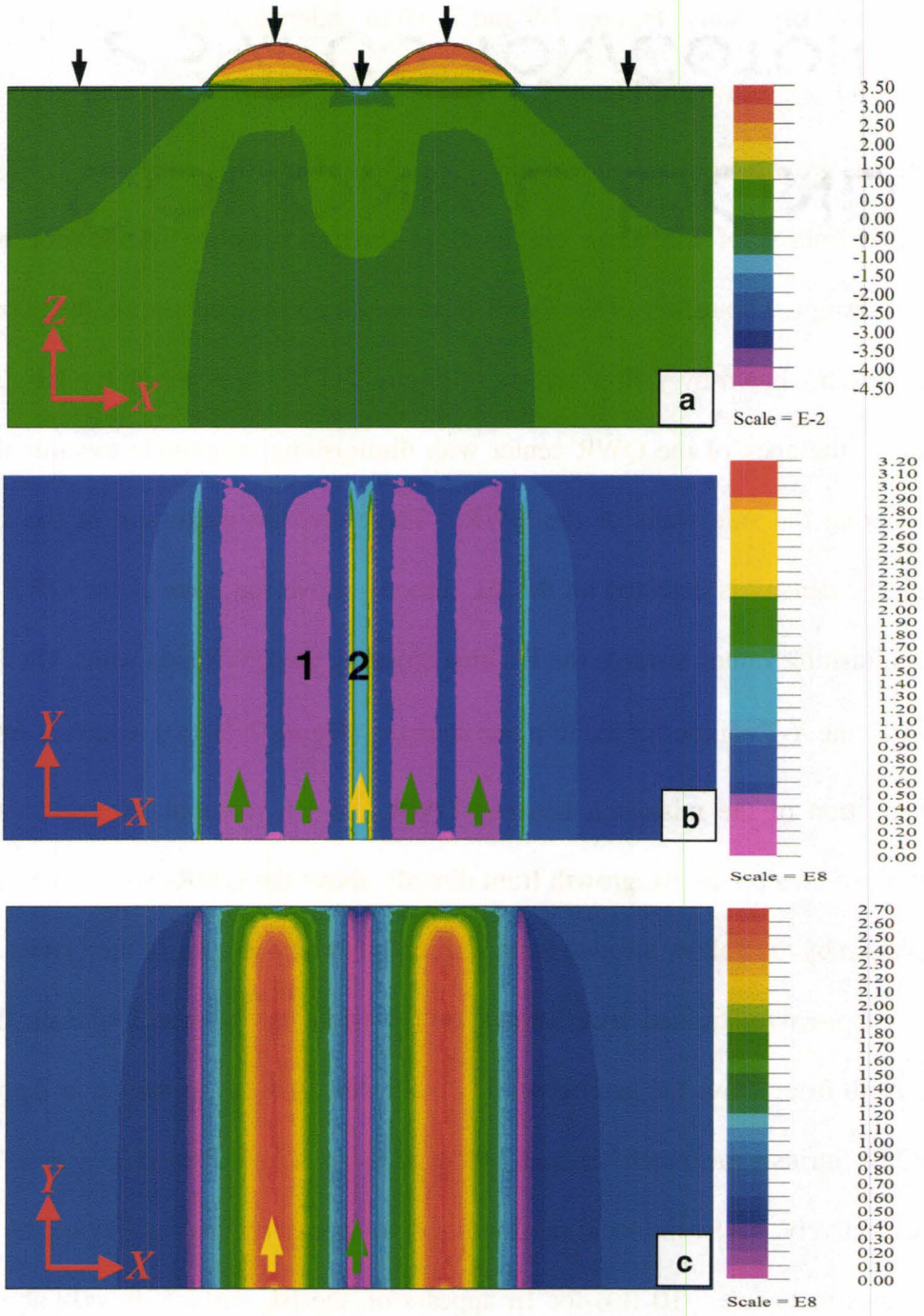

Figure 7-8: (a) *X-Z* contour of ε_{xx}. (b) *X-Y* contour of μ_{In} on the growth front surface and (c) *X-Y* contour of μ_{Ga} on the growth front surface. The scales for (b) and (c) are in units of J/m^3.

Each component contributing to the PCPD in the bracket of equation (7-5) is plotted separately (Figures 7-9 and 7-10) to understand the different features of μ_{In} and μ_{Ga} shown in Figure 7-8. The curvature and surface energy density on the BL growth front are shown in Figures 7-9 (a) and (b), respectively. Based on the definition of the mean curvature in three-dimensions (**Appendix F**), the convex upper boundary of the QWR possesses a positive curvature, the maximum of which (shown by yellow arrows in Figure 7-9 (a)) appears on the BL directly above the apex of the QWR center with diminishing magnitude towards the BL covering the side walls of the QWR. Therefore, the maximum of the surface energy density is detected on the BL directly above the apex of the QWRs with diminishing values towards the BL area covering the QWR side walls. On the one hand, the *X*-*Y* contour of the in-plane strain ε_{xx} (Figure 7-10 (a)), which is from the relaxation of the mismatch between QWR and BL materials, reveals a tensile strained area on the BL growth front directly above the QWRs with the maximum (shown by the yellow arrows) located directly above the apex of the QWRs. Also, a compressive strained area (shown by the white arrow) was found on the BL growth front above the gap between two adjacent QWRs. As shown in **Appendix F**, the intrinsic mismatch between InAs and GaAs with InP are 3.23% and -3.67%, respectively. Thus, the local minimum of strain energy density (shown by green arrows in Figure 7-10 (b)) for **In** appears on the BL surface directly above the QWRs, while the maximum (shown by yellow arrow in Figure 7-10 (b)) shows up

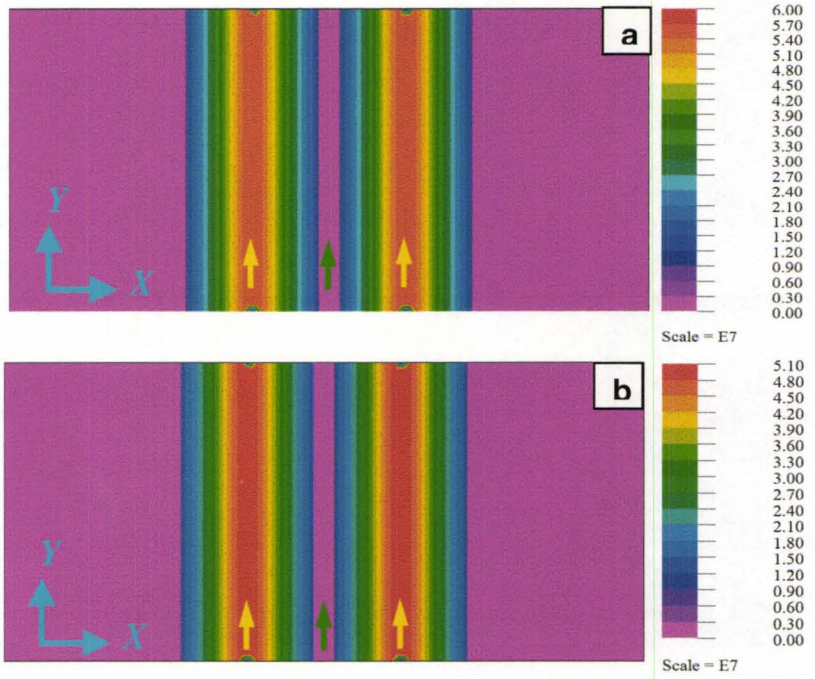

Figure 7-9: *X-Y* contours of (a) curvature and (b) surface energy density on the growth front surface. The scales for (a) and (b) are in units of m^{-1} and J/m^3, respectively.

on the BL surface above the gap between QWRs. In contrast, the maximum (shown by yellow arrows in Figure 7-10 (c)) and minimum (shown by green arrows in Figure 7-10 (c)) of the strain energy density for **Ga** appear on the BL surface above QWRs and that above the gap between adjacent QWRs, respectively.

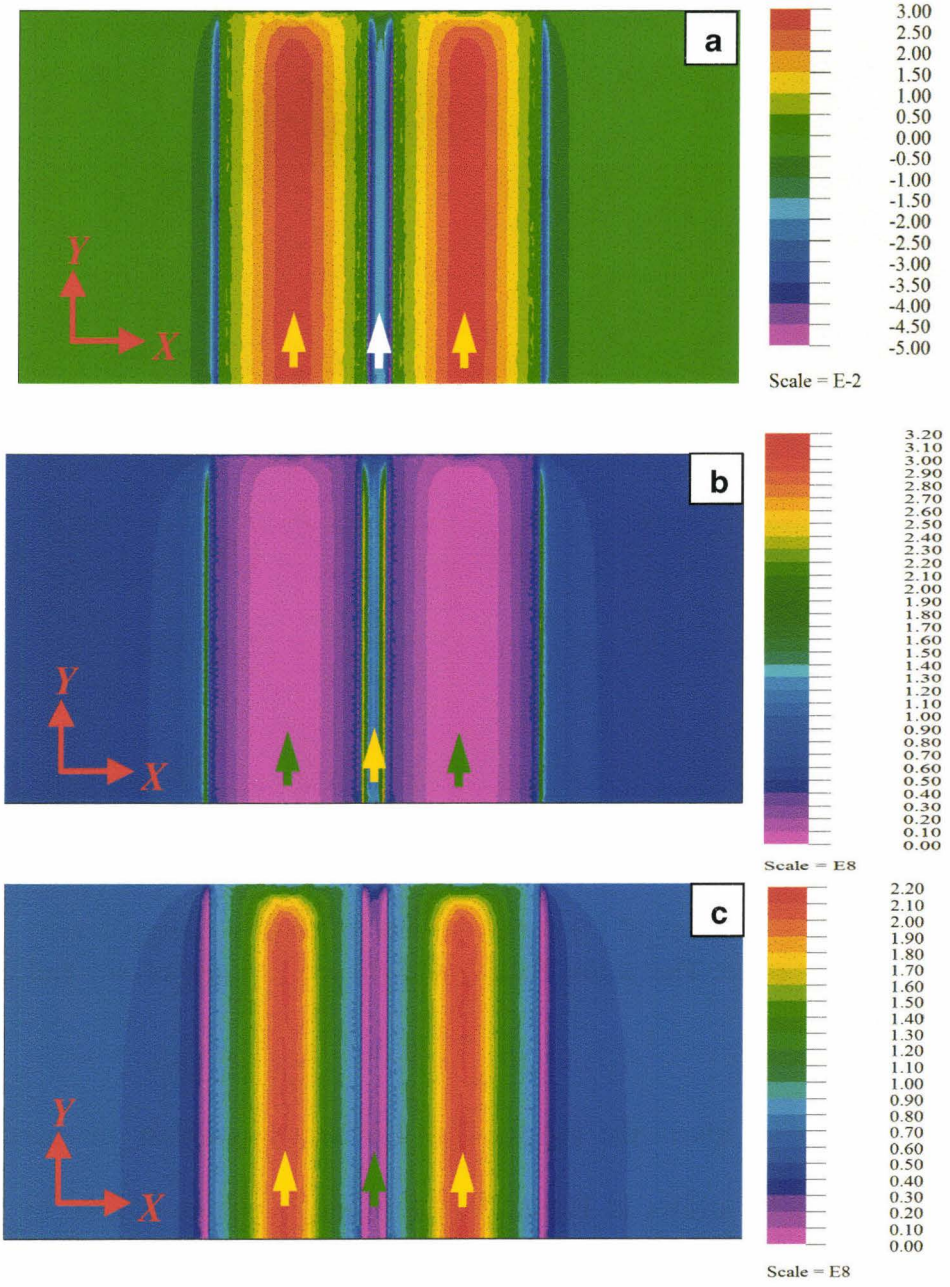

Figure 7-10: *X-Y* contours of (a) strain (ε_{xx}); strain energy density of (b) **In** and (c) **Ga** on the growth front. The scales for (b) and (c) are in units of J/m^3.

The details of PCPD contours in Figure 7-8 can be understood by considering the combined contribution of surface and strain energy density. For μ_{In}, the presence of the two bands of local minima on the BL surface above QWRs side-walls can be interpreted as a result of the combined effect of the surface (Figure 7-9 (b)) and strain energy densities (Figure 7-10 (b)). Whereas, the presence of local maximum of μ_{In} on the BL above the gap between QWRs is due to the maximal compressive strain, which induces the maximum of strain energy density for **In** on the growth front, although the minimum of surface energy density(curvature equals zero) was achieved there. For μ_{Ga}, the situation is simpler than that for μ_{In} since the local minima (maxima) of the surface and strain energy density overlap on the BL above the gap between two adjacent QWRs (above the QWRs) as shown in Figures 7-9 (b) and 7-10 (c). Therefore, the local minimum (maximum) of μ_{Ga} appears on the BL surface above the gap between QWRs (above the QWRs) as shown in Figure 7-8 (c).

During the successive deposition of the BL, driven by the gradient of PCPD, the incoming **In** adatoms will preferably segregate on the BL surface directly above the QWRs, while the **Ga** adatoms will tend to accumulate on the BL surface above the gap between QWRs. As observed in single (Figures 4-18 and 19) or multilayer (Figures 5-7 (b) and 5-22 (b)) samples, a higher **In** or **Ga** signal than the average was detected in the BL/SL regions directly above or

between QWRs, respectively. These experimentally observed features agree well with the PCPD calculation results. Moreover, the splitting of the local minimum of μ_{In} (Figure 7-8 (b)) is a good explanation for the origin of the multi-**In**-rich stripes observed in Figures 4-18 (a), 5-22 (b) and 7-6 (a). Based on the PCPD calculations, **In** adatoms deposited on the BL surface above QWRs are expected to segregate towards the two marked bands (by green arrows) on both side walls of individual QWR, as shown in Figure 7-8 (b). Thus, one-dimensional **In**-rich stripes formed in the BL/SL above QWR and were observed in the HAADF and TEM images, as shown in Figures 4-13 (c) and 4-10 (c), respectively.

7.4.3 Step 2: amplitude of the In segregation

In this section, the amplitude (δ) of the **In** segregation i.e. the local **In** concentration in the **In**-rich stripes will be estimated based on the PCPD calculations. As shown in Figure 7-8 (b), driven by the gradient of μ_{In} on the growth front surface of $In_{0.53}Ga_{0.37}Al_{0.10}As$, **In** adatoms will re-distribute on the BL surface. This re-distribution will result in the **In**-rich regions (with local **In** concentration of $0.53+\delta$) at location **1** (with PCPD μ_{In1}), and the **In**-deficient regions (with local **In** concentration of $0.53-\delta$) at location **2** (with PCPD μ_{In2}). Under the assumption of thermodynamic equilibrium (Moison et al. 1991), the value of δ can be estimated according to equations (7-6) and (7-7). Then we have:

$$\mu_0 + \mu_{In1}\Omega + k_B T \ln(0.53+\delta) = \mu_0 + \mu_{In2}\Omega + k_B T \ln(0.53-\delta) \quad \text{——————} \quad (7\text{-}8)$$

The values of local PCPD are $\mu_{In1} = 5\times10^{7} J/m^{3}$, $\mu_{In2} = 1.6\times10^{8} J/m^{3}$, and the growth temperature is $T =$ 773 K, the atomic volume of **In** is $\Omega = 1.57\times10^{-5} m^{3}/mol$. The amplitude of **In** segregation is estimated as δ=7.1%. Thus, the **In** concentration is expected as 0.53+δ=60.1% at the **In**-rich stripes. This value is in good agreement with the experimental EDXS-SI, where a 60-65% of local **In** concentration was detected at the **In**-rich stripes, as shown in Figure 4-19.

7.4.4 Other issues

Although the current model can be applied to explain the presence of the two **In**-rich stripes distributed on both sides of individual QWRs (for example, Figure 4-18 (a) and the insert in Figure 5-22 (b)), it fails to explain the origin of other numbers (1 or those greater than 3) of **In**-rich stripes observed above individual QWR (such as the cases in Figures 4-10 (c) and 5-3 (a)). It is believed that the number and position of the **In**-rich stripes are sensitive to the actual shape (estimated by the aspect ratio, defined as height (h)/base width (d)), of the individual QWR based on two further calculations. Firstly, with the base width fixed at 20 nm, the splitting bands of the local minima of μ_{In} mergers into a single broad band locating on the BL surface directly above the center of individual QWR, as the height (h) of the QWRs is reduced from 6 nm (Figure 7-8 (b)) to 5 nm (Figure 7-11 (a)) and 4 nm (Figure 7-11 (b)). Secondly, when the QWR height was fixed at 5 nm, the single band of the local minimum of μ_{In} splits into two

bands on both sides of individual QWR, as the base width is decreased from 20 nm (Figure 7-11 (a)) to 16.67 nm (h/d=0.3, in Figure 7-12 (a)) and 13.3 nm (h/d=0.375, in Figure 7-12 (b)).

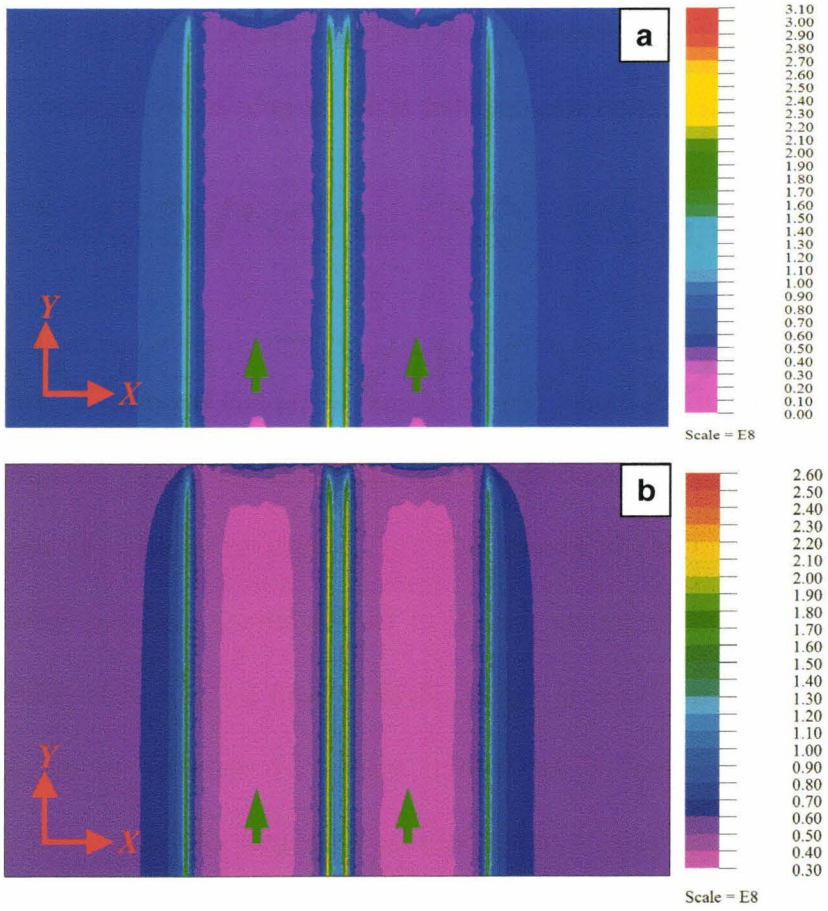

Figure 7-11: *X-Y* contours of μ_{In} for QWRs with a 20 nm base width, (a) 5 nm and (b) 4 nm in height, respectively. The scales for (a) and (b) are in units of J/m^3.

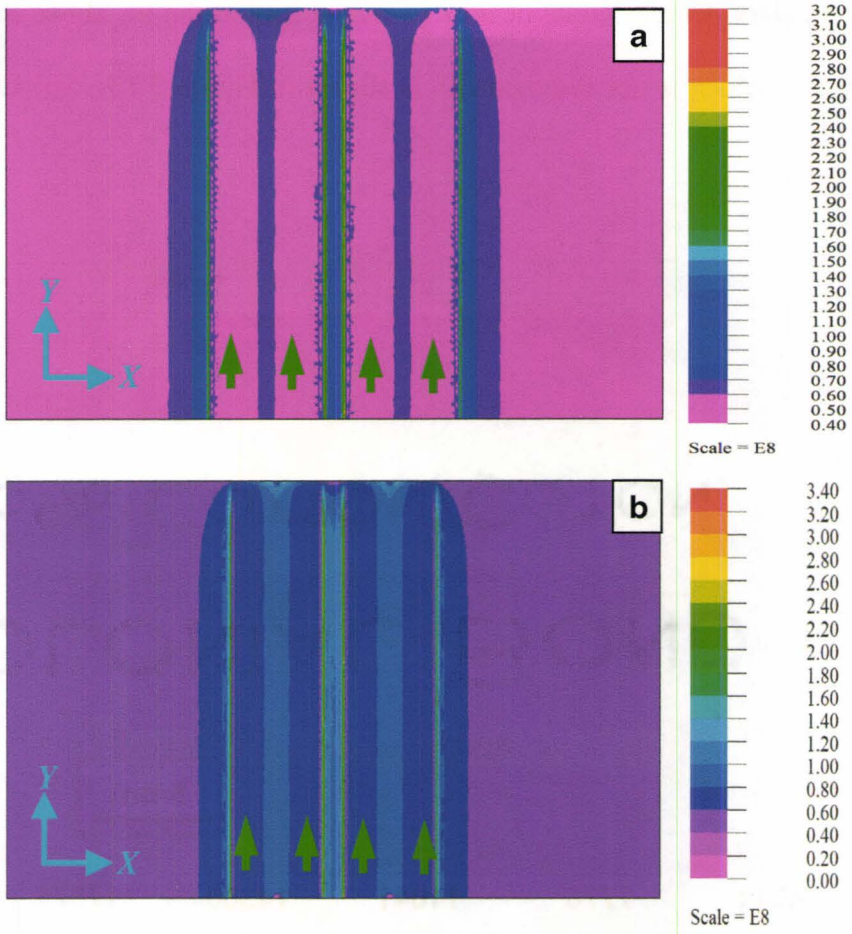

Figure 7-12: *X-Y* contours of μ_{In} for QWRs with 5 nm in height, and aspect ratio h/d of (a) 0.3 and (b) 0.375, respectively. The scales for (a) and (b) are in units of J/m^3.

Also, the QWRs in the current model were assumed to possess a perfect and symmetrical lens-shape. However, this is not the case for every individual QWR and the variation of the local curvature on the outer boundary of individual QWR may exist. Thus, multi-**In**-rich stripes are expected to start from certain locations with negative curvature (concave surface) on the BL immediately above

QWR boundary. One example of four **In**-rich stripes in the SL above one QWR, the shape of which is not symmetrical, is shown in Figure 7-13. Stripes **1** and **4**

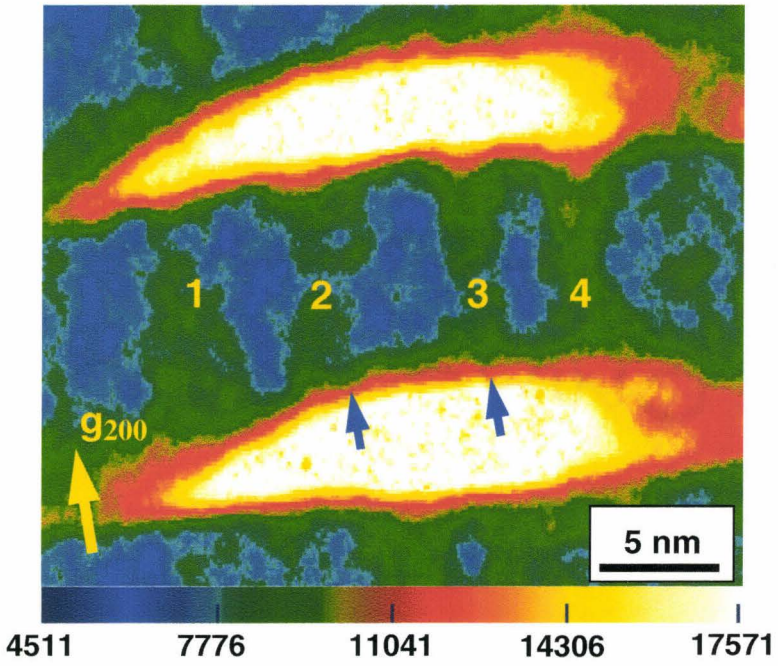

Figure 7-13: DF TEM image with $\mathbf{g}_{200}$ showing a QWR with four **In**-rich stripes in the SL. The numbers on the scale bar represent the image intensity.

were distributed close to the edge of the side walls of the QWRs and were interpreted as a result from the combined effect of the surface and strain energy density, similar to the case shown in Figure 7-8 (b). While, stripes **2** and **3** locatd close to the convex center of the QWR. A close observation on the interface between the stripes and QWR reveals the existence of small concave features (which means negative local curvature) associated with stripes **2** and **3**, as indicated by the blue arrows in the figure. Therefore, both single and multi-**In**-

rich stripes coexist in the BL/SL above individual QWR as observed in the cross-sectional TEM diffraction contrast (Figure 4-10 (c) and Figure 5-21 (b)) and HAADF images (Figure 4-13 (c) and Figure 5-3 (a)).

7.4.5 Stacking pattern variations of QWRs in different SL/BL

As shown in Figures 5-21 and 5-22, different alignments of the multilayer QWRs were observed as the **Al** content in the SL/BL layer was changed. In this section, the μ_{In} distribution on the BL growth front was calculated to investigate how the stacking pattern of the InAs QWRs varied with different covering materials and growth front surface morphologies.

7.4.5.1 Model

To simplify the models for multilayer QWR/SL structures, PCPD calculations were performed only for the first QWRs/SL unit. The main assumption is that the deposition of the second layer of InAs QWRs does not change the growth front morphology of the first SL. The growth front morphology of the SL can be estimated by the contrast variation along the interface between the second layer of QWRs and the first layer of SL in the chemically sensitive DF TEM images (with $\mathbf{g}_{200}$, such as Figure 5-22). Also, the composition of the QWR is regarded as pure InAs and only μ_{In} distribution on the growth front is investigated to determine the preferred nucleation sites (centers of QWRs) for the incoming InAs QWRs.

Based on these assumptions, from the bottom to the top, the model includes 49 nm $In_{0.53}Ga_{0.47-x}Al_xAs$ BL, 0.5 nm WL and two InAs QWRs directly above the WL and 8 nm SL covering the QWRs. PCPD calculations were performed for three SL compositions of $In_{0.53}Ga_{0.47-x}Al_xAs$ with x=0, 0.1, 0.48. The geometrical arrangements of each model can be viewed through the *X-Z* and *X-Y* contours in Figures 7-14 to 7-16. The surface morphology of the SL growth front for each model was determined from the corresponding TEM images in Figure 5-22.

7.4.5.2 Calculation results

(1) QWRs within $In_{0.53}Ga_{0.37}Al_{0.10}As$

The model for the QWRs embedded in $In_{0.53}Ga_{0.47}Al_{0.10}As$ SL/BL (sample M2 (8 nm $In_{0.53}Ga_{0.47}Al_{0.10}As$ SL/BL, 5 ML InAs) in Table 2-2 is shown by the *X-Z* contour of materials in Figure 7-14 (a). Based on the observations of Figure 5-22 (b), two InAs QWRs (green) and two **In**-rich stripes (red in Figure 7-14 (a)) with the composition of $In_{0.60}Ga_{0.30}Al_{0.10}As$ (determined by EDXS-SI results shown in Figure 4-19) extending from both side-walls of each QWR to the flat BL growth front surface, were included in the model. Local minima of μ_{In} are detected at the locations where the **In**-rich stripes intercept the growth front, as indicated by the green arrows in Figure 7-14 (b). The distance between centers of the two adjacent minima (marked as **A1** and **A2** in the figure) is about 4 nm, which is significantly

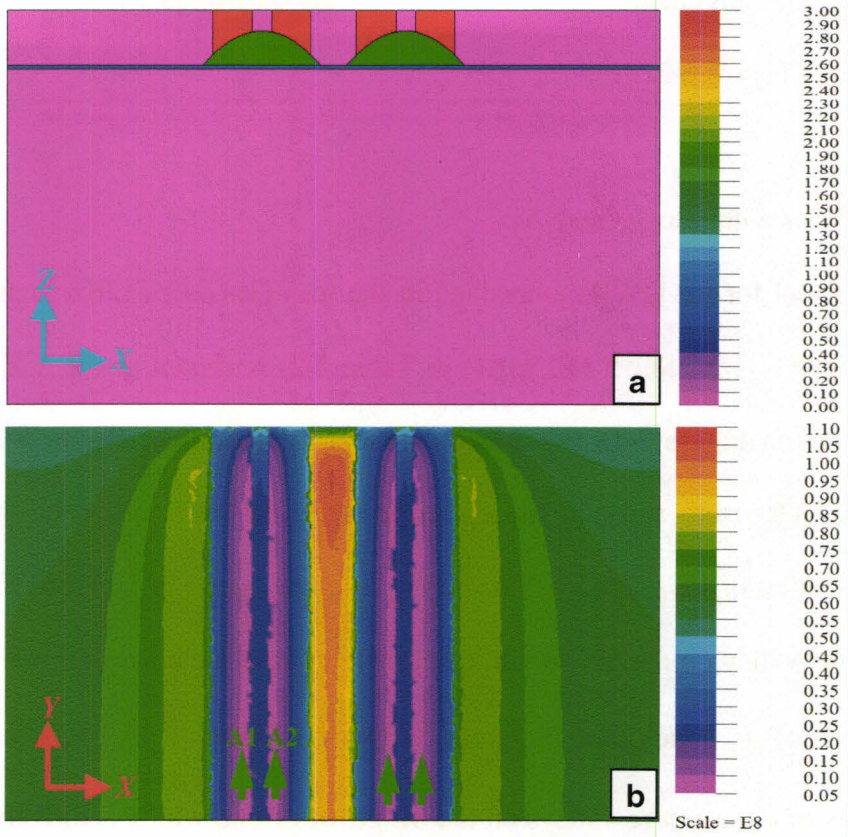

Figure 7-14: QWRs in $In_{0.53}Ga_{0.37}Al_{0.10}As$ BL/SL. (a) *X-Z* contour showing different materials and (b) *X-Y* contour of μ_{In} on the SL growth front surface. The numbers on scale bars for (b) are in units of J/m^3.

smaller than base width (estimated as 20 nm from Figure 5-22 (b)) of each individual QWR. Thus, during the deposition of the second layer of QWRs, one large QWR is expected to form directly above the QWR in the first layer through the coalescence of two small QWRs, which initially nucleated at the two local minimum neighbors of μ_{In} (**A1** and **A2**). The merging of small QWRs is advantageous for minimizing the total energy increase (Priester et al. 2001) from the mismatch between the InAs QWR and the $In_{0.53}Ga_{0.37}Al_{0.10}As$ SL. Therefore,

a correlated alignment was detected for QWRs on $In_{0.53}Ga_{0.37}Al_{0.10}As$ SL/BL, as shown in Figure 5-22 (b).

(2) QWRs within $In_{0.53}Ga_{0.47}As$

The model for the QWRs embedded in the $In_{0.53}Ga_{0.47}As$ SL/BL (sample M1 (8 nm $In_{0.53}Ga_{0.47}As$ SL, 5 ML InAs) in Table 2-2) is shown as the *X*-*Z* contour of materials in Figure 7-15 (a). Based on the observations of Figure 5-22 (a), two InAs QWRs (red) and one **In**-rich stripe (green in the figure, with the assigned composition of $In_{0.60}Ga_{0.40}As$) extending from the center of QWR to the center of concave valley on the SL growth front surface were included in the model. Local minima of μ_{In} (indicated by green arrows in Figure 7-15 (b)) locates at the centers of the concave valleys on the SL growth front, which is directly above the center of individual QWR. The position of the local minimum of μ_{In} is believed to arise from the overlap of the minimal values of the strain energy density and surface energy density at the concave valleys. Therefore, the incoming InAs QWRs of the second and later layers will preferably reside at the center of the concave valleys on the BL growth front and form a correlated stacking pattern with the QWRs in the layer below.

In the above models, the **In**-rich stripes with a 7% fluctuation of **In** concentration from the nominal composition of the $In_{0.53}Ga_{0.47}As$ SL was

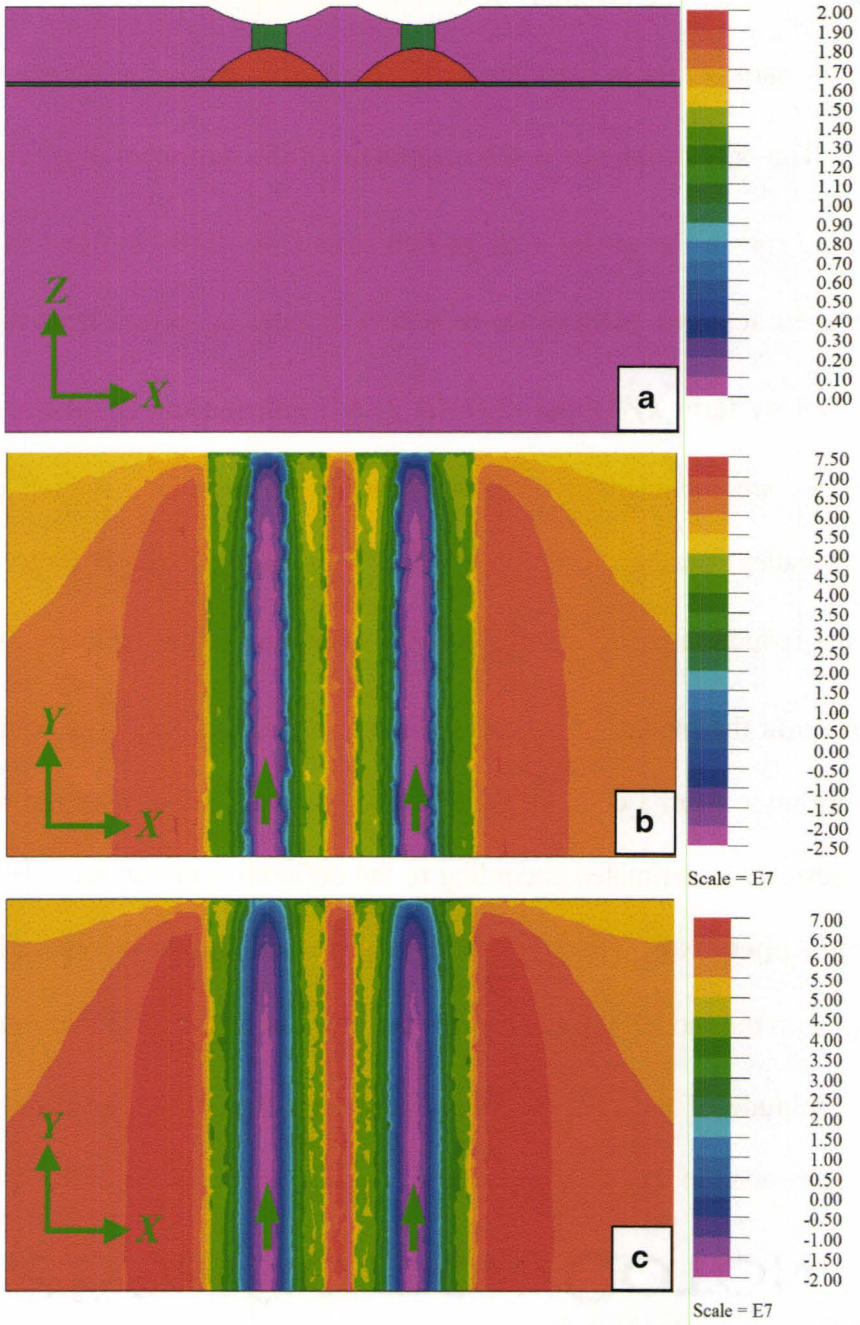

Figure 7-15: QWRs in $In_{0.53}Ga_{0.47}As$ BL/SL. (a) *X-Z* contour of different materials, (b) μ_{In} on SL growth front calculated from the model in (a), and(c) μ_{In} on SL growth front calculated without the **In**-rich stripes in (a). The numbers on scale bars for (b) and (c) are in units of J/m^3.

considered. The PCPD calculated without the **In**-rich stripe in the model is shown in Figure 7-15 (c). The positions of the local minima (shown by green arrows) of μ_{In} are the same as those calculated with the **In**-rich stripes, as shown in Figure 7-15 (b). The only difference is the magnitude of the minimum of μ_{In} varies from $-2.5\times10^{7}\,J/m^{3}$ in the model with **In**-rich stripes to $-2.0\times10^{7}\,J/m^{3}$ in the case without these features. Most of the reduction of local μ_{In} comes from the surface energy density term $\kappa\gamma$ (about $-2.8\times10^{7}\,J/m^{3}$, independent of whether the **In**-rich stripes are included or not), whenever there exists a negative curvature (concave valley) on the growth front. This value is significantly larger than the additional reduction of μ_{In} about $-0.5\times10^{7}\,J/m^{3}$ due to the inclusion of the **In**-rich stripes in the model. Also, the reduction of $-0.5\times10^{7}\,J/m^{3}$ is equivalent to the contribution from a concave valley with the amplitude of 0.48 nm below the flat SL surface, as estimated according to the definitions of curvature and surface energy in **Appendix F.** Therefore, qualitatively speaking, the incorporation of the **In**-stripe into the model will not change the position of the local minimum of μ_{In} if the amplitude of the concave valley is greater than 0.48 nm in the case for QWRs embedded in $In_{0.53}Ga_{0.47}As$ BL/SL.

(3) QWRs within $In_{0.52}Al_{0.48}As$

As stated in Chapter 5, a weaker **In** composition modulation was found in the $In_{0.52}Al_{0.48}As$ BL/SL than in $In_{0.53}Ga_{0.47}As$ and $In_{0.53}Ga_{0.37}Al_{0.10}As$ BL/SL. Thus,

an even smaller modification of the local minimum of μ_{In} is expected from the inclusion of the **In**-rich stripes in the model for QWRs in $In_{0.52}Al_{0.48}As$ than that for QWRs in $In_{0.53}Ga_{0.47}As$. Therefore, no **In**-rich stripes were included in the calculation.

The model for the QWRs embedded in the $In_{0.52}Al_{0.48}As$ SL/BL (sample M4 (8 nm $In_{0.52}Al_{0.48}As$ SL, 5 ML InAs) in Table 2-2) is shown as the *X-Z* contour of materials in Figure 7-16 (a). Based on the observations of Figure 5-22 (c), two InAs QWRs (red) and the rippled SL growth front surface with a morphology composed of alternative convex peaks directly above QWRs and concave valleys above the gap between QWRs, were included in the model. The *X-Y* contour of μ_{In} distribution on the SL growth front surface is displayed in Figure 7-16 (b). On the middle concave valley above the gap between the two QWRs (since the influence from the two QWRs are included for such valleys), two local minima are present on both sides of the valley, as pointed out by the arrows and dashed lines in green. The separation of the two minima is 7 nm, which is smaller than the base width (estimated as 15 nm from Figure 5-22 (c)) of the QWRs embedded within the $In_{0.52}Al_{0.48}As$ BL/SL. Also, the maximum of μ_{In} appears on the convex peak of the BL growth front, as indicated by the arrow and dashed line in yellow. Thus, during the deposition of the second layer of QWRs, one large QWR is expected to form in the concave valley through the coalescence

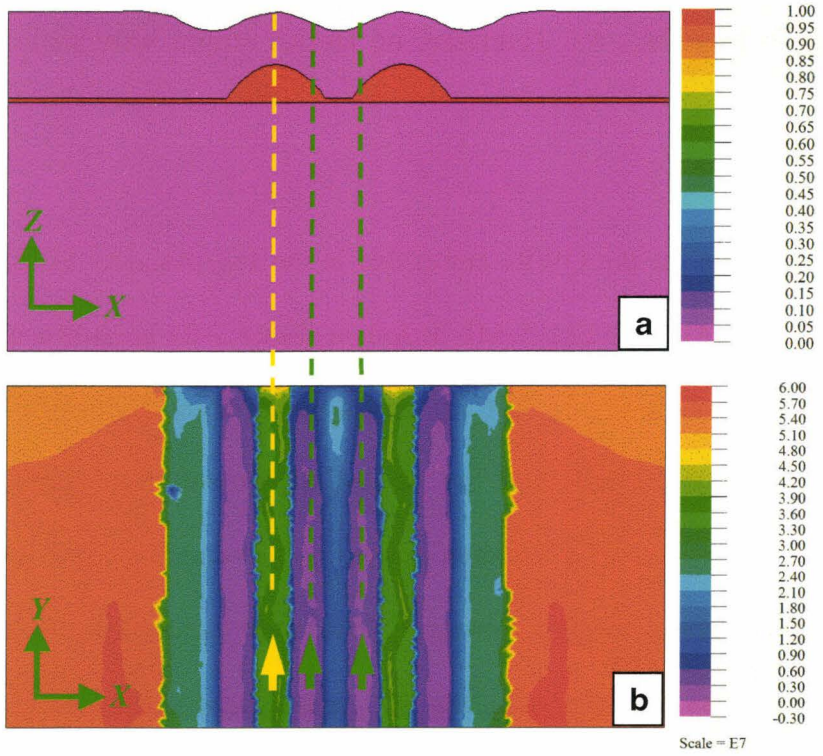

Figure 7-16: QWRs in $In_{0.52}Al_{0.47}As$ BL/SL. (a) *X-Y* contour of different materials, and (b) μ_{In} on SL growth front. The numbers on scale bar for (b) are in units of J/m^3.

of two small QWRs, which initially nucleated at the two local minima neighbors as shown Figure 7-16 (b). Such coalescence is advantageous in minimizing the total energy increase (Priester et al. 2001) from the mismatch between InAs QWR and $In_{0.5}Al_{0.48}As$ SL. Therefore, an anti-correlated alignment was detected for QWRs within $In_{0.53}Al_{0.48}As$ SL/BL, as shown in Figure 5-22 (c).

The μ_{In} distribution is believed to result from the combined effect of the strain energy and surface energy densities. More specifically, the minimum of the strain energy density appears on the convex peak of the SL directly above QWRs, while the maximum lies in the concave valleys between QWRs. According to the definition of the curvature and surface energy in **Appendix F**, the maximum of surface energy density shows up on the convex peak while the minimum locates at the concave valley of the SL growth front. The sum of these two terms for μ_{In} in equation (7-5) results in the two local minima appearing on the two side walls of the concave valley and maximum on the convex peak of the SL growth front surface.

According to the discussions in section 7.4.2 and 7.4.5, both the presence of the **In**-rich stripes and different QWR stacking patterns are determined by the PCPD distribution of **In** (μ_{In}) on the SL growth front. The PCPD is modulated by the combined contribution from surface and strain energy densities on the growth front surface.

7.4.6 Discussions on other growth phenomena

The FE calculations were applied to explain the experimental results in the sections above. A preliminary discussion of two other important issues: (1) the morphology evolution of the SL growth front surface; and (2) the propagation direction of the **In**-rich stripes are given in the following section. The

experimental observations of these two effects have been shown in Figure 5-22 and more experimental evidence may be required for conclusive proof.

7.4.6.1 Growth front morphology variations of the spacer layers

As shown in Figure 5-22, the morphologies of the SL growth front directly above QWRs vary with the **Al** content in the SL/BL: concave valleys in sample M1 ($In_{0.53}Ga_{0.47}As$ BL/SL, 5 ML InAs); a flat surface in sample M2 ($In_{0.53}Ga_{0.37}Al_{0.10}As$ BL/SL, 5 ML InAs); a slightly convex peak in sample L2 ($In_{0.53}Ga_{0.27}Al_{0.20}As$ BL/SL, 5 ML InAs, shown in Figure 7-6) and the convex peaks in sample M4 ($In_{0.52}Al_{0.48}As$ BL/SL, 5 ML InAs). The distribution of μ_{In} and μ_{Ga} on the growth front of 1 ML SL covering QWRs (similar to the model in Figure 7-8) is investigated for different SL materials. The *X-Y* contours in Figures 7-17 through 7-19 as well as Figure 7-8 demonstrate that for all available BL/SL materials, driven by the gradient of the PCPD on the SL growth front surface at the initial capping stages of QWRs, a certain portion of the incoming **In** adatoms accumulate preferably on the SL surface directly above QWRs, while a portion of **Ga** adatoms will tend to occupy the regions above gap between adjacent QWRs (indicated by the green arrows in the μ_{Ga} contours in Figures 7-17 (b) and 7-18(b)). With the assumption that the mobility of **Al** is negligible compared to those of **In** and **Ga** (Kasu et al. 1993) under the current growth conditions, the growth front morphology evolution can be understood by considering the varied atomic fraction ratios of **In**/**Ga** in each BL/SL material.

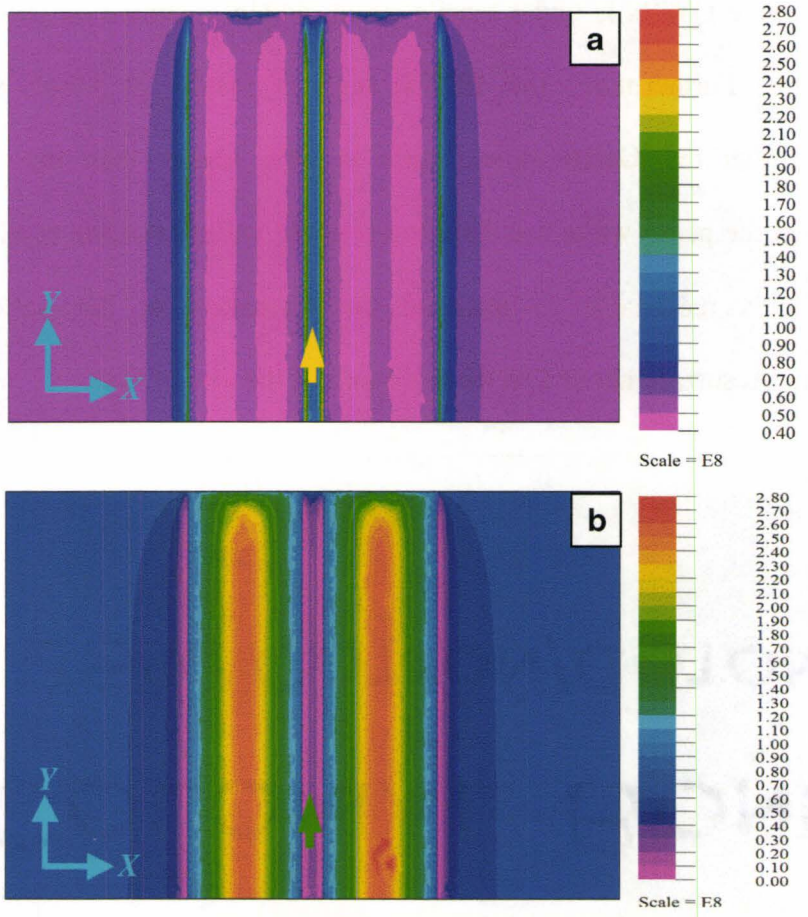

Figure 7-17: *X-Y* contours of surface PCPD for InAs QWRs covered with 1 ML $In_{0.53}Ga_{0.47}As$ BL. (a) μ_{In} and (b) μ_{Ga}. The numbers on scale bars for (a) and (b) are in units of J / m^3.

For $In_{0.53}Ga_{0.47}As$, which has the lowest **In/Ga** ratio, the formation of valleys on SL surface is suggested to result from the continuous loss of **Ga** from SL directly above QWRs during the capping stage. This hypothesis is given based on the work of Okada et al. (Okada et al. 1997), where the periodic peak/valley surface morphology was found for the tensile strained $In_xGa_{1-x}As$ layer grown on

an InP substrate. In the case of the $In_{0.53}Ga_{0.47}As$ SL covering the InAs QWRs, the SL directly above QWRs is under tensile strain, which is similar as the case in Okada's work. Furthermore, the EDXS analysis results in Okada's work demonstrated that the **Ga/In** atomic ratio is 24% higher than the average composition at the peaks while it is 18% lower at the valleys (Okada et al. 1997). Therefore, it is reasonable to attribute the formation of the valleys on $In_{0.53}Ga_{0.47}As$ SL surface above QWRs as a result of the loss of **Ga**.

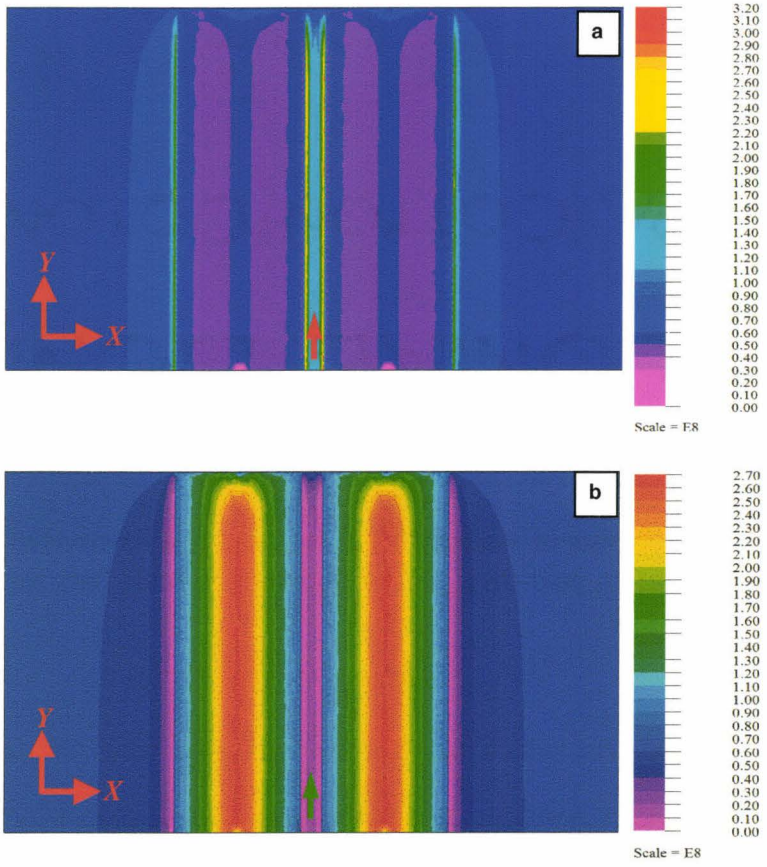

Figure 7-18: *X-Y* contours of surface PCPD for InAs QWRs covered with 1 ML $In_{0.53}Ga_{0.27}Al_{0.20}As$ BL. (a) μ_{In} and (b) μ_{Ga}. The numbers on scale bars for (a) and (b) are in units of J/m^3.

With the introduction of **Al** into the $In_{0.53}Ga_{0.37}Al_{0.10}As$ SL, the **In/Ga** ratio increases and the loss of **Ga** on the SL surface above QWRs can be compensated by the accumulation of **In**, resulting in a relatively flat growth front. With more **Al** introduced into the $In_{0.53}Ga_{0.27}Al_{0.20}As$ and $In_{0.52}Al_{0.48}As$ SLs, the accumulation of **In** on the SL surface above QWRs outweighs the loss of **Ga** (or loss of very small portion of Al) and results in a convex growth front directly above QWRs, as shown by TEM images in Figure 5-22 and Figure 7-6.

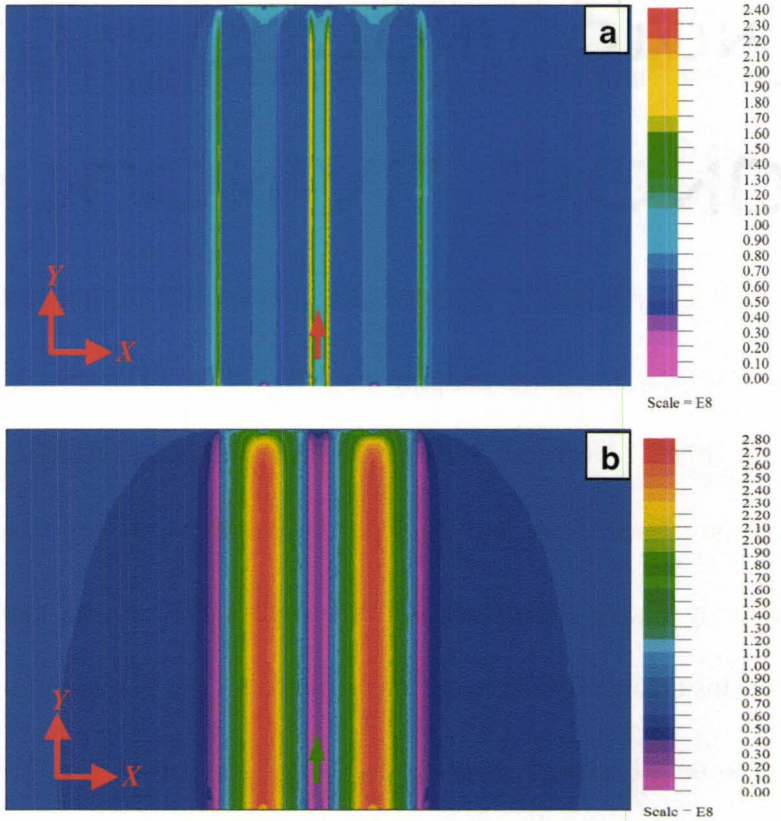

Figure 7-19: *X-Y* contours of surface PCPD for InAs QWRs covered with 1 ML $In_{0.52}Al_{0.48}As$ BL. (a) μ_{In} and (b) μ_{Al}. The numbers on scale bars for (a) and (b) are in units of J/m^3.

*7.4.6.2 Propagation of the **In**-rich stripes*

The propagating direction of the **In**-rich stripes is discussed under the assumption that these stripes were formed by connecting the initial and consequent positions of local minima of μ_{In} on the SL growth front surface. In other words, the propagation direction of the **In**-rich stripes is assumed to represent the traces of the local minima of μ_{In} on the SL surface as the capping process continues. Therefore, the μ_{In} maps at the initial stages of the overgrowth of QWRs (such as Figures 7-8 (b), 7-17 (a) and 7-19 (a)) and those on the growth front after the complete deposition of 8 nm-SL (such as Figures 7-14 (b), 7-15 (b) and 7-16 (b)) were considered.

Two local minima of μ_{In} were detected on the SL above both sides of individual QWRs at the initial capping stage for all the SL materials, as shown in Figures 7-8 (b), 7-17 (a) and 7-19 (a). For the $In_{0.53}Ga_{0.47}As$ SL, valleys were formed on the growth front and the local minimum of μ_{In} re-located on the SL valleys directly above the center of individual QWR as the capping process continues. This change results in the convergence of the two initial minima of μ_{In} to the one on the SL growth front directly above the center of a QWR (Figure 7-15 (b)) and formed one **In**-rich stripe propagating through the center of QWRs in the same column, as shown in Figure 5-22 (a). For the QWRs covered with $In_{0.53}Ga_{0.37}Al_{0.10}As$, a relatively flat growth front surface was formed and the two

local minima of μ_{In} can propagate separately along the epitaxial direction [100] and creates two local minima on the growth front after the complete deposition of 8 nm-SL (Figure 7-14 (b)). Thus, two **In**-rich stripes were found propagating on both sides of QWRs through the SL/QWR column, as observed in Figure 5-22 (b). For the QWRs covered with $In_{0.52}Al_{0.48}As$, as the capping process continues, convex peaks were formed on the SL growth front directly above the QWR center and the local minima of μ_{In} appears on the SL valley above the gap between two adjacent QWRs (Figure 7-16 (b)). Thus, the **In**-rich stripes from adjacent QWRs were found to diverge from each QWR and converge in the SL region above the gap between QWRs, as shown in Figure 5-22 (d).

7.5 Summary

The displacement field, in-plane strain and chemical potential density distribution are calculated by finite element method in this chapter to interpret the experimentally observed growth phenomena in previous chapters. The results are summarized below:

(1) The diffraction contrast patterns observed in single layer QWR sample in TEM images with $\mathbf{g}_{400}$ or $\mathbf{g}_{022}$ can be explained by the displacement field distribution along and perpendicular to the epitaxial growth direction [100], respectively. The different contrast patterns observed in TEM images with $\mathbf{g}_{022}$ for multilayer QWRs are attributed to the overlap and cancellation of the *X*-

displacement field from adjacent QWRs in correlated and anti-correlated stacks, respectively.

(2) The presence of the misfit dislocations in some multilayer QWR samples (M1 and M2 with $In_{0.53}Ga_{0.47}As$ and $In_{0.53}Ga_{0.37}Al_{0.10}As$ SLs/BLs, respectively) are interpreted as the result of the larger magnitude of in-plane strain ε_{xx} and the larger strained area present in the correlated QWR stacks than those in the samples with anti-correlated QWR stacks (such as sample M4 with $In_{0.52}Al_{0.48}As$ SLs/BLs) .

(3) The presence of the **In**-rich stripes observed in TEM images with $\mathbf{g}_{200}$ and HAADF images are interpreted as a result of the combined effect of the strain energy and surface energy densities of **In** on the SL growth front during the initial capping stage of QWRs.

(4) The variation of the multilayer QWR alignment from correlated (samples M1, M2) to anti-correlated stacks (sample M4) are attributed to the combined effect of the surface morphology and strain energy from the relaxation of underlying QWRs, as revealed by the calculations of the chemical potential density distribution of **In** on the SL growth front surface for different SL/BL materials.

(5) The surface morphology variations for the SL/BL materials are attributed to the different **In**/**Ga** ratios. The propagation directions of the **In**-rich stripes in different BL/SL materials can be understood by considering chemical potential density distribution of **In** on the SL growth front at the initial and final stages of the QWR capping process.

Chapter 8

Conclusions

8.1 General conclusions

8.1.1 QWR growth

Single and multilayer quantum wires (QWRs) were successfully fabricated by depositing InAs on $In_xGa_yAl_{1-x-y}As$ (x=0.52 or 0.53, y ranges from 0 to 0.47) grown lattice matched on InP substrates using gas source molecular beam epitaxy (GSMBE). Under the investigated range of growth parameters (shown in Tables 2-1 and 2-2), anisotropic QWRs were the predominantly observed nanostructures, and it was proposed that these features arise from the nucleation of the InAs layer on the anisotropic steps extending along $[0\bar{1}1]$ direction on the $In_xGa_yAl_{1-x-y}As$ surface.

By characterizing single layer QWR samples embedded within $In_{0.53}Ga_{0.37}Al_{0.10}As$ barrier layers (BLs), the growth conditions favoring QWR formation in GSMBE were determined as follows: (1) a deposition rate for the QWR layer of 0.4 ML/s; (2) QWR layer thickness of 3.5 ML-5.6 ML; and (3) substrate temperature of 520 °C for growing the BL/spacer layer (SL) and QWR layers. These parameters were also applied in fabricating multilayer QWR

samples with different (1) SL thicknesses; (2) QWR layer thicknesses; and (3) BL/SL compositions.

8.1.2 Structural features of QWRs

The main tools used for characterization and the experimentally observed structural features are summarized as follows.

(1) Qualitative structural information was achieved through diffraction contrast TEM imaging under different conditions for both single and multilayer QWRs. The compositional variation between QWRs and surrounding materials, the alignment patterns of QWR stacks was visually observed in TEM images taken under two beam conditions with $\mathbf{g}_{200}$. Also, the contrast patterns observed in images with $\mathbf{g}_{400}$ and $\mathbf{g}_{022}$ were interpreted as due to displacements of atomic planes parallel and perpendicular to the epitaxial growth direction, respectively. This was based on the comparison between experimental and finite element (FE) simulation results. Through displacement sensitive imaging, misfit dislocations were detected in some multilayer samples which were due to the accumulation of the strain energy according to the FE calculations.

(2) The lens-shape cross-section of the QWR was determined through the atomic number contrast recorded in high-resolution high angle annular dark field (HR-HAADF) images. Simultaneously, the height and base width of individual

QWR were determined and estimated as 6 nm and 20 nm for 5.6 ML InAs embedded within $In_{0.53}Ga_{0.37}Al_{0.10}As$, (Figure 4-13 (d)), respectively.

(3) Quantitative compositional analysis was carried out for QWR and BL/SLs with electron energy loss spectrometry (EELS) or energy dispersive X-ray spectrometry (EDXS) spectrum imaging (SI). The compositional map of **In** for individual QWRs in both single (Figure 4-17) and multilayer (Figure 5-3 (a)) QWR samples displayed three different regions based on the **In** concentrations; i.e. (1) **In**-rich centers comprising 70% ~75% **In** of the total group-III atomic concentration; (2) a thin intermediate layer with 65%~70% **In**; and (3) a outer layer with 60% **In**. The existence of a wetting layer (WL) with 60% **In** was confirmed through EELS-SI. Because of the presence of the WL, the formation of QWRs was interpreted as resulting from the Stranski-Krastanow (S-K) growth mode.

It was shown in a single layer QWR sample that a "stripe-like" contrast pattern is observed in upper BL using the diffraction contrast imaging ($\mathbf{g}_{200}$) and it was confirmed by EELS-SI that this arose from a composition modulation between **In** and **Ga**. The amplitude of this modulation is about 7%~12% increased **In** concentration above the nominal composition of the BL materials. The **In** compositional modulation in the upper BL was induced by the presence of the QWRs since the amplitude was greater than that in the spontaneous lateral

composition modulations (LCM) normally observed in material with the BL composition. As shown by the FE calculations of the surface chemical potential density, the presence of **In**-rich stripes resulted from the combined effect of the elastic strain energy and surface energy on the growth front surface of SL/BL covering the QWR. However, the positions and the number of such stripes were sensitive to the aspect ratio of individual QWRs. Moreover, the propagation direction of the **In**-rich stripes depended on the morphological evolution of the growth front surface, which is suggested based on the FE simulations for multilayer QWR samples.

(4) The alignment pattern of QWR stacks was investigated as a function of the SL thickness, the QWR layer thickness and the composition of SL/BLs. For the samples with 4 ML InAs the stacking pattern varied, due mainly to the strain field, from vertically aligned QWRs to randomly distributed QWRs as the SL thickness was increased from 8 nm to 25 nm. With the SL thickness fixed at 8 nm, the alignment of QWRs varied from an oblique stacking in a sample with 3 ML InAs to vertical alignment QWRs in samples with 4 ML, 5 ML and 7 ML InAs. When both the thickness of QWR layers (5 ML) and SLs (8 nm) were fixed, vertically aligned QWR stacks were observed in the samples embedded within $In_{0.53}Ga_{0.47}As$ and $In_{0.53}Ga_{0.37}Al_{0.10}As$ SL/BLs. While anti-correlated QWR stacks were achieved as the composition of the SL/BLs was changed to $In_{0.52}Al_{0.48}As$. As was shown by the FE simulations on the surface chemical potential density, this

transition in the alignment patterns was achieved through the modulation of the nucleation sites of QWRs, which were controlled by the combined effects of the strain field and surface morphology on the growth front of the SL.

8.1.3 Optical properties of QWRs

The optical emission wavelength was controllable by tuning SL thickness, the QWR layer thickness or the composition of the SL/BLs. A red-shift was detected in the photoluminescence (PL) spectra from both single and multilayer samples with: (1) increase of the QWR layer thickness; or (2) decrease of **Al** content in the SL/BLs; or (3) decrease of SL thickness. The experimentally observed red-shifts are mainly attributed either to the increase in QWR heights (Kümmell et al. 2006; Maes et al. 2004; Fuster et al. 2005) in cases (1) and (3), or to the reduced band discontinuities (ΔV_e and ΔV_h in Figure 1-2) between QWR layers and BLs/SLs (Ustinov et al. 1998; Tournié et al. 1993) in case (2).

Multiple-peak components were detected in low temperature PL spectra from QWR stacks with 3 ML and 4 ML InAs, and 8 nm $In_{0.53}Ga_{0.37}Al_{0.20}As$ SL. These components were attributed to photons generated from the recombination of the carriers between ground states within QWRs belonging to two predominant height families in each sample. Transfer of carriers between QWRs of the two families was proposed based on the PL spectra taken at different temperatures and those at low temperature with different excitation laser powers.

Optical emission at room temperature (RT) was achieved by post-growth treatment of two selected samples with etching and rapid thermal annealing. The anisotropic shape of QWRs were conserved after these treatments and the emission wavelength at RT ranged from 1.53~1.72 μm, which is suitable for potential applications in devices for telecommunications.

The investigations on the growth and characterizations of InAs QWRs grown on InGaAlAs lattice matched with an InP substrate and interpretations on the growth phenomena with FE models, provide the insights necessary to further control and modify the optical and structural properties of QWRs and the design of suitable samples for various device applications. Also, the work in this thesis contributes information for modeling the physical properties and to understand the growth process of semiconductor QWR structures.

8.2 Suggested future work

Proposed future work can be summarized in terms of growth and characterizations.

8.2.1 Growth

(1) Further investigation should be focused on establishing and optimizing the growth conditions for multilayer QWRs. For example, by changing the SL, QWR

layer thicknesses or the number of QWR and SL layers, defect-free QWR stacks with relatively uniform size distribution are desirable. Also, a sharp emission centered at 1.55 μm from the QWR structures at room temperature would be of interest for telecommunications applications.

(2) In order to capture the charged carriers more effectively than that in the QWR/SL stacks, QWR-in-a-quantum well structure should be designed. According to results shown in literature (Lelarge et al. 2007), higher gain and lower threshold current has been found in a laser device based on the QWR-in-a-quantum well structure than that in a device based on QWR-in-a-barrier structure. Thus, an improved device performance is expected from the QWR-in-a-quantum well structure.

(3) A laser device should be fabricated based on the QWR-in-a-quantum well structures with the further optimized growth conditions in (1). The performance of the device, in terms of gain and threshold current should be studied.

8.2.2 Ultrahigh resolution characterization

Ultra-high resolution characterization of the multilayer QWRs by HR-HAADF images with the new generation of aberration-corrected STEM should be undertaken. Firstly, the bi-model height distribution for QWRs in certain samples,

where the multiple-components in PL spectra were detected, can be confirmed explicitly through the atomic number contrast. As shown in Chapter 5, the height difference between the two main groups of QWRs was on the order of 2 ML (about 0.6 nm), which can not be resolved unambiguously by either the diffraction contrast imaging in CTEM or HAADF images taken on STEM without aberration-corrections. For example, the calibrated beam size for HAADF image (with ADF detector inner angle $\beta = 70\,\text{mrad}$) taken on JEOL 2010 is 0.9 nm, as mentioned in Chapter 4. Also, the resolution of atomic column positions in HR-HAADF images facilitates the strain analysis by geometric phase analysis (GPA) through image processing. More knowledge of the growth for multilayer QWRs could be obtained since the penetration of the strain field through SLs and its role in controlling the nucleation sites of QWRs in different layers can be visually observed in the GPA strain maps.

Appendix A

Calculation of structure factors and contrast for the $In_{1-x-y}Ga_xAl_yAs$ alloy on InP substrate

A.1 Atomic scattering factors for different elements on InP substrate

From Bragg's law: $\frac{\sin\theta}{\lambda}=\frac{1}{2d}$;

For **g**=200, $\frac{\sin\theta}{\lambda}=\frac{1}{2d_{200}}=\frac{1}{a_{InP}}=0.17$

Using the data from literature (Edington 1976), we have

$f_{In}=6.538\,\text{Å}$; $f_{Ga}=4.162\,\text{Å}$; $f_{Al}=2.798\,\text{Å}$; and $f_{As}=5.034\,\text{Å}$.

A.2 Calculations for different alloys

A.2.1 $In_xGa_{0.9-x}Al_{0.1}As$ ($0\le x\le 0.9$)

We assume that **Al** is uniformly distributed in the BLs, then $F=4\times(xf_{In}+(0.9-x)f_{Ga}+0.1\times f_{Al}-f_{As})$. Therefore, when x=0.37, F=0; x=0.9, F=4.52; x=0, F= -4.0336.

For lattice-matched quaternary alloy with InP, x=0.53. The DF TEM image contrast with **g**=200 between the $In_xGa_{0.9-x}Al_{0.1}As$ alloy and

$In_{0.53}Ga_{0.37}Al_{0.10}As$ is defined as: $C = \frac{I_{(x)} - I_{0.53}}{I_{0.53}}$, where $I_{(x)} \propto \left|F_{(x)}\right|^2$. Thus, the structure factor, square of structure factor and contrast are shown in the Figure A-1.

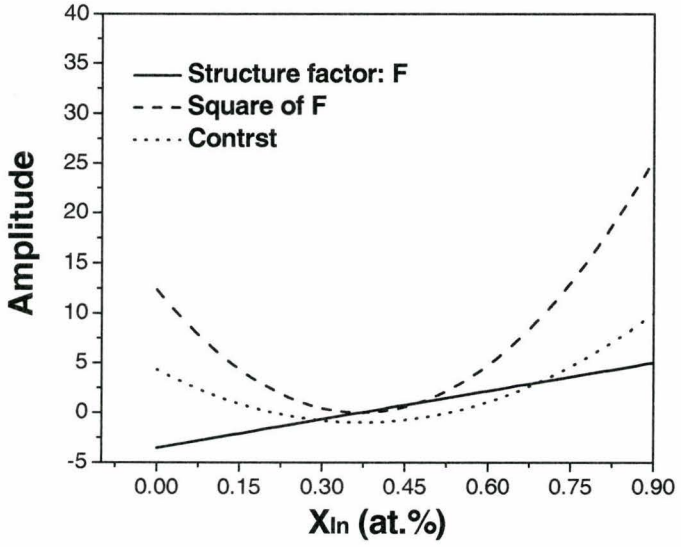

Figure A-1: Structure factor and contrast calculated based on the square of the structure factor for $In_xGa_{0.9-x}Al_{0.1}As$ alloy as a function of **In** content x.

From the plot above, we can see that positive contrast appears when $1 \geq x \geq 0.54$ or $0 \leq x \leq 0.2$. Therefore, quantification results showing 60% of **In** (EDXS results in Figure 4-19) corresponding to the brighter-stripes observed in DF (Figure 4-10 (c)) and HAADF (Figure 4-13 (c)) images agree well with the calculations.

A.2.2 $In_xGa_{0.8-x}Al_{0.2}As$ ($0 \leq x \leq 0.8$)

We assume that Al is distributed homogenously in the cladding layer area. $F = 4\times(xf_{In} + (0.8-x)f_{Ga} + 0.2\times f_{Al} - f_{As})$. When x=0.482, F=0; x=0.8, F=3.024; x=0, F=-4.5792.

For lattice-matched quaternary alloy with InP, x=0.53. The DF TEM image contrast with **g**=200 between the $In_xGa_{0.8-x}Al_{0.2}As$ alloy and $In_{0.53}Ga_{0.37}Al_{0.10}As$ is defined as: $C = \frac{I_{(x)} - I_{0.53}}{I_{0.53}}$, where $I_{(x)} \propto \left|F_{(x)}\right|^2$. Thus, the structure factor, square of structure factor and contrast are shown in the Figure A-2.

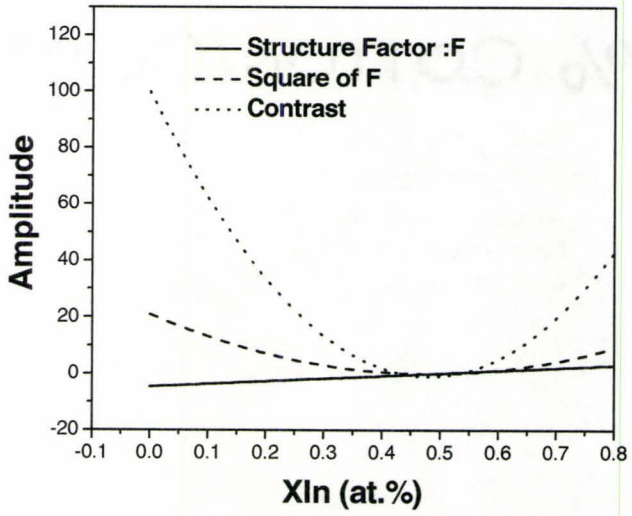

Figure A-2: Structure factor and contrast calculated based on the square of the structure factor for $In_xGa_{0.8-x}Al_{0.2}As$ alloy as a function of **In** content x.

From the plot above, we can see that positive contrast appears when $1 \geq x \geq 0.54$ or $0 \leq x \leq 0.43$. Therefore, quantification results showing 60% of **In** (EELS-SI results in Figure 5-3 (a)) corresponding to the brighter-stripes observed

in DF (Figure 5-2 (b)) and HAADF (Figure 5-2 (c)) images agree well with the calculations.

A.2.3 $In_xGa_{1-x}As$ ($0 \leq x \leq 1$)

$F = 4 \times (x f_{In} + (1-x) f_{Ga} - f_{As})$, when x=36.7%, F=0; x=0, F=-3.488; x=1, F= 6.016.

For lattice-matched quaternary alloy with InP, x=0.53, The DF TEM image contrast with **g**=200 between the $In_xGa_{1-x}As$ alloy and $In_{0.53}Ga_{0.47}As$ is defined as: $C = \frac{I_{(x)} - I_{0.53}}{I_{0.53}}$. Thus, the structure factor, square of structure factor and contrast are shown in the Figure A-3.

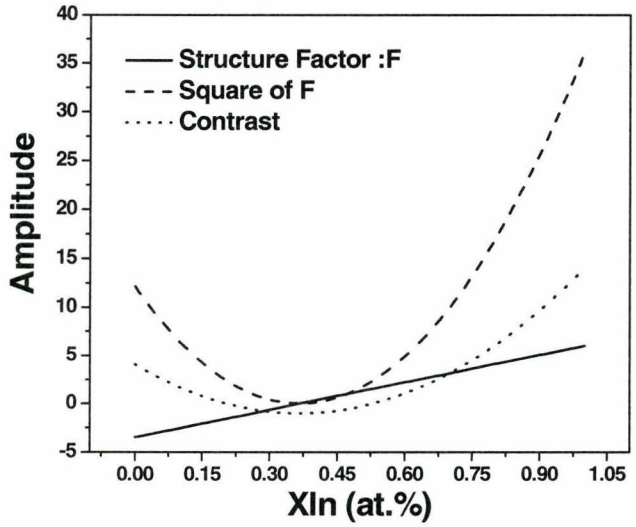

Figure A-3: Structure factor and contrast calculated based on the square of the structure factor for $In_xGa_{1-x}As$ alloy as a function of **In** content x.

Positive contrast should be theoretically expected when $0 \leq x \leq 20.4\%$ or $54\% \leq x \leq 1$. An **In** segregation with the amplitude about (53%-36.7%) =32.6% is not favorable (Pearson et al. 2004) due to the high mismatch energy. Also, the brighter contrast in $In_{0.53}Ga_{0.37}Al_{0.10}As$ has been assigned as **In**-rich regions and the structure factor, square of structure factor and contrast are very close for $In_xGa_{1-x}As$ and $In_xGa_{0.9-x}Al_{0.1}As$. Therefore, the brighter stripes in DF **g**=200 TEM images can be directly interpreted as the **In**-rich regions.

Appendix B

Calculation of inelastic mean free path in $In_{0.53}Ga_{0.37}Al_{0.10}As$

For $In_{0.53}Ga_{0.37}Al_{0.1}As$ BLs, the mean free path is calculated as:

$$\lambda = \frac{106FE_0}{\left\{E_m \ln\left(\frac{2\beta E_0}{E_m}\right)\right\}}$$ (Williams et al. 1996)

$$F = \frac{\left\{1+\frac{E_0}{1022}\right\}}{\left\{1+\left(\frac{E_0}{511}\right)\right\}^2} = \frac{\left\{1+\frac{200}{1022}\right\}}{\left\{1+\left(\frac{200}{511}\right)\right\}^2} = 0.6176$$

$$Z_{eff} = \frac{\sum_i f_i Z_i^{1.3}}{\sum_i f_i Z_i^{0.3}} = \frac{\left(\frac{0.53\times 49^{1.3}+0.37\times 31^{1.3}+0.1\times 13^{1.3}+1\times 33^{1.3}}{2}\right)}{\left(\frac{0.53\times 49^{0.3}+0.37\times 31^{0.3}+0.1\times 13^{0.3}+1\times 33^{0.3}}{2}\right)} = 36.59$$

$$E_m = 7.6\times Z_{eff}^{0.36} = 27.773\text{eV}$$

$\beta = 32.585$ (calibrated with the convergent electron beam diffraction)

Therefore,

$$\lambda = \frac{106FE_0}{\left\{E_m \ln\left(\frac{2\beta E_0}{E_m}\right)\right\}} = \frac{106\times 0.6176\times 200}{\left\{27.773\times \ln\left(\frac{2\times 32.585\times 200}{27.773}\right)\right\}} = 76.640\text{nm}$$

According to the measurements in the low loss region (zero loss plus plasma peaks) of the EELS spectrum, the sample thickness for EELS-SI in Chapter 4: $t \sim 0.4 - 0.7\lambda$, i.e. $t \sim 30$ nm-55 nm.

Appendix C

Estimation of beam broadening in EELS-SI

C.1 Convergence and collection angles for EELS-SI

As calibrated by the convergent beam electron diffraction pattern, EELS spectra were taken under following settings of JEOL 2010: C2 aperture: 50 mrad; ADF annular detector inner angle: β_0=70 mrad; the diameter of the EELS spectrometer entrance aperture is 5 mm; the convergence angle α of the electron beam and spectrum collection angle β are calibrated: α=6 mrad, β=32.58 mrad, respectively.

Based on the statements in Egerton's book (Egerton 1986), two comments can be made: (1) We have $\alpha<\beta$ therefore, no correction concerning the convergence angle of incident beam need to be made on the quantitative analysis equation (4-1) in Chapter 4. (2) No considerations for errors induced by "electron beam diffraction" need to be applied.

C.2 Beam broadening

The **In** distribution map (Figure 4-17) will be used as an example to estimate beam broadening.

(1) The absolute thickness of the investigated area is 54.10 nm, as estimated using the software of Digital Micrograph (Gatan, Inc., GMS 1.6.0).

(2) For the worst case, beam broadening should be estimated as βt (Egerton 1986), $\beta t \approx \sin\beta \times t = \sin(32.585\times10^{-3})\times54.10 = 1.76\text{nm}$.

(3) A more reasonable estimation should be carried out based on the cut-off angle above which the inelastic scattering associated with **In** $M_{4,5}$ edge is zero. As defined in the book of Williams (Williams et al. 1996), the cut-off angle $\theta_c = (2\theta_E)^{0.5}$;

where $\theta_E = \frac{E_{loss}}{(\gamma m_0 v^2)}$ and $\gamma = \left(1-\frac{v^2}{c^2}\right)^{-0.5} = \left(1-\left(\frac{2.086}{3}\right)^2\right)^{-0.5} = 1.3914$

Since the integral window ranges from 470 eV to 530 eV, the average energy loss of 500 eV is employed for calculations, therefore,

$$\theta_E = \frac{E_{loss}}{(\gamma m_0 v^2)} = \frac{E_{loss}}{(2\gamma E_0)} = \frac{500\text{eV}}{(2\times1.3914\times200\times1000\text{eV})} = 0.898\text{mrad}.$$

The cut-off angle is: $\theta_c = (2\theta_E)^{0.5} = (2\times0.898)^{0.5} = 1.340\text{mrad}$ and the beam broadening estimated with cut-off angle for **In** $M_{4,5}$ edge is:

$\theta_c t = \sin\theta_c \times t = \sin(1.340\times10^{-3})\times54.10 = 0.0725\text{nm}$.

Appendix D

Delocalization of the inelastic scattering

According to Egerton's book (Egerton 1986), the delocalization (d_d) of electrons associated with an edge in EELS spectrum is: $d_d \approx \frac{0.5\lambda}{\theta_E^{0.75}}$, where λ (nm) is the wavelength of incoming electrons and θ_E (radian) is the characteristic angle associated with the **In** $M_{4,5}$ edge, which has been calculated in **Appendix C**.

$$d_d \approx \frac{0.5\lambda}{\theta_E^{0.75}} = \frac{0.5\times 0.00273}{(0.898\times 10^{-3})^{0.75}} = 0.26\text{nm}$$

Apendix E

FlexPDE code for calculating displacement and strain field in two aligned QWR columns

```
TITLE 'Two columns of aligned QWRs within In0.53Ga0.37Al0.10As SL/BLs-Three QWRs in each-Compostional map included'

{Taking sample M2 in Figure 5-21 (b) as example}
SELECT                  {Method controls}
 NOMINMAX=ON            {Turn off min-max value locators from obscuring plot}
 FEATUREPLOT=OFF
 ERRLIM=3e-3            {Control the erroe limit for final results}

{***********************************************}

COORDINATES
 Cartesian3             {Sets up 3d solver}

 {***********************************************}

VARIABLES               {System variables}
 U                      {X displacement.}
 V                      {Y displacement.}
 W                      {Z displacement.}

 {***********************************************}

DEFINITIONS             {Parameter definitions}
{ M_Z = matrix thickness along Z direction, which is along the epitaxial direction of [100];
 M_X = matrix width in the X direction of [011];
 M_Y = matrix width in the Y direction of [0-11];
 WL = wetting layer thickness along Z direction;
 D = distance of the wetting layer from the bottom surface along Z direction;
 Core_H= the height of indium-rich core (yellow portion in Figure 4-17(a));
 Core_R= radius of the indium-rich core;
 DflH_Below=the height of indium diffusion layer (green portion in Figure 4-17(a)) below the WL;
 DflH_Up=the distance between the top of WL and upper indium diffusion layer;
 Dfl_R=radius of indium diffusion layer below or above the WL;
 Shell_H=height of the shell (red portion in Figure 4-17(a)) between the core and diffusion layer.
 Shell_R=radius of the shell between the core and diffusion layer
 Shell+Core=the QWR dimensions we see from atomic number contrast in HAADF images
 QWire_T_Z=total height of the diffusion layer above WL.
 xs1=center of QWRs in column 1
 xs2=center of QWRs in column 2
Zlens_Shell=Define the shape and boundary of the shell between indium-rich core and diffusion layer, the shell is above WL
Zlens_Core=Define the shape and boundary of the indium-rich core.
Zlens_Dfl_Up=Define the shape and boundary of the upper diffusion layer.
Zlens_Dfl_Below=Define the shape and boundary of the diffusion layer below the WL.
```

aInAs=Lattice constant of InAs
aGaAs=Lattice constant of GaAs
aInP=Lattice constant of InP
Cin=the compositional profile of Indium
f = the fractional lattice mismatch between the materials in different layers and InP

Zlens1 through Zlens5: to control the thickness of different len-shaped LAYERS in diffrent REGIONS.
Zlens1=the variable to control the top position of the diffusion layer below the WL
Zlens2=the variable to control the top position of the shell layler below the WL
Zlens3=the variable to control the top position of Indium rich core
Zlens4=the variable to control the top position of the shell between indium-rich core and diffusion layer
Zlens5=the variable to control the top position of the diffusion layer above the WL

SL= spacer layer thickness between adjacent QWR layers
C11,C12,C44= Elastic constants for different Zinc-Blend crystals}

M_X =100 {in nm}
M_Y =50 {in nm}
M_Z = 80 {in nm}
WL = 1 {in nm}
D =30 {in nm}
Core_H=4.60 {in nm}
Core_R=8.50 {in nm}
DflH_Below=1.85*5/6 {in nm}
ShellH_Below=0.93*5/6 {in nm}
Dfl_R=11.04 {in nm}
DflH_Up=7.69*5/6 {in nm}
Shell_H=6.57*5/6 {in nm}
Shell_R=10 {in nm}
xs1=14 {in nm}
xs2=-14 {in nm} {The 14 nm means the separation of adjacent QWRs is 4 nm}
QWire_T_Z=DflH_Up
SL=10 {in nm}
Zlens1
Zlens2
Zlens3
Zlens4
Zlens5

{Define the elastic constant under the <100> system}
C11
C12
C44

{Define the elastic constant under the [011]-[0-11]-[100] system, according to Okada et al. 1997}
C11T=0.5*(C11+C12)+C44
C12T=0.5*(C11+C12)-C44
C44T=C44

Cin=0.53

{Default value of indium concentration in matrix layer. The indium rich core is In0.75Ga0.25As, the shell layer In0.65Ga0.35As, the diffusion layer and the wetting layer are In0.60Ga0.30Al0.10As.}

f {mismatch between different layers}

{lattice parameters for binary alloys involving in the structure. From Vurgaftman et al. 2001}
aInAs=6.0583 {in astrom}
aGaAs=5.65325 {in astrom}
aInP=5.8687 {in astrom}
aAlAs=5.6611 {in astrom}

{Set the material identifier so that we can check if the shape of each region is defined properly }
{0.0 = matrix; 1.0 =indium diffusion layer and WL ;2.0= indium shell between the diffusion layer and core ; 3.0= indium-rich core}
Material = 0.0 {default value for matrix}

{outer boundary for QWRs in column 1}
Zlens_Dfl_Below1=D-min(max(DflH_Below*(1-(((x-xs1)^2)/(Dfl_R)^2)),0),DflH_Below)
Zlens_ShellH_Below1=D-min(max(ShellH_Below*(1-(((x-xs1)^2)/(Shell_R)^2)),0),ShellH_Below)
Zlens_Core1=min(max(Core_H*(1-(((x-xs1)^2)/(Core_R)^2)),0),Core_H)+D+WL
Zlens_Shell1=min(max(Shell_H*(1-(((x-xs1)^2)/(Shell_R)^2)),0),Shell_H)+D+WL
Zlens_Dfl_Up1=min(max(DflH_Up*(1-(((x-xs1)^2)/(Dfl_R)^2)),0),DflH_Up)+D+WL

{outer boundary for QWRs in column 2}
Zlens_Dfl_Below2=D-min(max(DflH_Below*(1-(((x-xs2)^2)/(Dfl_R)^2)),0),DflH_Below)
Zlens_ShellH_Below2=D-min(max(ShellH_Below*(1-(((x-xs2)^2)/(Shell_R)^2)),0),ShellH_Below)
Zlens_Core2=min(max(Core_H*(1-(((x-xs2)^2)/(Core_R)^2)),0),Core_H)+D+WL
Zlens_Shell2=min(max(Shell_H*(1-(((x-xs2)^2)/(Shell_R)^2)),0),Shell_H)+D+WL
Zlens_Dfl_Up2=min(max(DflH_Up*(1-(((x-xs2)^2)/(Dfl_R)^2)),0),DflH_Up)+D+WL

{Elastic constants in unit of 10^8 Pa for InAs from Adachi 2004.}
C11InAs=832.9
C12InAs=452.6
C44InAs=395.9

{Elastic constants in unit of 10^8 Pa for GaAs from Adachi 2004.}
C11GaAs=1221
C12GaAS=566
C44GaAs=600

{Elastic constants in unit of 10^8 Pa for AlAs from Adachi 2004.}
C11AlAs=1250
C12AlAs=534
C44AlAs=542

{Define the anisotropic elastic constants for the nominal In0.53Ga0.37Al0.1As cladding layers in Pa accoding to Vegard's law (Vegard 1921).}
C11MAT = (0.53*C11InAs+0.37*C11GaAs+0.1*C11AlAs)*100000000
C12MAT = (0.53*C12InAs+0.37*C12GaAs+0.1*C12AlAs)*100000000
C44MAT = (0.53*C44InAs+0.37*C44GaAs+0.1*C44AlAs)*100000000

```
 {Define the strain variables.}
ex = dx(U)
ey = dy(V)
ez = dz(W)
eh = ex+ey+ez+ex*ey+ex*ez+ey*ez+ex*ey*ez {Volume strain.}

 {Define the stress variables.}
 gxy = dy(U) + dx(V)
 gyz = dz(V) + dy(W)
 gzx = dx(W) + dz(U)

{Define the stress according the results listed in Okada et al. 1997}
 Sx = C11T*(ex-f) + C12T*(ey-f) + C12*(ez-f)
 Sy = C12T*(ex-f) + C11T*(ey-f) + C12*(ez-f)
 Sz = C12*(ex-f) + C12*(ey-f) + C11*(ez-f)
 Txy = C44T*gxy
 Tyz = C44T*gyz
 Tzx = 0.5*(C11-C12)*gzx

{Find mean translation and rotation. }
 Vol = Integral(1)                  {Intergral over all the box}
 Tx = integral(U)/Vol               {X-motion}
 Ty = integral(V)/Vol               {Y-motion}
 Tz = integral(W)/Vol               {Z-motion}
 Rz = integral(dx(V) - dy(U))/Vol   {Z-rotation}
 Rx = integral(dy(W) - dz(V))/Vol   {X-rotation}
 Ry = integral(dz(U) - dx(W))/Vol   {Y-rotation}

{Displacements with translation and rotation removed.}
 Up = U - Tx + Rz*y - Ry*z
 Vp = V - Ty + Rx*z - Rz*x
 Wp = W - Tz + Ry*x - Rx*y

{Derivatives required for Fortran TEM simulation program in [001] zone axis.}
 Uz=dz(Up)
 Vz=dz(Vp)
 Wz=dz(Wp)

 {***********************************************}

INITIAL VALUES
 U= 0
 V = 0
 W = 0

 {***********************************************}

EQUATIONS                           {PDE's, one for each variable.}
   U:    dx(Sx) + dy(Txy) + dz(Tzx) = 0   { the U-displacement equation }
   V:    dx(Txy) + dy(Sy) + dz(Tyz) = 0   { the V-displacement equation }
   W:    dx(Tzx) + dy(Tyz) + dz(Sz) = 0   { the W-displacement equation }
```

```
{*********************************************}

EXTRUSION
SURFACE 'Bottom' z=0
LAYER 'Underneath the Dfl_Below 1'
SURFACE 'Bottom of Dfl_Below 1' z = Zlens1
LAYER 'Diffusion layer below 1'
SURFACE 'Shell_Below layer Bottom 1' z = Zlens2
LAYER 'Shell layer below 1'
SURFACE 'Bottom of wetting layer 1' z=D
LAYER'Wetting Layer 1'
SURFACE 'Bottom of core 1' z=D+WL
LAYER'Core 1'
SURFACE' Bottom of the shell 1' z=Zlens3
LAYER'Shell 1'
SURFACE' Bottom of the diffusion layer 1' z=Zlens4
LAYER'Diffusion layer up 1'
SURFACE'Top of Dfl_up 1' z=Zlens5
LAYER'SL 1'
SURFACE 'Bottom of Dfl_Below 2' z=SL+WL+Zlens1
Layer 'Diffusion layer below 2'
SURFACE 'Shell_Below layer Bottom 2' z = Zlens2+SL+WL
LAYER 'Shell layer below 2'
SURFACE 'Bottom of wetting layer 2' z=D+WL+SL
LAYER'Wetting Layer 2'
SURFACE 'Bottom of core 2' z=D+SL+2*WL
LAYER'Core 2'
SURFACE' Bottom of the shell 2' z=Zlens3+SL+WL
LAYER'Shell 2'
SURFACE' Bottom of the diffusion layer 2' z=Zlens4+SL+WL
LAYER'Diffusion layer up 2'
SURFACE'Top of Dfl_up 2' z=Zlens5+SL+WL
LAYER'SL 2'
SURFACE 'Bottom of Dfl_Below 3' z=2*(SL+WL)+Zlens1
LAYER 'Diffusion layer below 3'
SURFACE 'Shell_Below layer Bottom 3' z = Zlens2+2*(SL+WL)
LAYER 'Shell layer below 3'
SURFACE 'Bottom of wetting layer 3' z=D+2*(WL+SL)
LAYER'Wetting Layer 3'
SURFACE 'Bottom of core 3' z=D+2*(SL+WL)+WL
LAYER'Core 3'
SURFACE' Bottom of the shell 3' z=Zlens3+2*(SL+WL)
LAYER'Shell 3'
SURFACE' Bottom of the diffusion layer 3' z=Zlens4+2*(SL+WL)
LAYER'Diffusion layer up 3'
SURFACE'Top of Dfl_up 3' z=Zlens5+2*(SL+WL)
LAYER'Above QWR'
SURFACE'ToP of the structure' z= M_Z

{*********************************************}

BOUNDARIES    {The domain definition.}
```

{Programs default to Natural boundary conditions on all of the surfaces. This is correct for the top and bottom surfaces but not for the sides which are effectively infinite in extent. Get around this by making the x and y dimensions large so that edge effects do not affect the result. }

{set boundary conditions}
Surface 'Top of the structure'
Natural (U)=0
Natural (V)=0
Natural (W)=0
{This set of boundary condistions is equivalent to the condition that the tractions are free on the top surface: Sz=Tzx=Tyz=0}

Surface 'Bottom'
Value (W)=0
{This means the displacement of the atomic plane at the bottom of the simulated box is zero}

REGION 1 'Matrix'
mesh_spacing=40
Zlens1=D
Zlens2=D
Zlens3=D+WL
Zlens4=D+WL
Zlens5=D+WL

LAYER'Underneath the Dfl_Below 1'
Material = 0.0
f = 0.0
C11 = C11MAT
C12 = C12MAT
C44 = C44MAT

LAYER 'Diffusion layer below 1'
Material = 0.0
f = 0.0
C11 = C11MAT
C12 = C12MAT
C44 = C44MAT

LAYER 'Shell layer below 1'
Material = 0.0
f = 0.0
C11 = C11MAT
C12 = C12MAT
C44 = C44MAT

LAYER 'Wetting Layer 1'
Material = 1.0
Cin=0.60
f = (Cin*aInAs+(0.9-Cin)*aGaAs+0.1*aAlAs-aInP)/aInP
C11 = (C11InAs*Cin+C11GaAs*(0.9-Cin)+C11AlAs*0.1)*100000000
C12 = (C12InAs*Cin+C12GaAs*(0.9-Cin)+C12AlAs*0.1)*100000000
C44 = (C44InAs*Cin+C44GaAs*(0.9-Cin)+C44AlAs*0.1)*100000000
{The composition of the wetting layer is In0.60Ga0.30Al0.10As}

```
LAYER'Core 1'
Material = 0.0
f = 0.0
C11 = C11MAT
C12 = C12MAT
C44 = C44MAT

LAYER'Shell 1'
Material = 0.0
f = 0.0
C11 = C11MAT
C12 = C12MAT
C44 = C44MAT

LAYER'Diffusion layer up 1'
Material = 0.0
f = 0.0
C11 = C11MAT
C12 = C12MAT
C44 = C44MAT

LAYER'SL 1'
Material = 0.0
f = 0.0
C11 = C11MAT
C12 = C12MAT
C44 = C44MAT

LAYER 'Diffusion layer below 2'
Material = 0.0
f = 0.0
C11 = C11MAT
C12 = C12MAT
C44 = C44MAT

LAYER 'Shell layer below 2'
Material = 0.0
f = 0.0
C11 = C11MAT
C12 = C12MAT
C44 = C44MAT

LAYER 'Wetting Layer 2'
Material = 1.0
Cin=0.60
f = (Cin*aInAs+(0.9-Cin)*aGaAs+0.1*aAlAs-aInP)/aInP
C11 = (C11InAs*Cin+C11GaAs*(0.9-Cin)+C11AlAs*0.1)*100000000
C12 =  (C12InAs*Cin+C12GaAs*(0.9-Cin)+C12AlAs*0.1)*100000000
C44 =  (C44InAs*Cin+C44GaAs*(0.9-Cin)+C44AlAs*0.1)*100000000
{The composition of the wetting layer is In0.60Ga0.30Al0.10As}

LAYER'Core 2'
```

```
Material = 0.0
f = 0.0
C11 = C11MAT
C12 = C12MAT
C44 = C44MAT

LAYER'Shell 2'
Material = 0.0
f = 0.0
C11 = C11MAT
C12 = C12MAT
C44 = C44MAT

LAYER'Diffusion layer up 2'
Material = 0.0
f = 0.0
C11 = C11MAT
C12 = C12MAT
C44 = C44MAT

LAYER'SL 2'
Material = 0.0
f = 0.0
C11 = C11MAT
C12 = C12MAT
C44 = C44MAT

LAYER 'Diffusion layer below 3'
Material = 0.0
f = 0.0
C11 = C11MAT
C12 = C12MAT
C44 = C44MAT

LAYER 'Shell layer below 3'
Material = 0.0
f = 0.0
C11 = C11MAT
C12 = C12MAT
C44 = C44MAT

LAYER 'Wetting Layer 3'
Material = 1.0
Cin=0.60
f = (Cin*aInAs+(0.9-Cin)*aGaAs+0.1*aAlAs-aInP)/aInP
C11 = (C11InAs*Cin+C11GaAs*(0.9-Cin)+C11AlAs*0.1)*100000000
C12 =  (C12InAs*Cin+C12GaAs*(0.9-Cin)+C12AlAs*0.1)*100000000
C44 =  (C44InAs*Cin+C44GaAs*(0.9-Cin)+C44AlAs*0.1)*100000000
{The composition of the wetting layer is In0.60Ga0.30Al0.10As}

LAYER'Core 3'
Material = 0.0
 f = 0.0
```

```
C11 = C11MAT
C12 = C12MAT
C44 = C44MAT

LAYER'Shell 3'
Material = 0.0
f = 0.0
C11 = C11MAT
C12 = C12MAT
C44 = C44MAT

LAYER'Diffusion layer up 3'
Material = 0.0
f = 0.0
C11 = C11MAT
C12 = C12MAT
C44 = C44MAT

LAYER'Above QWR'
Material = 0.0
f = 0.0
C11 = C11MAT
C12 = C12MAT
C44 = C44MAT

START (-M_X/2,-M_Y/2)
 VALUE(V) = 0.0
LINE TO(M_X/2,-M_Y/2)
 VALUE(U) = 0.0
LINE TO(M_X/2,M_Y/2)
 VALUE(V) = 0.0
LINE TO(-M_X/2,M_Y/2)
 VALUE(U) = 0.0
LINE TO CLOSE
{the positions of the side walls are fixed}

{************************************************}

REGION 2 'Diffusion Wire xs1'
mesh_spacing=40
Zlens1=Zlens_Dfl_Below1
Zlens2=D
Zlens3=D+WL
Zlens4=D+WL
Zlens5=Zlens_Dfl_Up1

LAYER'Underneath the Dfl_Below 1'
Material = 0.0
f = 0.0
C11 = C11MAT
C12 = C12MAT
C44 = C44MAT
```

```
LAYER 'Diffusion layer below 1'
Material = 1.0
Cin=0.60
f = (Cin*aInAs+(0.9-Cin)*aGaAs+0.1*aAlAs-aInP)/aInP
C11 = (C11InAs*Cin+C11GaAs*(0.9-Cin)+0.1*C11AlAs)*100000000
C12 = (C12InAs*Cin+C12GaAs*(0.9-Cin)+0.1*C12AlAs)*100000000
C44 = (C44InAs*Cin+C44GaAs*(0.9-Cin)+0.1*C44AlAs)*100000000
{the composition of the diffusion layer is In0.60Ga0.30Al0.10As}

LAYER 'Shell layer below 1'
Material = 1.0
Cin=0.60
f = (Cin*aInAs+(0.9-Cin)*aGaAs+0.1*aAlAs-aInP)/aInP
C11 = (C11InAs*Cin+C11GaAs*(0.9-Cin)+0.1*C11AlAs)*100000000
C12 = (C12InAs*Cin+C12GaAs*(0.9-Cin)+0.1*C12AlAs)*100000000
C44 = (C44InAs*Cin+C44GaAs*(0.9-Cin)+0.1*C44AlAs)*100000000

LAYER 'Wetting Layer 1'
Material = 1.0
Cin=0.60
f = (Cin*aInAs+(0.9-Cin)*aGaAs+0.1*aAlAs-aInP)/aInP
C11 = (C11InAs*Cin+C11GaAs*(0.9-Cin)+0.1*C11AlAs)*100000000
C12 = (C12InAs*Cin+C12GaAs*(0.9-Cin)+0.1*C12AlAs)*100000000
C44 = (C44InAs*Cin+C44GaAs*(0.9-Cin)+0.1*C44AlAs)*100000000

LAYER'Core 1'
Material = 1.0
Cin=0.60
f = (Cin*aInAs+(0.9-Cin)*aGaAs+0.1*aAlAs-aInP)/aInP
C11 = (C11InAs*Cin+C11GaAs*(0.9-Cin)+0.1*C11AlAs)*100000000
C12 = (C12InAs*Cin+C12GaAs*(0.9-Cin)+0.1*C12AlAs)*100000000
C44 = (C44InAs*Cin+C44GaAs*(0.9-Cin)+0.1*C44AlAs)*100000000

LAYER'Shell 1'
Material = 1.0
Cin=0.60
f = (Cin*aInAs+(0.9-Cin)*aGaAs+0.1*aAlAs-aInP)/aInP
C11 = (C11InAs*Cin+C11GaAs*(0.9-Cin)+0.1*C11AlAs)*100000000
C12 = (C12InAs*Cin+C12GaAs*(0.9-Cin)+0.1*C12AlAs)*100000000
C44 = (C44InAs*Cin+C44GaAs*(0.9-Cin)+0.1*C44AlAs)*100000000

LAYER'Diffusion layer up 1'
Material = 1.0
Cin=0.60
f = (Cin*aInAs+(0.9-Cin)*aGaAs+0.1*aAlAs-aInP)/aInP
C11 = (C11InAs*Cin+C11GaAs*(0.9-Cin)+0.1*C11AlAs)*100000000
C12 = (C12InAs*Cin+C12GaAs*(0.9-Cin)+0.1*C12AlAs)*100000000
C44 = (C44InAs*Cin+C44GaAs*(0.9-Cin)+0.1*C44AlAs)*100000000

LAYER'SL 1'
Material = 0.0
f = 0.0
C11 = C11MAT
```

```
C12 = C12MAT
C44 = C44MAT

LAYER 'Diffusion layer below 2'
Material = 1.0
Cin=0.60
f = (Cin*aInAs+(0.9-Cin)*aGaAs+0.1*aAlAs-aInP)/aInP
C11 = (C11InAs*Cin+C11GaAs*(0.9-Cin)+0.1*C11AlAs)*100000000
C12 = (C12InAs*Cin+C12GaAs*(0.9-Cin)+0.1*C12AlAs)*100000000
C44 = (C44InAs*Cin+C44GaAs*(0.9-Cin)+0.1*C44AlAs)*100000000
{the composition of the diffusion layer is In0.60Ga0.30Al0.10As}

LAYER 'Shell layer below 2'
Material = 1.0
Cin=0.60
f = (Cin*aInAs+(0.9-Cin)*aGaAs+0.1*aAlAs-aInP)/aInP
C11 = (C11InAs*Cin+C11GaAs*(0.9-Cin)+0.1*C11AlAs)*100000000
C12 = (C12InAs*Cin+C12GaAs*(0.9-Cin)+0.1*C12AlAs)*100000000
C44 = (C44InAs*Cin+C44GaAs*(0.9-Cin)+0.1*C44AlAs)*100000000
{the composition of the diffusion layer is In0.60Ga0.30Al0.10As}

LAYER 'Wetting Layer 2'
Material = 1.0
Cin=0.60
f = (Cin*aInAs+(0.9-Cin)*aGaAs+0.1*aAlAs-aInP)/aInP
C11 = (C11InAs*Cin+C11GaAs*(0.9-Cin)+0.1*C11AlAs)*100000000
C12 = (C12InAs*Cin+C12GaAs*(0.9-Cin)+0.1*C12AlAs)*100000000
C44 = (C44InAs*Cin+C44GaAs*(0.9-Cin)+0.1*C44AlAs)*100000000

LAYER'Core 2'
Material = 1.0
Cin=0.60
f = (Cin*aInAs+(0.9-Cin)*aGaAs+0.1*aAlAs-aInP)/aInP
C11 = (C11InAs*Cin+C11GaAs*(0.9-Cin)+0.1*C11AlAs)*100000000
C12 = (C12InAs*Cin+C12GaAs*(0.9-Cin)+0.1*C12AlAs)*100000000
C44 = (C44InAs*Cin+C44GaAs*(0.9-Cin)+0.1*C44AlAs)*100000000
{the composition of the diffusion layer is In0.60Ga0.30Al0.10As}

LAYER'Shell 2'
Material = 1.0
Cin=0.60
f = (Cin*aInAs+(0.9-Cin)*aGaAs+0.1*aAlAs-aInP)/aInP
C11 = (C11InAs*Cin+C11GaAs*(0.9-Cin)+0.1*C11AlAs)*100000000
C12 = (C12InAs*Cin+C12GaAs*(0.9-Cin)+0.1*C12AlAs)*100000000
C44 = (C44InAs*Cin+C44GaAs*(0.9-Cin)+0.1*C44AlAs)*100000000
{the composition of the diffusion layer is In0.60Ga0.30Al0.10As}

LAYER'Diffusion layer up 2'
Material = 1.0
Cin=0.60
f = (Cin*aInAs+(0.9-Cin)*aGaAs+0.1*aAlAs-aInP)/aInP
C11 = (C11InAs*Cin+C11GaAs*(0.9-Cin)+0.1*C11AlAs)*100000000
C12 = (C12InAs*Cin+C12GaAs*(0.9-Cin)+0.1*C12AlAs)*100000000
```

```
C44 = (C44InAs*Cin+C44GaAs*(0.9-Cin)+0.1*C44AlAs)*100000000
{the composition of the diffusion layer is In0.60Ga0.30Al0.10As}

LAYER'SL 2'
Material = 0.0
f = 0.0
C11 = C11MAT
C12 = C12MAT
C44 = C44MAT

LAYER 'Diffusion layer below 3'
Material = 1.0
Cin=0.60
f = (Cin*aInAs+(0.9-Cin)*aGaAs+0.1*aAlAs-aInP)/aInP
C11 = (C11InAs*Cin+C11GaAs*(0.9-Cin)+0.1*C11AlAs)*100000000
C12 = (C12InAs*Cin+C12GaAs*(0.9-Cin)+0.1*C12AlAs)*100000000
C44 = (C44InAs*Cin+C44GaAs*(0.9-Cin)+0.1*C44AlAs)*100000000
{the composition of the diffusion layer is In0.60Ga0.30Al0.10As}

LAYER 'Shell layer below 3'
Material = 1.0
Cin=0.60
f = (Cin*aInAs+(0.9-Cin)*aGaAs+0.1*aAlAs-aInP)/aInP
C11 = (C11InAs*Cin+C11GaAs*(0.9-Cin)+0.1*C11AlAs)*100000000
C12 = (C12InAs*Cin+C12GaAs*(0.9-Cin)+0.1*C12AlAs)*100000000
C44 = (C44InAs*Cin+C44GaAs*(0.9-Cin)+0.1*C44AlAs)*100000000

LAYER 'Wetting Layer 3'
Material = 1.0
Cin=0.60
f = (Cin*aInAs+(0.9-Cin)*aGaAs+0.1*aAlAs-aInP)/aInP
C11 = (C11InAs*Cin+C11GaAs*(0.9-Cin)+0.1*C11AlAs)*100000000
C12 = (C12InAs*Cin+C12GaAs*(0.9-Cin)+0.1*C12AlAs)*100000000
C44 = (C44InAs*Cin+C44GaAs*(0.9-Cin)+0.1*C44AlAs)*100000000

LAYER'Core 3'
Material = 1.0
Cin=0.60
f = (Cin*aInAs+(0.9-Cin)*aGaAs+0.1*aAlAs-aInP)/aInP
C11 = (C11InAs*Cin+C11GaAs*(0.9-Cin)+0.1*C11AlAs)*100000000
C12 = (C12InAs*Cin+C12GaAs*(0.9-Cin)+0.1*C12AlAs)*100000000
C44 = (C44InAs*Cin+C44GaAs*(0.9-Cin)+0.1*C44AlAs)*100000000

LAYER'Shell 3'
Material = 1.0
Cin=0.60
f = (Cin*aInAs+(0.9-Cin)*aGaAs+0.1*aAlAs-aInP)/aInP
C11 = (C11InAs*Cin+C11GaAs*(0.9-Cin)+0.1*C11AlAs)*100000000
C12 = (C12InAs*Cin+C12GaAs*(0.9-Cin)+0.1*C12AlAs)*100000000
C44 = (C44InAs*Cin+C44GaAs*(0.9-Cin)+0.1*C44AlAs)*100000000

LAYER'Diffusion layer up 3'
Material = 1.0
```

```
Cin=0.60
f = (Cin*aInAs+(0.9-Cin)*aGaAs+0.1*aAlAs-aInP)/aInP
C11 = (C11InAs*Cin+C11GaAs*(0.9-Cin)+0.1*C11AlAs)*100000000
C12 = (C12InAs*Cin+C12GaAs*(0.9-Cin)+0.1*C12AlAs)*100000000
C44 = (C44InAs*Cin+C44GaAs*(0.9-Cin)+0.1*C44AlAs)*100000000

LAYER'Above QWR'
Material = 0.0
 f = 0.0
C11 = C11MAT
C12 = C12MAT
C44 = C44MAT

START (-(Dfl_R-xs1),-M_Y/2) LINE TO((Dfl_R+xs1),-M_Y/2) LINE TO((Dfl_R+xs1),M_Y/2)
LINE TO(-(Dfl_R-xs1),M_Y/2) LINE TO CLOSE
{**********************************************}


REGION 3 'Shell Wire xs1'
mesh_spacing=40
Zlens1=Zlens_Dfl_Below1
Zlens2=Zlens_ShellH_Below1
Zlens3=D+WL
Zlens4=Zlens_Shell1
Zlens5=Zlens_Dfl_Up1

LAYER'Underneath the Dfl_Below 1'
Material = 0.0
f = 0.0
C11 = C11MAT
C12 = C12MAT
C44 = C44MAT

LAYER 'Diffusion layer below 1'
Material = 1.0
Cin=0.60
f = (Cin*aInAs+(0.9-Cin)*aGaAs+0.1*aAlAs-aInP)/aInP
C11 = (C11InAs*Cin+C11GaAs*(0.9-Cin)+0.1*C11AlAs)*100000000
C12 = (C12InAs*Cin+C12GaAs*(0.9-Cin)+0.1*C12AlAs)*100000000
C44 = (C44InAs*Cin+C44GaAs*(0.9-Cin)+0.1*C44AlAs)*100000000
{the compostion of the diffusion layer is In0.60Ga0.30Al0.1As}

LAYER 'Shell layer below 1'
Material = 2.0
Cin=0.65
f = (Cin*aInAs+(1-Cin)*aGaAs-aInP)/aInP
C11 = (C11InAs*Cin+C11GaAs*(1-Cin))*100000000
C12 =  (C12InAs*Cin+C12GaAs*(1-Cin))*100000000
C44 =  (C44InAs*Cin+C44GaAs*(1-Cin))*100000000

{the composition of the shell layer is In0.65Ga0.35As}

LAYER 'Wetting Layer 1'
```

```
Material = 2.0
Cin=0.65
f = (Cin*aInAs+(1-Cin)*aGaAs-aInP)/aInP
C11 = (C11InAs*Cin+C11GaAs*(1-Cin))*100000000
C12 =  (C12InAs*Cin+C12GaAs*(1-Cin))*100000000
C44 =  (C44InAs*Cin+C44GaAs*(1-Cin))*100000000

LAYER'Core 1'
Material = 2.0
Cin=0.65
f = (Cin*aInAs+(1-Cin)*aGaAs-aInP)/aInP
C11 = (C11InAs*Cin+C11GaAs*(1-Cin))*100000000
C12 =  (C12InAs*Cin+C12GaAs*(1-Cin))*100000000
C44 =  (C44InAs*Cin+C44GaAs*(1-Cin))*100000000

LAYER'Shell 1'
Material = 2.0
Cin=0.65
f = (Cin*aInAs+(1-Cin)*aGaAs-aInP)/aInP
C11 = (C11InAs*Cin+C11GaAs*(1-Cin))*100000000
C12 =  (C12InAs*Cin+C12GaAs*(1-Cin))*100000000
C44 =  (C44InAs*Cin+C44GaAs*(1-Cin))*100000000

LAYER'Diffusion layer up 1'
Material = 1.0
Cin=0.60
f = (Cin*aInAs+(0.9-Cin)*aGaAs+0.1*aAlAs-aInP)/aInP
C11 = (C11InAs*Cin+C11GaAs*(0.9-Cin)+0.1*C11AlAs)*100000000
C12 = (C12InAs*Cin+C12GaAs*(0.9-Cin)+0.1*C12AlAs)*100000000
C44 = (C44InAs*Cin+C44GaAs*(0.9-Cin)+0.1*C44AlAs)*100000000

LAYER'SL 1'
Material = 0.0
f = 0.0
C11 = C11MAT
C12 = C12MAT
C44 = C44MAT

LAYER 'Diffusion layer below 2'
Material = 1.0
Cin=0.60
f = (Cin*aInAs+(0.9-Cin)*aGaAs+0.1*aAlAs-aInP)/aInP
C11 = (C11InAs*Cin+C11GaAs*(0.9-Cin)+0.1*C11AlAs)*100000000
C12 = (C12InAs*Cin+C12GaAs*(0.9-Cin)+0.1*C12AlAs)*100000000
C44 = (C44InAs*Cin+C44GaAs*(0.9-Cin)+0.1*C44AlAs)*100000000
 {the compostion of the diffusion layer is In0.60Ga0.30Al0.1As}

LAYER 'Shell layer below 2'
Material = 2.0
Cin=0.65
f = (Cin*aInAs+(1-Cin)*aGaAs-aInP)/aInP
C11 = (C11InAs*Cin+C11GaAs*(1-Cin))*100000000
C12 =  (C12InAs*Cin+C12GaAs*(1-Cin))*100000000
```

```
C44 =  (C44InAs*Cin+C44GaAs*(1-Cin))*100000000
 {the composition of the shell layer is In0.65Ga0.35As}

LAYER 'Wetting Layer 2'
Material = 2.0
Cin=0.65
f = (Cin*aInAs+(1-Cin)*aGaAs-aInP)/aInP
C11 = (C11InAs*Cin+C11GaAs*(1-Cin))*100000000
C12 =  (C12InAs*Cin+C12GaAs*(1-Cin))*100000000
C44 =  (C44InAs*Cin+C44GaAs*(1-Cin))*100000000

LAYER'Core 2'
Material = 2.0
Cin=0.65
f = (Cin*aInAs+(1-Cin)*aGaAs-aInP)/aInP
C11 = (C11InAs*Cin+C11GaAs*(1-Cin))*100000000
C12 =  (C12InAs*Cin+C12GaAs*(1-Cin))*100000000
C44 =  (C44InAs*Cin+C44GaAs*(1-Cin))*100000000

 LAYER'Shell 2'
Material = 2.0
Cin=0.65
f = (Cin*aInAs+(1-Cin)*aGaAs-aInP)/aInP
C11 = (C11InAs*Cin+C11GaAs*(1-Cin))*100000000
C12 =  (C12InAs*Cin+C12GaAs*(1-Cin))*100000000
C44 =  (C44InAs*Cin+C44GaAs*(1-Cin))*100000000

LAYER'Diffusion layer up 2'
Material = 1.0
Cin=0.60
f = (Cin*aInAs+(0.9-Cin)*aGaAs+0.1*aAlAs-aInP)/aInP
C11 = (C11InAs*Cin+C11GaAs*(0.9-Cin)+0.1*C11AlAs)*100000000
C12 = (C12InAs*Cin+C12GaAs*(0.9-Cin)+0.1*C12AlAs)*100000000
C44 = (C44InAs*Cin+C44GaAs*(0.9-Cin)+0.1*C44AlAs)*100000000

LAYER'SL 2'
Material = 0.0
f = 0.0
C11 = C11MAT
C12 = C12MAT
C44 = C44MAT

LAYER 'Diffusion layer below 3'
Material = 1.0
Cin=0.60
f = (Cin*aInAs+(0.9-Cin)*aGaAs+0.1*aAlAs-aInP)/aInP
C11 = (C11InAs*Cin+C11GaAs*(0.9-Cin)+0.1*C11AlAs)*100000000
C12 = (C12InAs*Cin+C12GaAs*(0.9-Cin)+0.1*C12AlAs)*100000000
C44 = (C44InAs*Cin+C44GaAs*(0.9-Cin)+0.1*C44AlAs)*100000000
 {the compostion of the diffusion layer is In0.60Ga0.30Al0.1As}

LAYER 'Shell layer below 3'
Material = 2.0
```

```
Cin=0.65
f = (Cin*aInAs+(1-Cin)*aGaAs-aInP)/aInP
C11 = (C11InAs*Cin+C11GaAs*(1-Cin))*100000000
C12 =  (C12InAs*Cin+C12GaAs*(1-Cin))*100000000
C44 =  (C44InAs*Cin+C44GaAs*(1-Cin))*100000000
 {the composition of the shell layer is In0.65Ga0.35As}

LAYER 'Wetting Layer 3'
Material = 2.0
Cin=0.65
f = (Cin*aInAs+(1-Cin)*aGaAs-aInP)/aInP
C11 = (C11InAs*Cin+C11GaAs*(1-Cin))*100000000
C12 =  (C12InAs*Cin+C12GaAs*(1-Cin))*100000000
C44 =  (C44InAs*Cin+C44GaAs*(1-Cin))*100000000

LAYER'Core 3'
Material = 2.0
Cin=0.65
f = (Cin*aInAs+(1-Cin)*aGaAs-aInP)/aInP
C11 = (C11InAs*Cin+C11GaAs*(1-Cin))*100000000
C12 =  (C12InAs*Cin+C12GaAs*(1-Cin))*100000000
C44 =  (C44InAs*Cin+C44GaAs*(1-Cin))*100000000

LAYER'Shell 3'
Material = 2.0
Cin=0.65
f = (Cin*aInAs+(1-Cin)*aGaAs-aInP)/aInP
C11 = (C11InAs*Cin+C11GaAs*(1-Cin))*100000000
C12 =  (C12InAs*Cin+C12GaAs*(1-Cin))*100000000
C44 =  (C44InAs*Cin+C44GaAs*(1-Cin))*100000000

LAYER'Diffusion layer up 3'
Material = 1.0
Cin=0.60
f = (Cin*aInAs+(0.9-Cin)*aGaAs+0.1*aAlAs-aInP)/aInP
C11 = (C11InAs*Cin+C11GaAs*(0.9-Cin)+0.1*C11AlAs)*100000000
C12 = (C12InAs*Cin+C12GaAs*(0.9-Cin)+0.1*C12AlAs)*100000000
C44 = (C44InAs*Cin+C44GaAs*(0.9-Cin)+0.1*C44AlAs)*100000000

LAYER'Above QWR'
Material = 0.0
f = 0.0
C11 = C11MAT
C12 = C12MAT
C44 = C44MAT

START (-(Shell_R-xs1),-M_Y/2) LINE TO ((Shell_R+xs1),-M_Y/2) LINE TO
((Shell_R+xs1),M_Y/2) LINE TO(-(Shell_R-xs1),M_Y/2) LINE TO CLOSE
 {*********************************************}

REGION 4 'Core xs1'
mesh_spacing=40
Zlens1=Zlens_Dfl_Below1
```

```
Zlens2=Zlens_ShellH_Below1
Zlens3=Zlens_Core1
Zlens4=Zlens_Shell1
Zlens5=Zlens_Dfl_Up1

LAYER'Underneath the Dfl_Below 1'
Material = 0.0
f = 0.0
C11 = C11MAT
C12 = C12MAT
C44 = C44MAT

LAYER 'Diffusion layer below 1'
Material = 1.0
Cin=0.60
f = (Cin*aInAs+(0.9-Cin)*aGaAs+0.1*aAlAs-aInP)/aInP
C11 = (C11InAs*Cin+C11GaAs*(0.9-Cin)+0.1*C11AlAs)*100000000
C12 = (C12InAs*Cin+C12GaAs*(0.9-Cin)+0.1*C12AlAs)*100000000
C44 = (C44InAs*Cin+C44GaAs*(0.9-Cin)+0.1*C44AlAs)*100000000
 {The composition of the diffusion layer is In0.60Ga0.30Al0.10As}

LAYER 'Shell layer below 1'
Material = 2.0
Cin=0.65
f = (Cin*aInAs+(1-Cin)*aGaAs-aInP)/aInP
C11 = (C11InAs*Cin+C11GaAs*(1-Cin))*100000000
C12 =  (C12InAs*Cin+C12GaAs*(1-Cin))*100000000
C44 =  (C44InAs*Cin+C44GaAs*(1-Cin))*100000000
 {The composition of the shell layer is In0.65Ga0.35As}

LAYER 'Wetting Layer 1'
Material = 2.0
Cin=0.65
f = (Cin*aInAs+(1-Cin)*aGaAs-aInP)/aInP
C11 = (C11InAs*Cin+C11GaAs*(1-Cin))*100000000
C12 =  (C12InAs*Cin+C12GaAs*(1-Cin))*100000000
C44 =  (C44InAs*Cin+C44GaAs*(1-Cin))*100000000

LAYER'Core 1'
mesh_spacing=15
Material = 3.0
Cin=0.75
f = (Cin*aInAs+(1-Cin)*aGaAs-aInP)/aInP
C11 = (C11InAs*Cin+C11GaAs*(1-Cin))*100000000
C12 = (C12InAs*Cin+C12GaAs*(1-Cin))*100000000
C44 = (C44InAs*Cin+C44GaAs*(1-Cin))*100000000
{The composition of the indium-rich core is In0.75Ga0.25As}

LAYER'Shell 1'
Material = 2.0
Cin=0.65
f = (Cin*aInAs+(1-Cin)*aGaAs-aInP)/aInP
C11 = (C11InAs*Cin+C11GaAs*(1-Cin))*100000000
```

```
C12 =  (C12InAs*Cin+C12GaAs*(1-Cin))*100000000
C44 =  (C44InAs*Cin+C44GaAs*(1-Cin))*100000000

LAYER'Diffusion layer up 1'
Material = 1.0
Cin=0.60
f = (Cin*aInAs+(0.9-Cin)*aGaAs+0.1*aAlAs-aInP)/aInP
C11 = (C11InAs*Cin+C11GaAs*(0.9-Cin)+0.1*C11AlAs)*100000000
C12 = (C12InAs*Cin+C12GaAs*(0.9-Cin)+0.1*C12AlAs)*100000000
C44 = (C44InAs*Cin+C44GaAs*(0.9-Cin)+0.1*C44AlAs)*100000000

LAYER'SL 1'
Material = 0.0
f = 0.0
C11 = C11MAT
C12 = C12MAT
C44 = C44MAT

LAYER 'Diffusion layer below 2'
Material = 1.0
Cin=0.60
f = (Cin*aInAs+(0.9-Cin)*aGaAs+0.1*aAlAs-aInP)/aInP
C11 = (C11InAs*Cin+C11GaAs*(0.9-Cin)+0.1*C11AlAs)*100000000
C12 = (C12InAs*Cin+C12GaAs*(0.9-Cin)+0.1*C12AlAs)*100000000
C44 = (C44InAs*Cin+C44GaAs*(0.9-Cin)+0.1*C44AlAs)*100000000
 {The composition of the diffusion layer is In0.60Ga0.30Al0.10As}

LAYER 'Shell layer below 2'
Material = 2.0
Cin=0.65
f = (Cin*aInAs+(1-Cin)*aGaAs-aInP)/aInP
C11 = (C11InAs*Cin+C11GaAs*(1-Cin))*100000000
C12 =  (C12InAs*Cin+C12GaAs*(1-Cin))*100000000
C44 =  (C44InAs*Cin+C44GaAs*(1-Cin))*100000000
 {The composition of the shell layer is In0.65Ga0.35As}

LAYER 'Wetting Layer 2'
Material = 2.0
Cin=0.65
f = (Cin*aInAs+(1-Cin)*aGaAs-aInP)/aInP
C11 = (C11InAs*Cin+C11GaAs*(1-Cin))*100000000
C12 =  (C12InAs*Cin+C12GaAs*(1-Cin))*100000000
C44 =  (C44InAs*Cin+C44GaAs*(1-Cin))*100000000

LAYER'Core 2'
mesh_spacing=15
Material = 3.0
Cin=0.75
f = (Cin*aInAs+(1-Cin)*aGaAs-aInP)/aInP
C11 = (C11InAs*Cin+C11GaAs*(1-Cin))*100000000
C12 = (C12InAs*Cin+C12GaAs*(1-Cin))*100000000
C44 = (C44InAs*Cin+C44GaAs*(1-Cin))*100000000
{The composition of the indium-rich core is In0.75Ga0.25As}
```

```
LAYER'Shell 2'
Material = 2.0
Cin=0.65
f = (Cin*aInAs+(1-Cin)*aGaAs-aInP)/aInP
C11 = (C11InAs*Cin+C11GaAs*(1-Cin))*100000000
C12 =  (C12InAs*Cin+C12GaAs*(1-Cin))*100000000
C44 =  (C44InAs*Cin+C44GaAs*(1-Cin))*100000000

LAYER'Diffusion layer up 2'
Material = 1.0
Cin=0.60
f = (Cin*aInAs+(0.9-Cin)*aGaAs+0.1*aAlAs-aInP)/aInP
C11 = (C11InAs*Cin+C11GaAs*(0.9-Cin)+0.1*C11AlAs)*100000000
C12 = (C12InAs*Cin+C12GaAs*(0.9-Cin)+0.1*C12AlAs)*100000000
C44 = (C44InAs*Cin+C44GaAs*(0.9-Cin)+0.1*C44AlAs)*100000000

LAYER'SL 2'
Material = 0.0
f = 0.0
C11 = C11MAT
C12 = C12MAT
C44 = C44MAT

LAYER 'Diffusion layer below 3'
Material = 1.0
Cin=0.60
f = (Cin*aInAs+(0.9-Cin)*aGaAs+0.1*aAlAs-aInP)/aInP
C11 = (C11InAs*Cin+C11GaAs*(0.9-Cin)+0.1*C11AlAs)*100000000
C12 = (C12InAs*Cin+C12GaAs*(0.9-Cin)+0.1*C12AlAs)*100000000
C44 = (C44InAs*Cin+C44GaAs*(0.9-Cin)+0.1*C44AlAs)*100000000
 {The composition of the diffusion layer is In0.60Ga0.30Al0.10As}

LAYER 'Shell layer below 3'
Material = 2.0
Cin=0.65
f = (Cin*aInAs+(1-Cin)*aGaAs-aInP)/aInP
C11 = (C11InAs*Cin+C11GaAs*(1-Cin))*100000000
C12 =  (C12InAs*Cin+C12GaAs*(1-Cin))*100000000
C44 =  (C44InAs*Cin+C44GaAs*(1-Cin))*100000000
 {The composition of the shell layer is In0.65Ga0.35As}

LAYER 'Wetting Layer 3'
Material = 2.0
Cin=0.65
f = (Cin*aInAs+(1-Cin)*aGaAs-aInP)/aInP
C11 = (C11InAs*Cin+C11GaAs*(1-Cin))*100000000
C12 =  (C12InAs*Cin+C12GaAs*(1-Cin))*100000000
C44 =  (C44InAs*Cin+C44GaAs*(1-Cin))*100000000

LAYER'Core 3'
mesh_spacing=15
Material = 3.0
```

```
Cin=0.75
f = (Cin*aInAs+(1-Cin)*aGaAs-aInP)/aInP
C11 = (C11InAs*Cin+C11GaAs*(1-Cin))*100000000
C12 = (C12InAs*Cin+C12GaAs*(1-Cin))*100000000
C44 = (C44InAs*Cin+C44GaAs*(1-Cin))*100000000
 {The composition of the indium-rich core is In0.75Ga0.25As}

LAYER'Shell 3'
Material = 2.0
Cin=0.65
f = (Cin*aInAs+(1-Cin)*aGaAs-aInP)/aInP
C11 = (C11InAs*Cin+C11GaAs*(1-Cin))*100000000
C12 =  (C12InAs*Cin+C12GaAs*(1-Cin))*100000000
C44 =  (C44InAs*Cin+C44GaAs*(1-Cin))*100000000

LAYER'Diffusion layer up 3'
Material = 1.0
Cin=0.60
f = (Cin*aInAs+(0.9-Cin)*aGaAs+0.1*aAlAs-aInP)/aInP
C11 = (C11InAs*Cin+C11GaAs*(0.9-Cin)+0.1*C11AlAs)*100000000
C12 = (C12InAs*Cin+C12GaAs*(0.9-Cin)+0.1*C12AlAs)*100000000
C44 = (C44InAs*Cin+C44GaAs*(0.9-Cin)+0.1*C44AlAs)*100000000

LAYER'Above QWR'
Material = 0.0
f = 0.0
C11 = C11MAT
C12 = C12MAT
C44 = C44MAT

START(-(Core_R-xs1),-M_Y/2) LINE TO ((Core_R+xs1),-M_Y/2) LINE
TO((Core_R+xs1),M_Y/2) LINE TO (-(Core_R-xs1),M_Y/2) LINE TO CLOSE


{**********************************************}


REGION 5 'Diffusion Wire xs2'
mesh_spacing=40
Zlens1=Zlens_Dfl_Below2
Zlens2=D
Zlens3=D+WL
Zlens4=D+WL
Zlens5=Zlens_Dfl_Up2

LAYER'Underneath the Dfl_Below 1'
Material = 0.0
f = 0.0
C11 = C11MAT
C12 = C12MAT
C44 = C44MAT
```

```
LAYER 'Diffusion layer below 1'
Material = 1.0
Cin=0.60
f = (Cin*aInAs+(0.9-Cin)*aGaAs+0.1*aAlAs-aInP)/aInP
C11 = (C11InAs*Cin+C11GaAs*(0.9-Cin)+0.1*C11AlAs)*100000000
C12 = (C12InAs*Cin+C12GaAs*(0.9-Cin)+0.1*C12AlAs)*100000000
C44 = (C44InAs*Cin+C44GaAs*(0.9-Cin)+0.1*C44AlAs)*100000000

LAYER 'Shell layer below 1'
Material = 1.0
Cin=0.60
f = (Cin*aInAs+(0.9-Cin)*aGaAs+0.1*aAlAs-aInP)/aInP
C11 = (C11InAs*Cin+C11GaAs*(0.9-Cin)+0.1*C11AlAs)*100000000
C12 = (C12InAs*Cin+C12GaAs*(0.9-Cin)+0.1*C12AlAs)*100000000
C44 = (C44InAs*Cin+C44GaAs*(0.9-Cin)+0.1*C44AlAs)*100000000

LAYER 'Wetting Layer 1'
Material = 1.0
Cin=0.60
f = (Cin*aInAs+(0.9-Cin)*aGaAs+0.1*aAlAs-aInP)/aInP
C11 = (C11InAs*Cin+C11GaAs*(0.9-Cin)+0.1*C11AlAs)*100000000
C12 = (C12InAs*Cin+C12GaAs*(0.9-Cin)+0.1*C12AlAs)*100000000
C44 = (C44InAs*Cin+C44GaAs*(0.9-Cin)+0.1*C44AlAs)*100000000

LAYER'Core 1'
Material = 1.0
Cin=0.60
f = (Cin*aInAs+(0.9-Cin)*aGaAs+0.1*aAlAs-aInP)/aInP
C11 = (C11InAs*Cin+C11GaAs*(0.9-Cin)+0.1*C11AlAs)*100000000
C12 = (C12InAs*Cin+C12GaAs*(0.9-Cin)+0.1*C12AlAs)*100000000
C44 = (C44InAs*Cin+C44GaAs*(0.9-Cin)+0.1*C44AlAs)*100000000

LAYER'Shell 1'
Material = 1.0
Cin=0.60
f = (Cin*aInAs+(0.9-Cin)*aGaAs+0.1*aAlAs-aInP)/aInP
C11 = (C11InAs*Cin+C11GaAs*(0.9-Cin)+0.1*C11AlAs)*100000000
C12 = (C12InAs*Cin+C12GaAs*(0.9-Cin)+0.1*C12AlAs)*100000000
C44 = (C44InAs*Cin+C44GaAs*(0.9-Cin)+0.1*C44AlAs)*100000000

LAYER'Diffusion layer up 1'
Material = 1.0
Cin=0.60
f = (Cin*aInAs+(0.9-Cin)*aGaAs+0.1*aAlAs-aInP)/aInP
C11 = (C11InAs*Cin+C11GaAs*(0.9-Cin)+0.1*C11AlAs)*100000000
C12 = (C12InAs*Cin+C12GaAs*(0.9-Cin)+0.1*C12AlAs)*100000000
C44 = (C44InAs*Cin+C44GaAs*(0.9-Cin)+0.1*C44AlAs)*100000000

LAYER'SL 1'
Material = 0.0
f = 0.0
C11 = C11MAT
C12 = C12MAT
```

C44 = C44MAT

LAYER 'Diffusion layer below 2'
Material = 1.0
Cin=0.60
f = (Cin*aInAs+(0.9-Cin)*aGaAs+0.1*aAlAs-aInP)/aInP
C11 = (C11InAs*Cin+C11GaAs*(0.9-Cin)+0.1*C11AlAs)*100000000
C12 = (C12InAs*Cin+C12GaAs*(0.9-Cin)+0.1*C12AlAs)*100000000
C44 = (C44InAs*Cin+C44GaAs*(0.9-Cin)+0.1*C44AlAs)*100000000

LAYER 'Shell layer below 2'
Material = 1.0
Cin=0.60
f = (Cin*aInAs+(0.9-Cin)*aGaAs+0.1*aAlAs-aInP)/aInP
C11 = (C11InAs*Cin+C11GaAs*(0.9-Cin)+0.1*C11AlAs)*100000000
C12 = (C12InAs*Cin+C12GaAs*(0.9-Cin)+0.1*C12AlAs)*100000000
C44 = (C44InAs*Cin+C44GaAs*(0.9-Cin)+0.1*C44AlAs)*100000000

LAYER 'Wetting Layer 2'
Material = 1.0
Cin=0.60
f = (Cin*aInAs+(0.9-Cin)*aGaAs+0.1*aAlAs-aInP)/aInP
C11 = (C11InAs*Cin+C11GaAs*(0.9-Cin)+0.1*C11AlAs)*100000000
C12 = (C12InAs*Cin+C12GaAs*(0.9-Cin)+0.1*C12AlAs)*100000000
C44 = (C44InAs*Cin+C44GaAs*(0.9-Cin)+0.1*C44AlAs)*100000000

LAYER'Core 2'
Material = 1.0
Cin=0.60
f = (Cin*aInAs+(0.9-Cin)*aGaAs+0.1*aAlAs-aInP)/aInP
C11 = (C11InAs*Cin+C11GaAs*(0.9-Cin)+0.1*C11AlAs)*100000000
C12 = (C12InAs*Cin+C12GaAs*(0.9-Cin)+0.1*C12AlAs)*100000000
C44 = (C44InAs*Cin+C44GaAs*(0.9-Cin)+0.1*C44AlAs)*100000000

LAYER'Shell 2'
Material = 1.0
Cin=0.60
f = (Cin*aInAs+(0.9-Cin)*aGaAs+0.1*aAlAs-aInP)/aInP
C11 = (C11InAs*Cin+C11GaAs*(0.9-Cin)+0.1*C11AlAs)*100000000
C12 = (C12InAs*Cin+C12GaAs*(0.9-Cin)+0.1*C12AlAs)*100000000
C44 = (C44InAs*Cin+C44GaAs*(0.9-Cin)+0.1*C44AlAs)*100000000

LAYER'Diffusion layer up 2'
Material = 1.0
Cin=0.60
f = (Cin*aInAs+(0.9-Cin)*aGaAs+0.1*aAlAs-aInP)/aInP
C11 = (C11InAs*Cin+C11GaAs*(0.9-Cin)+0.1*C11AlAs)*100000000
C12 = (C12InAs*Cin+C12GaAs*(0.9-Cin)+0.1*C12AlAs)*100000000
C44 = (C44InAs*Cin+C44GaAs*(0.9-Cin)+0.1*C44AlAs)*100000000

LAYER'SL 2'
Material = 0.0
f = 0.0

```
C11 = C11MAT
C12 = C12MAT
C44 = C44MAT

LAYER 'Diffusion layer below 3'
Material = 1.0
Cin=0.60
f = (Cin*aInAs+(0.9-Cin)*aGaAs+0.1*aAlAs-aInP)/aInP
C11 = (C11InAs*Cin+C11GaAs*(0.9-Cin)+0.1*C11AlAs)*100000000
C12 = (C12InAs*Cin+C12GaAs*(0.9-Cin)+0.1*C12AlAs)*100000000
C44 = (C44InAs*Cin+C44GaAs*(0.9-Cin)+0.1*C44AlAs)*100000000


LAYER 'Shell layer below 3'
Material = 1.0
Cin=0.60
f = (Cin*aInAs+(0.9-Cin)*aGaAs+0.1*aAlAs-aInP)/aInP
C11 = (C11InAs*Cin+C11GaAs*(0.9-Cin)+0.1*C11AlAs)*100000000
C12 = (C12InAs*Cin+C12GaAs*(0.9-Cin)+0.1*C12AlAs)*100000000
C44 = (C44InAs*Cin+C44GaAs*(0.9-Cin)+0.1*C44AlAs)*100000000

LAYER 'Wetting Layer 3'
Material = 1.0
Cin=0.60
f = (Cin*aInAs+(0.9-Cin)*aGaAs+0.1*aAlAs-aInP)/aInP
C11 = (C11InAs*Cin+C11GaAs*(0.9-Cin)+0.1*C11AlAs)*100000000
C12 = (C12InAs*Cin+C12GaAs*(0.9-Cin)+0.1*C12AlAs)*100000000
C44 = (C44InAs*Cin+C44GaAs*(0.9-Cin)+0.1*C44AlAs)*100000000

LAYER'Core 3'
Material = 1.0
Cin=0.60
f = (Cin*aInAs+(0.9-Cin)*aGaAs+0.1*aAlAs-aInP)/aInP
C11 = (C11InAs*Cin+C11GaAs*(0.9-Cin)+0.1*C11AlAs)*100000000
C12 = (C12InAs*Cin+C12GaAs*(0.9-Cin)+0.1*C12AlAs)*100000000
C44 = (C44InAs*Cin+C44GaAs*(0.9-Cin)+0.1*C44AlAs)*100000000

LAYER'Shell 3'
Material = 1.0
Cin=0.60
f = (Cin*aInAs+(0.9-Cin)*aGaAs+0.1*aAlAs-aInP)/aInP
C11 = (C11InAs*Cin+C11GaAs*(0.9-Cin)+0.1*C11AlAs)*100000000
C12 = (C12InAs*Cin+C12GaAs*(0.9-Cin)+0.1*C12AlAs)*100000000
C44 = (C44InAs*Cin+C44GaAs*(0.9-Cin)+0.1*C44AlAs)*100000000

LAYER'Diffusion layer up 3'
Material = 1.0
Cin=0.60
f = (Cin*aInAs+(0.9-Cin)*aGaAs+0.1*aAlAs-aInP)/aInP
C11 = (C11InAs*Cin+C11GaAs*(0.9-Cin)+0.1*C11AlAs)*100000000
C12 = (C12InAs*Cin+C12GaAs*(0.9-Cin)+0.1*C12AlAs)*100000000
C44 = (C44InAs*Cin+C44GaAs*(0.9-Cin)+0.1*C44AlAs)*100000000
```

```
LAYER'Above QWR'
Material = 0.0
f = 0.0
C11 = C11MAT
C12 = C12MAT
C44 = C44MAT

START (-(Dfl_R-xs2),-M_Y/2) LINE TO((Dfl_R+xs2),-M_Y/2) LINE TO((Dfl_R+xs2),M_Y/2)
LINE TO(-(Dfl_R-xs2),M_Y/2) LINE TO CLOSE
{*******************************************}

REGION 6 'Shell Wire xs2'
mesh_spacing=40
Zlens1=Zlens_Dfl_Below2
Zlens2=Zlens_ShellH_Below2
Zlens3=D+WL
Zlens4=Zlens_Shell2
Zlens5=Zlens_Dfl_Up2

LAYER'Underneath the Dfl_Below 1'
Material = 0.0
f = 0.0
C11 = C11MAT
C12 = C12MAT
C44 = C44MAT

LAYER 'Diffusion layer below 1'
Material = 1.0
Cin=0.60
f = (Cin*aInAs+(0.9-Cin)*aGaAs+0.1*aAlAs-aInP)/aInP
C11 = (C11InAs*Cin+C11GaAs*(0.9-Cin)+0.1*C11AlAs)*100000000
C12 = (C12InAs*Cin+C12GaAs*(0.9-Cin)+0.1*C12AlAs)*100000000
C44 = (C44InAs*Cin+C44GaAs*(0.9-Cin)+0.1*C44AlAs)*100000000
{the compostion of the diffusion layer is In0.60Ga0.30Al0.1As}

LAYER 'Shell layer below 1'
Material = 2.0
Cin=0.65
f = (Cin*aInAs+(1-Cin)*aGaAs-aInP)/aInP
C11 = (C11InAs*Cin+C11GaAs*(1-Cin))*100000000
C12 =  (C12InAs*Cin+C12GaAs*(1-Cin))*100000000
C44 =  (C44InAs*Cin+C44GaAs*(1-Cin))*100000000
{the composition of the shell layer is In0.65Ga0.35As}

LAYER 'Wetting Layer 1'
Material = 2.0
Cin=0.65
f = (Cin*aInAs+(1-Cin)*aGaAs-aInP)/aInP
C11 = (C11InAs*Cin+C11GaAs*(1-Cin))*100000000
C12 =  (C12InAs*Cin+C12GaAs*(1-Cin))*100000000
C44 =  (C44InAs*Cin+C44GaAs*(1-Cin))*100000000

LAYER'Core 1'
```

```
Material = 2.0
Cin=0.65
f = (Cin*aInAs+(1-Cin)*aGaAs-aInP)/aInP
C11 = (C11InAs*Cin+C11GaAs*(1-Cin))*100000000
C12 =  (C12InAs*Cin+C12GaAs*(1-Cin))*100000000
C44 =  (C44InAs*Cin+C44GaAs*(1-Cin))*100000000

LAYER'Shell 1'
Material = 2.0
Cin=0.65
f = (Cin*aInAs+(1-Cin)*aGaAs-aInP)/aInP
C11 = (C11InAs*Cin+C11GaAs*(1-Cin))*100000000
C12 =  (C12InAs*Cin+C12GaAs*(1-Cin))*100000000
C44 =  (C44InAs*Cin+C44GaAs*(1-Cin))*100000000

LAYER'Diffusion layer up 1'
Material = 1.0
Cin=0.60
f = (Cin*aInAs+(0.9-Cin)*aGaAs+0.1*aAlAs-aInP)/aInP
C11 = (C11InAs*Cin+C11GaAs*(0.9-Cin)+0.1*C11AlAs)*100000000
C12 = (C12InAs*Cin+C12GaAs*(0.9-Cin)+0.1*C12AlAs)*100000000
C44 = (C44InAs*Cin+C44GaAs*(0.9-Cin)+0.1*C44AlAs)*100000000

LAYER'SL 1'
Material = 0.0
f = 0.0
C11 = C11MAT
C12 = C12MAT
C44 = C44MAT

LAYER 'Diffusion layer below 2'
Material = 1.0
Cin=0.60
f = (Cin*aInAs+(0.9-Cin)*aGaAs+0.1*aAlAs-aInP)/aInP
C11 = (C11InAs*Cin+C11GaAs*(0.9-Cin)+0.1*C11AlAs)*100000000
C12 = (C12InAs*Cin+C12GaAs*(0.9-Cin)+0.1*C12AlAs)*100000000
C44 = (C44InAs*Cin+C44GaAs*(0.9-Cin)+0.1*C44AlAs)*100000000
{the compostion of the diffusion layer is In0.60Ga0.30Al0.1As}

LAYER 'Shell layer below 2'
Material = 2.0
Cin=0.65
f = (Cin*aInAs+(1-Cin)*aGaAs-aInP)/aInP
C11 = (C11InAs*Cin+C11GaAs*(1-Cin))*100000000
C12 =  (C12InAs*Cin+C12GaAs*(1-Cin))*100000000
C44 =  (C44InAs*Cin+C44GaAs*(1-Cin))*100000000
{the composition of the shell layer is In0.65Ga0.35As}

LAYER 'Wetting Layer 2'
Material = 2.0
Cin=0.65
f = (Cin*aInAs+(1-Cin)*aGaAs-aInP)/aInP
C11 = (C11InAs*Cin+C11GaAs*(1-Cin))*100000000
```

```
C12 =  (C12InAs*Cin+C12GaAs*(1-Cin))*100000000
C44 =  (C44InAs*Cin+C44GaAs*(1-Cin))*100000000

LAYER'Core 2'
Material = 2.0
Cin=0.65
f = (Cin*aInAs+(1-Cin)*aGaAs-aInP)/aInP
C11 = (C11InAs*Cin+C11GaAs*(1-Cin))*100000000
C12 =  (C12InAs*Cin+C12GaAs*(1-Cin))*100000000
C44 =  (C44InAs*Cin+C44GaAs*(1-Cin))*100000000

LAYER'Shell 2'
Material = 2.0
Cin=0.65
f = (Cin*aInAs+(1-Cin)*aGaAs-aInP)/aInP
C11 = (C11InAs*Cin+C11GaAs*(1-Cin))*100000000
C12 =  (C12InAs*Cin+C12GaAs*(1-Cin))*100000000
C44 =  (C44InAs*Cin+C44GaAs*(1-Cin))*100000000

LAYER'Diffusion layer up 2'
Material = 1.0
Cin=0.60
f = (Cin*aInAs+(0.9-Cin)*aGaAs+0.1*aAlAs-aInP)/aInP
C11 = (C11InAs*Cin+C11GaAs*(0.9-Cin)+0.1*C11AlAs)*100000000
C12 = (C12InAs*Cin+C12GaAs*(0.9-Cin)+0.1*C12AlAs)*100000000
C44 = (C44InAs*Cin+C44GaAs*(0.9-Cin)+0.1*C44AlAs)*100000000

LAYER'SL 2'
Material = 0.0
f = 0.0
C11 = C11MAT
C12 = C12MAT
C44 = C44MAT

LAYER 'Diffusion layer below 3'
Material = 1.0
Cin=0.60
f = (Cin*aInAs+(0.9-Cin)*aGaAs+0.1*aAlAs-aInP)/aInP
C11 = (C11InAs*Cin+C11GaAs*(0.9-Cin)+0.1*C11AlAs)*100000000
C12 = (C12InAs*Cin+C12GaAs*(0.9-Cin)+0.1*C12AlAs)*100000000
C44 = (C44InAs*Cin+C44GaAs*(0.9-Cin)+0.1*C44AlAs)*100000000
{the compostion of the diffusion layer is In0.60Ga0.30Al0.1As}

LAYER 'Shell layer below 3'
Material = 2.0
Cin=0.65
f = (Cin*aInAs+(1-Cin)*aGaAs-aInP)/aInP
C11 = (C11InAs*Cin+C11GaAs*(1-Cin))*100000000
C12 =  (C12InAs*Cin+C12GaAs*(1-Cin))*100000000
C44 =  (C44InAs*Cin+C44GaAs*(1-Cin))*100000000
{the composition of the shell layer is In0.65Ga0.35As}

LAYER 'Wetting Layer 3'
```

```
Material = 2.0
Cin=0.65
f = (Cin*aInAs+(1-Cin)*aGaAs-aInP)/aInP
C11 = (C11InAs*Cin+C11GaAs*(1-Cin))*100000000
C12 =  (C12InAs*Cin+C12GaAs*(1-Cin))*100000000
C44 =  (C44InAs*Cin+C44GaAs*(1-Cin))*100000000

LAYER'Core 3'
Material = 2.0
Cin=0.65
f = (Cin*aInAs+(1-Cin)*aGaAs-aInP)/aInP
C11 = (C11InAs*Cin+C11GaAs*(1-Cin))*100000000
C12 =  (C12InAs*Cin+C12GaAs*(1-Cin))*100000000
C44 =  (C44InAs*Cin+C44GaAs*(1-Cin))*100000000

LAYER'Shell 3'
Material = 2.0
Cin=0.65
f = (Cin*aInAs+(1-Cin)*aGaAs-aInP)/aInP
C11 = (C11InAs*Cin+C11GaAs*(1-Cin))*100000000
C12 =  (C12InAs*Cin+C12GaAs*(1-Cin))*100000000
C44 =  (C44InAs*Cin+C44GaAs*(1-Cin))*100000000

LAYER'Diffusion layer up 3'
Material = 1.0
Cin=0.60
f = (Cin*aInAs+(0.9-Cin)*aGaAs+0.1*aAlAs-aInP)/aInP
C11 = (C11InAs*Cin+C11GaAs*(0.9-Cin)+0.1*C11AlAs)*100000000
C12 = (C12InAs*Cin+C12GaAs*(0.9-Cin)+0.1*C12AlAs)*100000000
C44 = (C44InAs*Cin+C44GaAs*(0.9-Cin)+0.1*C44AlAs)*100000000

LAYER'Above QWR'
Material = 0.0
f = 0.0
C11 = C11MAT
C12 = C12MAT
C44 = C44MAT

START (-(Shell_R-xs2),-M_Y/2) LINE TO((Shell_R+xs2),-M_Y/2) LINE
TO((Shell_R+xs2),M_Y/2) LINE TO(-(Shell_R-xs2),M_Y/2) LINE TO CLOSE
{*********************************************}

REGION 7 'Core xs2'
mesh_spacing=40
Zlens1=Zlens_Dfl_Below2
Zlens2=Zlens_ShellH_Below2
Zlens3=Zlens_Core2
Zlens4=Zlens_Shell2
Zlens5=Zlens_Dfl_Up2

LAYER'Underneath the Dfl_Below 1'
Material = 0.0
 f = 0.0
```

```
C11 = C11MAT
C12 = C12MAT
C44 = C44MAT

LAYER 'Diffusion layer below 1'
Material = 1.0
Cin=0.60
f = (Cin*aInAs+(0.9-Cin)*aGaAs+0.1*aAlAs-aInP)/aInP
C11 = (C11InAs*Cin+C11GaAs*(0.9-Cin)+0.1*C11AlAs)*100000000
C12 = (C12InAs*Cin+C12GaAs*(0.9-Cin)+0.1*C12AlAs)*100000000
C44 = (C44InAs*Cin+C44GaAs*(0.9-Cin)+0.1*C44AlAs)*100000000
{The composition of the diffusion layer is In0.60Ga0.30Al0.10As}

LAYER 'Shell layer below 1'
Material = 2.0
Cin=0.65
f = (Cin*aInAs+(1-Cin)*aGaAs-aInP)/aInP
C11 = (C11InAs*Cin+C11GaAs*(1-Cin))*100000000
C12 =  (C12InAs*Cin+C12GaAs*(1-Cin))*100000000
C44 =  (C44InAs*Cin+C44GaAs*(1-Cin))*100000000
{The composition of the shell layer is In0.65Ga0.35As}

LAYER 'Wetting Layer 1'
Material = 2.0
Cin=0.65
f = (Cin*aInAs+(1-Cin)*aGaAs-aInP)/aInP
C11 = (C11InAs*Cin+C11GaAs*(1-Cin))*100000000
C12 =  (C12InAs*Cin+C12GaAs*(1-Cin))*100000000
C44 =  (C44InAs*Cin+C44GaAs*(1-Cin))*100000000

LAYER'Core 1'
mesh_spacing=15
Material = 3.0
Cin=0.75
f = (Cin*aInAs+(1-Cin)*aGaAs-aInP)/aInP
C11 = (C11InAs*Cin+C11GaAs*(1-Cin))*100000000
C12 = (C12InAs*Cin+C12GaAs*(1-Cin))*100000000
C44 = (C44InAs*Cin+C44GaAs*(1-Cin))*100000000
 {The composition of the indium-rich core is In0.75Ga0.25As}

LAYER'Shell 1'
Material = 2.0
Cin=0.65
f = (Cin*aInAs+(1-Cin)*aGaAs-aInP)/aInP
C11 = (C11InAs*Cin+C11GaAs*(1-Cin))*100000000
C12 =  (C12InAs*Cin+C12GaAs*(1-Cin))*100000000
C44 =  (C44InAs*Cin+C44GaAs*(1-Cin))*100000000

LAYER'Diffusion layer up 1'
Material = 1.0
Cin=0.60
f = (Cin*aInAs+(0.9-Cin)*aGaAs+0.1*aAlAs-aInP)/aInP
C11 = (C11InAs*Cin+C11GaAs*(0.9-Cin)+0.1*C11AlAs)*100000000
```

```
C12 = (C12InAs*Cin+C12GaAs*(0.9-Cin)+0.1*C12AlAs)*100000000
C44 = (C44InAs*Cin+C44GaAs*(0.9-Cin)+0.1*C44AlAs)*100000000

LAYER'SL 1'
Material = 0.0
f = 0.0
C11 = C11MAT
C12 = C12MAT
C44 = C44MAT

LAYER 'Diffusion layer below 2'
Material = 1.0
Cin=0.60
f = (Cin*aInAs+(0.9-Cin)*aGaAs+0.1*aAlAs-aInP)/aInP
C11 = (C11InAs*Cin+C11GaAs*(0.9-Cin)+0.1*C11AlAs)*100000000
C12 = (C12InAs*Cin+C12GaAs*(0.9-Cin)+0.1*C12AlAs)*100000000
C44 = (C44InAs*Cin+C44GaAs*(0.9-Cin)+0.1*C44AlAs)*100000000
{The composition of the diffusion layer is In0.60Ga0.30Al0.10As}

LAYER 'Shell layer below 2'
Material = 2.0
Cin=0.65
f = (Cin*aInAs+(1-Cin)*aGaAs-aInP)/aInP
C11 = (C11InAs*Cin+C11GaAs*(1-Cin))*100000000
C12 =  (C12InAs*Cin+C12GaAs*(1-Cin))*100000000
C44 =  (C44InAs*Cin+C44GaAs*(1-Cin))*100000000
{The composition of the shell layer is In0.65Ga0.35As}

LAYER 'Wetting Layer 2'
Material = 2.0
Cin=0.65
f = (Cin*aInAs+(1-Cin)*aGaAs-aInP)/aInP
C11 = (C11InAs*Cin+C11GaAs*(1-Cin))*100000000
C12 =  (C12InAs*Cin+C12GaAs*(1-Cin))*100000000
C44 =  (C44InAs*Cin+C44GaAs*(1-Cin))*100000000

LAYER'Core 2'
mesh_spacing=15
Material = 3.0
Cin=0.75
f = (Cin*aInAs+(1-Cin)*aGaAs-aInP)/aInP
C11 = (C11InAs*Cin+C11GaAs*(1-Cin))*100000000
C12 = (C12InAs*Cin+C12GaAs*(1-Cin))*100000000
C44 = (C44InAs*Cin+C44GaAs*(1-Cin))*100000000
{The composition of the indium-rich core is In0.75Ga0.25As}

LAYER'Shell 2'
Material = 2.0
Cin=0.65
f = (Cin*aInAs+(1-Cin)*aGaAs-aInP)/aInP
C11 = (C11InAs*Cin+C11GaAs*(1-Cin))*100000000
C12 =  (C12InAs*Cin+C12GaAs*(1-Cin))*100000000
C44 =  (C44InAs*Cin+C44GaAs*(1-Cin))*100000000
```

```
LAYER'Diffusion layer up 2'
Material = 1.0
Cin=0.60
f = (Cin*aInAs+(0.9-Cin)*aGaAs+0.1*aAlAs-aInP)/aInP
C11 = (C11InAs*Cin+C11GaAs*(0.9-Cin)+0.1*C11AlAs)*100000000
C12 = (C12InAs*Cin+C12GaAs*(0.9-Cin)+0.1*C12AlAs)*100000000
C44 = (C44InAs*Cin+C44GaAs*(0.9-Cin)+0.1*C44AlAs)*100000000

LAYER'SL 2'
Material = 0.0
f = 0.0
C11 = C11MAT
C12 = C12MAT
C44 = C44MAT

LAYER 'Diffusion layer below 3'
Material = 1.0
Cin=0.60
f = (Cin*aInAs+(0.9-Cin)*aGaAs+0.1*aAlAs-aInP)/aInP
C11 = (C11InAs*Cin+C11GaAs*(0.9-Cin)+0.1*C11AlAs)*100000000
C12 = (C12InAs*Cin+C12GaAs*(0.9-Cin)+0.1*C12AlAs)*100000000
C44 = (C44InAs*Cin+C44GaAs*(0.9-Cin)+0.1*C44AlAs)*100000000
{The composition of the diffusion layer is In0.60Ga0.30Al0.10As}

LAYER 'Shell layer below 3'
Material = 2.0
Cin=0.65
f = (Cin*aInAs+(1-Cin)*aGaAs-aInP)/aInP
C11 = (C11InAs*Cin+C11GaAs*(1-Cin))*100000000
C12 =  (C12InAs*Cin+C12GaAs*(1-Cin))*100000000
C44 =  (C44InAs*Cin+C44GaAs*(1-Cin))*100000000
{The composition of the shell layer is In0.65Ga0.35As}

LAYER 'Wetting Layer 3'
Material = 2.0
Cin=0.65
f = (Cin*aInAs+(1-Cin)*aGaAs-aInP)/aInP
C11 = (C11InAs*Cin+C11GaAs*(1-Cin))*100000000
C12 =  (C12InAs*Cin+C12GaAs*(1-Cin))*100000000
C44 =  (C44InAs*Cin+C44GaAs*(1-Cin))*100000000

LAYER'Core 3'
mesh_spacing=15
Material = 3.0
Cin=0.75
f = (Cin*aInAs+(1-Cin)*aGaAs-aInP)/aInP
C11 = (C11InAs*Cin+C11GaAs*(1-Cin))*100000000
C12 = (C12InAs*Cin+C12GaAs*(1-Cin))*100000000
C44 = (C44InAs*Cin+C44GaAs*(1-Cin))*100000000
{The composition of the indium-rich core is In0.75Ga0.25As}

LAYER'Shell 3'
```

```
Material = 2.0
Cin=0.65
f = (Cin*aInAs+(1-Cin)*aGaAs-aInP)/aInP
C11 = (C11InAs*Cin+C11GaAs*(1-Cin))*100000000
C12 =  (C12InAs*Cin+C12GaAs*(1-Cin))*100000000
C44 =  (C44InAs*Cin+C44GaAs*(1-Cin))*100000000

LAYER'Diffusion layer up 3'
Material = 1.0
Cin=0.60
f = (Cin*aInAs+(0.9-Cin)*aGaAs+0.1*aAlAs-aInP)/aInP
C11 = (C11InAs*Cin+C11GaAs*(0.9-Cin)+0.1*C11AlAs)*100000000
C12 = (C12InAs*Cin+C12GaAs*(0.9-Cin)+0.1*C12AlAs)*100000000
C44 = (C44InAs*Cin+C44GaAs*(0.9-Cin)+0.1*C44AlAs)*100000000

LAYER'Above QWR'
Material = 0.0
f = 0.0
C11 = C11MAT
C12 = C12MAT
C44 = C44MAT

START (-(Core_R-xs2),-M_Y/2) LINE TO((Core_R+xs2),-M_Y/2) LINE
TO((Core_R+xs2),M_Y/2) LINE TO(-(Core_R-xs2),M_Y/2) LINE TO CLOSE

{*********************************************}

MONITORS    {Show progress.}

 GRID(x,z) on y = 0 as "XZ Projection"
 CONTOUR(Material)  PAINTED on y = 0 as "Material - XZ Projection"
 CONTOUR(Up)  PAINTED on y = 0 as "X-Displacement - XZ Projection"
 CONTOUR(Wp) PAINTED on y = 0 as "Z-Displacement"
 CONTOUR(Uz) PAINTED on y = 0 as "dU/dz"
 CONTOUR(Wz) PAINTED on y = 0 as "dW/dz"
 CONTOUR(ex)  PAINTED on y = 0 as "X-Strain - XZ Projection"
 Contour (Cin) painted on y=0 as "Cin-XZ Projection"

{*********************************************}

PLOTS   {Save result displays.}
 GRID(x,z) on y = 0 as "XZ Projection"
 CONTOUR(Material)  PAINTED on y = 0 as "Material - XZ Projection"
 CONTOUR(Up)  PAINTED on y = 0 as "X-Displacement - XZ Projection"
 CONTOUR(Wp) PAINTED on y = 0 as "Z-Displacement"
 CONTOUR(Uz) PAINTED on y = 0 as "dU/dz"
 CONTOUR(Wz) PAINTED on y = 0 as "dW/dz"
 CONTOUR(ex)  PAINTED on y = 0 as "X-Strain - XZ Projection"
 Contour (Cin) painted on y=0 as "Cin-XZ Projection"

END
```

Appendix F

Parameters for chemical potential calculations

The parameters employed for FE simulations are listed below.

F.1 Intrinsic mismatch

The intrinsic mismatches between III-As (III=**In**, **Ga** or **Al**) and InP are:

$$\varepsilon^{In}{}_0 = \frac{a_{InAs} - a_{InP}}{a_{InP}} = \frac{6.0584 - 5.8686}{5.8686} = 3.23\%$$

$$\varepsilon^{Ga}{}_0 = \frac{a_{GaAs} - a_{InP}}{a_{InP}} = \frac{5.6533 - 5.8686}{5.8686} = -3.67\%$$

$$\varepsilon^{Al}{}_0 = \frac{a_{AlAs} - a_{InP}}{a_{InP}} = \frac{5.6605 - 5.8686}{5.8686} = -3.55\%$$

F.2 Young's modulus (Y_{oung})

The Young's modulus of each binary alloy on (100) plane along [011] direction at 300 K are adopted from (Adachi 2004) and listed below.

$$Y_{oung-AlAs} = 1.179\times10^{12}\, dyn/cm^2 = 1.179\times10^{11}\, N/m^2$$

$$Y_{oung-GaAs} = 1.213\times10^{12}\, dyn/cm^2 = 1.213\times10^{11}\, N/m^2$$

$$Y_{oung-InAs} = 0.793\times10^{12}\, dyn/cm^2 = 0.793\times10^{11}\, N/m^2$$

The Young's moduli for ternary and quaternary alloys are interpolated by composition according to Vegard's law.

F.3 Surface energy (γ)

{100} surface energy for each binary alloy is listed below*.

$\gamma_{InAs} = 0.704\ J/m^2$ (Pehlke et al. 1997, calculation)

$\gamma_{GaAs} = 1.06\ J/m^2$ (Adachi 2005, experiment)

$\gamma_{AlAs} = 1.23\ J/m^2$ (Chen et al. 1995)**

The surface energies for ternary and quaternary alloys are interpolated by composition according to Vegard's law (Vegard 1921).

---

* There is no single recent reference showing all the surface energies for InAs, GaAs and AlAs. The values adopted for calculations showing a very close ratio of $\gamma_{InAs} : \gamma_{GaAs} : \gamma_{AlAs}$ =1:1.51:1.75 to that of an early theoretical calculation by Cahn et al. (Cahn et al. 1964) where $\gamma_{InAs} : \gamma_{GaAs} : \gamma_{AlAs}$ =1:1.57:1.86. The data from Cahn's work is not adopted because the surface energy for each binary alloy is double those published in the recent literature (Adachi 2005; Pehlke et al. 1997).

** γ_{AlAs} is estimated by the ratio of the product of the experimental bond energy (E_B) and surface atom density (N_S , number of atoms per unit area) for GaAs (100) and AlAs (100) using $\gamma_{AlAs} = \frac{N_{S-AlAs}}{N_{S-GaAs}} \times \frac{E_{B-AlAs}}{E_{B-GaAs}} \times \gamma_{GaAs}$ (Porter et al. 2001). This equation can be simplified by $\gamma_{AlAs} = \frac{E_{B-AlAs}}{E_{B-GaAs}} \times \gamma_{GaAs}$ since AlAs and GaAs possess the same lattice structure (zinc-blend) and very close lattice constants (shown in section F.1 of this appendix.)

F.4 Elastic modulus

The elastic moduli for binary alloys (Adachi 2004) are listed in table 1 below.

Table F-1: Elastic moduli for binary alloys.

	C11 (10^9 Pa)	C12 (10^9 Pa)	C44 (10^9 Pa)
InAs	83.3	45.3	39.6
GaAs	118.8	53.8	59.4
AlAs	120.2	57.0	58.9

The elastic moduli for ternary and quaternary alloys are interpolated by composition according to Vegard's law.

F.5 Curvature ($\kappa(r)$)

Based on the geometric shape of the QWRs in the FE model, the mean curvature at a point on a surface in three dimensions (Spivak 1999) can be defined as:

$$\kappa(r) = 0.5 \times \frac{-\frac{\partial^2 h}{\partial x^2}}{\left[1+\left(\frac{\partial h}{\partial x}\right)^2\right]^{1.5}}$$

since the QWR height h is a function of only x, as shown in the models (for example, Figure 7-1) and codes (**Appendix E** and **G**) for the FE simulations. The unit of curvature is m^{-1}.

From the definition above, for a convex surface, where $\frac{\partial^2 h}{\partial x^2} < 0$ and $\kappa(r) > 0$; a positive curvature is obtained. An increase in the chemical potential density is expected based equation (7-4) in chapter 7. While for a concave surface, where $\frac{\partial^2 h}{\partial x^2} > 0$ and $\kappa(r) < 0$; a negative curvature is obtained and a reduction in the chemical potential density is expected.

Apendix G

FlexPDE code for calculating chemical potential distribution on the growth front

```
TITLE ' Two QWRs in the same layer - Chemical potential calculation'

SELECT                  {Method controls. }
NOMINMAX=ON             {Turn off min-max value locators from obscuring plot.}
FEATUREPLOT=OFF
ERRLIM=2e-3             {set up the expected convergence for the solutions}

COORDINATES
 Cartesian3             {Sets up 3d solver.}

VARIABLES               {System variables. }
 U                      {X displacement.}
 V                      {Y displacement.}
 W                      {Z displacement.}

DEFINITIONS             {Parameter definitions.}

{I. Geometric parameters of the structure
 M_Z = matrix thickness.  z in planview.
 M_X = matrix width in the x direction in planview.
 M_Y = matrix width in the y direction in planview.
 WL = wetting layer thickness in z direction in planview.
 D = z distance of the wetting layer from the bottom surface.
 QWire_R = the radius of the QWR.
 h=thickness of caldding Layer (CL) above top of QWR
 QWire_T_Z = the height of a lens-shaped QWR.

Zlens1=control the boundary of QWRs
Zlens2=control the boundary of covering BL
ZlensQWire1=define the boundary of QWR1
ZlensQWire2=define the boundary of covering BL1
ZlensQWire3=define the boundary of QWR2
ZlensQWire4=define the boundary of covering BL2

R0=the half base width of QWR
R1=the half base width of the upper covering barrier layrer
XS1=the center of QWR1 and covering BL1
XS2=the center of QWR2 and covering BL2}

{II. Parameters for calculations
 f = is the fractional lattice mismatch between the QWR and matrix material.
Young=Young's modulus for InGaAlAs BL.
e0In=Intrinsic mismatch between InAs and InGaAlAs (InP).
e0Ga=Intrinsic mismatch between GaAs and InGaAlAs (InP).
e0Al=Intrinsic mismatch between AlAs and InGaAlAs (InP).
```

k= curvature on each spot of the grwoth front surface, mean curvature for 3D structure is used.
gama=surface energy for InGaAlAs growth front

The values of the above parameters are listed in Appendix F}
CPIn=chemical potential density of In adatom
CPGa=chemical potential density of Ga adatom
CPAl=chemical potential density of Al adatom}

```
M_X =100.0          {in nm}
M_Y =50.0           {in nm}
M_Z=70
Zlens1
Zlens2

WL = 0.50           {in nm}
D =49.0             {in nm}
QWire_Z=6           {in nm}
QWire_T_Z =6        {in nm}

QWire_R = 10        {in nm}
R0 = QWire_R
R1=R0+0.5
```

h=0.3 {in nm, controling the thickness of covering BL above the QWR, which is close to 1ML}
h1=0.05
XS1=12
XS2=-12 {the separation of QWR1 and QWR2 is 4nm definined by XS1 and XS2}
{elastic modulus defined under <100> coordinate system}
C11
C12
C44

{elastic modulus defined under [011]-[0-11]-[100] system, which are transformed from C11,C12 and C44}

C11T=0.5*(C11+C12)+C44
C12T=0.5*(C11+C12)-C44
C44T=C44

{Set the default lattice mismatch for the matrix and the QWire.}

```
f = 0.0             {Default for matrix.}
fQWire = 0.0323     {Mismatch between QWR materail InAs and InP }
fwl=0.0047          {Mismatch bwtween WL material In0.60Ga0.40As and InP}
```

{Set the material identifier to so that we know which material is associated with a given elastic modulus: 0.0 = matrix, 1.0 = wetting layer and QWire}
Material = 0.0

{Define the outer boundary of the QWire.}
ZlensQWire1=min(max(QWire_Z*(1-(((x-XS1)^2)/R0^2)),0),QWire_T_Z)+D+WL
{the boundary of InAs QWR1}

ZlensQWire2= min(max((QWire_Z+h)*(1-(((x-XS1)^2)/R1^2)),0),QWire_T_Z+h)+D+WL+h1
{the boundary of the BL1 covering the InAs QWR1}

```
ZlensQWire3=min(max(QWire_Z*(1-(((x-XS2)^2)/R0^2)),0),QWire_T_Z)+D+WL
{the boundary of InAs QWR2}

ZlensQWire4=    min(max((QWire_Z+h)*(1-(((x-XS2)^2)/R1^2)),0),QWire_T_Z+h)+D+WL+h1
{the boundary of the BL2 covering the InAs QWR2}

Young  {Young's modulus}
Young_InAs=793.0e08              {N/m^2=Pa} {For InAs}
Young_InGaAs=961.0e08            {N/m^2=Pa} {For In0.60Ga0.40As}
Young_InGaAlAs=987.0e08          {N/m^2=Pa} {For In0.53Ga0.37Al0.10As}

{Intrinsic mismatch between InAs, GaAs, AlAs and InP}
e0In=0.0323
e0Ga=-0.0367
e0Al=-0.0355

gama {Surface Energy }

gama_InAs100=0.704   {J/m^2}
gama_GaAs100=1.06    {J/m^2}
gama_AlAs100=1.23    {J/m^2}

gama_InGaAs100=(0.60*gama_InAs100)+(0.40*gama_GaAs100) {J/m^2}
{For In0.60Ga0.40As 100 surface}

gama_InGaAlAs100=(0.53*gama_InAs100)+(0.37*gama_GaAs100)+(0.10*gama_AlAs100)
{J/m^2}
{For In0.53Ga0.37Al0.10As 100 surface}


{Curvature definition}
k
k0=0.5*1000*1000*1000*(-dx(dx(Zlens2)))/((1+(dx(Zlens2))^2)^1.5)   {m^-1}

a {lattice constant}
a_InAs=0.60584 {in nm} {lattice constant of InAs}
a_InGaAs=0.58964    {in nm}  {lattice constant of In0.60Ga0.40As layer}
a_InGaAlAs=0.58686  {in nm} {lattice constant of In0.53Ga0.37Al0.10As layer}

{Define the anisotropic elastic constants for In0.53Ga0.37Al0.10As in Pa according to Vegard's
law}
C11MAT = 100.125e09
C12MAT = 49.615e09
C44MAT = 48.856e09

{Define the anisotropic elastic constants for In0.60Ga0.40As in Pa}
C11WL=97.5e09
C12WL=48.7e09
C44WL=47.52e09

{Define the anisotropic elastic constants for InAs in Pa.}
 C11QWire = 83.3e09
```

```
C12QWire = 45.3e09
C44QWire = 39.6e09

{Define the strain variables.}
 ex = dx(U)
 ey = dy(V)
 ez = dz(W)
 eh = ex+ey+ez+ex*ey+ex*ez+ey*ez+ex*ey*ez        {Volume strain.}

{Define the stress variables.}
 gxy = dy(U) + dx(V)
 gyz = dz(V) + dy(W)
 gzx = dx(W) + dz(U)
 Sx = C11T*(ex-f) + C12T*(ey-f) + C12*(ez-f)
 Sy = C12T*(ex-f) + C11T*(ey-f) + C12*(ez-f)
 Sz = C12*(ex-f) + C12*(ey-f) + C11*(ez-f)
 Txy = C44T*gxy
 Tyz = C44T*gyz
 Tzx = 0.5*(C11-C12)*gzx

{Find mean translation and rotation. }
 Vol = Integral(1)                          {Intergral over all the box}

 Tx = integral(U)/Vol                {X-motion}
 Ty = integral(V)/Vol                {Y-motion}
 Tz = integral(W)/Vol                {Z-motion}
 Rz = integral(dx(V) - dy(U))/Vol    {Z-rotation}
 Rx = integral(dy(W) - dz(V))/Vol    {X-rotation}
 Ry = integral(dz(U) - dx(W))/Vol    {Y-rotation}

{Displacements with translation and rotation removed.}
 Up = U - Tx + Rz*y - Ry*z
 Vp = V - Ty + Rx*z - Rz*x
 Wp = W - Tz + Ry*x - Rx*y

{Derivatives required for Fortran TEM simulation program in [001] zone axis.}
 Uz=dz(Up)
 Vz=dz(Vp)
 Wz=dz(Wp)

{Define the partial chemical potentials for each group III element.}
{Elastic energy component}
EIn=0.5*Young*(ex-e0In)^2
EGa=0.5*Young*(ex-e0Ga)^2
EAl=0.5*Young*(ex-e0Al)^2

{Surface energy component}
SurE=k*gama

{partical chemical potential density definition}
CPIn=EIn+SurE
CPGa=EGa+SurE
CPAl=EAl+SurE
```

```
INITIAL VALUES
 U= 0
 V = 0
 W = 0

EQUATIONS                          {PDE's, one for each variable.}
   U:    dx(Sx) + dy(Txy) + dz(Tzx) = 0   { the U-displacement equation }
   V:    dx(Txy) + dy(Sy) + dz(Tyz) = 0   { the V-displacement equation }
   W:    dx(Tzx) + dy(Tyz) + dz(Sz) = 0   { the W-displacement equation }

EXTRUSION
 SURFACE 'Bottom' z=0
  LAYER 'Underneath QWire'
 SURFACE 'Wetting Layer Bottom' z = D
  LAYER 'Wetting Layer'
 SURFACE 'QWire Bottom' z = D+WL
  LAYER 'QWire Layer'
 SURFACE 'QWire Top' z=Zlens1
  Layer 'covering CL'
SURFACE 'Top' z=Zlens2


BOUNDARIES   {The domain definition.}
{Programs default to Natural boundary conditions on all of the surfaces.  This is correct for the top
and bottom surfaces but not for the sides which are effectively infinite in extent. Get around this
by making the x and y dimensions large so that edge effects do not affect the result. }

{Free surface boundary conditions}
Surface'Top'
Natural (U)=0
Natural (V)=0
Natural (W)=0
{it means traction free, Sz=Tzx=Tyz=0}

Surface'Bottom'
Value (W)=0
{it means fixed bottom of the simulation box}

REGION 1 'Matrix'
 Zlens1=D+WL
Zlens2=D+WL+h1

LAYER 'Underneath QWire'
   Material = 0.0
   f = 0.0
   C11 = C11MAT
   C12 = C12MAT
   C44 = C44MAT
   Young=Young_InGaAlAs
   gama=gama_InGaAlAs100
   k=0
   a=a_InGaAlAs
```

```
LAYER 'Wetting Layer'
   Material = 1.0
   f = fwl
   C11 = C11WL
   C12 = C12WL
   C44 = C44WL
   Young=Young_InGaAs
   gama=gama_InGaAs100
    k=0
    a=a_InGaAs

LAYER 'QWire Layer'
   Material = 0.0
   f = 0.0
   C11 = C11MAT
   C12 = C12MAT
   C44 = C44MAT
   Young=Young_InGaAlAs
    gama=gama_InGaAlAs100
    k=0
    a=a_InGaAlAs

Layer 'covering CL'
 Material = 0.0
   f = 0.0
   C11 = C11MAT
   C12 = C12MAT
   C44 = C44MAT
   Young=Young_InGaAlAs
    gama=gama_InGaAlAs100
    k=0
    a=a_InGaAlAs


START (-M_X/2,-M_Y/2)
Value (V)=0
LINE TO(M_X/2,-M_Y/2)
VALUE(U) = 0.0
LINE TO(M_X/2,M_Y/2)
 VALUE(V) = 0.0
 LINE TO(-M_X/2,M_Y/2)
VALUE(U) = 0.0
 LINE TO CLOSE

 {****************************************}

REGION 2 'Capping layer 1'

 Zlens1=D+WL
 Zlens2= ZlensQWire2

LAYER 'Underneath QWire'
  Mesh_spacing=10
```

```
  Material = 0.0
   f = 0.0
   C11 = C11MAT
   C12 = C12MAT
   C44 = C44MAT
   Young=Young_InGaAlAs
    gama=gama_InGaAlAs100
     k=0
     a=a_InGaAlAs

LAYER 'Wetting Layer'
  Mesh_spacing=10
    Material = 1.0
   f = fwl
   C11 = C11WL
   C12 = C12WL
   C44 = C44WL
   Young=Young_InGaAs
   gama=gama_InGaAs100
     k=0
     a=a_InGaAs

LAYER 'QWire Layer'
  Mesh_spacing=10
  Material = 0.0
   f = 0.0
   C11 = C11MAT
   C12 = C12MAT
   C44 = C44MAT
   Young=Young_InGaAlAs
    gama=gama_InGaAlAs100
     k=k0
     a=a_InGaAlAs

Layer'covering CL'
 Mesh_spacing=10
  Material = 0.0
   f = 0.0
   C11 = C11MAT
   C12 = C12MAT
   C44 = C44MAT
   Young=Young_InGaAlAs
    gama=gama_InGaAlAs100
     k=k0
     a=a_InGaAlAs

  START(-(R1-XS1),-M_Y/2)
   LINE TO((R1+XS1),-M_Y/2)
   LINE TO((R1+XS1),M_Y/2)
   LINE TO(-(R1-XS1),M_Y/2)
   LINE TO CLOSE

 {****************************************}
```

```
REGION 3 'QWR1'

Zlens1 = ZlensQWire1
Zlens2= ZlensQWire2

LAYER 'Underneath QWire'
  Material = 0.0
   f = 0.0
   C11 = C11MAT
   C12 = C12MAT
   C44 = C44MAT
   Young=Young_InGaAlAs
    gama=gama_InGaAlAs100
     k=0
     a=a_InGaAlAs

LAYER 'Wetting Layer'
      Material = 1.0
   f = fwl
   C11 = C11WL
   C12 = C12WL
   C44 = C44WL
   Young=Young_InGaAs
   gama=gama_InGaAs100
    k=0
    a=a_InGaAs

 LAYER 'QWire Layer'
  Material = 2.0
   f = fQWire
   C11 = C11QWire
   C12 = C12QWire
   C44 = C44QWire
   Young=Young_InAs
   gama=gama_InAs100
    k=k0
   a=a_InAs


Layer 'covering CL'
  Material = 0.0
   f = 0.0
   C11 = C11MAT
   C12 = C12MAT
   C44 = C44MAT
   Young=Young_InGaAlAs
    gama=gama_InGaAlAs100
     k=k0
     a=a_InGaAlAs

 START(-(R0-XS1),-M_Y/2)
   LINE TO((R0+XS1),-M_Y/2)
```

```
   LINE TO((R0+XS1),M_Y/2)
   LINE TO(-(R0-XS1),M_Y/2)
   LINE TO CLOSE

{*****************************************}


REGION 4 'Capping layer 2'

 Zlens1=D+WL
 Zlens2= ZlensQWire4

LAYER 'Underneath QWire'
   Mesh_spacing=10
   Material = 0.0
    f = 0.0
    C11 = C11MAT
    C12 = C12MAT
    C44 = C44MAT
    Young=Young_InGaAlAs
     gama=gama_InGaAlAs100
      k=0
      a=a_InGaAlAs

LAYER 'Wetting Layer'
   Mesh_spacing=10
     Material = 1.0
    f = fwl
    C11 = C11WL
    C12 = C12WL
    C44 = C44WL
    Young=Young_InGaAs
    gama=gama_InGaAs100
      k=0
      a=a_InGaAs

LAYER 'QWire Layer'
   Mesh_spacing=10
   Material = 0.0
    f = 0.0
    C11 = C11MAT
    C12 = C12MAT
    C44 = C44MAT
    Young=Young_InGaAlAs
     gama=gama_InGaAlAs100
      k=k0
      a=a_InGaAlAs

 Layer'covering CL'
 Mesh_spacing=10
  Material = 0.0
    f = 0.0
    C11 = C11MAT
```

```
  C12 = C12MAT
  C44 = C44MAT
  Young=Young_InGaAlAs
   gama=gama_InGaAlAs100
    k=k0
    a=a_InGaAlAs

 START(-(R1-XS2),-M_Y/2)
  LINE TO((R1+XS2),-M_Y/2)
  LINE TO((R1+XS2),M_Y/2)
  LINE TO(-(R1-XS2),M_Y/2)
  LINE TO CLOSE

{****************************************}

 REGION 5 'QWR2'

 Zlens1=ZlensQWire3
 Zlens2=ZlensQWire4

LAYER 'Underneath QWire'
  Material = 0.0
   f = 0.0
   C11 = C11MAT
   C12 = C12MAT
   C44 = C44MAT
   Young=Young_InGaAlAs
    gama=gama_InGaAlAs100
     k=0
     a=a_InGaAlAs

LAYER 'Wetting Layer'
      Material = 1.0
   f = fwl
   C11 = C11WL
   C12 = C12WL
   C44 = C44WL
   Young=Young_InGaAs
   gama=gama_InGaAs100
    k=0
    a=a_InGaAs


LAYER 'QWire Layer'
  Material = 2.0
   f = fQWire
   C11 = C11QWire
   C12 = C12QWire
   C44 = C44QWire
   Young=Young_InAs
   gama=gama_InAs100
    k=k0
   a=a_InAs
```

```
Layer 'covering CL'
  Material = 0.0
   f = 0.0
   C11 = C11MAT
   C12 = C12MAT
   C44 = C44MAT
   Young=Young_InGaAlAs
    gama=gama_InGaAlAs100
     k=k0
     a=a_InGaAlAs

 START(-(R0-XS2),-M_Y/2)
   LINE TO((R0+XS2),-M_Y/2)
   LINE TO((R0+XS2),M_Y/2)
   LINE TO(-(R0-XS2),M_Y/2)
   LINE TO CLOSE

MONITORS       {Show progress.}
 GRID(x,z) on y = 0 as "XZ Projection"
 Contour (Material) painted on y = 0 as "Material - XZ Projection"
 Contour (Material)  painted on z=D+QWire_T_Z/2+WL as "Material - XY Projection"
 Contour (Up)  painted on y = 0 as "X-Displacement - XZ Projection"
 Contour (Up^2+Vp^2)^0.5) painted on z=D+QWire_T_Z/2+WL as "R-Displacement"
 Contour (Wp) painted on y = 0 as "Z-Displacement"
 Contour (Uz) painted on y = 0 as "dU/dz"
 Contour (Wz)painted on y = 0 as "dW/dz"

Contour (CPIn) painted on y=0  as "partial chemical potential In-XZ projection"
Contour (CPGa)painted on y=0  as "partial chemical potential Ga-XZ projection"
Contour (CPAl)painted on y=0  as "partial chemical potential Al-XZ projection"

Contour (k) painted on surface 'Top'  as "curvature on top surface"
Contour (SurE) painted on surface 'Top' as 'Surface energy'
Contour (EIn) painted on surface 'Top'
Contour (EGa) painted on surface 'Top'
Contour (EAl) painted on surface 'Top'

Contour (CPIn) painted on surface 'Top'  as "partial chemical potential In"
Contour (CPGa) painted on surface 'Top'   as "partial chemical potential Ga"
Contour (CPAl) painted on surface 'Top' as "partial chemical potential Al"

Contour (CPIn) painted on surface 'QWire Bottom'
Contour (CPGa) painted on surface 'QWire Bottom'
Contour (CPAl) painted on surface 'QWire Bottom'
Contour (ex) painted on surface 'Top'


PLOTS    {Save result displays.}
  GRID(x,z) on y = 0 as "XZ Projection"
  GRID(x,y) on z = D + QWire_T_Z/2+WL as "XY Projection"
 Contour (Material) painted on y = 0 as "Material - XZ Projection"
GRID(x,z) on y = 0 as "XZ Projection"
```

```
Contour (Material) painted on y = 0 as "Material - XZ Projection"
Contour (Material)  painted on z=D+QWire_T_Z/2+WL as "Material - XY Projection"
Contour (Up)  painted on y = 0 as "X-Displacement - XZ Projection"
Contour (Up^2+Vp^2)^0.5) painted on z=D+QWire_T_Z/2+WL as "R-Displacement"
Contour (Wp) painted on y = 0 as "Z-Displacement"
Contour (Uz) painted on y = 0 as "dU/dz"
Contour (Wz)painted on y = 0 as "dW/dz"


Contour (CPIn) painted on y=0  as "partial chemical potential In-XZ projection"
Contour (CPGa)painted on y=0  as "partial chemical potential Ga-XZ projection"
Contour (CPAl)painted on y=0  as "partial chemical potential Al-XZ projection"

Contour (k) painted on surface 'Top'  as "curvature on top surface"
Contour (SurE) painted on surface 'Top' as 'Surface energy'
Contour (EIn) painted on surface 'Top'
Contour (EGa) painted on surface 'Top'
Contour (EAl) painted on surface 'Top'

Contour (CPIn) painted on surface 'Top'  as "partial chemical potential In"
Contour (CPGa) painted on surface 'Top'   as "partial chemical potential Ga"
Contour (CPAl) painted on surface 'Top' as "partial chemical potential Al"
Contour (CPIn) on surface 'Top'
Contour (CPGa)on surface 'Top'
Contour (CPAl) on surface'Top'

Contour (CPIn) painted on surface 'QWire Bottom'
Contour (CPGa) painted on surface 'QWire Bottom'
Contour (CPAl) painted on surface 'QWire Bottom'
Contour (ex) painted on surface 'Top'


END
```

References

Adachi, S. 2004. *Handbook on physical properties of semiconductors.* Kluwer Academic Publishers, Boston.

Adachi, S. 2005. *Properties of Group-IV, III–V and II–VI Semiconductors*. John Wiley & Sons Ltd, The Atrium, Southern Gate and Chichester.

Alén, B., Matínez-Pastor, J., González, L., García, J.M., Molina, S.I., Ponce, A. & García, R. 2002. *Size-filtering effects by stacking InAs/InP (001) self-assembled quantum wires into multilayers.* Physical Review B. **65** (24) 241301.

Alferov, Z.I. 2001. *Nobel Lecture: The double heterostructure concept and its applications in physics, electronics, and technology.* Review of Modern Physics. **73** (3) 767-782.

Androussi, Y., Benabbas, T., & Lefebvre, A. 1999. *Transmission electron microscopy analysis of the shape and size of semiconductor quantum dots.* Philosophical Magazine Letter. **79** (4) 201-208

Backstrom, G. 2005. *Fields of Physics by Finite Element Analysis. Using FlexPDE version 5.* GB publishing and Gunnar Backstrom, Malmo, Sweden.

Bansal, B. 2006. *A model for the temperature dependence of photoluminescence from self-assembled quantum dots.* Journal of Applied Physics. **100** (9) 093107.

Beanland, R. 2005. *Dark field transmission electron microscope images of III–V quantum dot structures.* Ultramicroscopy. **102** (2) 115-125.

Bernard, J.E., & Zunger, A. 1994. *Is there an elastic anomaly for a (001) monolayer of InAs embedded in GaAs?* Applied Physics Letters. **65** (2) 165-167.

Biasiol, G., & Kapon, E. 1998. *Mechanisms of Self-Ordering of Quantum Nanostructures Grown on Nonplanar Surfaces.* Physical Review Letters. **81** (14) 2962-2965.

Bithell, E.G., & Stobbs, W.M. 1991. *III-V ternary semiconductor heterostructures: The choice of an appropriate compositional analysis technique.* Journal of Applied Physics. **69**(4) 2149-2155.

Brault, J., Gendry, M., Grenet, G., Hollinger, G., Desières, Y., & Benyattou, T. 1998. *Role of buffer surface morphology and alloying effects on the properties of InAs nanostructures grown on InP(001).* Applied Physics Letters. **73** (20) 2932-2934.

Brault, J., Gendry, M., Marty, O., Pitaval, M., Olivares, J., Grenet, G., and Hollinger, G., 2000. *Staggered vertical self-organization of stacked InAs/InAlAs quantum wires on InP(001).* Applied Surface Science. **162-163** 584-589.

Brault, J., Gendry, M., Grenet, G., Hollinger, G., Olivares, J., Salem, B., Benyattou, T., & Bremond, G. 2002. *Surface effects on shape, self-organization and photoluminescence of InAs islands grown on InAlAs/InP(001).* Journal of Applied Physics. **92** (1) 506-510.

Browning, N.D., Chisholm, M.F., & Pennycook, S.J. 1993. *Atomic-resolution analysis using a scanning transmission electron microscope.* Nature. **366** (6451) 143-146.

Browning, N.D., Arslan, I., Moexck, P., & Topuria, P. 2001. *Atomic resolution scanning transmission electron microscopy.* Physica Status Solidi B. **227** (1) 229-245.

Brusaferri, L., Sanguinetti, S., Grilli, E., Guzzi, M., Bignazzi, A., Bogani, F., Carraresi, L., Colocci, M., Bosacchi, A., Frigeri, P. & Franchi, S. 1996. *Thermally activated carrier transfer and luminescence line shapes in self-organized InAs quantum dots.* Applied Physics Letters. **69** (22) 3354-3356.

Bryant, G.W. & Solomon, G.S. (Eds) 2005. *Optics of Quantum Dots and Wires.* Artech House, Inc., Boston/London.

Cahn, J.W., & Hanneman, R.E., 1964. *(111) Surface tensions of III–V compounds and their relationship to spontaneous bending of thin crystal.* Surface Science. **1** (4) 387-398.

Chen, A-B., Sher, A. 1995. *Semiconductor alloy: physics and materials engineering.* Plenum Press, New York.

Chew, N.G., & Cullis A.G. 1987. *The preparation of transmission electron microscope specimens from compound semiconductors by ion milling.* Ultramicroscopy. **23** (2) 175-198.

Chou, S-T. 2000. *Abnormal temperature dependence of band-gap energies observed in (InAs)/(GaAs) and (InP)/(GaP) superlattices with strong lateral composition modulation.* Journal of Applied Physics. **87** (1) 285-288.

Chung, H.-C., Lai, Y.-F., Liu, C.-P., & Lai, Y.-L., 2008. *Correlation of In-Ga intermixing with band-tail states in InAs/GaAs quantum dots.* Applied Physics Letters. **92**(5) 051903.

Colliex, C. 1985. *An illustrated review of various factors governing the high spatial resolution capabilities in EELS analysis.* Ultramicroscopy. **18** (1-4) 131-150.

Crozier, P.A., Catalano, M., & Cingolani, R. 2003. *A modeling and convolution method to measure compositional variations in strained alloy quantum dots.* Ultramicroscopy. **94** (1) 1-18

Cui, K., Robertson, M.D., Robinson, B.J., Andrei, C.M., Thompson, D.A., & Botton, G.A. 2009. *Quantitative compositional analysis and strain study of InAs quantum wires with InGaAlAs barrier layer.* Journal of Applied Physics. **105** (9) 094313.

Cullis, A.G., Norris, D.J., Walther, T., Migliorato M.A., & Hopkinson, M., 2002. *Stranski-Krastanow transition and epitaxial island growth.* Physical Review B. **66** (8) 081305

Czaban, J.A., & Thompson, D.A. 2006. *The influence of lateral composition modulation on the photoluminescence of tensile strained InGaAs quantum wells at room temperature.* Journal of Applied Physics. **99** (11) 113109.

Dai, Y.T., Fan, J.C., Chen, Y.F., Lin, R.M., Lee, S.C.& Lin, H.H. 1997. *Temperature dependence of photoluminescence spectra in InAs/GaAs quantum dot supperlattice with large thickness.* Journal of Applied Physics. **82** (9) 4489-4492.

DeGiorgi, M., Passaseo, A., Rinaldi, R., Johal, T., Cingolani, R., Taurino, A., Catalano, M., & Crozier, P. 2001. *Nanoscale compositional fluctuations in single InGaAs/GaAs quantum dots.* Physical Status Solidi (b). **224** (1) 17-20.

Digital Instruments. 2000. *Scanning probe microscopy training notebook.* Version 3.0. Santa Barbara, CA.

Djie, H.S., Wang, Y., Ooi, B.S., Wang, D-N., Hwang, J.C.M., Dang, G.T., & Chang, W.H. 2006. *Defect annealing of InAs-InGaAlAs quantum-dash-in-asymmetric-well laser.* IEEE Photonics Technology Letters. **18** (22) 2329-2331.

Djie, H.S., Wang, Y., Ding, Y.H., Wang, D.N., Hwang, J.C.M., Fang, X.M., Wu, Y., Fastenau, J.M., Liu, A.W.K., Dang, G.T., Chang, W.H., & Ooi, B.S. 2008.

Quantum dash intermixing. IEEE Journal of Selected Topics in Quantum Electronics. **14** (4) 1239-1249.

Dorin, C., & Mirecki Millunchick, J. 2002. *Lateral composition modulation in AlAs/InAs and GaAs/InAs short period superlattices structures: The role of surface segregation.* Journal of Applied Physics. **91** (1) 237-244.

Edington, J.W. 1976. *Practical Electron Microscopy in Materials Science.* Van Nostrand Reinhold Company, New York.

Egerton, R.F., 1986. *Electron Energy Loss Spectroscopy in the Electron Microscope.* Plenum, New York.

Eisele, H., Lenz, A., Heitz, R., Timm, R., Dähne, M., Temko, Y., Suzuki, T., & Jacobi, K. 2008. *Change of InAs/GaAs quantum dot shape and composition during capping.* Journal of Applied Physics. **104** (12) 124301

Franchi, S., Trevisi, G., Seravalli, L. & Frigeri, P. 2003. *Quantum dot nanostructures and molecular beam epitaxy.* Progress in Crystal Growth and Characterization of Materials. **47** (2-3) 166-195.

Fuster, D., González, L., González, Y., González, M.U., & Martínez-Pastor, J. 2005. *Size and emission wavelength control of InAs/InP quantum wires.* Journal of Applied Physics. **98** (3) 033502.

Galindo, P.L., Kret, S., Sanchez, A.M., Laval, J-Y., Yáñez, A., Pizarro, J., Guerrero, E., Ben, T., & Molina, S.I. 2007. *The Peak Pairs algorithm for strain mapping from HRTEM images.* Ultramicroscopy. **107** (12) 1186-1193.

García, J.M., González, L., González, M.U., Silveira, J.P., González, Y., & Briones, F. 2001. *InAs/InP(001) quantum wire formation due to anisotropic stress relaxation: in situ stress measurements.* Journal of Crystal Growth. **227-228** 975-979.

Gfroerer, T.H. 2000. *Photoluminescence in Analysis of Surfaces and Interfaces.* in Meyers, R.A. (Ed.) *Encyclopedia of Analytical Chemistry.* John Wiley & Sons Ltd, Chichester.

Gioannini, M. 2004. *Numerical modeling of the emission characteristics of semiconductor quantum dash materials for lasers and optical amplifiers.* IEEE Journal of Quantum Electronics. **40** (4) 364-373.

Gelczuk, Ł., Dąbrowska-Szat, M., Jóźwiak, G., Radziewicz, D., Serafińczuk, J., & Dłużewski, P. 2007. *Dislocation-related electronic states in partially strain-*

relaxed InGaAs/GaAs heterostructures grown by MOVPE. Physica Status Solidi (c). **4** (8) 3037-3042.

Gendry, M., Monat, C., Brault, J., Regreny, P., Hollinger,G., Salem, B., Guillot, G., Benyattou, T., Bru-chevallier, C., Bremond, G., & Marty, O. 2004. *From large to low height dispersion for self-organized InAs quantum sticks emitting at 1.55 μm on InP (001).* Journal of Applied Physics. **95** (9) 4761-4766.

Goodhew, P.J. 1985. *Thin foil preparation for electron microscopy.* Elsevier, Amsterdam, New York.

Grundmann, M. (Ed.) 2002. *Nano-Optoelectronics,* Springer-Verlag, Berlin Heidelberg.

Gutiérrez, M., Hopkinson, M., Liu, H.Y., Herrera, M., González, D., & García, R. 2005 a .*Characterization of structure and defects in dot-in-well laser structures.* Materials Science and Engineering: C. **25** (5-8) 793-797.

Gutiérrez, M., Hopkinson, M., Liu, H.Y., Ng, J.S., Herrera, M., González, D., García, R., & Beanland, R. 2005 b. *Strain interactions and defect formation in stacked InGaAs quantum dot and dot-in-well structures.* Physica E. **26** (1-4) 245-251.

Harrison, P. 2005. *Quantum wells, wires and dots, theoretical and computational physics of semiconductor nanostructures.* 2nd Edition, John Wiley& Sons, Ltd., Chichester.

Harvey, A., Davock, H., Dunbar, A., Bangert, U., & Goodhew, P.J. 2001. *Three-dimensional compositional analysis of quantum dots.* Journal of Physics D: Applied Physics. **34** (4) 636-644.

Hawkes, P.W., & Spence, J.C.H. (Eds.) 2006. Science of Microscopy, Vol.1, Chapter 4. Analytical electron microscopy. Springer, New York.

Herman, M.A., Richter, W., & Sitter, H. 2004. *Epitaxy: Physical Principles and Technical Implementation.* Springer-Verleg, Berlin, Heidelberg, New York.

Higashiwaki, M., Yamamoto, M., Higuchi, T., Shimomura, S., Adachi, A., Okamoto, Y., Sano, N., & Hiyamizu, S. 1996. *High-Density GaAs/AlAs Quantum Wires Grown on (775)B-Oriented GaAs Substrates by Molecular Beam Epitaxy.* Japanese Journal of Applied Physics. **35** (5B) L606-L608.

Hirth, J.P., & Lothe, J. 1992. *Theory of Dislocations.* 2nd Edition, Krieger, Malabar, FL.

Hovsepian, A., Cherns, D., & Jaeger, W. 1999. *Analysis of ultrathin Ge layer in Si by large angle convergent beam electron diffraction.* Philosophical Magazine A **79** (6) 1395-1410.

Houdré, R., Gueissaz, F., Gailhanou, M., Ganière, J.-D., Rudra, A., & Ilegems, M. 1991. *Characterization of InGaAs and InAlAs layers on InP by four-crystal high resolution X-ray diffraction and wedge transmission electron microscopy.* Journal of Crystal Growth. **111** (1-4) 456-460.

Hulko, O., Thompson, D.A., Czaban, J.A., & Simmons J.G. 2006. *The effect of different proximity caps on quantum well intermixing in InGaAsP/InP QW structures.* Semiconductor Science and Technology. **21** (7) 870-875.

Hulko, O., Thompson, D.A., & Simmons, J.G. 2008. *Comparison of quantum well interdiffusion on group III, group V, and combined groups III and V sublattices in GaAs-based structures.* IEEE Journal of Selected Topics in Quantum Electronics. **14** (4) 1104-1112.

Hÿtch, M.J., Snoeck, E., & Kilaas R. 1998. *Quantitative measurement of displacement and strain fields from HRTEM micrographs.* Ultramicroscopy. **74** (3) 131-146.

Jiang, C., Fujikura, H., & Hasegawa, H. 2000. *Vertical barrier layer formation during selective MBE growth of InGaAs ridge quantum wires on InP pattern substrate.* Physica E. **7** (3-4) 902-906.

Jogai, B. 2000. *Three-dimensional strain field calculations in coupled InAs/GaAs quantum dots.* Journal of Applied Physics. **88** (9) 5050-5055.

Jonas Ohlsson, B., & Miller, M.S. 1998. *Growth of strained GaAs islands on (001) GaP:a RHEED study of quantum wire formation.* Journal of Crystal Growth. **188** (1-4) 387-391.

Joyce, B.A., & Vvedensky, D.D. 2004. *Self-organized growth on GaAs surfaces.* Materials Science and Engineering R. **46** (6) 127-176.

Joyce, B.A., Kelires, P.C., Naumovets, A.G., & Vvedensky, D.D. (Eds) 2005. *Quantum dots: fundamentals, applications, and frontiers.* Springer, Dordrecht, New York.

Kaminow, I., & Li, T. (Eds.) 2002. *Optical Fiber Telecommunications.* IVA. Academic Press, San Diego.

Kapon, E. 1993. *"Quantum wire semiconductor lasers"* in *Quantum well lasers,* edited by Zory, P.S., Academic Press, New York.

Karim, A., Elfving, A., Larsson, M., Ni, W.-X., & Hansson, G.V. 2006. *Compositional analysis of Si/SiGe quantum dots using STEM and EDX.* Proceedings of SPIE. **6129** 6129C1-6129C9.

Kash, K., Scherer, J.M., Worlock, J.M., Craighead, H.G., & Tamargo, M.C. 1986. *Optical spectroscopy of ultrasmall structures from etched quantum wells.* Applied Physics Letters. **49** (16) 1043-1045.

Kasu, M., & Kobayashi, N. 1993. *Equilibrium multiatomic step structure of GaAs(001) vicinal surfaces grown by metalorganic chemical vapor deposition.* Applied Physics Letters. **62** (11) 1262-1264.

Kim, J.S., Lee, J.H., Hong, S.U., Han, W.S., Kwack, H.-S., Lee, C.W., & Oh, D.K. 2003. *Formation of self-assembled InAs quantum dots on InAl(Ga)As/InP and effects of a thin GaAs layer.* Journal of Crystal Growth. **259** (3) 252-256.

Komori, K., & Arakawa, M. 1997. *Electronic States in Crescent-Shaped GaAs Coupled Quantum Wires.* Japanese Journal of Applied Physics. **36** (3B) 1927-1932.

Kümmell T., Sauerwald, A., Spranger, D., Bacher, G., Krebs, R., Reirhmaier, J.P., & Forchel, A. 2005. S*TEM-study of 1.3 μm InAs/InGaAs quantum dot structures.* Physica E, **26** (1-4) 241-244.

Kümmell, T., Sauerwald, A., Somers, A., Löffer, A., Reithmaier, J.P., Forchel, A., & Bacher, G. 2006. *Structural and optical analysis of size-controlled InAs quantum dashes.* Physica E. **32** (1-2)108-110.

Lang, C., 2003. *Compostion of self-assembled quantum dots.* Materials Science and Technology. **19** (4) 411-421.

Lapierre, R.R., Okada, T., Robinson, B.J., Thompson, D.A., & Weatherly, G.C., 1996. *Lateral composition modulation in InGaAsP strained layers and quantum wells grown on (100) InP by gas source molecular beam epitaxy.* Journal of Crystal Growth **158** (1-2) 6-14.

LaPierre, R.R., Robinson, B.J., & Thompson, D.A. 1998. *Growth mechanisms of III–V compounds by atomic hydrogen-assisted epitaxy.* Journal of Crystal Growth. **191** (3) 319-331.

Lee, T-P. 1991. *Recent advances in long-wavelength semiconductor lasers for optical fiber communication.* Proceedings of the IEEE. **79** (3) 253-276.

Lee, A.S.W., Hulko, O., Thompson, D.A., Robinson, B.J., & Simons, J.G. 2006. *Comparison of quantum well intermixing in GaAs structure using a low temperature grown epitaxial layer or a SiO_2 cap.* Journal of Applied Physics. **100** (2) 023101.

Ledentsov, N.N., Shchukin, V.A., Grundmann, M., Kirstaedter, N., Bohrer, J., Schmidt, O., Bimberg, D., Ustinov, V.M., Egorov, A.Y., Zhukov, A.E., Kopev, P.S., Zaitsev, S.V., Gordeev, N.Y., Alferov, Z.I., Borovkov, A.I., Kosogov, A.O., Ruvimov, S.S., Werner, P., Gosele, U., & Heydenreich, J. 1996. *Direct formation of vertically coupled quantum dots in Stranski-Krastanow growth.* Physical Review B. **54** (12) 8743-8750.

Lei, W., Chen, Y.H., Xu, B., Jin, P., Wang, Y.L., Zhao, C., & Wang, Z.G. 2006 a. *Anomalous temperature dependence of photoluminescence peak energy in InAs/InAlAs/InP quantum dots.* Solid State Communications. **137** (11) 606-610.

Lei, W., Chen, Y.H., Jin, P., Ye, X.L., Wang, Y.L., Xu, B., & Wang, Z.G. 2006 b. *Shape and spatial correlation control of InAs-InAlAs-InP(001) nanostructures superlattices.* Applied Physics Letters. **88** (6) 063114.

Leifer, K., Buffat, P.A., Cagnon, J., Kapon, E., Rudra, A., & Stadelmann, P.A., *Quantitative imaging of InGaAs/GaAs layers using transmission electron microscopy methods: Characterization of stresses and chemical composition.* 2002. Journal of Crystal Growth. **237-239** (2) 1471-1475.

Lelarge, F., Dagens, B., Renaudier, J., Brenot, R., Accard, A., van Dijk, F., Make, D., Le Gouezigou, O., Provost, J.G., Poingt, F., Landreau, J., Drisse, O., Derouin, E., Rousseau, B., Pommereau, F. & Duan, G.H. 2007. *Recent advances on InAs/InP quantum dash based, semiconductor lasers and optical amplifiers operating at 1.55 μm.* EEE Journal of Selected Topics in Quantum Electronics. **13** (1) 111-124.

LemaÎtre, A., Patriarche, G., & Glas, F. 2004. *Compositional profiling of InAs/GaAs quantum dots.* Applied Physics Letters. **85** (17) 3717-3719.

Li, H., Wu, J., Wang, Z.G., & Daniels-Race, T. 1999. *High-density InAs nanowires realized in situ on (100) InP.* Applied Physics Letters. **75** (8) 1173-1175.

Li, Y.F., Lin, F., Xu, B., Liu, F.Q., Ye, X.L., Ding, D., & Wang, Z.G. 2001. *Influence of growth conditions on self-assembled InAs nanostructures grown on*

(001)InP substrate by molecular beam epitaxy. Journal of Crystal Growth. **223** (4) 518-522.

Liao, X.Z., Zou, J., Cockayne, D.J.H., Jiang, Z.M., & Wang, X. 2001. *Extracting composition and alloying information of coherent Ge(Si)/Si(001) islands from [001] on-zone bright-field diffraction contrast images.* Journal of Applied Physics. **90** (6) 2725-2729 .

Liao, X.Z., Zou, J., Cockayne, D.J.H., Wan, J., Jiang, Z.M., Jin, G., & Wang, K.L. 2002. *Alloying, elemental enrichment, and interdiffusion during the growth of Ge(Si)/Si (001) quantum dots.* Physical Review B. **65** (15) 153306.

Lin, Z-C., Lu, C-Y., & Lee, C-P. 2006. *Self-assembled InAs quantum wire lasers.* Semiconductor Science and Technology. **21** (9) 1221-1223.

Lin, Z.C., Lin, S.D., & Lee, C.P. 2008. *Ordering of stacked InAs/GaAs quantum-wires in InAlAs/InGaAs matrix on (100) InP substrates.* Physica E. **40** (3) 512-515.

Liu, F-Q., Wang, Z-G., Xu, B., Wu, J., & Qian J-J. 1998. *Metamorphosis of self-organized quantum dots into quantum wires.* Physics Letters A. **249** (5-6) 555-559.

Liu, X, Prasad, A., Nishio, G., Weber, E.R., Liliental-Weber, Z., & Walukiewicz, W. 1995. *Native point defects in low-temperature-grown GaAs.* Applied Physics Letters. **67** (2) 279-281.

Lochtefeld, A.J., Melloch, M.R., Chang, J.C.P., & Harmon, E.S. 1996. *The role of point defects and arsenic precipitates in carrier trapping and recombination in low-temperature grown GaAs.* Applied Physics Letters. **69** (10) 1465-1467.

Ma, W., Nötzel, R. Trampert, A., Ramsteiner, M., Zhu, H., Schönherr, H-P., & Ploog, K.H. 2001. *Self-organized quantum wires formed by elongated dislocation-free islands in (In,Ga)As/GaAs(100).*Applied Physics Letters. **78** (9) 1297-1299.

Maranganti, R., & Sharma, P. 2007. *Strain filed calculations in embedded quantum dots and wires.* Journal of Computational and Theoretical Nanoscience. **4** (4) 715-738.

Maes, J., Hayne, M., Sidor, Y., Partoens, B., Peeters, P.M., González, Y., González, L., Fuster, D., García, J.M., & Moshchalkov, V.V. 2004. *Electron wave-function spillover in self-assembled InAs/InP quantum wires.* Physical Review B. **70** (15) 155311.

Mazur, Yu. I., Liang, B. L., Wang, Z. M., Guzun, D., Salamo, G. J., Zhuchenko, Z. Ya. & Tarasov, G. G. 2006. *Excitonic transfer in coupled InGaAs/GaAs quantum well to InAs quantum dots.* Applied Physics Letters. **89** (15) 151914.

Meixner, M., Kunert, R., & Schöll, E. 2003. *Control of strain-mediated growth kinetics of self-assembled semiconductor quantum dots.* Physical Review B. **67** (19) 195301.

Michon, A., Saint-Girons, G., Beaudoin, G., Sagnes,I., Largeau, L., & Patriarche, G. 2005. *InAs/InP(001) quantum dots emitting at 1.55 μm grown by low-pressure metalorganic vapor-phase epitaxy.* Applied physics Letters. **87** (25) 253114.

Moison, J.M., Houzay, F., Barthe, F., Gérard, J.M., Jusserand, B., Massies, J.,& Turco-Sandroff, F.S. 1991. *Surface segregation in III-V alloys.* Journal of Crystal Growth. **111** (1-4) 141-150.

Molina, S.I., Ben, T., Sales, D.L., Pizarro, J., Galindo, P.L., Varela, M., Pennycook, S.J., Fuster, D., González, Y., & González, L. 2006. *Determination of the strain generated in InAs/InP quantum wires: prediction of nucleation sites.* Nanotechnology. **17** (22) 5652- 5658.

Molina, S.I., Varela, M., Sales, D.L., Ben, T., Pizarro, J., Galindo, P.L., Fuster, D., González, Y., González, L., & Pennycook, S.J. 2007. *Direct imaging of quantum wires nucleated at diatomic steps.* Applied Physics Letters. **91** (14) 143112.

Molina, S.I., Varela, M., Ben, T, Sales, D.L., Pizarro, J., Galindo, P.L., Fuster, D., Gonzalez, Y., Gonzalez, L., Pennycook, S.J. 2008. *A method to determine the strain and nucleation sites of stacked nano-objects.* Journal of Nanoscience and Nanotechnology. **8** (7) 3422-3426.

Nötzel, R., Ramsteiner, M., Menniger, J., Trampert, A., Schönherr, H-P., Däweritz, L., & Ploog, K.H. 1996. *Micro-Photoluminescence Study at Room Temperature of Sidewall Quantum Wires Formed on Patterned GaAs (311)A Substrates by Molecular Beam Epitaxy.* Japanese Journal of Applied Physics. **35** (3A) L297-L300.

Ohring, M. 2002. *The Materials Science of Thin Films.* 2nd edition, Academic Press, San Diego.

Okada, T., Weatherly, G.C. & McComb, D.W. 1997. *Growth of strained InGaAs layer on InP substrates.* Journal of Applied Physics. **81** (5) 2185-2196.

Ooi, B.S., Djie, H.S., Wang, Y., Tan, C.L., Hwang, J.C.M., Fang X.M., Fastenau, J.M., Liu, A.W.K., Dang, G.T.,& Chang, W.H. 2008. *Quantum dashes on InP substrate for broadband emitter applications.* IEEE Journal of Selected Topics in Quantum Electronics. **14** (4) 1230-1238.

Pan, L. 2002. *GS-MBE growth of In(Ga)As self-organized quantum dots*. Master Thesis, McMaster University.

Panish, M.B., & Temkin, H. 1993. *Gas source molecular beam epitaxy. Growth and Properties of Phosphorus Containing III-V Heterostructures.* Springer-Verlag. Berlin, New York.

PDE Solutions, Inc., 2005. *FlexPDE User Guide,* Version 5.0. Antioch, CA.
Pearsall, T.P. (Ed.) 2000. *Quantum Semiconductor Devices and Technologies.* Kluwer Academic Publishers, Boston, Dordrecht, London.

Pearson, Chris., Dorin, C., Millunchick, Mirecki. J.,& Orr, B.G. 2004. *Imaging the evolution of lateral composition modulation in strained alloy superlattices.* Physical Review Letters. **92** (5) 056101.

Pehlke, E., Moll, N., Kley, A., & Scheffler, M. 1997. *Shape and stability of quantum dots.* Applied Physics A. **65** (6) 525-534.

Pei, Q.X., Lu, C., & Wang, Y.Y. 2003. *Effect of elastic anisotropy on the elastic fields and vertical alignment of quantum dots.* Journal of Applied Physics. **93** (3) 1487-1492.

Pennycook, S.J. 1989. *Z-contrast STEM for materials science.* Ultramicroscopy. **30** (1-2) 58-69.

Petroff, P.M., Logan, R.A., & Savage, A. 1980. *Nonradiative recombination at dislocations in III-V compound semiconductors.* Physical Review Letters. **44** (4) 287-291.

Petroff, P. M., Gossard, A. C., & Wiegmann, W. 1984. *Structure of AlAs-GaAs interfaces grown on (100) vicinal surfaces by molecular beam epitaxy.* Applied Physics Letters. **45** (6) 620-622.

Pfeiffer, L., West, K. W., Stormer, H. L., Eisenstein, J. P., Baldwin, K. W., Gershoni, D., & Spector, J. 1990. *Formation of a high quality two-dimensional electron gas on cleaved GaAs.* Applied Physics Letters. **56** (17) 1697-1699.

Polimeni, A., Patanè, A., Henini, M., Eaves, L. & Main, P.C. 1999. *Temperature dependence of the optical properties of InAs/$Al_yGa_{1-y}As$ self-organized quantum dots.* Physical Review B. **59** (7) 5064-5068.

Priester, C., & Grenet, G. 1998. *Surface roughness, strain and alloy segregation in lattice-matched heteroepitaxy.* Journal of Vacuum Science and Technology B. **16** (4) 2421-2425.

Priester, C., & Grenet, G. 2000. *Surface roughness and alloy stability interdependence in lattice-matched and lattice mismatched heteroepitaxy.* Physical Review B. **61** (23) 16029-16032.

Priester, C., & Grenet, G. 2001. *Role of spacer layers in non top-on-top vertical correlation in multistacked systems.* Physical Review B. **64** (12) 125312.

Porter, D.A., & Easterling, K.E. 2001. *Phase Transformations in Metals and Alloys.* 2nd edition, Nelson Thornes Ltd., Cheltenham, UK.

Raz, T., Shuall, N., Bahir, G., & Ritter, D. 2004. *Gallium diffusion into self-assembled InAs quantum dots grown on indium phosphide substrates.* Applied Physics Letters. **85** (16) 3578-3580.

Reithmaier, J.P., Somers, A., Deubert, S., Schwertberger, R., Kaiser, W., Forchel, A., Calligaro, M., Resneau, P., Parillaud, O., Bansropun, S., Krakowski, M., Alizon, R., Hadass, D., Bilenca, A., Dery, H., Mikhelashvili, V., Eisenstein, G., Gioannini, M., Montrosset, I., Berg, T.W., van der Poel, M., Mork, J. & Tromborg, B. 2005. *InP based laser and optical amplifier with wire-/dot-like regions.* Journal of Physics D: Applied Physics. **38** (13) 2088-2102.

Reithmaier, J.P., Eisenstein, G.,& Forchel, P. 2007. *InAs/InP quantum-dash laser and amplifiers.* Proceedings of the IEEE. **95** (9) 1779-1790.

Rickerby, D.G., Valdrè, G., & Valdrè, U. (Eds.) 1999. *Impact of electron and scanning probe microscopy on materials research.* Kluwer Academic Publishers, Dordrecht, Boston.

Robertson, M.D., Bennet, J.C., Webb, A.M., Corbett, J.M., Raymond, S.,& Poole, P.J. 2005. *The determination of the size and shape of buried InAs/InPquantum dots by transmission electron microscopy.* Ultramicroscopy. **103** (3) 205-219.

Robertson, M.D., Burns, M., & Morrison, T. 2006 a. *The preparation of semiconductor TEM specimens by Low-angle Polishing.* Microscopy Society of Canada Bulletin. **33** (1) 19-28.

Robertson, M.D., Bennett, J.C., Burns, M.M.J., & Currie, D. 2006 b. *The simulation of annular dark filed images of InAs/InP quantum dots.* Microscopy and Microanalysis. **12** (Supp 2) 714CD-715CD.

Rodt, S., Türck, V., Heitz, R., Guffarth, F., Engelhardt, R., Pohl, U.W., Straßburg, M., Dworzak, M., Hoffmann, A., & Bimberg, D. 2003. *Lateral carrier transfer in $Cd_xZn_{1-x}Se/ZnS_ySe_{1-y}$ quantum dot layers.* Physical Review B. **67** (23) 235327.

Rosenauer, A. 2003. *Transmission electron microscopy of semiconductor nanostructures –An analysis of composition and strain state.* Springer-Verleg, Berlin, Heidelberg, New York.

Roura, P., Bosch, J., Clark, S.A., Peiró, F., Cornet, A., Morante, J.R., & Williams, R.H. 1996. *Quantification by optical absorption of the coarse modulation observed by transmission electron microscopy in InGaAs layers grown on InP(100).* Semiconductor Science and Technology. **11** (9) 1310-1316.

Rouvière, J.L., & Sarigiannidou, E. 2005. *Theoretical discussions on the geometrical phase analysis.* Ultramicroscopy. **106** (1) 1-17.

Sanguinetti, S., Henini, M., Grassi Alessi, M., Capizzi, M., Frigeri, P., & Franchi, S. 1999. *Carrier thermal escape and retrapping in self-assembled quantum dots.* Physical Review B. **60** (11) 8276-8283.

Sarigiannidou, E. 2004. *Electron Microscopy and III-Nitride Nanostructure.* Ph.D Thesis, Université Joseph Fourier – Grenoble I Sciences & Géographie.

Sarigiannidou, E., Monroy, E., Daudin, B., Rouviere, J.L., & Andreev, A.D. 2005. *Strain distribution in GaN/AlN quantum-dot superlattices.* Applied Physics Letters. **87** (20) 203112.

Sauerwald, A., Kümmell, T., Bacher, G., Somers, A., Schwerberger, R. Reithmaier, J.R., & Forchel, A. 2005. *Size control of InAs quantum dashes.* Applied Physics Letters. **86** (25) 253112.

Schliwa, A., Stier, O., Heitz, R., Grundmann, M., & Bimberg, D. 2001. *Exciton level crossing in coupled InAs/GaAs quantum dot pairs.* Physica Status Solidi (B). **224** (2) 405-408.

Schneider, R., Kirmse, H., Hähnert, I., & Neumann, W. 1999. *High-resoultion analytical transmission electron microscopy of semiconductor quantum structures.* Fresenius' Journal of Analytical Chemistry. **365** (1-3) 217-220.

Shchukin, V.A., Ledentsov N.N., & Bimberg, D. 2004. *Epitaxy of nanostructures.* Springer, Berlin, New York.

Sidor, Y., Partoens, B., Peeters, F. M., Ben, T., Ponce, A., Sales, D. L., Molina, S. I., Fuster, D., Gonzalez, L., & Gonzalez, Y. 2007. *Excitons in coupled InAs/InP self-assembled quantum wires.* Physical Review B. **75** (12) 125120.

Solomn, G., Komarov, S., Harris, J., & Yamamoto, Y. 1997. *Increased size uniformity through vertical quantum dot columns.* Journal of Crystal Growth. **175/176** (2) 707-712.

Spence, J.C.H. 2003. *High-resolution electron microscopy.* Oxford University Express, New York.

Spivak, M. 1999. *A comprehensive introduction to differential geometry.* Chapter 3, Volume 3, 3rd edition, Publish or Perish, Inc. Huston, Texas.

Springholz G. 2005. *Three-dimensional stacking of self-assembled quantum dots in multilayer structures.* Comptes Rendus Physique. **6** (1) 89-103.

Sritirawisarn, N., van Otten, F.W.M., Eijkemans, T.J., & Nötzel, R. 2007. *Surface morphology induced InAs quantum dot or dash formation on InGaAsP/InP (100).* Journal of Crystal Growth. **305** (1) 63-69.

Stangl, J., Holý, V., & Bauer, G. 2004. *Structural properties of self-organized semiconductor nanostructures.* Review of Modern Physics **76** (3) 725-783.

Stintz, A., Rotter, T.J., & Malloy, K.J. 2003. *Formation of quantum wires and quantum dots on buffer layers grown on InP substrates.* Journal of Crystal Growth. **255** (3-4) 266-272.

Suárez, F., Fuster, D., González, L., González, Y., García, J. M., & Dotor, M. L. 2006. *Self-assembled InAs quantum wire lasers on (001) InP at 1.6 μm.* Applied Physics Letters. **89** (9) 091123.

Takeuchi, M., Shiba, K., Huang, H. K., Sato, K., Inoue, K., Maehashi, K., & Nakashima, H. 1995. *Structural analysis of AlGaAs quantum wires on vicinal (110) GaAs by transmission electron microscopy and energy dispersive X-ray spectroscopy.* Journal of Crystal Growth, **150** (1-4) 441-445.

Tersoff, J., Teichert, C., & Lagally, M. 1996. *Self-organization in growth of quantum dot superlattices.* Physical Review Letters. **76** (10) 1675-1678.

Tournié, E., Brandt, O., & Ploog, K. 1993. *Optical properties of InAs quantum wells emitting between 0.9 μm and 2.5μm.* Semiconductor Science and Technology. **8** (1S) S236-S239.

Tuck, B. 1988. *Atomic Diffusion in III-V Semiconductors.* Adam Hilger, Bristol and Philadelphia.

Ustinov, V.M., Weber, E.R., Ruvimov, S., Liliental-Weber, Z., Zhukov, A.E., Egorov, A.Yu., Kovsh, A.R., Tsatsul'nikov, A.F.,& Kop'ev, P.S. 1998. *Effect of matrix on InAs self-organized quantum dots on InP substrate.* Applied Physics Letters. **72** (3) 362-364.

Vegard, L. 1921. *Die Konstitution der Mischkristalle und die Raumfüllung der Atome.* Zeitschrift für Physik. **5** (1) 17-26.

Voyles, P.M., Grazul, J.L.,& Muller, D.A. 2003. *Imaging individual atoms inside crystals with ADF-STEM.* Ultramicroscopy. **96** (3-4) 251-273.

Vurgaftman, I., Meyer, J.R., & Ram-Mohan, L.R. 2001. *Band parameters for III–V compound semiconductors and their alloy.* Journal of Applied Physics. **89** (11) 5815-5875.

Walther, T., & Humphreys, C.J. 1997. *Quantification of the composition of germanium/silicon structures by high angle annular dark filed imaging.* Electron Microscopy and Analysis. **153** (8) 303-306.

Wang, J., Robinson, B.J., Thompson, D.A., & Simmons, J.G. 1995. *InGaAs/InP quantum wires grown by gas source molecular beam epitaxy onto V-grooved InP substrates with (111)A facet sidewall.* Applied Physics Letters. **67** (16) 2358-2360.

Wang, P., Bleloch, A.L., Falke, M., Goodhew P.J., Ng, J., & Missous, M. 2006. *Direct measurement of composition of buried quantum dots using aberration-corrected scanning transmission electron microscopy.* Applied Physics Letters. **89** (7) 072111.

Wang, X.L., Voliotis, V., Grousson, R., & Ogura, M. 2000. *Improved heterointerface quality of V-shaped AlGaAs/GaAs quantum wires characterized by atomic force microscopy and micro-photoluminescence.* Journal of Crystal Growth. **213** (1-2) 19-26.

Wang, X.L., Chen, Y.H., Wu, J., Wang, Z.G., & Zeng, Y.P. 2005. *Self-organized superlattices along the [001] growth direction in $In_{0.52}Al_{0.48}As$ layers grown on nominally (001) InP substrates by molecular beam epitaxy.* Superlattices and Microstructures. **38** (3)151-160.

Wang, X.L., & Voliotis, V. 2006. *Epitaxial growth and optical properties of semiconductor quantum wires.* Journal of Applied Physics. **99** (12) 121301.

Wang, Y., Djie, H.S., & Ooi, B. S. 2006. *Group-III intermixing in InAs/InGaAlAs quantum dots-in-well.* Applied Physics Letters. **88** (11) 111110.

Wang, Z.L. (Ed.) 2000. *Characterization of nanophase materials.*Wiley-VCH, Weinheim, New York.

Wang, Z.M. (Ed.) 2008. *Self-assembled quantum dots.* Springer, New York.

Werner, P., Scheerschmidt, K., Zakharov, D.N., Hillebrand, R., Grundmann, M., & Schneider, R. 2000. *Quantum Dot Structures in the InGaAs System Investigated by TEM Techniques.* Crystal Research and Technology. **35** (6-7) 759-768.

Williams, D.B., & Carter, C.B. 1996. *Transmission Electron Microscopy-A Textbook for Materials Science.* Plenum Press, New York, London.

Wohlert, D.E., Chou, S.T., Chen, A.C., Cheng, K.Y., & Hsieh, K.C. 1996. *Observation of temperature-insensitive emission wavelength in InGaAs strained multi-quantum-wire heterostructures.* Applied Physics Letters. **68** (17) 2386-2388.

Wu, J., Chen, Y.H., & Wang, Z.G. 2008. *Epitaxial semiconductor quantum wires.* Journal of Nanoscience and Nanotechnology. **8** (7) 3300-3314.

Wu, X., Robertson, M.D., Gupta, J.A., & Baribeau, J-M. 2008. *Strain contrast of GaNyAs1-y (y=0.029 and 0.045) epitaxial layers on (100) GaAs substrates in annular dark filed images.* Journal of Physics-Condensed Matter. **20** (7) 075215.

Yin, Z., & Tang, X. 2007. *A review of energy bandgap engineering in III-V semiconductor alloys for mid-infrared laser applications.* Solid-State Electronics. **51** (1) 6-15.

Yoo, Y-H., Lee, W., & Shin, H. 2004. *Inhomogeneous strain state in a rectangular InGaAs quantum wire/GaAs barrier specimen for cross sectional high-resolution transmission electron microscopy.* Journal of Applied Physics. **96** (3) 1644-1648.

Zhang, Y.C., Huang, C.J., Liu, F.Q., Xu, B., Wu, J., Chen, Y.H., Ding, D., Jiang, W.H., Ye, X.L., & Wang, Z.G. 2001. *Thermal redistribution of photocarriers between bimodal quantum dots.* Journal of Applied Physics. **90** (4) 1973-1976.

Zhang, Q., Zhu, J., Ren, X., Li, H., & Wang, T. 2001. *Mismatch and chemical composition analysis of vertical $In_xGa_{1-x}As$ quantum-dot arrays by transmission electron microscopy.* Applied Physics Letters. **78** (24) 3830-3832.

Zhang, Z.H., Pickrell, G.W., Chang, K. L., Lin, H. C., Hsieh, K. C., & Cheng, K. Y. 2003. *Surface morphology control of InAs nanostructures grown on InGaAs/InP.* Applied Physics Letters. **82** (25) 4555-4557.

Zhao, F.A., Wu, J., Jin, P., Xu, B., Wang, Z.G.,& Zhang, C.L. 2004 a. *InAs nanostructure grown with different growth rate in InAlAs matrix on InP (0 0 1) substrate.* Physica E. **23** (1-2) 31-35.

Zhao, F.A., Chen, Y.H., Ye, X.L., Jin, P., Xu, B., Wang, Z.G., & Zhang C.L. 2004 b. *Growth of nanostructures on composition-modulated InAlAs surfaces.* Journal of Physics: Condensed Matter. **16** (43) 7603-7610.

Zhi, D., Davock, H., Murray, R., Roberts, C., Jones, T.S., Pashley, D.W., Goodhew, P.J., & Joyce, B.A. 2001. *Quantitative compositional analysis of InAs/GaAs quantum dots by scanning transmission electron microscopy.* Journal of Applied Physics. **89** (4) 2079-2083.